

UNCLASSIFIED

AD 417572

DEFENSE DOCUMENTATION CENTER

FOR

SCIENTIFIC AND TECHNICAL INFORMATION

CAMERON STATION, ALEXANDRIA, VIRGINIA



UNCLASSIFIED

NOTICE: When government or other drawings, specifications or other data are used for any purpose other than in connection with a definitely related government procurement operation, the U. S. Government thereby incurs no responsibility, nor any obligation whatsoever; and the fact that the Government may have formulated, furnished, or in any way supplied the said drawings, specifications, or other data is not to be regarded by implication or otherwise as in any manner licensing the holder or any other person or corporation, or conveying any rights or permission to manufacture, use or sell any patented invention that may in any way be related thereto.

417572

Technical Report

No. 299

Phased Array Radar Studies

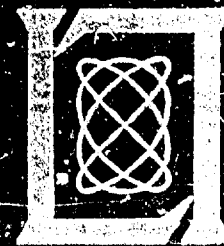
1 July 1961 to 1 January 1963

J. L. Allen
D. M. Bernella
W. W. Carpenter
W. P. Delaney
J. DiBartolo
A. J. Fallo
H. J. Greenberger
W. J. Ince
M. Siegel
S. Sperrin
D. H. Temme
L. Cartledge, Editor

20 February 1963

Lincoln Laboratory

MASSACHUSETTS INSTITUTE OF TECHNOLOGY



MASSACHUSETTS INSTITUTE OF TECHNOLOGY
LINCOLN LABORATORY

PHASED ARRAY RADAR STUDIES

1 JULY 1961 to 1 JANUARY 1963

J. L. ALLEN
D. M. BERNELLA
W. W. CARPENTER
W. P. DEJANEY
J. DIBARTOLO
A. J. FALLO

H. J. GREENBERGER
W. J. INCE
M. SIEGEL
S. SPOERRI
D. H. TEMME
L. CARTLEDGE, *Editor*

Group 41

TECHNICAL REPORT NO. 299

20 FEBRUARY 1963

LEXINGTON

MASSACHUSETTS

ABSTRACT

This is the third in a series of reports describing the work of the Lincoln Laboratory phased array project. This report covers the period from 1 July 1961 to 1 January 1963. Effort prior to this time is covered in Lincoln Laboratory Technical Reports No. 228 and No. 236.

The project effort is directed toward investigation of components, techniques and the fundamental theoretical limitations of arrays for high-power high-resolution radar applications.

The range of components investigated includes low-noise R.F. amplifiers, stable IF amplifiers, high-power modularized transmitters, high-speed microwave switches and several types of digital microwave phase shifters. Basic limitations to the power-handling capabilities of semiconductor diodes and strip transmission lines are being investigated. Specialized test equipment has been assembled to aid in components investigations.

Techniques work continues in the area of synthesis and use of low-loss passive simultaneous multiple beam-forming systems.

A modular electronically steered transmitter has been added to the 16-element linear test array to replace the original fixed broad-beam illuminator, and a receiving system using simultaneous beam-forming techniques is under construction.

Studies of the fundamentals of arrays include consolidation of the mutual coupling theory and studies of the effects of such coupling on unequally spaced arrays. The relationship between transmitter efficiency and transmitted pulsewidth is examined and expressions are derived for minimizing the cost of certain array systems when the per-element costs are known.

All these activities are guided and directed by continuing studies of system applications for high-resolution arrays. Since these studies are classified, they are not reported in this document.

TABLE OF CONTENTS

Abstract	iii
----------	-----

PART 1 INTRODUCTORY MATERIAL

Chapter	
I. PROJECT AND REPORT ORGANIZATION	1
A. Introduction	1
B. Project Philosophy	1
C. Report Contents and Organization	2
II. TEST FACILITIES	3
A. Linear Array Radar Facility	3
B. Receiver Test Facility	3
C. High-Power Facility	7
D. Transmitter Test Facility	7
E. Power Supply and Distribution	7
F. Phased Array Receiver Operation	10
G. Typical Stability	10

PART 2 TECHNIQUES AND COMPONENTS

I. MICROWAVE TECHNIQUES AND COMPONENTS	13
Summary	13
A. Introduction	13
B. RF Diode Strip Line Switch Design	15
C. A 900-Mcps Digital Phase Shifter	18
D. Variation in Phase Shifter Attenuation	27
E. Phase Shifter Alignment and Measurement Procedure	27
F. Limitations of Stepped Phase Shifters and Time Delays	28
G. 900-Mcps Duplexer-Monitor Board	29
H. Limiters	33
I. Modulator Switches	33
J. Beam-Forming Studies	34
K. Impedance Measurements on Array Antenna Elements	35
L. A 900-Mcps Bridge	36
M. Ferrite Phase Shifters	38
II. LOW-NOISE AMPLIFIERS	41
Summary	41
A. Introduction	41
B. Tunnel Diode Amplifiers	42
C. Tunnel Diode Down-Converters	72
D. Local Oscillator Effects in Tunnel Diode Receivers	74
E. Electron-Beam Parametric Amplifier (EBPA) Evaluation Program	77
III. INTERMEDIATE-FREQUENCY AMPLIFIERS FOR PHASED ARRAYS	79
Summary	79
A. Introduction	79
B. Basic Transformer Requirements for Good Frequency Response	80
C. Analysis of a Typical Stage	85
D. Practical Amplifiers	85

PART 2 (Continued)

Chapter

IV. A PHASED ARRAY RECEIVING SYSTEM	91
Summary	91
A. Introduction	91
B. RF Beam-Forming and Beam-Selection System	93
C. Solid State Receivers	99
D. Interbeam Interpolation System	99
V. TRANSMITTER DEVELOPMENT	109
Summary	109
A. Introduction	109
B. 900-Mcps Transmitter System	109
C. Circuit and Component Description of 900-Mcps System	113
D. 900-Mcps Amplifier Performance	129
E. Transmitter Power Control Circuits	131
F. Solid State Modulator Studies for 100-kw Phased Array Transmitter Tube	132
G. Hybrid Arrays for Greater Bandwidth	135
H. Power Amplifier Tubes for Phased Arrays	137
VI. SPECIAL-PURPOSE TEST EQUIPMENT	141
Summary	141
A. Introduction	141
B. Automatic Data Printer	141
C. Coherent Frequency Synthesizer	146
D. Short-Pulse Test Equipment	151

PART 3

SUPPORTING STUDIES

I. MUTUAL COUPLING IN LARGE ARRAYS	159
Summary	159
A. Introduction	159
B. Basic Investigations	160
C. Effects of Mutual Coupling on an Unequally Spaced Dipole Array	176
Appendix A	185
II. A QUANTITATIVE EXAMINATION OF THE RADAR RESOLUTION PROBLEM	189
III. SHORT PULSE EFFECTS ON TRANSMITTER EFFICIENCY	191
Summary	191
A. Introduction	191
B. Beam Pulse Efficiency	191
C. Total Pulse Efficiency	196
D. Practical Examples	198
E. Conclusions	202
IV. MINIMUM-COST ARRAY CONFIGURATIONS	205
Summary	205
A. Introduction	205
B. Surveillance Case	205
C. Tracking Case	206
Appendix A. Partial Differentiation with a LaGrangian Multiplier	209

For convenience in ordering copies of Lincoln Laboratory reports cited in this document, each reference is followed by its ASTIA number. In addition, Unclassified (released) reports have also been assigned Hayden serials (designated H-), indicating that they are obtainable, at cost, as microfilm or photoprint copies from the Microreproduction Laboratory, Hayden Memorial Library, M. I. T., Cambridge 39, Massachusetts.

PART 1
INTRODUCTORY MATERIAL

CHAPTER I
PROJECT AND REPORT ORGANIZATION

L. Cartledge

A. INTRODUCTION

This report describes the activity of the phased array radar program of the Special Radars Group of Lincoln Laboratory for the period 1 July 1961 to 1 January 1963. This is the third summary report of this project, the other two being Lincoln Laboratory Technical Reports No. 228* and No. 236.†

This report, like the earlier ones, describes all work carried out during the stated period as well as work still in progress. The work is reported in considerable detail, each section being written by the engineer directly responsible for the investigation. The report is intended primarily for workers in the field.

B. PROJECT PHILOSOPHY

Interest in phased array radar systems has increased over the past few years to the point where moderate-size, phased array radars are being developed by each of the three services. Problems encountered in the design and construction of these radars have made the need for development of components and techniques quite obvious. This project was conceived to help meet this need by concentrating efforts on the conception, design, construction and continued improvement of components and techniques for phased array radars.

While a separate project of moderate size concerned primarily with the development of components and techniques might well have been of questionable value in the conventional radar era, in the context of phased array radars such a project can produce significant results from a relatively small investment of time and money. The justification for this statement lies in the fact that while array radars are composed of very large numbers of duplicate parts, only a few distinct types are used. Just as manufacturers of "building blocks" for digital computers have made possible the economical and speedy construction of such computers, the development of components for arrays can make possible the reasonably economical and rapid construction of array radars. Indeed, with the present interest in "one-of-a-kind" arrays on the part of the various using agencies, an effort toward standardizing the components for arrays may be the only method for realizing the mass production economies that are commonly attributed to large phased arrays. For example, our studies and conversations with tube manufacturers indicate that true mass production economies are not realized until the manufacturer reaches a sustained production level on the order of a thousand tubes per month. Clearly, a single array would have to be very large or have a real maintenance problem to consume that kind of production.

*J. L. Allen, et al., "Phased Array Radar Studies, 1 July 1959 to 1 July 1960," Technical Report No. 228 [U], Lincoln Laboratory, M. I. T. (12 August 1960), ASTIA 249470, H-335.

†J. L. Allen, et al., "Phased Array Radar Studies, 1 July 1960 to 1 July 1961," Technical Report No. 236 [U], Lincoln Laboratory, M. I. T. (13 November 1961), ASTIA 271724, H-474.

Hence, guided by systems studies of potential long-range radar uses, the members of this project are trying to help meet the need for "building blocks" for the construction of high-power phased array radars. Toward this end, in addition to the direct work in component design and development, special test facilities have been constructed. These facilities are used to evaluate the various parts of the "building blocks" in appropriate environments over long periods of time and are modified as often as necessary to keep up with changing parameters in component development.

To guide the technique and component development, in addition to the systems studies mentioned previously, a continuing program of studies of the fundamental theory and limitations of arrays is being carried out.

In order to be of maximum benefit to the national phased array effort, a project such as this must maintain a continuous flow of information to and from other workers in array technology. Therefore, members of this project are continuing their attempt to maintain close contact with similar work by other organizations and have encouraged others to become familiar with this effort. Publication of reports such as this one represents only one part of the effort in this direction. We attempt to maintain personal contact with other government-supported array work in the country and encourage workers in both government and industry to visit with us here at the Laboratory. Despite the burden that such visits impose upon the available time of personnel, it is felt that the results have been well worth while, and we intend to continue this policy in the future. To maximize the utility of future meetings, however, it is hoped that those contemplating discussions with us will first avail themselves of the background information contained in this report and in TR-228 and TR-236.

C. REPORT CONTENTS AND ORGANIZATION

As stated in the introduction, this is a progress report. It describes work both completed and in progress during the period covered. We have attempted to discuss all significant work in detail, including projects that were unsuccessful where the lack of success would be meaningful to others in the field.

Since the responsibility for various facets of the project has been undertaken by individual engineers, the report has been written by the people directly concerned, with a minimum of alteration on the part of the editors. To promote further direct interchange of ideas on the topics discussed, the authors of individual sections have been indicated in the appropriate places. Where no name appears on a section, the author of the next highest division of the report is also the author of that section.

The report is divided into three parts. The first contains introductory material and a summary of the test facilities of the project. The second part deals with component and technique development and is subdivided so that each chapter deals with a major area of development. The third part deals with the supporting studies of array fundamentals and limitations. Most of the chapters in the report are preceded by a brief summary of the material contained therein. These summaries, along with the Table of Contents, should serve to acquaint the casual reader with the over-all content of the report and, hopefully, will direct the interested reader to the material of primary concern to him.

CHAPTER II TEST FACILITIES

A. LINEAR ARRAY RADAR FACILITY

L. Cartledge

The linear array radar facility described in TR-228 and TR-236 has been modified by the addition of a transmitting array and an alternate set of receiving electronics. This section will give a very brief overview of the facility. More detailed discussions of the various parts will be found later in this chapter, in subsequent chapters, and in previous reports.

Antenna and Feed System:— The antenna for the linear array facility consists of a line feed driving a solid-surfaced, offset-fed, parabolic cylinder reflector. The reflector, shown in Figs. 1-1 and 1-2, has a vertical aperture of 15 feet, a horizontal width of 24 feet and a focal length of 5 feet. It is mounted on a rotatable pedestal, along with supports for the feed and the array electronics.

The feed described in TR-236 has been replaced with a line of 18 dipoles that are vertically polarized.

The entire structure is still mounted in a 55-foot rigid radome on the roof of one of the Lincoln Laboratory buildings.

Transmitting System:— The transmitting array consists of 16 modular elements, each of which contains a digital diode phase shifter, a modulator, a power amplifier, a duplexer and a monitoring system. These modules, which are water-cooled, are shown in Fig. 1-3 and are described in detail in Part 2, Ch. VI. They are supplied from a centralized power supply system and provide 5 to 10 kw of peak power at a 1 percent duty ratio at a carrier frequency of 900 Mcps. The transmitter described in TR-236 is used as an RF driver, and a video driver is installed in the array control area.

Receiver Systems:— In addition to the receiver system described in TR-236, a receiver system consisting of a multiple beam-forming matrix, a low-level beam-selection switch, two solid-state receiver channels and an interpolator subsystem is being installed. A block diagram of this receiver setup is shown in Fig. 1-4. The beam-forming and beam-selection system is described in detail in Part 2, Ch. I. The other receiver sections are described in Part 2, Ch. IV. The array steering system described in TR-228 has been modified by the addition of switch drivers to drive the beam-selector switches.

Test Equipment:— The semiautomatic test systems described in the two previous Technical Reports have been modified and augmented. In particular, a centralized frequency synthesizer has been built, and a distribution system has been designed and is being constructed. This synthesizer (Fig. 1-5) will allow synchronized coherent operation of all equipment in the project (see Part 2, Ch. VI).

To ensure that the phase and amplitude measurements on the pulsed transmitters would be sufficiently accurate, it was necessary to design and build a high-quality microwave bridge. This bridge is shown in Fig. 1-6 and described in detail in Part 2, Ch. I.

B. RECEIVER TEST FACILITY

Because of the difficulties experienced in testing low-noise receivers in the "open," an 11 x 14-foot shielded receiver test room has been procured and installed. Inside the shielded



Fig. 1-1. Test facility reflector and array mount (through wide-angle lens).

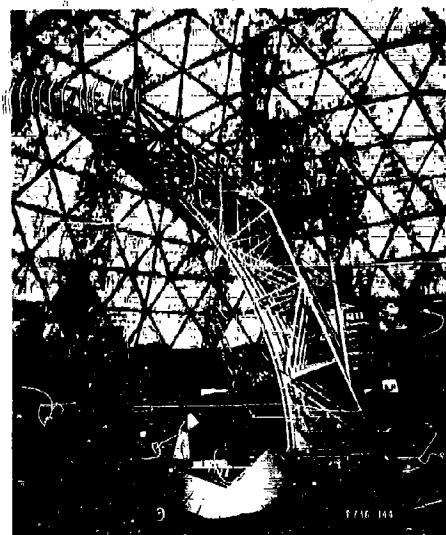


Fig. 1-2. Transmitting antenna mounted on present receiving reflector.

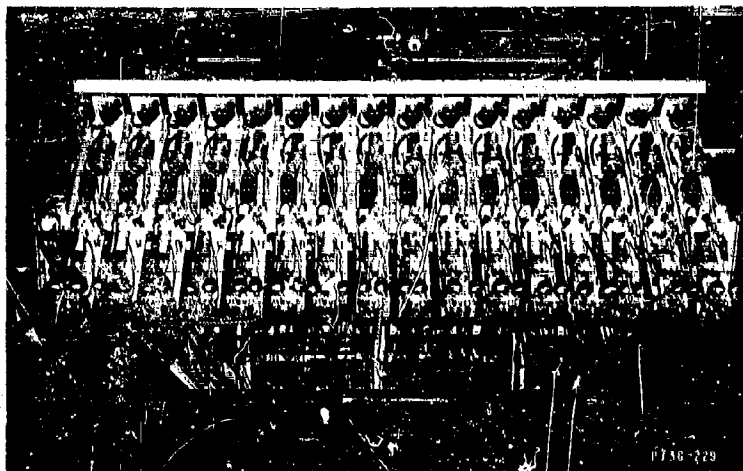


Fig. 1-3. Linear transmitting array with 16 modules installed.

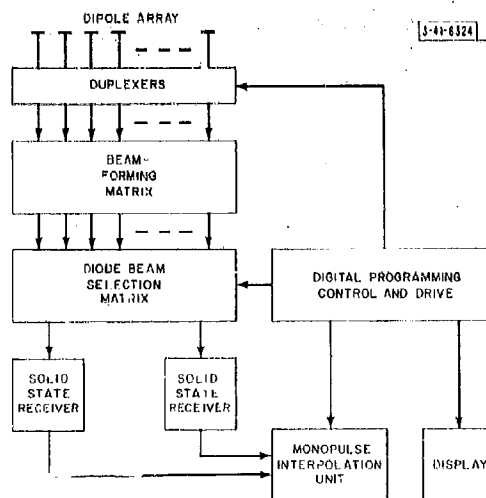


Fig. 1-4. Block diagram of receiver.

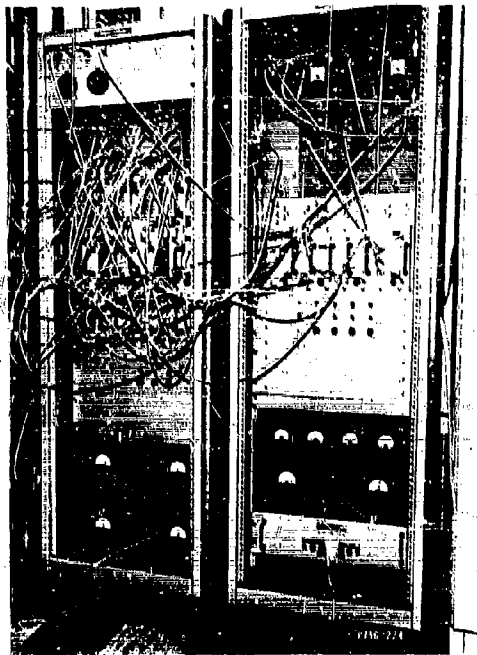


Fig. 1-5. Frequency synthesizer.

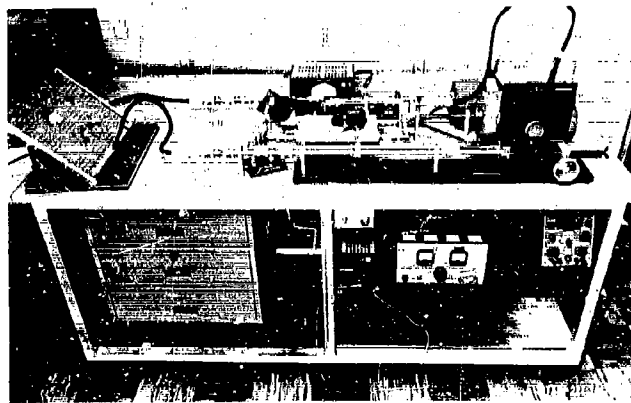


Fig. 1-6. 900-Mcps bridge.

room are an RF sampler and phase meter, as well as provisions for mounting several test receivers. A large number of through connections are supplied for the injection into the shielded room of low-frequency power and local oscillator and test-signal voltages from the centralized frequency synthesizer. This installation will allow long-term stability tests of low-noise receivers to be made semiautomatically in a relatively interference-free environment. Figure 1-7 shows 8 tunnel diode amplifiers, together with RF strips installed for test purposes.

C. HIGH-POWER FACILITY

The high-power RF testing facility described in TR-236 has been augmented with a corona water and a radioactive source that is used to assure the initiation of corona at the lowest possible gradients. These facilities are being used in a continuing investigation of the power-handling capabilities of strip line and microwave components. In addition, some facilities have been added for testing power distribution components at DC with video pulses applied. Figure 1-8 shows a high-voltage test bench which includes a source of direct-current voltage that is variable from 0 to 25 kv, and a source of short video pulses that can be varied from 0 to 25 kv. This bench is used for testing cables, connectors and other high-voltage components. The project recently acquired a 0- to 50-kv power supply and modulator complex that can produce a few kilowatts of average power at low duty ratios. This system, which is presently being installed, will be used for the testing of transmitting tubes and high-power DC and video components.

A centralized cooling water system has been installed (Fig. 1-9). This system is capable of holding coolant water temperature at 90°F while removing up to 15 kw of heat. It supplies ion-free and filtered cooling water to the linear array transmitter and to high-power and transmitter test facilities as needed.

D. TRANSMITTER TEST FACILITY

The 16 modules installed in the linear array are being tested for operational life. In addition, facilities are available for the bench operation of up to four more of the 900-Mcps transmitter modules. These facilities include complete test harnesses with dummy loads and measuring equipment. Modulation drive, RF drive, DC power and cooling water are supplied from the same systems that supply the transmitting array. This setup allows modules to be repaired, modified or readjusted in an environment closely matched to the one in which they are life-tested.

E. POWER SUPPLY AND DISTRIBUTION

A centralized power supply, distribution and control system (Fig. 1-10) for all the test array electronics has been implemented. Since no special effort has been expended to standardize the voltages, approximately 20 different DC voltages are required to operate the existing equipment. Well-regulated sources of these voltages have been obtained, and the voltages are now distributed in buses so that they are available essentially everywhere in the array area. A "standard" control panel and a remote switch have been developed so that any of these voltages can be applied to the equipment in a predetermined sequence. One-minute and 5-minute time delays are available. These control circuits are integrated with the transmitter control circuitry described in detail in Part 2, Ch. V.



Fig. 1-7. Receiver test setup installed in the shielded room.

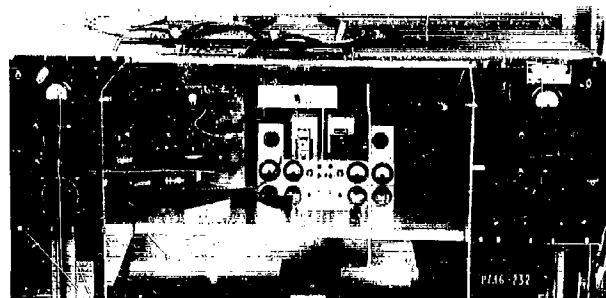


Fig. 1-8. High-voltage test bench.

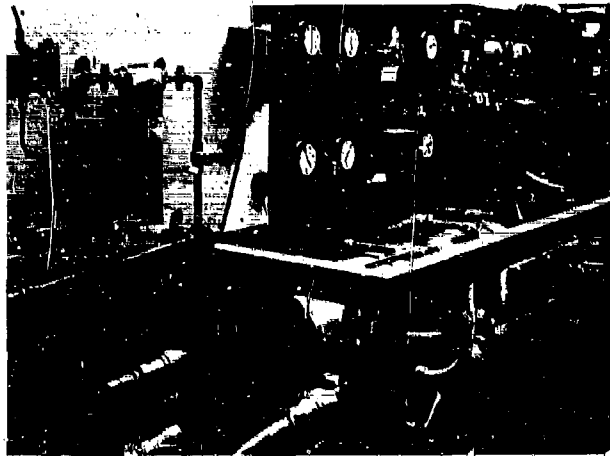


Fig. 1-9. Cooling water recirculator and heat exchanger.

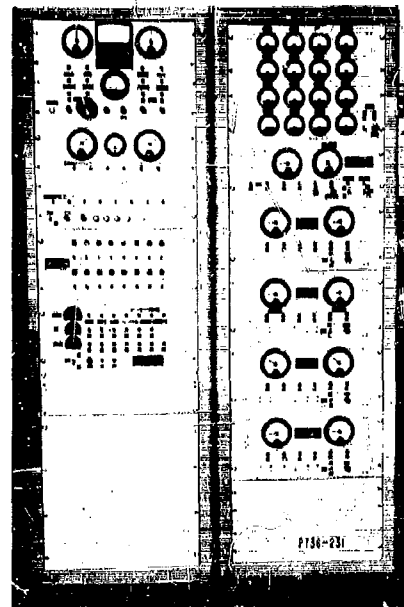


Fig. 1-10. Linear test array power controls.

F. PHASED ARRAY RECEIVER OPERATION

A. J. Fallo

The receiver array described in TR-236 has been operating on an 8-hour work day basis for over 6000 hours. Phases and amplitudes of the 16 channels are displayed simultaneously on an oscilloscope. In addition, a simulated antenna pattern is displayed on a 17-inch oscilloscope. This provides a means of checking the antenna sidelobes the result of which, in turn, is an indication of the array alignment.

A detailed report of results obtained with electron-beam parametric amplifiers in the receiver array can be found in G-Report 41G-1⁵. Although this report is concerned mainly with the electron-beam parametric amplifiers, a general idea of the phase and amplitude stability of the whole system can be deduced.

G. TYPICAL STABILITY

A. J. Fallo

1. The Test System

The test system described in TR-236 is an integral part of the phased array test facility. One of the many functions of the test system is the testing of phased array components for long-term phase and amplitude stability. The following test description is presented as an example of this function.

Several 900-Mcps balanced mixers were installed in four channels of the test rack in the system. The frequency synthesizer supplied appropriate signal and local oscillator inputs to the individual channels, each of which, from input to output, consisted of a 900-Mcps SAGE balanced mixer, a wideband 30-Mcps transistorized IF amplifier, a 2-Mcps transistorized converter and a 2-Mcps constant-amplitude phase shifter. The phase shifter was required for initial setting of phase and amplitude levels.

TABLE 1-1
AMPLITUDE LEVELS TAKEN AT ONE CLOCK TIME
(25 June 1962, 1208:00)

Amplitudes of various input signals	L1	-0.236	L2	-0.345	L3	-0.379	L4	-0.539
Output amplitudes (0.02 volt \Rightarrow 1 db)	A1	+0.169	A2	+0.167	A3	+0.169	A4	+0.170
Output phases (0.05 volt \approx 1°)	P1	-0.013	P2	-0.013	P3	-0.017	P4	+0.004

The 2-Mcps outputs from each channel were then fed into the IF sampler, which sampled the output of each channel and converted it into a 200-keps signal. The 200-keps sampled signal was then applied to the system's semiautomatic phase meter and also to a commercial AC-to-DC converter. The DC voltages, which were proportional to the phase and amplitude level of each channel, were thus produced for record by the automatic data printer. The automatic data printer also was used to advance the IF sampler to the next channel for another reading. Along

* J. H. Teele, "Operational Characteristics of 16 Electron-Beam Parametric Amplifiers in a 900 Mcps Phased Array," 41G-1101, Lincoln Laboratory, M. I. T. (6 August 1962), ASTIA 288223, H-444.

with this information, the amplitude levels of the signal and local oscillator sources were also recorded. A sample of the output record taken at one clock time is shown in Table 1-I. Readings may be taken automatically at preset intervals of 1 minute to 1 hour.

A computer program was written that calculates the rms error of a set of individual channel errors. The data were entered on IBM cards and processed (Figs. 1-11 and 1-12). Figure 1-11 is a plot of rms phase and amplitude vs time. Figure 1-12 is a plot of the phases and amplitudes of the 4 channels compared with each other as a function of time. Finally, Fig. 1-13, which was done by hand, is a plot of signal and local oscillator levels vs time.

2. Test Results

The rms graph (Fig. 1-11) indicates a variation in amplitude of 0 to 1.115 db and a phase difference of 0 to 5.931°. Note that the 4-channels graph (Fig. 1-12) varies in step with the rms graph. The information in Fig. 1-13 provides a clue to the explanation of these extreme variations. This graph shows that the large variation in the 900-Mcps signal and the 870-Mcps local oscillator levels occurred in the same time period as the extreme variations. Thus, a correlation exists between the graphs which suggests that the phase and amplitude variations were due to the changes in test signal and local oscillator levels. The cause for the signal and local oscillator level variation was found to be an unstable unit in the frequency synthesizer of the test system.

3. Conclusion

Although the results of the test were marred by the instability of the signal and local oscillator sources, it may be concluded that the test system operated satisfactorily.

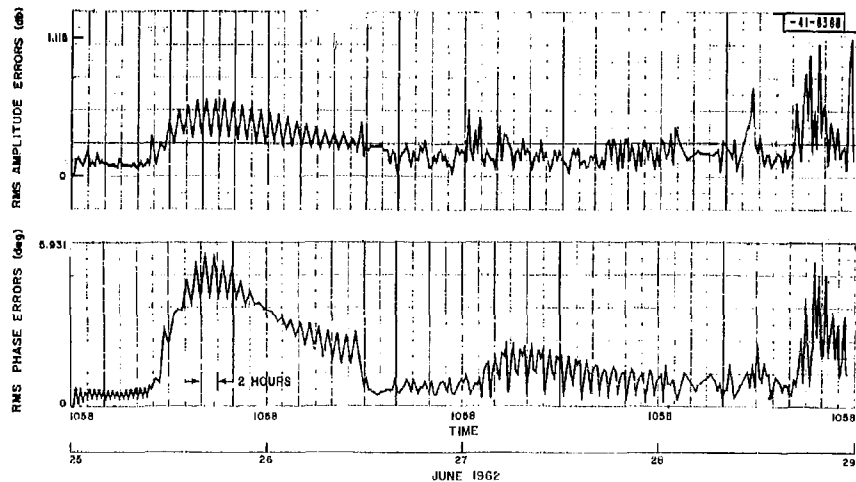


Fig. 1-11. Errors in rms phase and amplitude. Value at start of test is reference for zero errors.

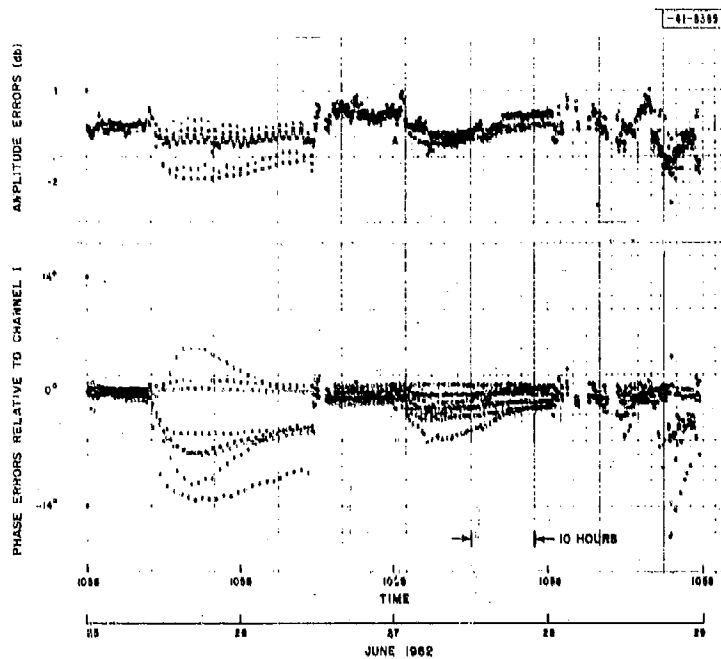


Fig. 1-12. Individual channel errors (for four channels under test).

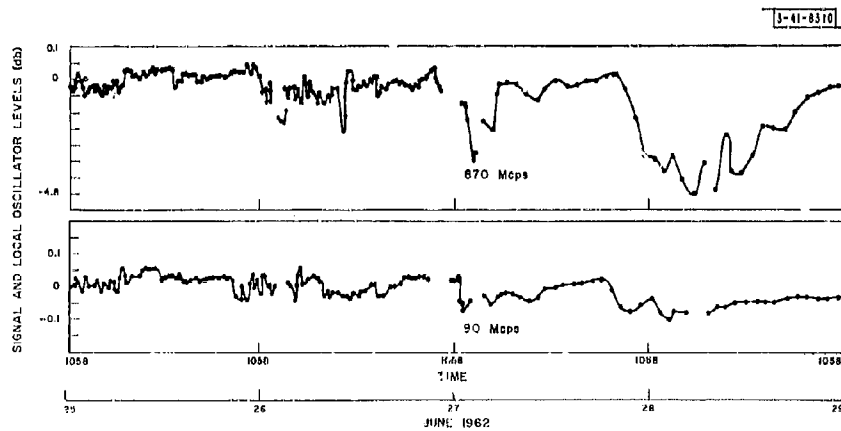


Fig. 1-13. Signal and local oscillator levels vs time (invalidated data indicated by a gap in the plots).

PART 2
TECHNIQUES AND COMPONENTS

CHAPTER I
MICROWAVE TECHNIQUES AND COMPONENTS

SUMMARY

This chapter describes the microwave component development work carried out during the reporting period. The first section describes the present RF diode switch that has been designed in strip line. An RF digital phase shifter, a duplexer, a modulator and a limiter employing similar switches or circuitry are then described. Subtopics include selection of diode types, phase-measuring considerations and techniques, phase and amplitude monitoring and strip line 3-db couplers. In the last sections, a passive multiple-beam beam-forming matrix, a small array for antenna element measurements and a very sensitive 900-Mcps RF bridge are described. Finally, some ferrite phase shifter development work supported by the Lincoln Laboratory phased array project is mentioned briefly.

A. INTRODUCTION*

D. H. Temme

The role of RF switches as digital microwave components useful in digital electronic scanning array control has been discussed in Technical Reports 228[†] and 236[‡]. Since most arrays will have a digital controller, the microwave elements being controlled should simply accept logic signals. The function of these logic signals is to control the routing and delaying of microwave signals to and from antennas. The reception and execution of such digital signals can readily be accomplished with good RF switches.

Such switches should have attributes like those of good digital logic components. They should be simple, cheap, reliable and operate with wide control signal margins. Intensive effort on the part of many workers has brought about good digital logic components for computers. It seems quite probable that only similar intensive effort will make arrays practical and that good RF switches and switchable delays will be among the basic "building blocks."

This chapter reports the past year's work with RF strip line diode switches. The design aspects of a single switch as currently conceived are discussed first, since they are a part of every application. In the discussion of applications, some subtopics appear that have broader scope than just switch design. However, since these topics arose in conjunction with switch work, they are included here.

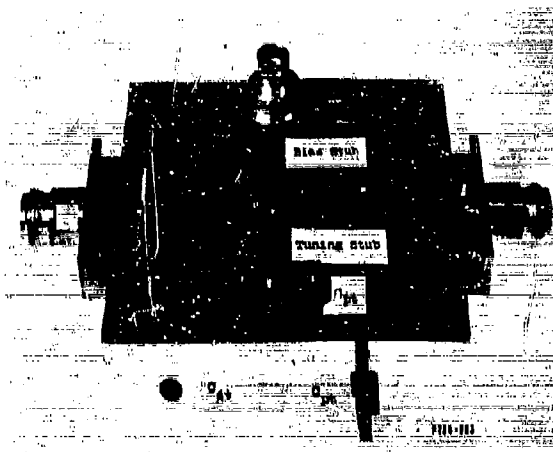
* The author would like to acknowledge the helpful discussions and advice of Dr. R. H. Rediker of Group 85 and Dr. A. Ullir of Microwave Associates. Also, a great deal of general information has been obtained from the following reports:

Bell Telephone Laboratories, "Microwave Solid State Devices," U. S. Army contract No. DA36-039 SC-85325.

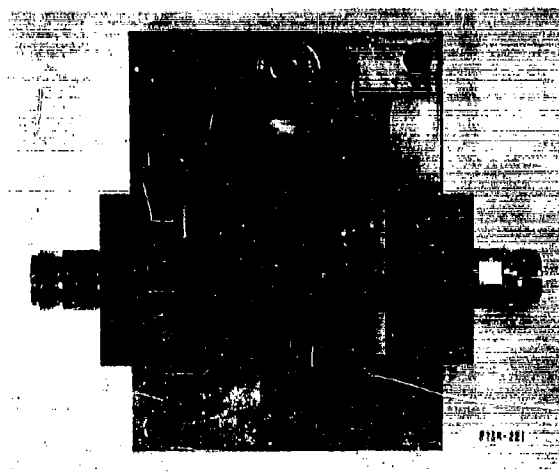
Microwave Associates, "Phase Shifter Study Program," Navy Department Bureau of Ships, Electronics Division, Contract No. NObnr-81470, Index No. SR 0080302-148.

† J. L. Allen, *et al.*, "Phased Array Radar Studies, 1 July 1959 to 1 July 1960," Technical Report No. 228 [U], Lincoln Laboratory, M. I. T. (12 August 1960), ASTIA 249470, H-335.

‡ J. L. Allen, *et al.*, "Phased Array Radar Studies, 1 July 1960 to 1 July 1961," Technical Report No. 236 [U], Lincoln Laboratory, M. I. T. (13 November 1961), ASTIA 271724, H-474.



(a) Opened structure.



(b) Assembled structure.

Fig. 2-1. RF diode strip line switch design.

B. RF DIODE STRIP LINE SWITCH DESIGN

D. H. Temme

Figures 2-1(a) and (b) show the present shunt RF diode strip line switch design, made of Teflon dielectric strip line. Figure 2-2 shows the lumped circuit equivalent. The significant circuit parameters when the switch provides isolation between the source and load are shown in Fig. 2-3. The DC forward bias is applied through the high-impedance branch composed of the inductive stub L_{iso} and bypass capacitor C_{bp} . The bias causes C_d to be effectively infinite. Two branches in Fig. 2-2, namely, the L_t, C_{pt} branch and the L_{iso}, C_{bp} branch, are high-impedance branches and can be neglected in calculating the isolation. The diode series resistance R_s , the mounting inductance L_B and the series tuning capacitance C_{st} are series-resonant at the center frequency. The isolation I is

$$I = \left| 1 + \frac{Z_0}{2Z_s} \right|^2 \quad (4)$$

where $Z_s = R_s + j(\omega L_B - 1/\omega C_{st})$.

The significant circuit parameters when the switch is reverse-biased and connects the source and the load are shown in Fig. 2-4. The net diode branch reactance X_c is essentially the reactance of diode reverse-bias capacitance C_d . The net inductive reactance X_l of the tuning stub consists of L_t and C_{pt} . These reactances are parallel-resonant, and the resultant insertion loss I is

$$I = \left| 1 + \frac{Z_0}{2Z_p} \right|^2 \quad (2)$$

where

$$\begin{aligned} Z_p &= jX_l || (R_s + jX_c) \\ &\approx \frac{L_B}{C_d R_s} \text{ at the resonant frequency} \\ &= R_s \left(\frac{L_B}{R_s} \right)^2 \end{aligned}$$

The cutoff frequency generally given in the diode specification is $f_c = 2\pi R_s C_d$.

In the structure, C_{st} is a parallel plate capacitor consisting of aluminum electrodes on Mylar. The electrodes are formed by evaporating at least one micron of aluminum on Mylar. Reproducible values of C_{st} have been obtained by this technique. The loss of Mylar is negligible at L-band for single diode switch isolations of less than about 50 db. The thickness tolerance of Mylar is superior to lower-loss dielectrics like Teflon and polyethylene.

An etched beryllium-copper tab 2 two mils thick placed between the capacitor and the diode provides the connection to the high-impedance DC bias stub. The quarter-wavelength stub is "shorted" with an RF bypass capacitor C_{bp} .

Several types of RF bypass were tried. A low-impedance quarter-wavelength open stub works well but takes considerable space. Figure 2-5 shows a more compact "symmetrical" capacitor construction in the board that seems to have negligible series inductance. The ground planes are extended inward to the center of the board. The center conductor (a two-mil-thick

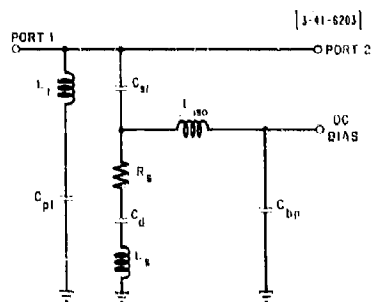


Fig. 2-2. Lumped circuit equivalent.

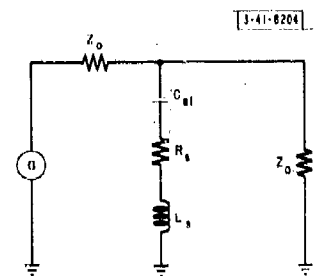


Fig. 2-3. Isolation state.

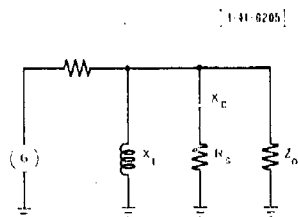
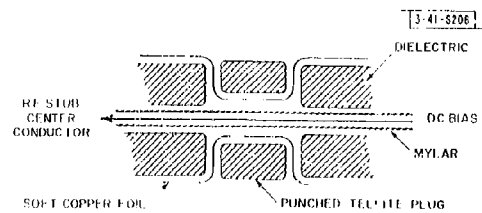


Fig. 2-4. Transmission state.

Fig. 2-5. Internal symmetrical capacitor.



piece of beryllium copper, sandwiched between Mylar) connects to the center strip of the dielectric board. At L-band frequencies, the insertion loss can be computed with sufficient accuracy by computing the parallel plate capacitance and inserting the reactance in the insertion loss formula [Eq. (4)]. The use of only one block is structurally simpler. However, this unbalances the line and "introduces series inductance." If the dimensions are carefully chosen to obtain series resonance, good isolation can be achieved over at least a 20 percent band. Another capacitor (Fig. 2-6), which has electrical symmetry between the input lead and ground, has been used successfully on the external surface of the board.

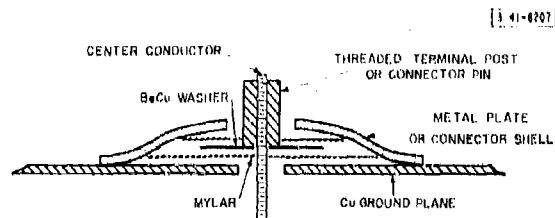


Fig. 2-6. External symmetrical capacitor.

Since the junction capacitance of some types of microwave diodes, unselected from a production run, varies considerably, a tunable inductive stub is provided with a variable capacitor terminating the stub. This is merely a screw extending from one ground plane to the center conductor. A piece of Mylar is placed between the center conductor and the screw to prevent shorting. This capacitor has some temperature sensitivity because of the thermal expansion of the Teflon board used. An integral, rigid two-plate capacitor could be, but has not been, constructed.

Some idea of the percentage bandwidths obtainable with such structures follows from circuit Q calculations of the lumped circuit equivalents in Figs. 2-3 and 2-4. These values set an upper limit. For the isolation state, $Q = \omega L_g / R_g$; for the transmission state, $Q \approx Z_0 / 2X_1$. The departure from these values is greatest for the transmission state because L_1 is a frequency-sensitive piece of transmission line. This departure is minimized by using the highest impedance readily attainable in strip line (about 200 ohms) and keeping the stub as short as possible to reduce the frequency sensitivity.

In phased array applications, the amplitude-phase characteristic (transfer function) is important. Generally, one can say that a switch or any network transfer function must satisfy at least the following two requirements.

- (1) It must insure the required signal summing in an array. A necessary and sufficient condition for meeting this requirement is that the deviation of the transfer function of corresponding networks from their nominal values be within appropriate tolerances (except the phase shifter or time delay discussed below, which has further restrictions). This can be checked simply by an amplitude-phase tracking measurement with two wideband 3-dB hybrids (Fig. 2-7). At L-band, it is possible to achieve an amplitude-phase sensitivity of 0.1 db - 1° over at least a 40 percent band.
- (2) The microwave network must preserve reasonably well the characteristics of video information required for signal processing. These requirements may vary greatly in different systems and must be analyzed for each system. Some measurements of this type are given below in the applications.

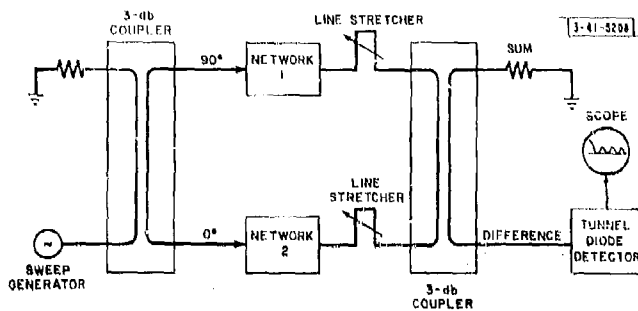


Fig. 2-7. Amplitude-phase tracking measurement.

Finally, the choice of circuit and diode parameters of the diode switch, which will depend on the application, is covered in each of the applications discussed below. (The reader interested in limitations imposed by the present diode fabrication technology is referred to a recent paper by Epperly.⁶)

C. A 900-Mcps DIGITAL PHASE SHIFTER

D. H. Tenney

In this section a 900-Mcps diode phase shifter is described and the experimental results obtained with it are given. Some design considerations, phase measurement techniques and state-of-the-art limitations of digital phase shifters are then discussed.

Figure 2-8 shows a 4-binary-digit RF diode phase shifter initially used in the Group 41 transmitting test array. Figure 2-9 is an RF schematic depicting the operation of two cascaded bits. It can be thought of as an "electronic line stretcher" that can be used for phase shifting or time delay. Energy entering port A is divided equally between the two diode arms. It is reflected from the diodes if forward-biased (isolating), or from the terminating capacitor if the diodes are reverse-biased (transmitting). This reflected energy sums at connection A and goes to the next bit. The differential line length introduced by one bit is equivalent to the change in phase of the reflection coefficient at a point in front of the diodes because of the introduction or removal of the sections of line behind them. If the diode were ideal, the terminating capacitor could be replaced by a fixed short, its location behind the diode being selected to give the differential line length desired. To accommodate varying junction capacitance of diodes and some tolerance in mechanical diode positioning, the effective electrical length of the stub behind the diode is appropriately adjusted with a terminating variable capacitor. This stub includes the reactance required to parallel-resonate the junction capacitance when the diode is reverse-biased. The bias structure is essentially the same as that described in the previous section. The RF bypass is the unbalanced series-resonant type described in Sec. B of this chapter, except that rivets instead of copper foil connect one capacitor plate to the ground plane.

Following is a list of test data obtained with units of the type shown in Fig. 2-8.

⁶W. F. Epperly, "Varactor Fabrication for Microwave Applications," Proc. National Electronics Conference, 18, 406 (1962).



(a) Opened structure.



(b) Assembled structure.

Fig. 2-8. Four-binary-digit RF diode phase shifter.

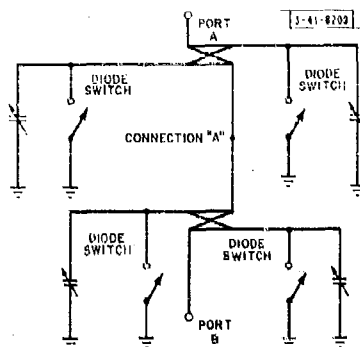


Fig. 2-9. RF schematic of two cascade bits.

Phase deviations	0° to 6° spread, 1.5° typical
Insertion loss	0.5 to 1.7-dB spread
VSWR	1.4 max, 1.2 typical
Power-handling capability	tested to 100-watt peak, 10- μ sec pulse, 1 percent duty
Reset time	about 1 μ sec
Forward bias	50 ma/diode, at least 25 percent variation permissible
Reverse bias	200 volts, 25 percent variation permissible

The device shown in Fig. 2-8 is temperature-sensitive because the terminating variable capacitors are temperature-sensitive. This problem has been solved by redesigning the capacitors in some later units.

There are numerous considerations in the design of a phase shifter or time delay. Those that have been investigated are reported next as subtopics.

3-dB Couplers:— The use of 3-dB cascade couplers with diode arms theoretically permits the construction of a balanced structure with a good match over a wide bandwidth. The construction of a "good" coupler has not yet been accomplished. The design criteria of Cohn* have been used as a guide. On the basis of these formulas, the parameters shown in Fig. 2-10 were chosen: $s = 27.0$ mils, $b = 277.0$ mils. Unfortunately, matching simply into the coupled section is difficult, and the type of entrance influences the coupling. Capacitive stubs have been used to tune the junction. The length of the stubs and the width of the coupled strip were varied until a VSWR of less than 1.1, an isolation of about 30 dB and an equal power division (within 0.1 dB) were achieved. The width of the coupled region in Fig. 2-8 is 127 mils. This contrasts with a width of 118 mils for a symmetrical coupler shown in Fig. 2-11.

The performance of a coupler is very apparent in a cascaded chain. Mismatches and unequal coupling are obvious in VSWR vs frequency plots. Figure 2-12 is a VSWR vs frequency trace of two different printed boards containing only the phase-shifter cascaded couplers. The physical difference is in the variation of the thickness of the center copper-clad 27-mil substrate board on

*S. B. Cohn, "Characteristic Impedances of Broadside-Coupled Strip Transmission Lines," Trans. IRE, PGMTT MTT-8, 633 (1960).

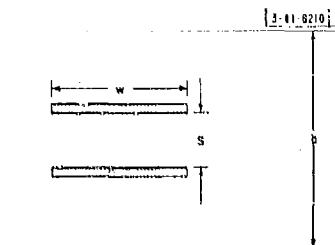
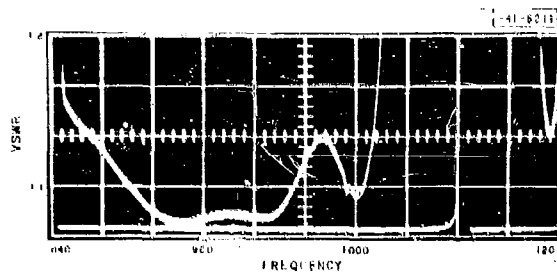


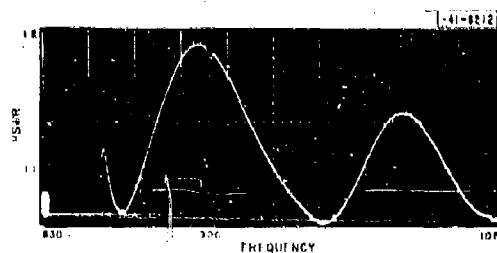
Fig. 2-10. Broadside coupled strips.



Fig. 2-11. Symmetrical coupler.



(a)



(b)

Fig. 2-12. VSWR vs frequency trace of two different four-cascaded coupler boards.

which the coupled strips were etched. The thickness tolerance on the Tellite board used was ± 1.5 mils. Recently, the manufacturer has been able to supply material having thickness tolerances of ± 0.5 mil. Improvements attainable with this tolerance have not been evaluated, but it is expected that such tolerances will permit the construction of "good" couplers. The insertion loss of a phase shifter without diodes is about 0.3 db. The phase shifters (without diodes) phase-track within 2° over a 10 percent band; the phase deviation from linear over this band is about $\pm 16^\circ$. This is probably satisfactory for systems using short pulse trains. The diode stubs, however, should have a constant electrical length characteristic, since they provide the phase shift or time delay.

Diode Selection:-- As a first step toward a 10-kw phase shifter, and in order to meet the present need of the 900-Mcps transmitting array, a diode with a power-handling capability of no more than a 100-watt peak for a 40- μ sec pulse was considered adequate. The PIN structure permits a large junction area and low reverse-bias capacitance. The large junction area helps to reduce the series resistance and to dissipate the heat due to losses. Several PIN types fabricated by Microwave Associates were tested by the manufacturer and the author. Some of the parameter variations of the PIN types were variations in the resistivity of starting materials, diffusion profiles and junction areas. Two lots of high-voltage varactors were also included in the tests. Evaluation criteria included breakdown voltage, forward-bias/reverse-bias RF impedance ratio, variation of RF impedance with forward bias and switching time. One PIN lot now manufactured by Microwave Associates as the MA-4248 seemed superior in all respects.

Several MA4248 PIN's have been DC-tested to a reverse voltage of 500 volts with no apparent avalanche current. A few of the units have avalanche voltages between 300 and 500 volts. The typical RF junction capacitance is 0.6 pf (a spread of about 0.1 pf) for reverse bias greater than 10 volts. The RF capacitance for a particular unit is essentially constant for voltages greater than 10 volts. When forward-biased to 50 ma, the series resistance is typically less than 1 ohm.

Although a thorough investigation of the power-handling capability of these diodes has not been made, some trials of an experimental procedure that may be adequate for such determinations have been made to ensure that the MA4248 is adequate for power levels required in the test transmitter. When the diode is forward-biased, the heat dissipation capability of the diode is the limiting factor. Therefore, information about the thermal properties of the diode is required. If the thermal properties of the silicon wafer and the connections to the wafer determine the dominant thermal factor, then the following first-order differential equation may be an adequate description of the thermal properties of a diode for engineering purposes:

$$C \frac{dT}{dt} = P_D - KT$$

where

C - thermal mass of the silicon wafer,

T - temperature rise of the wafer above the case temperature,

t - time,

P_D - diode dissipation,

K - heat conductivity factor relating the heat flow from the wafer to temperature.

The diode dissipation can readily be measured. Since the DC voltage-current characteristic of a diode function is temperature-dependent (see Fig. 2-13), the diode itself is a thermometer specifying the temperature (a detailed description would account for temperature variation within the wafer). The solution of the equation is

$$T = T_f(1 - e^{-t/\tau})$$

where

$T_f = P_D/K$, the final or steady-state temperature,

$\tau = C/K$, the thermal time constant.

Such a description is probably adequate for most diode applications, and Fig. 2-14 shows a diagram of the circuit that has been used to measure the two diode parameters τ and K when the above description does, indeed, hold. A pulse of RF power is applied to a forward-biased diode that terminates the line. The DC voltage drop of the diode is observed with an oscilloscope after the pulse. The bias-monitoring branch of the circuit must have good RF-DC isolation, and the circuit time constants must be chosen so as not to obscure the thermal time constants to be observed (readily checked by replacing the diode with a short). Figure 2-15 shows an oscillograph trace obtained with the circuit for an MA4248 diode. This particular diode was one from an early run and the time constant is on the order of 300 μ sec. Present units cluster around 700 μ sec, with

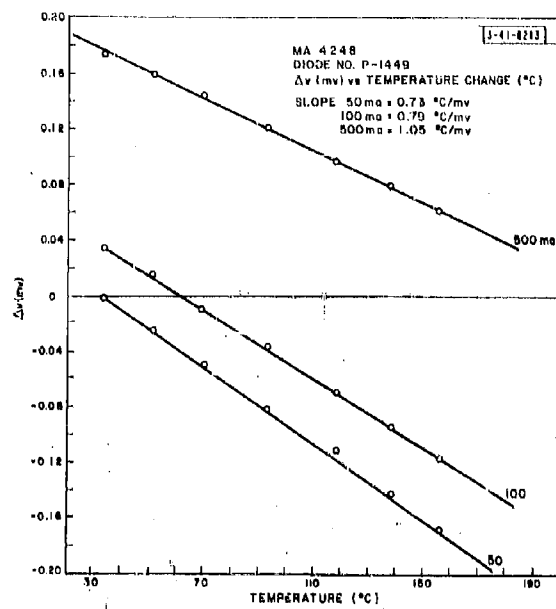


Fig. 2-13. Diode voltage vs temperature.

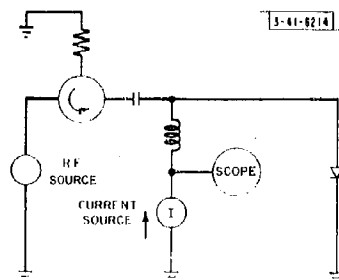
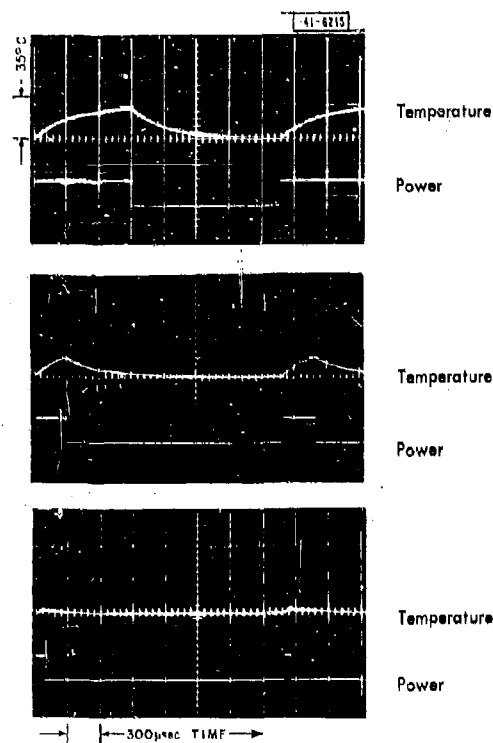


Fig. 2-14. Pulsed RF power dissipation test of diode.



An MA4248 diode of an early run
 Note: Peak RF Power = 60 watts

Fig. 2-15. Thermal time constant.

a spread of about 200 μsec . The typical value of K for a 50-ma bias is 0.2 watt/ $^{\circ}\text{C}$, with a spread of about 0.1. These values should be regarded only as indicative and should not be used for design purposes.

The next question is: What is a safe maximum junction temperature? There seems to be a considerable amount of life data on transistors, power rectifiers and varactors suggesting a relation between the logarithm of the failure rate and the inverse of the junction temperature.* A million-hour lifetime seems to be common for a junction temperature of 100 $^{\circ}\text{C}$. A junction temperature of 150 $^{\circ}\text{C}$ may increase the failure rate by a factor of 10. Similar life-test programs are being initiated for the MA4248.

A criterion for reverse-bias power-handling capability and reliability has not been found. The RF voltage can considerably exceed the reverse bias without forward conduction. Carriers cannot traverse the intrinsic region during an RF cyclic period. The charge injected during the positive swing is withdrawn during the negative swing before any substantial diffusion and recombination can occur. The injection and withdrawal of charge from the intrinsic region is not lossless.

* See, for example, D.S. Peck, "A Mesa Transistor Reliability Program," Solid State Journal 1, 25 (November/December 1960).

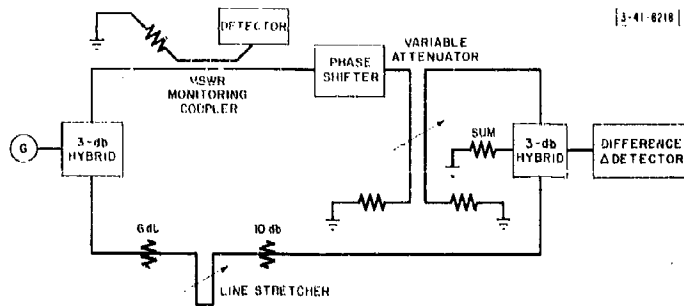


Fig. 2-16. Phase bridge for phase shifter alignment.

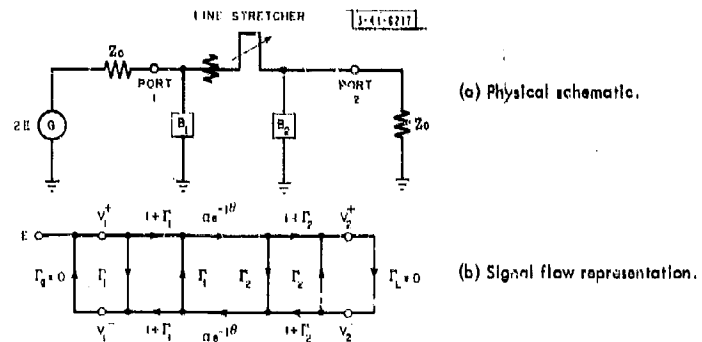
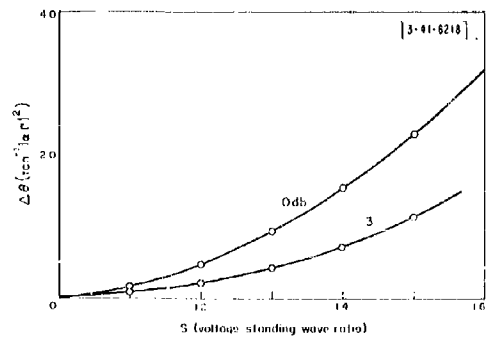


Fig. 2-17. Effect of mismatches on the phase of a transmitted signal.

Fig. 2-18. Phase errors due to mismatches.



the magnitude probably being functionally related to the amount of the injected charge. As an indication of the magnitude, the loss in db seems to be about double for RF swings of twice the bias voltage. Working-stress life tests of some sort seem in order if we are to learn more about reverse-bias power-handling capability, and such tests are under consideration.

For large reverse-bias power-handling capability, diode strings similar to power rectifier diode strings might be a solution. However, it seems that practicality for array application will be better assured by a better understanding of the reliability factors at RF frequencies.

D. VARIATION IN PHASE SHIFTER ATTENUATION

D. H. Tomme

No attempt was made to keep the attenuation of the phase shifter constant. This was not considered important for the Group 44 transmitting test array, since the power amplifier is run in a saturated state and can tolerate considerable input variation. If constant attenuation is desired, the reflection coefficient of the diode arm must be the same in each state. Either the junction area must be chosen appropriately for each bit or an appropriate characteristic impedance must be chosen for the diode arm of each bit. The latter choice requires an impedance transformer into the coupler. The choice will depend on system requirements such as bandwidth.

E. PHASE SHIFTER ALIGNMENT AND MEASUREMENT PROCEDURE

D. H. Tomme

Figure 2-16 is a schematic of the phase bridge used. This type of system was chosen because it does not have high standing waves anywhere and therefore permits good accuracy with reasonable component mismatches.

The effect of mismatches on the phase of the transmitted signal is illustrated in Fig. 2-17. When signal flow analysis is used,^{*} the ratio of the incident voltage V_1^+ at port 1 and load voltage $V_2 = V_2^+ + V_2^-$ at port 2 is

$$\frac{V_2}{V_1^+} = \frac{(1 + \Gamma_1)(1 + \Gamma_2) \alpha e^{-j\theta}}{1 - \alpha^2 \Gamma_1 \Gamma_2 e^{-j2\theta}}$$

$$= \frac{(1 + \Gamma)^2 \alpha e^{-j\theta}}{1 - \alpha^2 \Gamma^2 e^{-j2\theta}} \quad \text{when } \Gamma = \Gamma_1 = \Gamma_2 \quad (3)$$

where Γ_1, Γ_2 are the reflection coefficients corresponding to mismatch susceptances B_1, B_2 . Examination of this expression shows the variation from linear phase as the line stretcher is varied to be

$$\Delta\theta = \pm \tan^{-1} \left[\alpha^2 \Gamma^2 \right] \quad \text{for } |\alpha \Gamma| \ll 1 \quad (4)$$

It is common to define a mismatch in terms of the standing wave ratio S . Figure 2-18 is a plot of $\Delta\theta$ vs S . The inclusion of a pad with attenuation α shows how the judicious placement of "good" pads significantly reduces the deviation of phase from linear. Extension of this type of

* J. K. Hutton, "Analysis of Microwave Measurement Techniques by Means of Signal Flow Graphs," Trans. IRE, PGM-TT-8, 206 (1960).

analysis to a shunt and equal discontinuities with line stretchers, but no pads, between the discontinuities gives

$$\Delta\theta_n = n(n-1) \tan^{-1} |r|^2 \quad (5)$$

Many variable attenuators do not have constant input-output phase characteristics. A variable contradirectional coupler* was chosen as an attenuator, since it has quite constant phase between the input and the output signal at a spot frequency when the attenuation is about 15 db, for example. The coupling equation for the attenuator is

$$\frac{V_{out}}{V_{in}} = \frac{jk \sin \theta}{\sqrt{1 - k^2} \cos \theta + j \sin \theta} \quad (6)$$

where

k = voltage coupling factor,

θ = electrical length of the coupled region.

Thus, for a fixed frequency $k \ll 1$,

$$V_{out} \approx kV_{in} \quad (7)$$

When line stretchers and couplers of good quality are used, the phase bridge has a precision of 0.1° and an estimated accuracy of better than 0.5° .

To align the phase shifter, each bit is set to the desired value by adjusting the terminating variable capacitor while both the VSWR and phase shift are observed. How well the various bits sum is an indication of the "quality" of the phase shifter.

F. LIMITATIONS OF STEPPED PHASE SHIFTERS AND TIME DELAYS D. H. Temme

There are a number of factors that determine how well a stepped phase shifter or time delay will sum the individual steps. No attempt has been made to analyze the composite effect in one mathematical expression, because it is felt that it would be more unwieldy than valuable. However, the magnitude of these factors can be assessed. For this purpose, the phase shifter is thought of as cascaded line stretchers with shunt input susceptances. Equation (5) can be used to calculate the maximum errors of such "equivalent phase shifters." Magnitudes of such "equivalent susceptances" for various imperfections follow.

Mismatch of Coupler Junction:— The match of the junction into the coupled strip was empirical. A VSWR of 1.4, together with Eq. (5), indicated that one ought to make couplers with better VSWR.

Incorrect Coupling:— From scattering considerations, the input voltage standing wave ratio S of a coupler with unity reflecting arms and voltage coupling k is

$$S = \frac{k^2}{1 - k^2} \quad (8)$$

*B.M. Oliver, "Directional Electromagnetic Couplers," Proc. IRE 42, 1686 (1954).

For a 2.9-dB coupler, $S = 1.05$. From Eq. (5) it is apparent that this can cause a noticeable effect in the ability of a stepped phase shifter to sum the individual phase steps.

Dissimilar Diode Arms:— The input reflection coefficient of a perfect coupler with dissimilar diode arms and matched load is

$$\Gamma_{in} = 1/2(\Gamma_1 - \Gamma_2) \quad (9)$$

where Γ_1 and Γ_2 are the input reflection coefficients of the diode arms. To get a number, assume that good mechanical positioning of the diodes is possible and that tuning adjustments assure the same reflection coefficients (this is possible at a spot frequency — the application intended for the above phase shifter). If the standing wave ratio in one arm is 30 dB and that in the other is 34 dB (a value spread that has been experienced), the input standing wave ratio is 1.04. This can cause a noticeable summing effect.

The above cursory analysis indicates why summing errors of 6° (1.5° typical) have been measured. It is felt that the greatest payoff in effort will be in the improvement of the coupler, which appears feasible with the tighter Tallite board thickness tolerances that have just become available.

In conclusion, it is felt that a high-quality and reliable stepped phase shifter can be made if more attention is given to the many details during the development effort.

G. 900-Mcps DUPLEXER-MONITOR BOARD

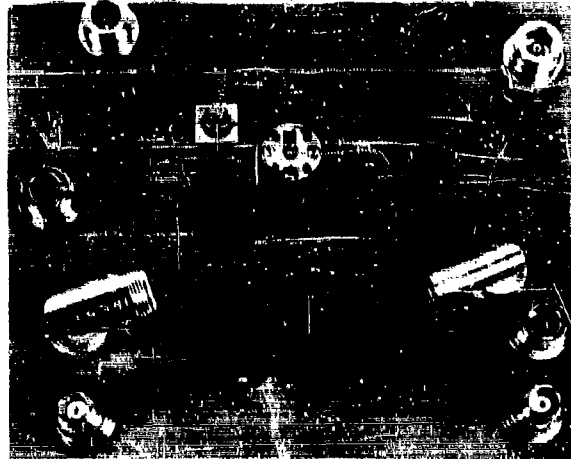
D. H. Temme

Figures 2-19(a) and (b) are photographs of the duplexer-monitor board used in the Group 41 transmitting test array. An RF schematic is shown in Fig. 2-20. Energy from the transmitter is routed via a circulator to the antenna. Reflection from the antenna due to mutual coupling goes back through the circulator and is routed by a balanced diode duplexer into a load. This scheme provides a good match for the transmitter. When it is received, the signal from the antenna goes through the circulator and is routed by the duplexer to the receiver.

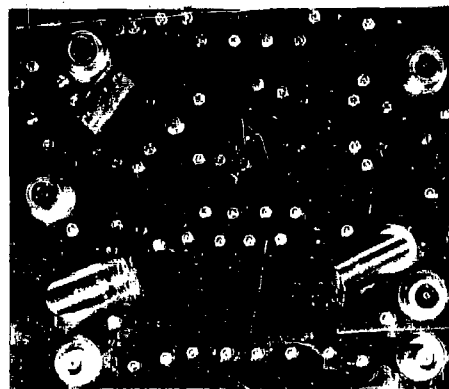
Following is a list of test data on the duplexer.

Receiver insertion loss	0.4 db at center frequency, 0.6 db at edge of 10 percent band
VSWR	less than 1.3 over 10 percent band for both receiver and transmitter
Receiver protection during transmit	greater than 60 db over 10 percent band
Power-handling capability	tested to 7-kw peak, 10- μ sec pulse, 1 percent duty
Diode switching time	about 1 μ sec
Forward bias	50 ma/mode
Reverse bias	30 volts

The 3-dB coupler design is identical to those used in the phase shifter. The diodes used in the balanced duplexer are Western Electric GA53692 PIN diodes. These units contribute about 0.2 dB toward the receiver insertion loss and about 40 dB of receiver protection at the center frequency. The switch following the balanced duplexer uses an MA4248 diode described under the phase shifter. This unit contributes about 0.4 dB to the receiver insertion loss and 30 dB of receiver protection at the center frequency.



(a) Opened structure.



P736-222

(b) Assembled structure.

Fig. 2-19. Monitor-duplexer assembly.

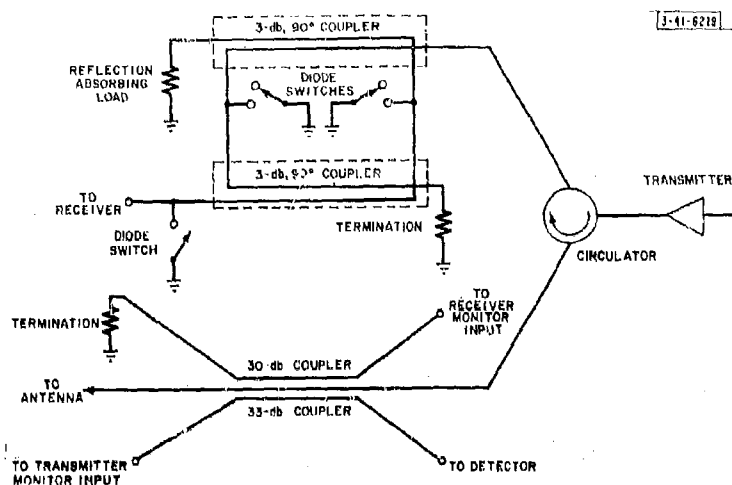


Fig. 2-20. Duplexer-monitor board.

Two couplers are included in the board. The upper (30-db) coupler is used to inject a test signal into the receiver. The internal termination on this coupler is a 50-ohm pill film resistor. The short capacitive stub behind the resistor parallel-resonates with the coupling inductance caused by the pill resistor unbalancing the line since it connects only to one ground plane. A VSWR of less than 1.4 for a 10 percent band can be obtained.

The lower coupler (33 db) is used for amplitude-phase monitoring of the transmitter module. Two signals fed into opposite arms of a 4-port coupler (see Fig. 2-21) will sum at one port and difference at the other port. If the reference input signal is -33 db of the transmitter output level and lags 90 degrees in phase, the reference signal and the transmitter output will sum at the antenna port and null at the detector port.

Originally, it was planned to put a glass packaged crystal detector in the board as an RF detector. This proved unsatisfactory for a number of reasons. First, the detector must withstand the sum power level, which is 43 db above the difference power corresponding to a 0.1-db amplitude error, or 1° phase error. For long life, a crystal detector should not be subjected to a peak power much above +20 dbm. For a transmitter power level of 10 kw (70 dbm), the signal at the detector port of the coupler should be 93 db [70 + (43 - 20)] below the main coupler line power level. It is difficult to suppress the parallel plate mode generated at points where the line is unbalanced, such as the coupler main-line right angle input connector, to this level.

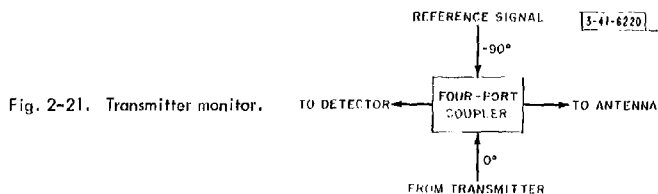


Fig. 2-21. Transmitter monitor.

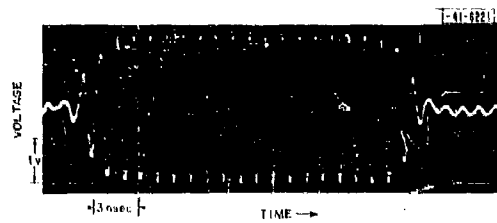


Fig. 2-22. Sample oscillograph of output of modulator switch.

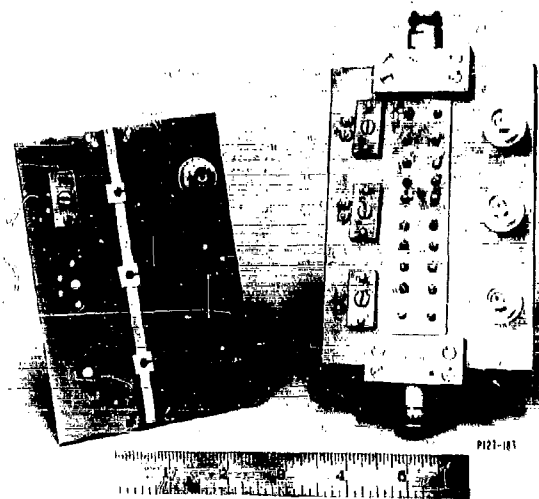


Fig. 2-23. Three-section one-watt modulator switch.

The minimum level at the detector port can be raised considerably by placing a varactor diode limiter in front of the crystal detector to protect it from sum power levels. If this is done, a harmonic filter must also be included in front of the crystal detector to remove the harmonics generated by the transmitter.

Simplicity was finally achieved by using a gold-doped P-N junction diode, the MA4303. It has sufficient rectification efficiency (1 mv across a 100-ohm load for input power of 5 mw) at 900 Mcps. A junction diode can withstand a much greater power level than most point contact diodes. Its rectification efficiency falls off with frequency and provides immunity to the transmitter harmonics. For expediency, the diode has been mounted in the alarm monitor box (Part 2, Ch. V). The mount is frequency-sensitive, but this is not a limitation since the transmitter operates at a spot frequency. A detected output with less than 1-db variation over greater than a 10 percent band can be obtained by placing the diode terminated by a symmetrical capacitor (see Fig. 2-5) in the strip line board.

H. LIMITERS

D. H. Temme

When the bias terminal of the switch in Fig. 2-1 is short-circuited, it is a limiter. For low signal levels, no appreciable charge is injected across the junction, and the zero bias capacitance of the diode shunts the line. For higher signal levels, some of the injected charge recombines and is effectively equivalent to a DC bias. The rest of the injected charge is recovered on the negative half of the RF cycle.

The insertion loss of the limiter rises to the insertion loss of the switch at high signal levels. The isolation can be peaked at intermediate power levels by adjusting the series tuning capacitor C_{st} (Fig. 2-2), since C_d is not infinite at these levels. The magnitude of the isolation at intermediate levels is somewhat lower than at high levels.

The insertion loss of the limiter is greater than, and the bandwidth of the limiter at low signal levels is less than, that of the switch, since the zero bias Q of the diode is typically one half, or less, of the Q of a reverse-biased diode.

I. MODULATOR SWITCHES

D. H. Temme

The generation of short, sharp RF pulses are of interest in many array applications. Such pulses can be generated readily by diode switches used as modulators. The switching speed of such switches depends upon their power-handling capability and operating frequency. Their power-handling capability depends primarily on the reverse voltage breakdown of the diode used. In general, the recovery time of a forward-biased diode is related to its reverse voltage breakdown; that is, a longer transition time from the low-impedance to high-impedance state is associated with a high-voltage breakdown. At low operating frequency, the bypass capacitance needed in the bias or drive circuit (see, for example, C_{bp} in Fig. 2-2) for good RF-DC isolation is large. The time required for the driver to change the charge of this capacitance can exceed the transition time and determine the switching time. The photograph in Fig. 2-22 shows the resulting switching speed of a 900-Mcps switch using a 6-volt varactor in which the RF isolation was sacrificed somewhat for switching speed.

A 3-section 1-watt modulator switch (diode type MA4335C) built for the PRESS radar program is shown in Fig. 2-23. Its performance is as follows:

Isolation	greater than 80 db over 10 percent band
Insertion loss	0.5 db at band center, less than 0.7 db at band edge
Input VSWR during transmission	less than 1.3 over the 10 percent band
Center frequency	1300 Mcps
Forward bias	3 ma/diode
Reverse bias	10 volts

The switching speed obtained with a driver built for the PRESS program was less than 10 nsec. The main switch construction problem was the suppression of the parallel plate mode caused by the diode shorting to only one ground plane. Screws placed within 100 mils of the center conductor edge provided sufficient mode suppression without seriously affecting the input VSWR during transmission.

J. BEAM-FORMING STUDIES

W. P. Delaney

A 900-Mcps, 16-element RF beam-forming matrix* that uses a new material and new packaging techniques to reduce the insertion loss has been tested. The matrix, which was designed and built by Advanced Development Laboratories, has good electrical and antenna performance with the added advantage of the compact package (18 x 32 x 1.5 inches) shown in Fig. 2-24. The

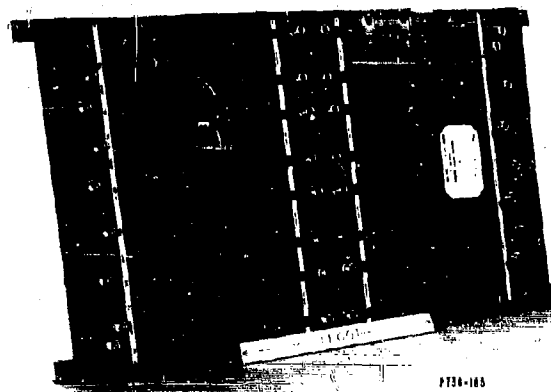


Fig. 2-24. 16-element beam-forming matrix.

matrix is fabricated in low-loss (Teflon 3A) strip transmission line. Line crossovers within the strip line sandwich and the feedthrough connections to a second strip line sandwich are used to achieve a small package. The directional couplers in the matrix are the branch-line type, and the fixed phase shifters are differential lengths of transmission line. Table 2-1 summarizes the 900-Mcps electrical characteristics of the new matrix.

*J. L. Allen, et al., TR-236, pp. 19-53.

TABLE 2-1	
900-Mcps CHARACTERISTICS OF 16-ELEMENT BEAM-FORMING MATRIX	
Insertion loss	0.40 db
VSWR-beam terminals	1.15 average (1.29 max)
VSWR-antenna terminals	1.10 average (1.19 max)
Isolation between beam terminals	43 db average (24 db min)
Isolation between antenna terminals	38 db average (24 db min)
Amplitude errors in the illumination	0.33 db, rms averaged over the 16 beams (0.54 db max)
Phase errors in the illumination	5.6°, rms averaged over the 16 beams (8.0° max)

The beam-forming matrix was tested in a 16-element dipole array at 900 Mcps. The uniform illumination beams had good antenna patterns with first sidelobes of 11 to 13 db for almost all beams. Beam-pointing errors ran less than 1°. All cosine and sine illumination beams were tested. Difference null depths ran from 19 to 27 db and the null positions were always within 1° of the theoretical position. The sum beams had first sidelobe levels in the 19- to 23-db range (theoretical value for 16-element array = 23 db).

The matrix has been used in a variety of antenna and beam-forming experiments. Its convenient mechanical configuration and its good electrical performance make it a useful experimental tool.

K. IMPEDANCE MEASUREMENTS ON ARRAY ANTENNA ELEMENTS

W. P. Delaney and J. L. Allen

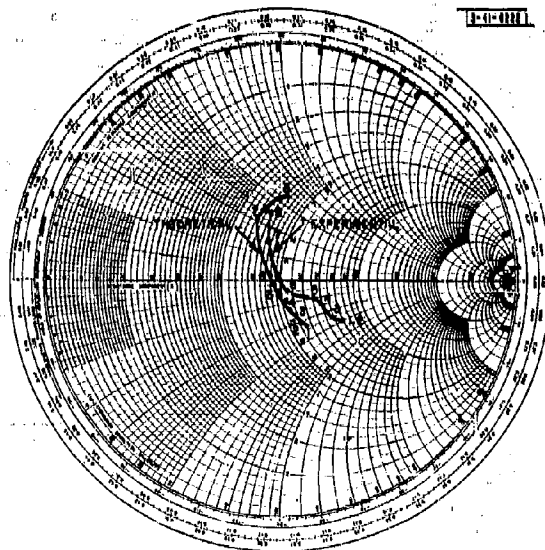
The impedance of an antenna element in an array of similar antenna elements is a function of the particular antenna element and its distance above the ground plane, the location of the element in the array, the spacing of the array elements, the amplitude and phase of the array illumination and the polarization properties of the element. For large arrays, most of the elements can be considered central elements; therefore, the variation in impedance with location becomes unimportant. Computational techniques are available for calculating the impedance of array antenna elements such as dipoles or slots. However, it is difficult to predict theoretically the impedance variations of more complex antenna elements such as log-periodics, polyrods or helices when they are used in an array. An experimental apparatus that can directly measure the impedance of an element in an active array as a function of scan angle, array illumination and array geometry is being assembled at present. The device consists of an RF beam-forming matrix* for an 8 × 8 planar† array of antenna elements with an impedance-measuring device located in the feed line to one of the central elements of the array. Thus, the impedance of this element is measured with all elements in the array driven. Scan angle is varied by feeding a different input port on the matrix, and the amplitude of the illumination can conveniently be varied from uniform to cosine, sine, cosine-squared and cosine-squared-on-a-pedestal by driving more than one input port. A frequency of 1300 Mcps has been chosen as center frequency because

* J. L. Allen, et al., TR-236, pp. 19-53.

† The sufficiency of an 8 × 8 test array for measurements has been discussed in TR-236, p. 217.

several small planar arrays of different types of antenna elements are available at this frequency. The use of this measuring technique coupled with the continuing mutual coupling study program should provide considerable insight into the impedance characteristics of complex array antenna elements.

This measuring technique has been checked against theoretical calculations for a 16-element linear array of parallel dipoles at 900 Mcps. The RF beam-forming matrix described in Sec. J of this chapter was used to feed the array and scan the beam. A Hewlett-Packard Model 805A slotted line was used as the impedance measuring device. Figure 2-25 shows the measured dipole impedance for H-plane scan angles between 3° and 54° from broadside. Figure 2-10 also shows the theoretical impedance variation with scan for thin dipoles* in an array with the same geometry as the test array. The experimental results are in good agreement with theoretical predictions, the small differences being due to experimental errors and the simplified theoretical model of the dipole (thin dipole, no feed structure, no gap at feed point).



Point No.	Scan Angle
1	3°
2	9°
3	16
4	22
5	29
6	36
7	45
8	54

Fig. 2-25. Dipole impedance vs scan angle for a linear array.

L. A 900-Mcps BRIDGE

D. M. Bernella

In order to measure the pulsed phase and amplitude characteristics of the various components in the transmitter modules and system, it was necessary to construct the bridge shown in Fig. 4-6. It was desirable to make measurements to within one electrical degree; therefore, it was felt that the bridge itself should be accurate to ± 0.1 electrical degree. This accuracy must not be in the sense of repeatability only; one must also be certain that the data obtained are

* The dipoles of the test array were not thin dipoles (length to diameter ratio = 17).

indicative of the performance of the device under test and not a composite of the device and the measuring system. It is simple enough to build phase measuring equipment with mechanical drives that will read to any small fraction of a millimeter, but quite a different problem to build the equipment in such a manner that the visual reading is absolute. Even very slight mismatches in transmission line connectors can add several degrees of phase error to the over-all electrical length, depending on the angles of reflection involved. An analysis of the magnitude of mismatch errors is given in Sec. E of this chapter.

All connections are padded with modified 6-db General Radio Series 874 pads (Fig. 2-26). The transmission lines are constructed of solid 5/8-inch diameter, 50-ohm air dielectric coaxial cable with General Radio locking connectors, except for the two flexible lines that connect to the unit being measured: When flexible cables are used, it is necessary to provide some means of keeping the outside braid from creeping in the connector when the cable is flexed. The adapters shown in Fig. 2-27 were designed and found quite adequate to hold the braid rigid.

In order to hold the error tolerance to ± 0.1 mm (0.925° at 900 Mcps) with component voltage mismatches as high as 2 to 1, it is necessary to use a minimum of 6 db of padding matched to a VSWR of less than 1.04. Commercially available stock pads are not completely satisfactory, but it was found that the standard General Radio 6-db pads could be improved over a narrow frequency range by carefully centering the resistive element and machining a few mils from the ends. This essentially tuned the pads to a VSWR less than 1.04 in the range of 850 to 950 Mcps. (The bridge

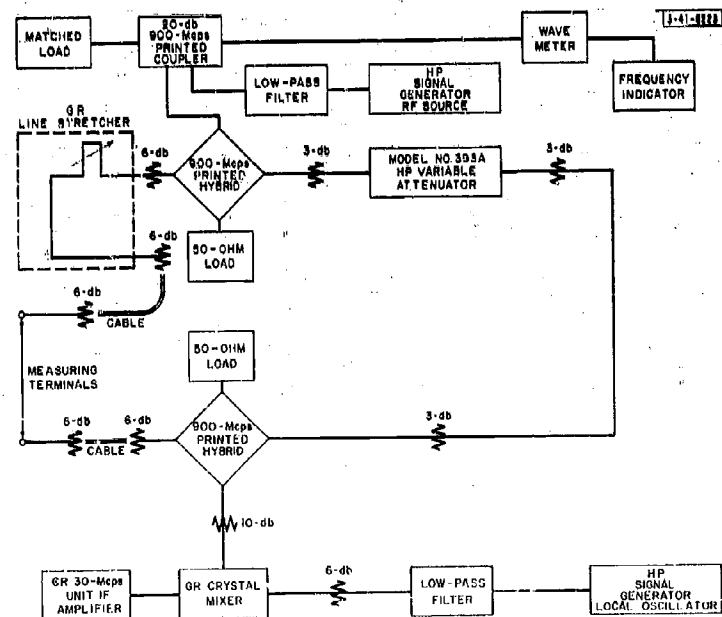


Fig. 2-26. 900-Mcps bridge, block diagram.



Fig. 2-27. Modified coaxial connectors.

TABLE 2-II RESULTS OF EXPERIMENTAL TESTS ON THE 900-Mcps BRIDGE			
Line	Length (cm)		Error (cm)
	Measured	Computed	
A	7.12		
B	7.13		
C	9.98		
A + B	14.26	14.25	0.01
A + C	17.08	17.10	0.02
B + C	17.09	17.11	0.02
A + B + C	24.25	24.23	0.02

is still useful at other frequencies, but the accuracy is reduced to approximately ± 1 electrical degree.)

The phase measuring unit was constructed by mounting a standard line stretcher on a solid bed with a 20-pitch rack and pinion drive. A linear vernier scale on the moving carriage indicated 0.1-mm divisions. A circular vernier was also added to the attenuator, which indicates to 0.1 db. Varying the setting of this attenuator introduces no measurable change in electrical length. In order to achieve 80-db deep nulls, it was necessary to add an additional 5-to-1 gear on the attenuator knob.

All components are bolted rigidly to the aluminum box-frame bench. Rubber wheels provide mobility of the system and also damp out minor vibrations that are bothersome during measurements. The system is quite sensitive to ambient temperature, and care must be exercised to hold the temperature constant within a few degrees during measurements.

Several sets of measurement checks were made by measuring connectors and line lengths separately and then in combinations. Table 2-II shows the results of some of these checks.

M. FERRITE PHASE SHIFTERS

D. H. Temme

During the first six months of this reporting period, two new interesting ferrite phase shifter approaches were sponsored. One was a rotating-field phaser design investigated by HYLETRONICS

Corporation. The other was a digital ferrite line delay or shifter investigated by General Electric Company. Sufficient progress during the first six months clearly indicated the latter approach best suited the Group 41 array requirements. This approach is still in the development stage.

The rotating-field phaser appears attractive for applications requiring continuous phase variation. Results of the initial six-month investigation were reported at the 1962 WESCON meeting.*

Present models of the digital ferrite phase shifter exhibit the following performance:

Insertion loss	low-power level ~1 db for 2π radians high-power level ~3 db peak before again decreasing
VSWR	less than 2:1 over an octave band
Drive requirement	memory type, switches in 1 μ sec with 15-amp pulse, with a 36-volt back voltage
Temperature sensitivity	$2^\circ/\text{C}/2\pi$ radians
Peak power	limited testing, once tested to 15 kw
Average power	unknown
Phase tolerance	unknown

Present studies are directed toward the understanding of increased insertion loss with power level and toward acceptable thermal design.

* J. A. Weiss, "Advances in Ferrite Rotating-Field Phaser Design," 1962 IRE WESCON Convention Record, Part 1, Paper No. 3.

CHAPTER II LOW-NOISE AMPLIFIERS

W. J. Ince

SUMMARY

The major portion of Chapter II is devoted to an investigation of tunnel diode amplifiers and a report on the progress made in the development of an inexpensive, reliable tunnel diode low-noise preamplifier for phased array receivers.

A brief review of the problems encountered in last year's work is given (Sec. A), followed by a discussion of the tunnel diode amplifier as a phased array component. An analysis of the circulator tunnel diode amplifier has been made that examines some of the effects resulting from the use of nonideal circulators in tunnel diode amplifiers. This analysis is followed by a discussion of the parameters of circulators for phased array receivers.

The practical tunnel diode amplifier circuits that were used are given, together with experimental data and performance specifications on the circuits and other receiver components.

A tunnel diode amplifier has been incorporated into an all-solid-state receiver package. Two of these receivers will be used in conjunction with an RF beam-forming matrix and beam-steering hardware for the purpose of studying such phased array receiver problems as the extraction of monopulse information. The components in the solid state receiver are described individually.

Section B is concerned with the use of tunnel diode down-converters.

Some undesirable interactions that are possible when tunnel diode amplifiers are used in superheterodyne receivers are discussed in Sec. C.

Finally, the status of the evaluation and test program on sixteen electron-beam parametric amplifiers in the 900-Mcps phased array receiver is reported (Sec. D).

A. INTRODUCTION

The development of a tunnel diode low-noise preamplifier, described in this chapter, is a continuation of the work described in an earlier report.⁸ In that work the performance of tunnel diodes operating as microwave amplifiers was demonstrated, but it was realized that there were many problems to be overcome before a suitable phased array component could be evolved. These problems have been overcome largely as a result of an improvement in amplifier design and the availability of better circulators.

It had been established previously that the circulator-coupled amplifier offered the best possibility of achieving a practical, readily reproducible amplifier. Accordingly, a number of amplifier designs utilizing a 3-port circulator were breadboarded. Several difficulties became apparent, most of them arising from the circulator.

First, the in-band match of the circulator was not good. The VSWR varied across the signal frequency range, causing the gain of the amplifier to vary. The VSWR at the edges of the band rose sharply and the amplifier had a tendency to oscillate because of this effect. Moreover, the VSWR of the circulator out of band varied wildly. Since tunnel diodes exhibit negative resistance

*J. L. Allen, et al., "Phased Array Radar Studies, 1 July 1960 to 1 July 1961," Technical Report No. 236 [U], Lincoln Laboratory, M. I. T. (13 November 1961), Part 2, Ch. IV, ASTIA 271724, H-474.

characteristics over a very wide frequency range from DC up to the diode cut-off frequency, the amplifier was extremely prone to oscillate outside the pass band of the circulator. It was evident that the tunnel diode had to be damped resistively outside the signal frequency range in order to ensure stability, as well as to restrict the in-band variations in circulator VSWR.

With the objective of designing a cheap, readily reproducible amplifier, all the earlier amplifiers were constructed in strip transmission line with a double ground plane and single center conductor configuration. The diode was mounted across the line between the center conductor and one ground plane, in an unbalanced manner. The unbalance tended to generate a parallel-plate mode of wave propagation. The use of shorting screws between the ground planes did not provide adequate mode suppression. Oscillations tended to be set up, either because of the introduction of inductance in series with the diode (resulting from the unbalanced transmission line caused by the method of mounting the diode) or because of a reactive impedance introduced by the parallel-plate mode of propagation. This source of trouble has been eliminated by the use of "microstrip" construction that utilizes a single ground plane and single conductor.

Another feature of previous design work was the use of coaxial monitor T-networks for DC bias injection. These have been eliminated, and a bias network has been integrated into the amplifier design.

Diodes made by several manufacturers were used, and it became apparent that no commercially available diode had adequately controlled parameters. In order to facilitate the designing of amplifiers with similar characteristics, diodes are now purchased with a specified minimum negative resistance.

With increased circuitry experience and improved components, it has been possible to build stable, reproducible amplifiers.

B. TUNNEL DIODE AMPLIFIERS

1. The Tunnel Diode Amplifier as a Phased Array Component

The fundamental requirements for a phased array RF preamplifier are that it have adequate gain, sensitivity and bandwidth compatible with the desired over-all system performance; it should be inexpensive, reliable and easily reproducible; any pair of amplifiers should track in phase and amplitude over the signal frequency band, and it is desirable to have a linear phase vs frequency response for short-pulse reception.

When the expense of installation and maintenance of a large array of about 1000 receivers is considered, the cost and reliability factors are of paramount importance; the simpler and less complex the design, the better it is. At the moment, the tunnel diode amplifier still appears to be the best compromise between electrical performance, cost and simplicity at frequencies in the high UHF through L-band region. It is unfortunate that the tunnel diode must be used in conjunction with a circulator, because the circulator is easily the most expensive component in the amplifier. For this reason, the transistor may yet replace the tunnel diode in the UHF range; however, the transistor has yet to equal the tunnel diode in noise figure in the L-band frequency range.

A useful property of the tunnel diode is that it is inherently a wideband device and is quite capable of providing any bandwidth that a practical array might require. While it is true that there are other classes of low-noise amplifiers that have a lower noise figure than the tunnel diode amplifier, the advantages to be obtained from using the latter probably outweigh the disadvantage of loss in sensitivity.

However, one disadvantage of the tunnel diode that might weigh heavily against it is its limited dynamic range; saturation output level is about -20 dbm. This could be extremely significant in a multiple-target environment where there is a wide variation in target cross section.

A possible configuration for a radar that has separate transmitting and receiving arrays is shown in Fig. 2-28. A tunnel diode amplifier is placed behind every antenna element. The tunnel diode amplifier outputs are combined in a beam-forming matrix. The source impedance seen by each amplifier is equal to the driving impedance of an antenna element as measured in the array, where the effects of mutual coupling greatly modify the behavior of the elements in free space.^{*} The antenna VSWR can be as high as 2.5:1; moreover, the VSWR is a function of scan angle.

The output match is likely to be much better. Measurements performed on a 16-element beam-forming matrix[†] indicate a maximum VSWR of 1.3.

A possible arrangement that utilizes a single array for transmitting and receiving is shown in Fig. 2-29. A duplexer consisting of a circulator and solid state switch combination provides the required protection for the tunnel diode during transmission. The advantage of this arrangement, apart from the reduction in cost obtained by the elimination of one array, is that it can use the same set of phase shifters for transmitting and receiving. In this arrangement, the reverse isolation provided by the duplexer circulator reduces the effective VSWR of the antenna element. Similarly, the output match is set by a circulator that routes the signal to the phase shifters. For this arrangement, both the input and output VSWR could be held to within 1.3.

It will be shown in the following analysis that the input and output matches are important in the operation of a tunnel diode amplifier and that steps should be taken to minimize the input and output VSWR.

2. Analysis of Circulator-Coupled Tunnel Diode Amplifier

a. Scope of Analysis

The purpose of this section is to derive some mathematical expressions that describe the performance of a tunnel diode reflection amplifier in association with a circulator. From the point of view of negative resistance amplifier applications, circulators are far from perfect. In fact, the circulator modifies the amplifier characteristics to the extent that the design of the amplifier must be tailored to accommodate variations in circulator parameters. In the following analysis, the tunnel diode is treated as a single, lumped mismatch on one of the circulator ports; arbitrary mismatches are also imposed at all other circulator ports. The algebra involved has been facilitated by the use of the topological circuit analysis.

b. Introduction

For reference, a typical tunnel diode I-V characteristic and the equivalent circuit are shown in Fig. 2-30, and a simple reflection amplifier is shown in Fig. 2-31. It is assumed that the reader is familiar with the elementary principles of tunnel diode operation.^{‡§} At high frequencies the equivalent circuit of the diode may be represented as a negative conductance G and a susceptance B .

* J. L. Allen, *et al.*, Technical Report 236, Part 3.

† *Ibid.*, Part 2, Ch. I; W. P. Delaney, pp. 34 and 35 of the present report.

‡ General Electric Company, "Tunnel Diode Manual" (1961).

§ M. E. Hines, "High-Frequency Negative-Resistance Circuit Principles for Esaki Diode Applications," BSTJ 39, 477 (1960).

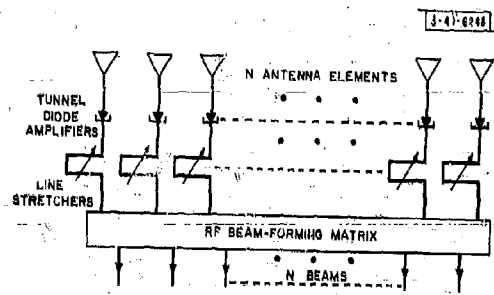


Fig. 2-28. Receiving array scheme.

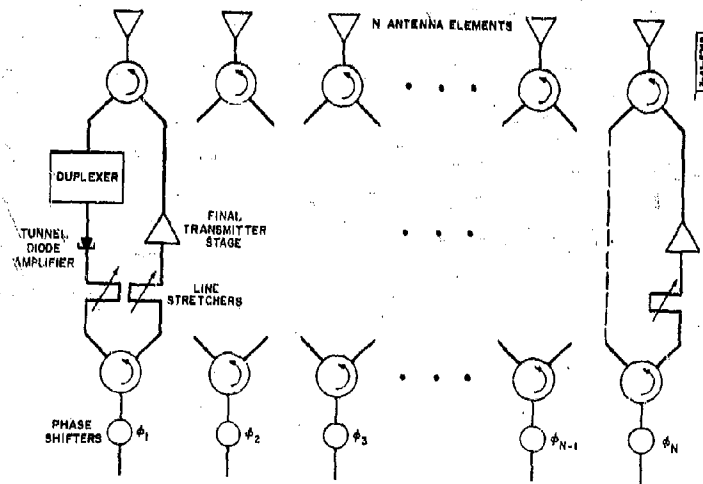
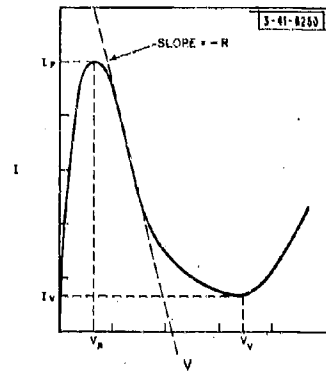


Fig. 2-29. Combined transmitter and receiver array scheme.

(a) Characteristic curve



(b) Equivalent circuit

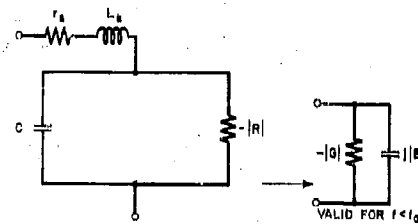


Fig. 2-30. Typical tunnel diode I-V.

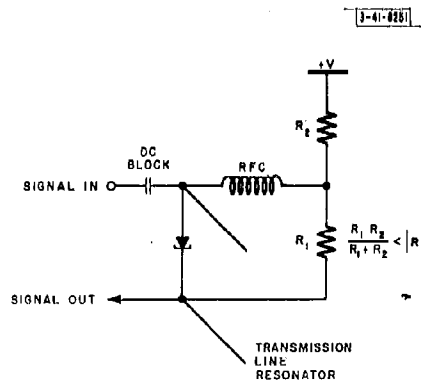


Fig. 2-31. Tunnel diode reflection amplifier.

Provided that the operating frequency is less than about one-third the cutoff frequency of the diode, both G and B vary only slowly with frequency. The amplifier shown in Fig. 2-31 has a single-tuned circuit response; the diode has been tuned into parallel resonance by a shunt inductor. The amplifier is not restricted to this type of tuning; however one may choose to tune the diode or arrange the layout of the circuit, the amplifier can always be characterized by the mismatch it presents to the network to which it is coupled. For example, when the amplifier is coupled to a circulator, the mismatch represents the difference between the characteristic impedance of the circulator and the tunnel diode amplifier. At any particular frequency the amplifier reflection coefficient ρ can be represented in polar coordinates by $\rho = |\rho| e^{j\Phi}$. For amplification to take place, $|\rho|$ must be greater than unity. The coefficient $|\rho|$ must take into account the variation of amplifier gain with frequency; Φ accounts for the phase shift through the amplifier.

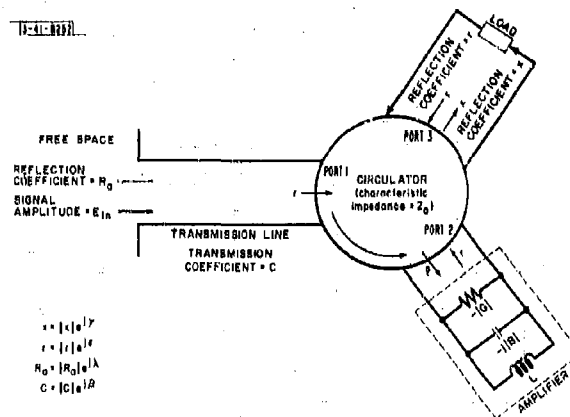


Fig. 2-32. Circulator-coupled amplifier.

The complete circulator-coupled amplifier is shown in Fig. 2-32. A 3-port circulator is shown for the purposes of this analysis. Mismatches external to the circulator have been added at ports 1 and 3. The mismatch X at port 3 may be due to an external component, such as a mixer or an RF beam-forming network, or it may be due to an internal mismatch between the two 3-port circulators that comprise a 4-port circulator.

The mismatch R_a on port 1 is considered that of the receiving antenna. For completeness, the inevitable length of transmission line between the antenna and amplifier has been included. This may or may not add significant loss, depending upon its length, but it will certainly introduce an additional phase shift.

The circulator is characterized by insertion loss S , leakage paths L , and reflection (internal) at each port r , together with their associated phase angles. The circulator is considered symmetrical.

c. Scattering Matrix Formulation

If voltage waves E_1^I, E_2^I, E_3^I are incident at the circulator ports and E_1^S, E_2^S, E_3^S signify reflected or scattered waves at the corresponding ports, then the two sets of waves are related by the matrix equation

$$\begin{bmatrix} E_1^S \\ E_2^S \\ E_3^S \end{bmatrix} = \begin{bmatrix} r & L & S \\ S & r & L \\ L & S & r \end{bmatrix} \begin{bmatrix} E_1^I \\ E_2^I \\ E_3^I \end{bmatrix} \quad (1)$$

Referring again to Fig. 2-32, let us consider that a voltage wave of amplitude E_{in} is incident at the antenna. A certain fraction S_a is coupled into the input transmission line to the amplifier and a certain fraction R_a is reflected; phase angles μ and λ , respectively, are to be associated with these quantities.

If E_0^S is the voltage wave scattered into free space from the antenna, then

$$E_0^S = R_a E_{in} + S_a C E_1^S$$

$$E_1^I = S_a C E_{in} + R_a C^2 E_1^S$$

or

$$\begin{bmatrix} E_0^S \\ E_1^S \end{bmatrix} = \begin{bmatrix} R_a - \frac{S_a^2}{R_a} & \frac{S_a}{R_a C} \\ -\frac{S_a}{R_a C} & \frac{1}{R_a C^2} \end{bmatrix} \begin{bmatrix} E_{in} \\ E_1^I \end{bmatrix} \quad (2)$$

d. Summary of Symbols Used

	Symbol	Magnitude and Phase
Circulator mismatch	r	$ r e^{j\epsilon}$
Circulator transmission path	S	$ S e^{j\alpha}$
Circulator leakage path	L	$ L e^{j\delta}$
Antenna mismatch	R_a	$ R_a e^{j\lambda}$
Antenna transmission	S_a	$ S_a e^{j\mu}$
Input transmission line	C	$ C e^{j\beta}$
Tunnel diode amplifier mismatch (port 2)	ρ	$ \rho e^{j\phi}$
Output mismatch (port 3)	X	$ X e^{j\gamma}$

e. Signal Flow Graph Representation

Figure 2-33 shows the complete signal flow-graph representation^{*} of the 3-port circulator with external mismatches. Signal flow-graph analysis permits the matrix Eqs. (1) and (2) to be solved readily.

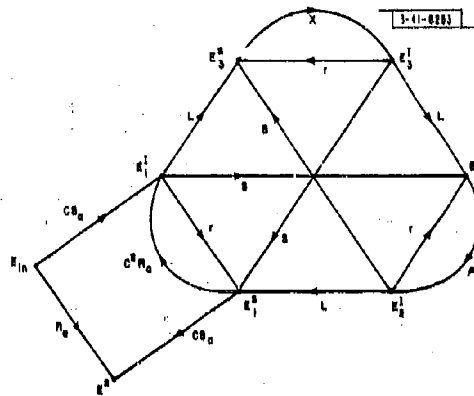


Fig. 2-33. Flow-graph representation of circulator-coupled tunnel diode amplifier with arbitrary mismatches at input and output ports.

The transmission between any two nodes is given by Mason's rule:

$$T = \frac{1}{\Delta} \sum_k P_k \Delta_k \quad (3)$$

where

T = required source-to-sink graph transmission

P_k = transmission of the k^{th} source-to-sink path

Δ = graph determinant

Δ_k = cofactor of the k^{th} path.

The definition of the graph determinant is

$$\Delta = 1 - \sum_i T_i + \sum_i \sum_j T_i T_j - \sum_i \sum_j \sum_k T_i T_j T_k + \dots$$

where the T_i 's are the values of all feedback loops and the $T_i T_j$'s are the products of pairs of loops that do not touch each other, etc. The cofactor Δ_k is equal to the value of Δ with the restriction that no loops or products of loops that touch the k^{th} transmission path can be counted.

*S. J. Mason and H. J. Zimmerman, *Electronic Circuits, Signals, and Systems* (Wiley, New York, 1960).

I. Calculation of Amplifier Gain

The amplifier gain, including the effect of circulator loss and terminal reflections, is given by the ratio E_3^S/E_{in}^S .

The direct transmissions between input and output and the loops can be written after inspection of Fig. 2-33.

Loops	Transmissions
$T_1 = R_a r C^2$	$P_1 = S_a C L$
$T_2 = S \rho L C^2 R_a$	$P_2 = S_a C S^2 \rho$
$T_3 = r \rho$	
$T_4 = X r$	
$T_5 = X S^3 C^2 R_a \rho$	
$T_6 = X S \rho L$	
$T_7 = X S L C^2 R_a$	
$T_8 = X \rho C^2 R_a L^3$	

Thus, the graph determinant is

$$\Delta = 1 - \sum_{i=1}^8 T_i + T_1 T_3 + T_1 T_4 + T_1 T_6 + T_2 T_4 + T_3 T_4 + T_7 T_3 - T_4 T_4 T_3$$

and

$$\Delta_1 = 1 - \rho r \quad \Delta_2 = 1 - \dots$$

Hence, after substitution of these quantities in Eq. (3), it follows that

$$\frac{E_3^S}{E_{in}^S} = \frac{S_a C (1 + r \rho + S^2 \rho)}{(1 - \rho r) (1 - R_a r C^2) - L R_a C^2 S \rho - X (R_a C^2 S^3 \rho + S \rho L - 3 R_a r C^2 S \rho L + L^3 \rho R_a C^2 + r (1 - r \rho) - r^2 R_a C^2 + r^3 \rho R_a C^2 + S R_a C^2 L)} \quad (4)$$

g. Calculation of Amplifier Input Match

The input reflection coefficient is given by the ratio E_{in}^S/E_{in}^S . After enumerating the direct transmissions and loops:

Loops	Direct Transmissions
$T_1 = R_a r C^2$	$P_1 = R_a$
$T_2 = X r$	$P_2 = S_a^2 C^2 r$
$T_3 = \rho r$	$P_3 = S_a^2 C^2 S \rho L$

Loops

$$T_4 = R_n C^2 S \rho L$$

$$T_5 = X R_n C^2 S^3 \rho$$

$$T_6 = X R_n C^2 L S$$

$$T_7 = X R_n C^2 L^3 \rho$$

$$T_8 = X S \rho L$$

Direct Transmissions

$$P_4 = X S_n^2 C^2 L S$$

$$P_5 = X S_n^2 C^2 S^3 \rho$$

$$P_6 = X S_n^2 C^2 L^3 \rho$$

we see that

$$\Delta = (1 - r\rho) (1 - rR_n C^2) - LR_n C^2 S \rho - X [r + S^3 C^2 R_n \rho + S \rho L + S L C^2 R_n + \rho C^2 R_n L^3 - r^2 \rho - R_n r^2 C^2 - 3S \rho L R_n r C^2 + r^3 \rho R_n C^2]$$

and

$$\Delta_1 = \Delta$$

$$\Delta_2 = 1 - r\rho - X [r + S \rho L - r^2 \rho]$$

$$\Delta_3 = 1 - Xr$$

$$\Delta_4 = 1 - r\rho$$

$$\Delta_5 = 1$$

$$\Delta_6 = 1$$

Hence,

$$\frac{E^S}{E_{in}^S} = \frac{1}{\Delta} \sum_k P_k \Delta_k = R_n + \frac{S^2 C^2}{\Delta} [S^3 \rho X + L S X - 3 L S X \rho r + r(1 - r\rho)(1 - Xr) + S \rho L] \quad (5)$$

Equations (4) and (5) are extremely complicated to work with, and little can be gained by pursuing their exact solution. However, some specific cases will be examined.

b. Amplifier with No Mismatches at Input and Output Terminals

The tunnel diode amplifier power gain is often taken to be equal to $|\rho|^2$. It can be seen from the above expressions that the power gain and input match of the amplifier are extremely dependent on the circulator parameters. Usually, the amplifier is tuned up and adjusted on the bench rather than under system operating conditions, with the input and output ports well padded to avoid spurious effects. In order to examine these conditions, X and R_n are set equal to zero, and C and S_n are set equal to unity. The expression

$$\frac{E_3^S}{E_{In}^S} \text{ becomes equal to } L + \frac{S^2 \rho}{1 - r\rho} \quad (6)$$

It can be seen that the output from the amplifier is composed of a small term due to leakage from port 1 to port 3, plus a much larger contribution due to the gain of the tunnel diode. For a practical circulator, L is never worse than -20 db (i.e., a voltage ratio of 0.1) within the pass band of the amplifier. If the amplifier is adjusted for any reasonable value of gain — for example, 17 db (a voltage ratio of 7) — the leakage contribution is negligible compared to the amplified contribution. Hence,

$$\frac{E_3^S}{E_{In}^S} = \frac{S^2 \rho}{1 - r\rho} = \frac{|S^2| |\rho| \exp \left\{ j \tan^{-1} \left[\frac{\tan(2\alpha + \phi) - |r| |\rho| \sin(2\alpha - \epsilon)}{1 - |r| |\rho| \frac{\cos(2\alpha - \epsilon)}{\cos(2\alpha + \phi)}} \right] \right\}}{(1 - 2|r| |\rho| \cos(\epsilon + \phi) + |r|^2 |\rho|^2)^{1/2}} \quad (7)$$

The ratio E_3^S/E_{In}^S is extremely dependent on the magnitude of both r and ρ and their phase difference. Consider a diode chosen to have a terminal negative resistance of 66 ohms, and assume the circulator VSWR to be 1.2 or less over the frequency range that is of interest. The nominal power gain, found by setting $r = 0$, is approximately 17 db ($\rho = 7.4$).

The minimum possible power gain is obtained when reflection from the diode is 180° out of phase with the reflection at port 2 of the circulator. The minimum power gain is equal to $(|S^2| |\rho|)/(1 + |r| |\rho|)^2$, or 12.6 db. Similarly, when the reflections are in phase, the maximum possible power gain is obtained and is equal to $(|S^2| |\rho|)/(1 - |r| |\rho|)^2$, or 26 db.

It is our experience that the VSWR of most circulators approaches 1.2 over some region of the pass band; also, tunnel diodes supplied by the manufacturer under a given type number can have a spread in minimum negative resistance of at least ± 10 percent. These parameter variations make the task of designing a number of amplifiers with identical characteristics extremely difficult.

It is evident from the condition of maximum possible gain that the product $|r| |\rho|$ must be less than unity to guarantee stability. For 17-db nominal gain, this restricts the VSWR of the circulator to less than 1.32.

One of the problems in ensuring stability is that the tunnel diode amplifier may have gain greater than unity over a frequency range considerably in excess of the signal bandwidth, and it is necessary to make sure that the criterion $|r| |\rho| < 1$ is obeyed at any frequency. The circulator should, therefore, have a bandwidth wider than that of the amplifier.

A characteristic common to many circulators is that the VSWR is a minimum at the band center and increases on either side toward the band edges. Hence, the gain variation from amplifier to amplifier at the band center may not be as great in practice as indicated in the calculations.

The variation in circulator VSWR across the band can be put to good use; if the amplifier is tuned to have maximum gain of the center frequency of the circulator pass band, the increase in circulator VSWR at the band edges can be made to compensate for the decrease in diode reflection coefficient in a manner that keeps the over-all gain of the amplifier constant. This can be seen from Eq. (7). At the band edges the numerator $S^2 \rho$ decreases, mainly because of the decrease in ρ with frequency, but partly because of an increase in the insertion loss of the

circulator. The denominator $1 - r\rho$ in the gain expression is very sensitive to changes in the product $r\rho$, which may be made to vary so that the magnitude $|S^2\rho/(1 - r\rho)|$ is constant with frequency. However, for this to occur, both the magnitude and phase of r must vary with frequency. To obtain the right phase relationship, the distance of the diode from the circulator must be chosen correctly. The correct distance is best determined empirically by constructing several circuits, each with the diode mounted at a different distance from the circulator, and selecting the circuit that gives the flattest gain-frequency characteristic.

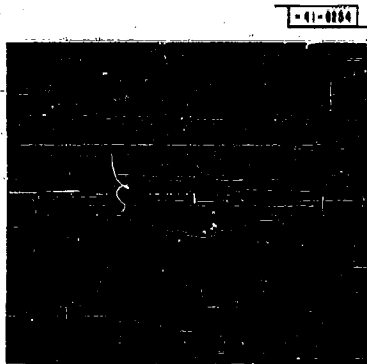


Fig. 2-34. Tunnel diode amplifier response (markers at 850 and 950 Mcps).

Figure 2-34 shows two swept gain-frequency plots of a tunnel diode amplifier with a General Radio line stretcher interposed between it and the circulator. The two plots correspond to the line stretcher adjusted first, so that the widest bandwidth possible was obtained, and next, so that the narrowest bandwidth possible was obtained. For the wideband case, r and ρ were 180° out of phase at the center frequency (900 Mcps). As a result, the gain at center frequency was minimum, given by $S^2\rho/(1 + |r||\rho|)$. For the line adjustment that gave the narrow bandwidth, r and ρ were in phase at the center frequency and the gain was maximum, equal to $S^2\rho/(1 - |r||\rho|)$. The center frequency gains were 13 and 27 db, respectively, which corresponded to a VSWR of 1.2 when $|\rho|$ was equal to 7.1. This calculated mismatch was the total mismatch of the line stretcher, two General Radio type N adapters and the circulator. The markers in the figure are at 850 and 950 Mcps.

In order to construct amplifiers with similar characteristics, it is necessary to adhere rigidly to one circulator design. By keeping to tight specifications on the VSWR and by selecting diodes that have a narrow spread in minimum negative resistance, amplifiers can be constructed that have gains within about 2 db of each other. Because of the dependency of gain and bandwidth on the phase of the circulator mismatch with respect to the position of the tunnel diode, the distance of the diode from the circulator must be optimized and the amplifier layout must be duplicated as closely as possible.

The input reflection coefficient of a tunnel diode operated with no external mismatches on input and output ports is given by putting X and R_a equal to zero [Eq. (5)] with C and S_d equal to unity. Hence,

$$\frac{E_r^S}{E_{in}^S} = r + \frac{S\rho L}{1 - r\rho}$$

The input reflection is composed of two terms; one is due to the inherent mismatch of the circulator alone. The other term is due to part of the signal that is amplified by the tunnel diode and leaks back to the input via the leakage path from port 2 to port 1. The magnitude of the first term is $|r|$, which, for a maximum VSWR of 1.2, is equal to 0.091. The magnitude of the latter term is equal to

$$\frac{|S| |\rho| |L|}{|1 - 2|r| |\rho| \cos(\epsilon + \phi) + |r|^2 |\rho|^2}^{1/2}$$

The extreme values that $(|S|/|I_{in}|)$ may take are calculated by putting $\cos(\epsilon + \phi)$ equal to ± 1 .

When $S = 0.96$ (0.3-dB insertion loss), $L = 0.1$ (20-dB isolation) and $\rho = 7.1$ (17-dB gain), then

$$\left| \frac{I_{in}^S}{I_{in}} \right|_{\max} = 1.92$$

$$\left| \frac{I_{in}^S}{I_{in}} \right|_{\min} = 0.5$$

These calculations demonstrate the fact that the tunnel diode amplifier input port is highly mismatched; under adverse phase conditions, an amplified signal is returned to the input. If one looks into the input terminal, a reflection gain greater than unity is observed. In order to ensure that the amplifier is unconditionally stable, it is necessary to increase the circulator isolation so that the magnitude of the observed input reflection gain is less than unity. Fortunately, increasing the circulator isolation automatically results in a lower circulator VSWR, giving additional stability. For the Lincoln Laboratory phased array project, circulators for tunnel diode amplifiers are purchased with an isolation specification of 25 dB, minimum. This implies a VSWR of 1.12. Using these values in the above expression, one obtains

$$\left| \frac{I_{in}^S}{I_{in}} \right|_{\max} = 0.64 \text{ (VSWR} = 4.5)$$

and

$$\left| \frac{I_{in}^S}{I_{in}} \right|_{\min} = 0.272 \text{ (VSWR} = 1.75)$$

Figure 2-35 shows a swept frequency plot of input VSWR vs frequency for a tunnel diode amplifier operating at 900 Mcps with 20 db of gain. The maximum VSWR, obtained at the center

-41-0258

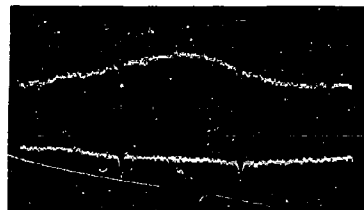


Fig. 2-35. VSWR of tunnel diode amplifier (markers at 880 and 920 Mcps).

frequency of the amplifier, was 3.5:1. The VSWR plot has the same shape as the amplitude response of the amplifier, which had a single resonant circuit. The plot was obtained with a reflectometer technique. The second trace in the picture is of a standard VSWR of 3:1 used for calibration purposes.

1. Amplifier with an External Mismatch at the Output Terminals

In considering the effect of a mismatch at the output port, some a priori restrictions can be imposed on the value of the VSWR to be expected. It is assumed that the VSWR will not be greater than 1.3, which will be the case if the amplifier is followed by an RF beam-forming network or a crystal mixer. In tunnel diode applications, it is usual to use a balanced mixer in order to minimize local oscillator leakage into the tunnel diode. In particular, for many applications where packaging is of importance, the most suitable type of balanced mixer uses a 90° coaxial hybrid. These have the additional advantage of presenting a reasonably good match to signal frequencies; typically, the VSWR can be kept within 1.3 over the pass band.

For the case of a good match at the input of the amplifier, the gain of the amplifier, from Eq. (4), is given by

$$\frac{E_3^S}{E_{in}^S} = \frac{S^2 \rho + I_A(1-r\rho)}{1-r\rho - X[S\rho L + r(1-r\rho)]} \quad (8)$$

and, by rearrangement of Eq. (5), the input reflection coefficient is found to be

$$\frac{E_3^S}{E_{in}^S} = r + \frac{X(S^3 \rho + SL - 2S\rho Lr) + S\rho L}{(1-r\rho)(1-Xr) - XS\rho L} \quad (9)$$

The magnitudes of the various terms in these expressions are listed in Table 2-III. The characteristics assumed for the circulator are typical for receiver applications: 0.3-db insertion loss ($S = 0.96$), 25-db minimum isolation ($L = 0.056$), VSWR = 1.12 ($r = 0.057$). When the less significant terms are dropped, the following approximations hold:

$$\frac{E_3^S}{E_{in}^S} \approx \frac{S^2 \rho}{1-r\rho}$$

$$\frac{E_3^S}{E_{in}^S} \approx \frac{S\rho L}{1-r\rho} + \frac{XS^3 \rho}{1-r\rho}$$

It can be seen that the gain is not greatly affected by the mismatch, but the input VSWR is affected. From a physical standpoint, one can see why this should be so; a VSWR of 1.3 introduces a reflection loss of about 0.1 db. Hence, a small loss in gain due to reflection loss is to be expected. However, most of the energy reflected from the output port of the circulator travels back through the path from port 3 to port 1 practically unattenuated, and a very small fraction is returned to the diode via the leakage path between ports 3 and 2. The wave reflected back to port 1 is comparable in magnitude to the input signal, and it changes the input VSWR considerably. At port 1, the reflected energy is almost entirely absorbed by the source impedance.

TABLE 2-III TERMS IN EQUATIONS (8) AND (9)			
Numerator		Denominator	
Quantity	Magnitude	Quantity	Magnitude
Eq. (8)			
S_p^2	6.46		
L	0.055		
L_{ip}	0.036	r_p	0.645
		X_{SpL}	0.049
Eq. (9)		X_r	0.012
$X_s^3 p$	0.815	$X_r^2 p$	0.0076
S_{pl}	0.382		
X_{SL}	0.0069		
$2X_{SpLr}$	0.009		

j. Amplifier with External Mismatches at Both Input and Output Terminals

In this case the energy reflected back by the output mismatch through the circulator to the input port is not absorbed entirely by the input termination; some fraction is returned to the amplifier, thereby completing a feedback loop. The conditions for oscillation are much more easily satisfied, and the gain is highly dependent on the phase relationships between the various reflections within the amplifier. The complete expression [Eq. (4)] must be used for the voltage gain.

In a phased array receiver, which has a tunnel diode amplifier behind every element, each amplifier will see at its input terminals the mismatch of the antenna element that drives it, transformed through a piece of interconnecting transmission line. In a worst-case situation, the antenna VSWR could be as high as 2.5:1. In order to see the effect of such a situation on the gain of the tunnel diode amplifier, the various terms or products of terms that make up Eq. (4), the gain equation, have been tabulated in Table 2-IV. As before, the circulator specifications assumed are: 0.3-dB insertion loss; 25-dB minimum isolation; VSWR = 1.12. Further, it has been assumed that the tunnel diode reflection is 17 dB and that the amplifier is working into a mixer having a VSWR of 1.3.

It can be noted that the greatest effect of external mismatches on the gain equation is to change the denominator. The numerator is changed only by the multiplication term CS_a , which is almost unity in magnitude and is important mainly for the addition of phase shift. The various terms in the denominator can be regarded as feedback factors that can affect the gain either adversely or regeneratively, depending on the phase of the feedback. The three terms of major importance are the products r_p , $X_{ra} C^2 S_p^3$ and $L R_a C^2 S_p$. The first one, which does not depend on the input and output mismatches, is due to multiple reflections between the diode and port 2 of the circulator. The second term, $X_{ra} C^2 S_p^3$, is due to a small fraction of the amplified signal

that is reflected at port 3 back through the circulator to port 1, where it is partially reflected back into the amplifier by the antenna mismatch. The third term, $LR_a C^2 S_p$, is the result of the part of the signal that returns to the input via the leakage path, port 2 to port 1, within the circulator after amplification by the diode; it is partly re-reflected back into the amplifier by the antenna.

The sum of the denominator terms in Table 2-IV can be made real and equal to unity by appropriate choice of phases; hence, the amplifier can easily be made to oscillate. However, a far greater margin of stability would be achievable if the output mismatch were eliminated. A very simple way of doing this is to use a 4-port circulator instead of a 3-port circulator.

TABLE 2-IV
TERMS IN EQUATION (4)

Numerator		Denominator	
Quantity	Magnitude	Quantity	Magnitude
$S_a C S_p^2$	5.9	rp	0.405
$S_a C L$	0.0505	$LR_a C^2 S_p$	0.163
$S_a C L r p$	0.0204	$r R_a C^2$	0.0244
		$r^2 p R_a C^2$	0.0099
		$X R_a C^2 S_p^3$	0.348
		$X S_p L$	0.0496
		$X r$	0.0074
		$X^3 R_a C^2 S_p L$	0.0036
		$X r^2 p$	0.003
		$X S R_a C^2 L$	0.003
		$X r^2 R_a C^2$	1.8×10^{-3}
		$X L^3 p R_a C^2$	7×10^{-5}
		$X r^3 p R_a C^2$	6×10^{-5}
$ S_a = 0.902$	$ L = 0.056$	$ X = 0.13$	
$ R_a = 0.428$	$ S = 0.96$	$ p = 7.1$	
$ C = 1.0$	$ r = 0.057$		

It is now possible for manufacturers to supply compact 4-port circulators having a 25-db isolation, a 1.12-db VSWR and 0.3-db insertion loss (port 1 to port 2). These are essentially two circulators in cascade; there is a minimum isolation of 25 db between ports 3 and 1, and any reflections from port 3 are removed from the system. A further advantage to be obtained from using a 4-port circulator is an isolation from port 3 to port 2 in excess of 40 db. Such an isolation is helpful in reducing local oscillator leakage from the mixer to the diode. This is a major consideration, because without the additional isolation provided by the 4-port circulator, a local oscillator rejection filter or isolator would be necessary anyway.

For phased array applications, as well as many others, the use of 4-port circulators in tunnel diode amplifiers is considered absolutely essential. Use can be made of this fact by putting X equal to zero in the gain expression. The gain equation reduces to

$$\frac{E_o^S}{E_{in}^S} = \frac{S_a^2 C S^2 \rho}{(1 - r\rho)(1 - rR_a C^2) - LR_a C^2 S \rho} \quad (10)$$

and the input reflection coefficient [Eq. (5)] also becomes

$$\frac{E_o^S}{E_{in}^S} = R_a + S_a^2 C^2 \left[\frac{r(1 - r\rho) + S \rho I}{(1 - r\rho)(1 - rR_a C^2) - LR_a C^2 S \rho} \right] \quad (11)$$

Consider now the effect of the antenna reflection R_a on the magnitude of the gain. To do this, the gain equation is written as

$$\frac{E_o^S}{E_{in}^S} = \left(\frac{S^2 \rho}{1 - r\rho} \right) \frac{S_a C}{1 - rR_a C^2 - \frac{LR_a C^2 S \rho}{1 - r\rho}} \quad (12)$$

The factor $S^2 \rho / (1 - r\rho)$ is the gain of the amplifier as it is set up in the laboratory before installation in the system. The right-hand side of Eq. (12) has its maximum value when the denominator is real and minimum; conversely, the minimum gain is obtained when the denominator is real and maximum. The term $LR_a C^2 S \rho / (1 - r\rho)$ has its maximum effect when r and ρ are in phase. The maximum possible gain vs the minimum possible gain is expressed as

$$\frac{1 + |rR_a C^2| + \frac{|LR_a C^2 S \rho|}{1 - |r||\rho|}}{1 - |rR_a C^2| - \frac{|LR_a C^2 S \rho|}{1 - |r||\rho|}}$$

If the amplifier is set to have a nominal gain of 17 db, then

$$20 \log_{10} \frac{S^2 \rho}{|r||\rho|} = 17 \text{ db}$$

Hence,

$$1 - |r||\rho| = 0.7$$

Substituting the values of $|rR_a C^2|$ and $|LR_a C^2 S \rho|$ from Table 2-IV yields

$$\frac{\text{maximum possible gain}}{\text{minimum possible gain}} = 4.6 \text{ db}$$

In order to obtain amplifiers with closely matched electrical characteristics, the physical layout must be rigidly adhered to from amplifier to amplifier. Hence, for any two amplifiers, it is not likely that the phase angle between the vectors r and ρ will differ by as much as 180° . The gain variation from the amplifier will, therefore, not be as much as 4.6 db.

This result indicates that the presence of the mismatch cannot make the diode oscillate under any condition. It can also be shown by substitution of the numerical values into Eq. (14) that the reflection coefficient of the amplifier is less than unity.

The phase shift through the amplifier and the way in which it is affected by the antenna mismatch are of interest.

If the substitutions $rR_a C^2 = V e^{jV}$ and $LR_a C^2 S \rho / (1 - r\rho) = W e^{jW}$ are made, Eq. (12) can be written as

$$\frac{E_3^S}{E_{in}^S} = \left(\frac{E_3^S}{E_{in}^S} \right)_0 \frac{S_a C}{1 - V e^{jV} - W e^{jW}}$$

where

$$\left(\frac{E_3^S}{E_{in}^S} \right)_0 = \left(\frac{S_a^2 \rho}{1 - r\rho} \right)$$

The quantity $V e^{jV}$ can be written as $V \cos v + jV \sin v$, and $W e^{jW}$ can be written as $W \cos w + jW \sin w$; therefore, after rationalizing the denominator,

$$\left(\frac{E_3^S}{E_{in}^S} \right) = \left(\frac{E_3^S}{E_{in}^S} \right)_0 \frac{|S_a| |C| e^{j(\mu+\beta)} e^{j \tan^{-1} \left[\frac{V \sin v + W \sin w}{1 - V \cos v - W \cos w} \right]}}{\left[(1 - V \cos v - W \cos w)^2 + (V \sin v + W \sin w)^2 \right]} \quad (13)$$

The total phase shift is equal to

$$\angle \left(\frac{E_3^S}{E_{in}^S} \right) = \angle \left(\frac{E_3^S}{E_{in}^S} \right)_0 + \mu + \beta + \tan^{-1} \left[\frac{V \sin v + W \sin w}{1 - V \cos v - W \cos w} \right]$$

Now consider that the amplifier alone has a flat amplitude response and linear phase with frequency. There is an additional gain and phase distortion factor introduced by the interaction of the input mismatch and the amplifier. The phase term is equal to

$$\tan^{-1} \left[\frac{V \sin v + W \sin w}{1 - V \cos v - W \cos w} \right]$$

In order to get an estimate of this quantity, it is first noted that

$$W = \left| \frac{LR_a C^2 S \rho}{1 - r\rho} \right| = \left| \frac{LR_a C^2}{S} \right| \times \left| \frac{S \rho}{1 - r\rho} \right| = \left| \frac{LR_a C^2}{S} \right| \times \left| \left(\frac{E_3^S}{E_{in}^S} \right)_0 \right|$$

If the quantities in Table 2-IV are assumed and if $|E_3^S/E_{in}| = 7.1$ (17 db of gain), then W is approximately 7.1 times the value of V . Hence,

$$\tan^{-1} \left[\frac{V \sin v + W \sin w}{1 - V \cos v - W \cos w} \right] \approx \tan^{-1} \left[\frac{W \sin w}{1 - W \cos w} \right]$$

The maximum-value of this expression is approximately $\tan^{-1} W$, or 10° .

k. Conclusion

The performance of the circulator-coupled tunnel diode amplifier has been examined. It has been shown that the circulator characteristics modify the performance of the amplifier. The effects of input and output mismatches are reduced by the use of 4-port circulators, but they still modify the performance of the amplifier. The residual effects must be kept to a minimum by specification of high circulator isolation. The VSWR of the circulator can be used to obtain increased bandwidth by optimizing the position of the diode with respect to the circulator.

4. Practical Tunnel Diode Receiver Design

a. Basic Considerations

The problem of designing a workable, stable, tunnel diode amplifier is made difficult by two fundamental properties of the device:

- (1) It exhibits the property of negative resistance from DC to microwave frequencies.
- (2) The tunnel diode is a two-terminal device.

The first property requires that careful attention be given to the value of the impedance presented to the diode over a very wide frequency range. The second property imposes the necessity for circulators.

The first stage of the tunnel diode program has been the construction of an amplifier centered at a frequency of 900 Mcps, and suitable for use in the Lincoln Laboratory linear array test facility. The linear array radar transmitter operates with a 10- μ sec pulsewidth. However, the design objective in the tunnel diode work has been a bandwidth more in keeping with the possible requirements for an operational array radar; it was considered that a few tens of megacycles would be satisfactory for a first-generation tunnel diode amplifier. This objective has been met, and further improvements are being made to obtain a wider bandwidth.

b. Circulator Parameters

According to the foregoing analysis, the prime requirement for stability within the amplifier pass band is that the circulator should have as high an isolation as possible; 25 db is the value considered minimal for a gain of about 17 db. This implies that the VSWR should be low, since the isolation and VSWR are directly related. It was also shown that stability is very difficult to achieve if mismatches are present simultaneously at the input and output, and that the problem is considerably lessened if a 4-port circulator is used instead of a 3-port circulator. Moreover, the 4-port circulator provides additional protection against local oscillator leakage, which should be kept below -40 dbm at the tunnel diode. Four-port circulators are being used exclusively in this tunnel diode amplifier development.

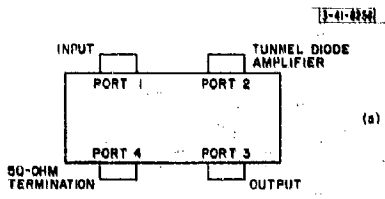


Fig. 2-36. Four-port circulator configuration:
(a) mechanical layout; (b) electrical layout.

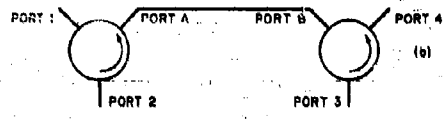


Fig. 2-37. Four-port circulator characteristics.

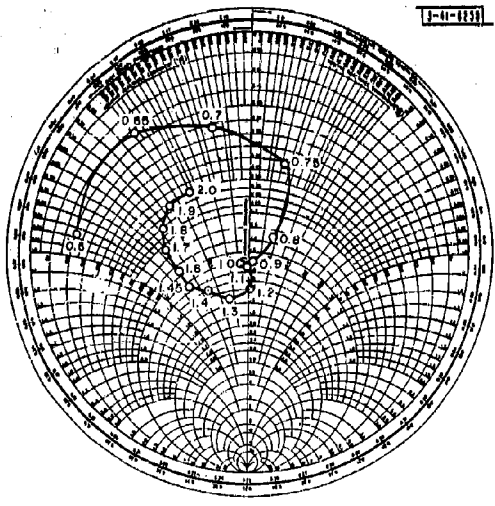
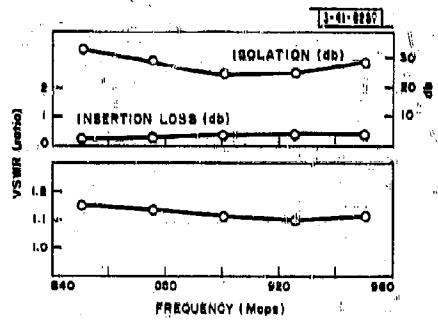


Fig. 2-38. Circulator impedance plot.
Frequencies are given in Gcps.

In order to obtain as low a noise figure as possible, the insertion loss for the path from port 1 to port 2 should be kept as low as possible, because this loss occurs in front of the diode. The effect of loss incurred beyond the diode is reduced by the gain of the amplifier.

Melaba Company has developed a 4-port circulator (model X615) having the following specifications:

Center frequency	900 Mcps
Frequency range	850 to 950 Mcps
Isolation: ports 2 to 1	25 db, min
Isolation: ports 3 to 1	25 db, min
Insertion loss: ports 1 to 2	0.3 db, max
Insertion loss: ports 2 to 3	<0.8 db
VSWR at port 2	1.2 max
Temperature range	45° to 120°F
Size	5½ × 3½ × 2 inches
Nominal impedance	50 ohms

The manufacturer supplied a termination on port 4 so that the performance of the circulator could be optimized. Each unit had sufficient magnetic shielding to allow the circulators of two amplifiers to be placed in contact with each other without changing the amplifier characteristics. The dimensions of the circulator design were chosen so that the complete amplifier package would conform with the plug-in module concept of array construction.

The layout of the circulator is shown in Figs. 2-36(a) and (b). The unit consists of two Y-circulators integrated into a single unit. The connectors are arranged in what is commonly referred to as an H configuration; the input and tunnel diode amplifier are on one side, and the output and termination are on the other. Figure 2-37 shows performance curves for a typical unit. The impedance looking into port 2 is given in Fig. 2-38. It can be seen that the VSWR climbs more steeply at the low-frequency end of the pass band than at the high-frequency end. It was found in earlier experiments with 3-port circulators having only 50 Mcps of bandwidth that amplifier instability occurred at the low-frequency end because of rapidly changing impedance.

It is of interest to examine further the advantages of the 4-port circulator as compared with the 3-port circulator. In the case of the 3-port circulator, the leakage from, say, port 2 and port 1 can be considered due to energy that travels by the direct transmission path from port 2 to port 3. At port 3 the energy is not all absorbed by the termination because of an imperfect match; therefore, a small amount is reflected back into the circulator and travels along the direct transmission path, port 3 to port 1. The circulator action produced by the ferrite is assumed to be perfect, so there is no direct transmission from port 2 to port 1.

Similarly, the leakage from port 3 to port 2 can be considered the result of a direct transmission from port 3 to port 1, plus a reflection due to an imperfect match at port 1, and, finally, a transmission of the reflected energy from port 1 to port 2. There is no direct transmission from port 3 to port 2. A similar argument holds for an explanation of the leakage from port 1 to port 3.

Let the leakage from port 2 to port 1 be 25 db; this implies that $1/316$ of the incident energy that travels to port 3 is reflected and arrives at port 1. Hence, $|\Gamma|^2 = 1/316$, which gives a reflection coefficient of 0.056, or a VSWR of 1.12.

Consider the transmission from port 1 to port 2. There is no direct transmission via the path 1 to 3, because this is against the direction of circulation. There is a reflection loss at port 1 which, together with a small dissipative loss along the path 1 to 2, comprises the insertion loss. Similar explanations hold for the transmission between ports 2 and 3 and between ports 3 and 1.

It can now be seen that in order to maintain high isolation and low insertion loss, the match at each port should be good. Suppose that a 3-port circulator were to be used in an array where the antenna VSWR at port 1 is 2.5:1 (a reflection coefficient of 0.43). The isolation between port 3 and port 2 would fall to 7 db. Similarly, an output mismatch on port 3 reduces the isolation on path 2 to 1.

Refer now to the layout of the 4-port circulator given in Fig. 2-36(b). The internal ports, where the first and second 3-port circulators are mated, are designated port A and port B, respectively. The leakage along the internal path port 3 to port B does not vary with the loading on ports 1 and 2, because port 4 is terminated in a well-matched load. In practice, the isolation measured between port 3 and port 1 is equal to the isolation from port 3 to port B, plus the insertion loss in the interconnection port B to port A and the insertion loss along the forward transmission, port A to port 1. This is found to be virtually invariant for the impedance placed on port 2.

If port 1 is well-terminated, the isolation obtained between ports 3 and 2 is roughly equal to twice the isolation obtained with a 3-port circulator (in excess of 40 db). The least isolation between port 3 and port 2 would be obtained with port 1 open-circuited; it would be roughly equal to the isolation between port 3 and port 1. For the X615 circulator, this is 25 db, minimum, and typically 30 db.

The flow-graph analysis of the circulator emphasized the importance of maintaining high isolation between port 2 and port 1 in the circulator-coupled tunnel diode amplifier for stability reasons. In the 4-port circulator, there is a stage of isolation between port 3 and port 1. Hence, the isolation between port 2 and port 1 is fairly independent of the loading on port 3.

It has been shown that the parameters of the 4-port circulator are far less sensitive to external mismatches than those of the 3-port circulator. The results of the analysis of the circulator-coupled amplifier could be applied to this problem simply by assigning the appropriate value to ρ , the mismatch on port 2. In the case of the amplifier, the imperfections of the circulator were magnified by the gain of the tunnel diode.

In conclusion, the difficulties experienced in the operation of tunnel diode amplifiers has led to the specification of high isolation and low VSWR. In the specification of isolation between ports 2 and 1, an extra requirement is now imposed: the isolation should not fall below 25 db when a sliding short is placed on port 3 and its position varied through 360° of phase.*

c. The Tunnel Diode Amplifier Circuit

The tunnel diode amplifier design is shown in Fig. 2-39. The design utilizes dielectric-filled microstrip transmission line. The heart of the amplifier is a piece of 50-ohm transmission line about 3 inches long that is connected to the circulator by a right-angle strip line to N transition. The strip line is terminated in a 50-ohm load to ensure a good wideband match.

* This test was brought to my attention by Mr. John Sie of Microstate Electronics Company, Murray Hill, New Jersey.

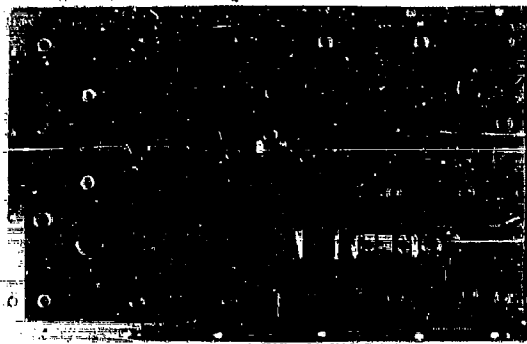


Fig. 2-39. Tunnel diode amplifier.

The diode is mounted in parallel, with the transmission line as near the connector as possible. A hole is drilled in the dielectric for insertion of the diode, and contact is made by a brass screw mounted on the ground plane. The brass screw is tipped with a gold-plated nickel bellows spring* for the purpose of cushioning the contact between the screw and the diode.

The 50-ohm RF termination provides the condition for DC stability; namely, the external resistance seen at DC by the diode across its terminals must be less than the minimum negative resistance of the diode, nominally 60 ohms. This termination also provides the necessary AC stability outside the pass band of the amplifier. The diode is tuned into parallel resonance by placing an RF short circuit between the center conductor and the ground plane of the strip transmission line at an appropriate distance from the diode. The distance is less than $\lambda/4$, so the transmission line appears inductive at the diode and is chosen so that the total capacitance at the diode is resonated at a frequency of 900 Mcps. The total capacitance at the diode is made up of the diode equivalent parallel capacitance plus the case capacitance, and the discontinuity capacitance set up by the introduction of the diode into the strip line structure.

The RF short circuit is achieved by shunting the strip line at the appropriate point with a quarter-wave open-circuited stub. A modification that provides the feature of tuning is termination of the stub in a variable capacitor. In both cases the equivalent circuit of the stub is a series trap tuned to resonance at the same frequency as the parallel resonance of the diode, i.e., 900 Mcps. The Q of the series trap must satisfy the following requirements:

- (1) It must be large, so that the RF termination is virtually shorted out over the pass band of the amplifier.
- (2) It must be large enough so that the series trap has a high impedance outside the range of frequencies where the amplifier must provide gain.

First, consider requirement (1). Figure 2-40 shows a plot of VSWR vs frequency for the amplifier, looking from the circulator into the strip line connector with the diode removed from the circuit. The VSWR is fairly low except in a range of frequencies where the stub behaves as a short circuit; over a 100-Mcps bandwidth the VSWR is at least 30 db. Outside this range the

*This bellows was reported in TR-236.

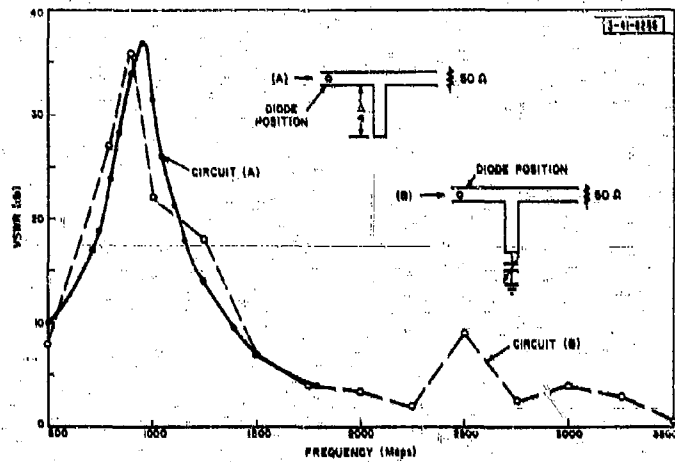


Fig. 2-40. VSWR of tunnel diode amplifier circuit (diode removed).

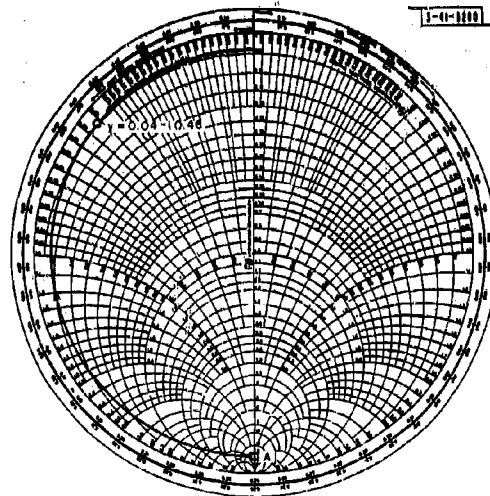


Fig. 2-41. Tunnel diode circuit impedance.

VSWR drops rapidly. The combined effect of the RF termination and the traps seen by the diode in the pass band of the amplifier is illustrated on a Smith-Chart admittance plot in Fig. 2-41. The series trap is assumed to be at resonance, and there is a voltage minimum on the transmission line at this point. Hence, the admittance is real and at a maximum. This is shown by point A on the chart. The distance from the voltage mode to the diode for this particular amplifier was 0.18λ . By rotating the chart a distance of 0.18λ on a constant VSWR circle of 31.6 (30 db) toward the generator, the admittance is transformed to the point $0.04 - j0.46$. The imaginary part of this admittance corresponds to the shunt inductor that brings the diode into parallel resonance. The real part of the admittance is an undesirable damping term.

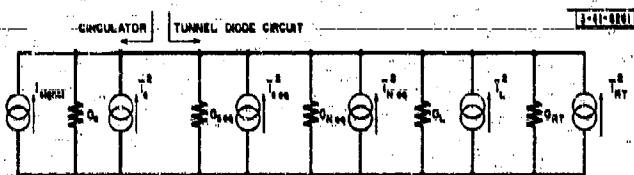


Fig. 2-42. Equivalent circuit for noise figure calculation.

To estimate the effect on the noise figure of the damping term, see the equivalent circuit shown in Fig. 2-42. In this equivalent circuit there are no reactive terms, because the diode is considered to be tuned. The term G_c represents the circulator conductance presented to the diode. The quantity $G_{s eq}$ is that part of the diode shunt conductance due to dissipation in the diode, represented by r_s in Fig. 2-30. The $G_{N eq}$ is the part of the diode shunt conductance due to the tunneling effect, G_N being negative. The term G_L represents any additional circuit losses excluding the damping effect of the RF termination; G_{RT} represents the damping term.

The mean square noise currents associated with these conductances are \bar{i}_c^2 , \bar{i}_s^2 , \bar{i}_N^2 , \bar{i}_L^2 and \bar{i}_{RT}^2 , respectively, where

$$\bar{i}_c^2 = 4KTBG_c$$

$$\bar{i}_s^2 = 4KTBG_{s eq}$$

$$\bar{i}_N^2 = 4KT|G_{N eq}|$$

$$\bar{i}_L^2 = 4KTBG_L$$

$$\bar{i}_{RT}^2 = 4KTBG_{RT}$$

The noise power out of the amplifier = $(KT B/G_c) [G_c + G_{s eq} + |G_{N eq}| + G_L + G_{RT}]$ times gain of amplifier. The noise power into the amplifier = $KT B$. By definition,

$$\text{noise figure} = \frac{\text{noise power out referred to the input}}{\text{noise power in}}$$

$$= 1 + \frac{G_{s eq}}{G_c} + \frac{|G_{N eq}|}{G_c} + \frac{G_L}{G_c} + \frac{G_{RT}}{G_c}$$

If we let N_1 be the noise figure of the amplifier without the contribution of the damping conductance G_{RT} taken into account, then

$$\text{noise figure} = N_1 + \frac{G_{RT}}{G_c}$$

The minimum noise figure obtainable with a germanium diode is about 4 db; that obtainable with a gallium-antimonide diode is about 3 db. Substituting these values for N_1 , and 0.04 for G_{RT}/G_c , we find that the additional damping imposed by G_{RT} increases the noise figure by only 0.08 db for the germanium diode and 0.1 db for the gallium-antimonide diode.

In order to estimate the effect of the damping term on the gain, it is assumed that the circulator is ideal and that the power gain is equal to the square of the magnitude of the reflection coefficient:

$$|\rho|^2 = \left[\frac{1 + \frac{(|G_{Neq}| - G_{seq} - G_L - G_{RT})}{G_c}}{1 - \frac{(|G_{Neq}| - G_{seq} - G_L - G_{RT})}{G_c}} \right]^2$$

If we substitute

$$\alpha = \frac{(|G_{Neq}| - G_{seq} - G_L)}{G_c}$$

then

$$|\rho|^2 = \left[\frac{1 + \alpha - \frac{G_{RT}}{G_c}}{1 - \alpha + \frac{G_{RT}}{G_c}} \right]^2 \quad (14)$$

Assume that the amplifier has 17 db of gain. Then, if the damping term is ignored, $\alpha = 0.753$. By substituting this value, and putting G_{RT}/G_c equal to 0.04 in Eq. (14), we reduce the gain to 15.6 db. Unfortunately, the ratio G_{RT}/G_c is not constant across the pass band because the impedance of the trap changes, causing some loss in bandwidth.

In summary, the Q of the trap is sufficiently large so that the RF termination contributes little to the noise figure of the amplifier, but some small decrease in bandwidth is observed.

Consider now requirement (2), that the impedance of the trap must be high outside the pass band of the amplifier. If this condition is met, the tunnel diode becomes resistively loaded by the RF termination, and the possibility of oscillations is reduced. Referring to the VSWR plot in Fig. 2-40, we see that the VSWR is quite low outside the signal frequency range. In practice, it is found that adequate damping is provided for the suppression of oscillations. An extra margin of stability is provided at the signal frequency band edges, where the VSWR of the tuning circuit is still high, by specifying that the circulator bandwidth be twice as wide as the instantaneous bandwidth of the amplifier.

The tunnel diode amplifier is designed to operate from a 6-volt, DC power supply. A potentiometer divider reduces the bias to about 120 mv for correct biasing of the tunnel diode;

the 50-ohm RF termination forms part of the bias network. The complete amplifier requires less than 4 ma of current. There is a DC block between the circulator and the tunnel diode. At a frequency of 900 Mcps, it is still possible to use a lumped capacitor, and a silvered mica capacitor without wire leads was used. Above 900 Mcps, it is possible to modify the connector and build a coaxial capacitor into the center conductor.

The amplifier is enclosed in an aluminum box to provide RF shielding. The capacitance between the box and the amplifier circuit modifies the performance of the amplifier, and has to be taken into account in the design. Bias connection is made into the amplifier with an Erie feed-through filter.

The diode used in the amplifier has a nominal minimum negative resistance of 60 ohms. This value was chosen so that the diode could be biased at a voltage somewhat in excess of the value required to give maximum gain; the bias point was chosen to give minimum noise figure. The gain was 17 db. The diode, Microstate MS1047, has the following specifications:

Peak current	1.65 ma \pm 10 percent
Noise constant	4.35 max
Capacitance	3 to 5 pf
Minimum negative resistance	60 \pm 2.5 ohms
Series resistance	2 ohms
Series inductance	0.3 m μ h
Resistive cutoff frequency	3.5 Gcps
Self-resonant frequency	4.5 Gcps
Peak valley ratio	8:1 typical, 6:1 max
Peak voltage	55 mv typical
Valley voltage	275 mv typical
Material	germanium

A number of amplifiers have been built to this design and these perform in a similar manner. Typically, the amplifiers have a 40- to 45-Mcps 3-db bandwidth at 17 db of gain and a broadband noise figure of 4.3 db. Eight of these units are now being installed in the phased array components test rack for long-term phase and amplitude stability tests. These units are shown mounted on the rack in Fig. 2-43.

Plots of gain vs frequency for two of these amplifiers are shown in Figs. 2-44(a) and (b), and the differential gain vs frequency is given in Fig. 2-45. It can be seen that the gains are within 1 db of each other over the entire signal frequency range.

The phase shifts through the amplifiers vs frequency are plotted in Figs. 2-46(a) and (b). The plots are somewhat S-shaped. More detailed plots over the frequency range 890 to 910 Mcps are given in Figs. 2-47(a) and (b). These plots are nearly linear. The differential phase vs frequency is shown in Fig. 2-48. It can be seen that the differential phase is within $+1.5^\circ$ to -1.0° over the frequency range 890 to 910 Mcps.

d. Wideband Amplifier

A wideband amplifier that utilizes the residual VSWR of the circulator as a tuning element is shown in Fig. 2-49. The distance from the diode to the circulator has been optimized to obtain the most favorable phase vs frequency relationship. A second tuning element has been introduced at the connector in the form of an open-circuit stub.

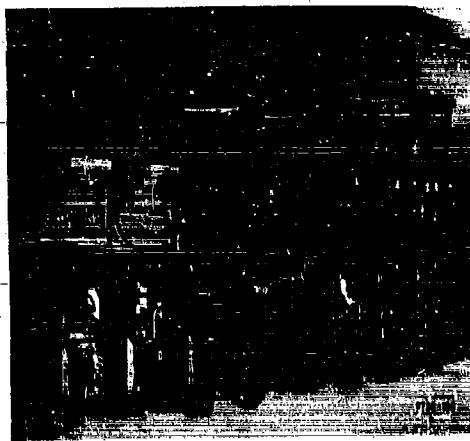
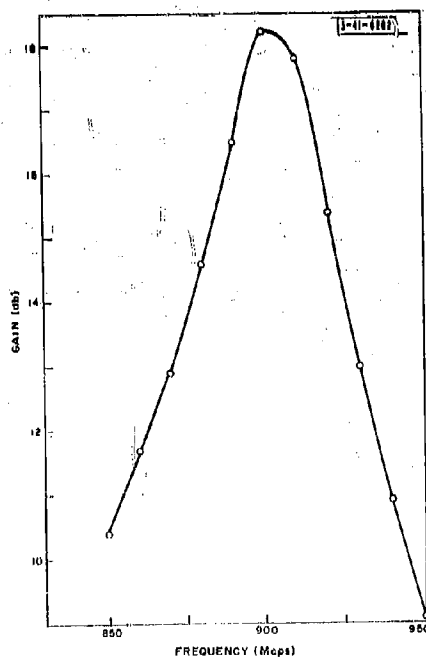
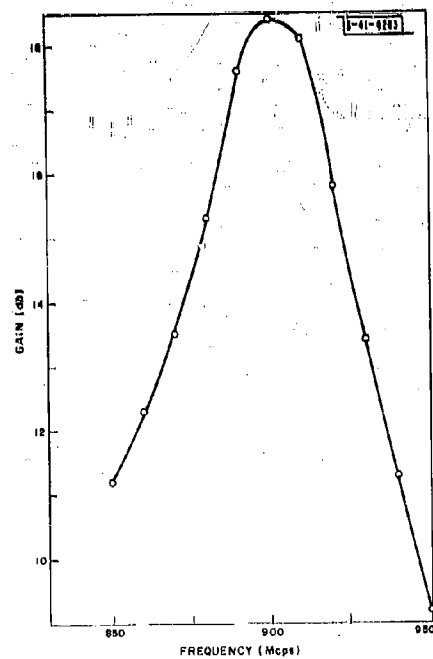


Fig. 2-43. Eight tunnel diode amplifiers mounted with mixers and IF amplifiers in a test rack.



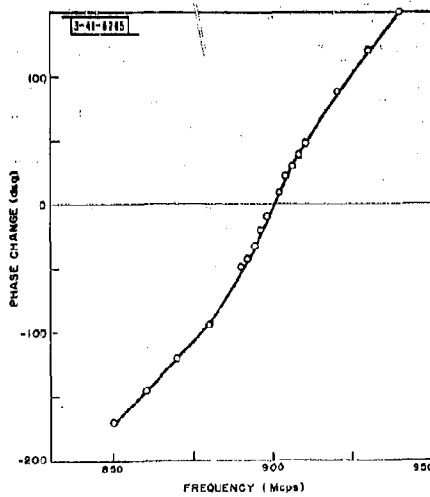
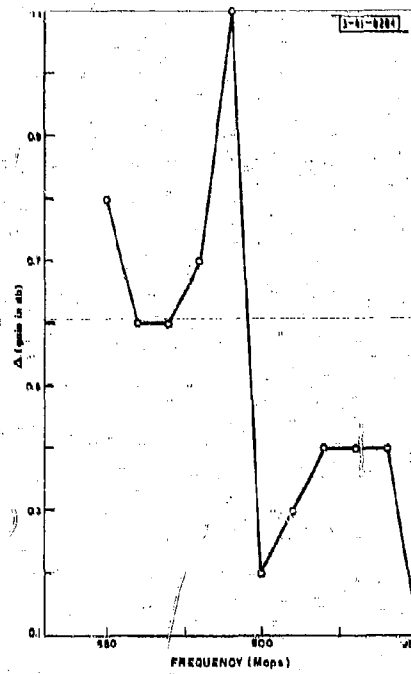
(a) Amplifier 1



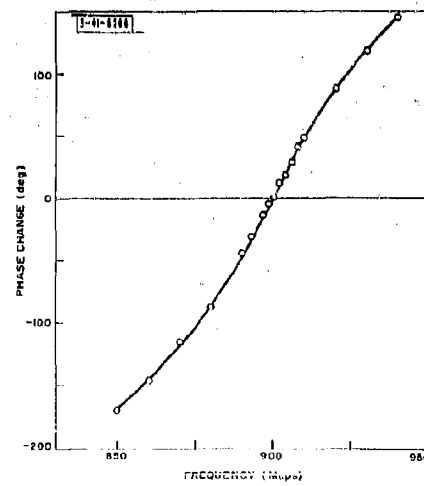
(b) Amplifier 2

Fig. 2-44. Gain vs frequency.

Fig. 2-45. Differential gain vs frequency
(amplifier 2--amplifier 1).

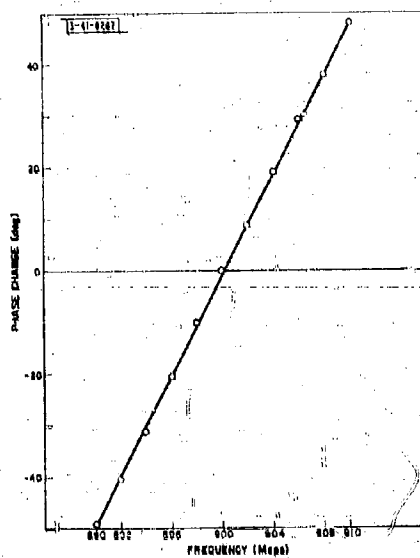


(a) Amplifier 1

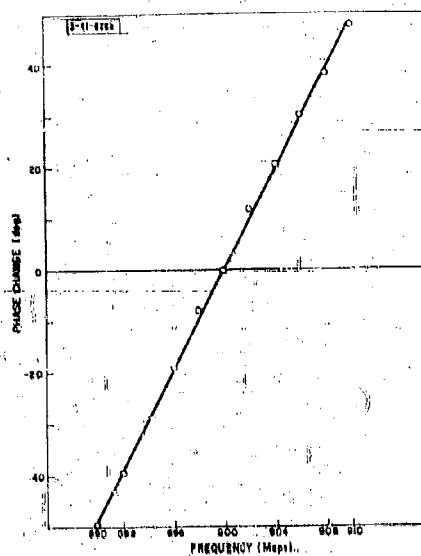


(b) Amplifier 2

Fig. 2-46. Phase vs frequency.



(a) Amplifier 1



(b) Amplifier 2

Fig. 2-47. Detailed plots of phase vs frequency, 890 to 910 Mcps.

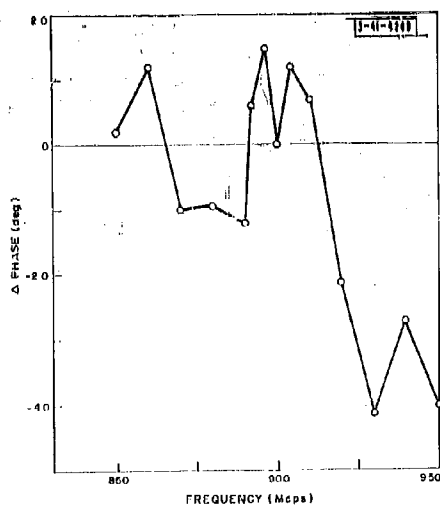


Fig. 2-48. Differential phase vs frequency.

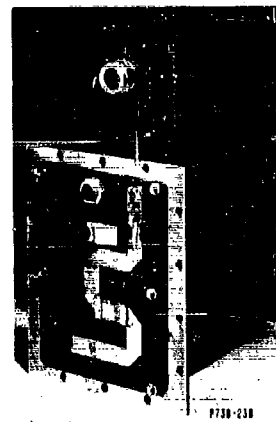
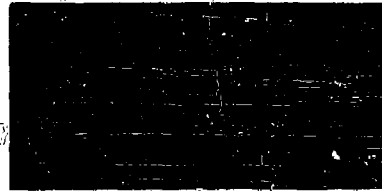


Fig. 2-49. Wideband amplifier.

The swept frequency response of the amplifier is shown in Fig. 2-50. The markers are at 860 and 955 Mcps, the 3-db bandwidth is 140 Mcps and the gain at center frequency is 17 db. A 20-db gain reference level is also shown in the picture. This wideband amplifier will supersede the narrowband version.

Fig. 2-50. Wideband amplifier response (markers at 860 and 955 Mcps). Top trace reference at 20-db gain; lower trace amplifier response (17-db maximum gain).



e. Tunnel Diodes

Two types of commercially available diodes are suitable for use in low-noise microwave amplifiers. One type is made from doped germanium and one from doped gallium antimonide.

The essential differences between these two types are brought out in Fig. 2-51, which shows the I-V characteristics for a germanium diode and a gallium-antimonide diode. Each diode was selected to have a negative resistance of 60 ohms. The optimum bias point is at a higher current for the germanium diode than for the GaSb diode. The main contribution to the amplifier noise is given by the shot-noise term $20I_0|R|$, where I_0 is the DC bias current. For these diodes, $|R|$ has the same value, 60 ohms. Hence, the ratio of the shot-noise contributions is equal to the ratio of the DC bias points. The lower shot noise of the GaSb diode gives it an improvement in noise figure of approximately 1.0 db. Substitution of the GaSb diode in the 900-Mcps amplifier gave a noise figure of 3.3 db.

It can also be seen from the curves that the range of the linear negative resistance region for the GaSb unit is about half the range for the germanium unit. Moreover, it can be expected that the saturation output level will be about 6 db less for the GaSb unit.

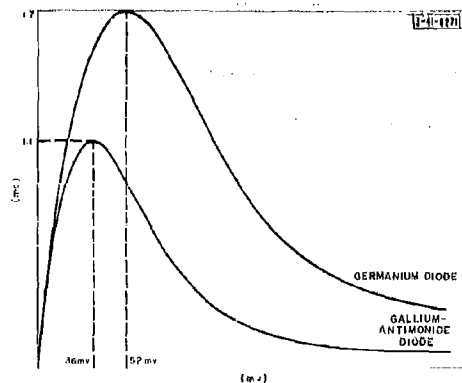


Fig. 2-51. Tunnel diode I-V characteristics.

f. Mixers

The specific requirements for a mixer that is to be used with tunnel diode amplifiers are:

- (1) Low VSWR at the signal port,
- (2) High isolation between the local oscillator and signal ports.

These requirements are best satisfied by a balanced mixer such as that developed by Sage Laboratories. This mixer is of a coaxial construction that utilizes a hybrid power divider and crystals of type 4N416E. For a local oscillator drive level of 2 mw, the VSWR at the signal and local oscillator ports is under 1.3 over the frequency range 850 to 950 Mcps, and the isolation is 12 db, minimum. Under maximum mismatch conditions at the antenna (2.5:1) the isolation provided by the 4-port circulator in the tunnel diode amplifier is, in the worst case, 32 db. Hence, the leakage to the tunnel diode is kept to -40 db, maximum.

C. TUNNEL DIODE DOWN-CONVERTERS

1. Introduction

Two tunnel diode down-converters of the type reported by F. Sterzer and A. Presser* were obtained from the Radio Corporation of America for purposes of evaluation. A conversion loss of 0 db and a wideband system noise figure of 2.5 to 3 db have been obtained by these workers. When the tunnel diode down-converter is compared with the conventional crystal mixer, its lower conversion loss and noise figure, along with its higher power output saturation level and greater resistance to burnout, make it an interesting device.

It must be emphasized that a phased array radar that employs RF beam-forming techniques will have unavoidable losses in front of the mixer due to the beam-forming hardware. For maximum sensitivity it is necessary to place an RF preamplifier behind every antenna element, and the system noise temperature is primarily defined by the preamplifier. In this situation, there is no real advantage to be gained in using the tunnel diode down-converter in place of the crystal mixer.

2. Experimental Results

The theory of operation and the characteristics of the tunnel diode down-converters are so extensively reported by Sterzer and Presser, that there appears to be little merit in presenting a verification of their experimental results. However, some of the properties of the two down-converters supplied are of interest.

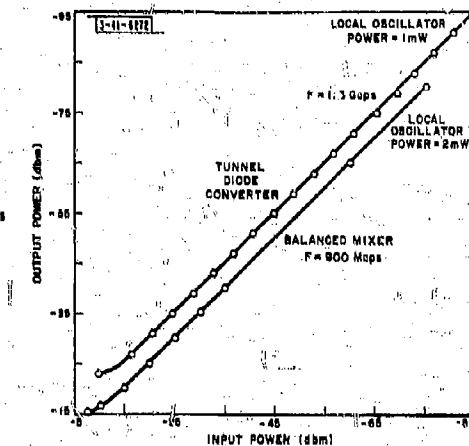
The down-converters were operated with the impedance presented to the device at the image frequency equal to the source impedance (50 ohms). Under these conditions, the broadband system noise figure was about 5 db.† About 2 db of improvement can be obtained if a short circuit is presented to the image frequency current by the use of an external image rejection filter. The converters had a gain of approximately unity and 30 Mcps of bandwidth centered at 1300 Mcps. No DC bias was required. Various local-oscillator (LO) drive levels were used, ranging from 1 to 3 mw. At zero LO drive, the signal VSWR's of the down-converters were 1.4:1 and 1.5:1, respectively, and increased to 2.5:1 and 2.2:1, respectively, at a 3-mw LO drive.

*F. Sterzer and A. Presser, "Stable Low-Noise Tunnel-Diode Frequency Converters," RCA Review 23, No. 1, 3 (March 1962).

† The noise figure of the IF amplifier that followed was equal to 1.7 db.

Figure 2-52 shows a plot of input power at 1300 Mcps vs output power at 30 Mcps for one of the units. For comparison, the same relationship has been plotted for a balanced crystal mixer at 900 Mcps, with the same LO drive per crystal. The comparison is not really meaningful because the IF input impedance in both cases was 50 ohms; this presented a good IF match to the crystal mixer, but a mismatch to the tunnel diode. The tunnel diode curve indicating a 10-db conversion loss for this unit is probably accounted for by the IF mismatch.

Fig. 2-52. Output power vs input power curves for tunnel diode converter and crystal mixer.



Amplitude and phase stability measurements were complicated by the fact that the output and input were at two different frequencies. Any reference channel had to use a frequency converting device that introduced uncertainties into the results. Consequently, only differential phase and amplitude measurements between the two tunnel diode converters were made.

The differential phase and amplitude characteristics vs input power were recorded at a frequency of 1.3 Gcps. These have been plotted in Fig. 2-53.

One down-converter was placed in an oven, while the other was kept at room temperature (25°C). The temperature of the oven was varied from 10° to 35°. At a frequency of 1.3 Gcps, the greatest difference in gain between the two channels was 0.7 db, and the phase difference was 1.25°.

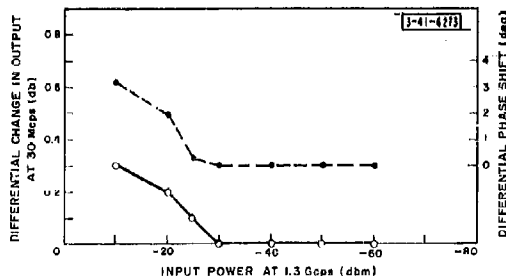


Fig. 2-53. Tunnel diode down-converter saturation characteristics.

D. LOCAL OSCILLATOR EFFECTS IN TUNNEL DIODE RECEIVERS

1. Introduction

It is common practice to use a preamplifier to set the system input noise temperature. The preamplifier is followed by a mixer that converts the signal to an intermediate frequency. Most of the receiver amplification is provided at the intermediate frequency, where it is usually easier to obtain high gain, rather than at the RF frequency.

The ideal mixer would have three pairs of terminals, corresponding to the IF, RF and LO frequencies, with zero leakage between any of the terminal pairs. Unfortunately, practical mixers do exhibit leakage. It is usually easy to obtain high isolation between the RF and IF ports and between the LO and IF ports, since the respective frequencies are widely spaced. It is a much more difficult task to obtain high isolation between the LO and RF ports, although this difficulty can be minimized in a well-designed balanced mixer.

The impedance that the mixer presents to the signal frequency is a function of the local oscillator drive. Provided that the signal power is at least 20 db below the local oscillator drive power, the mixer impedance at the signal frequency is not a function of the signal power level. Under these conditions, a linear relationship exists between the RF power into the mixer and the IF power out of it.

The function of the local oscillator is to drive the diodes in the mixer over a I-V characteristic that is essentially square-law. Hence, even if the local oscillator is free from harmonics, the mixer itself generates harmonics. It is the transfer of power from the local oscillator port to the signal frequency port by way of the LO harmonics generated within the mixer itself that makes it difficult to obtain high isolation.

2. Evaluation of Mixers

In order to illustrate the problem, some measurements taken on two types of balanced mixers are presented. (A bolometer was used to measure power at the fundamental frequency and at all harmonics.)

Type 1 (Sage Laboratories 252-1A)

Signal frequency	1320 Mcps
LO frequency	1260 Mcps
IF frequency	60 Mcps
LO drive	+3 dbm
Total power leakage, LO port to signal port	-2.4 dbm
Power leakage, LO port to signal port	
Fundamental	-2.7 dbm
2nd harmonic	-14.3 dbm
3rd harmonic	-19.7 dbm
Total power	-2.4 dbm

Type 2 (Sage Laboratories 2523-5)

Signal frequency	850 to 950 Mcps
LO frequency	825 Mcps

IF frequency	30 Mcps
LO drive	+3 dbm
Total power leakage, LO port to signal port	-10.7 dbm
Power leakage, LO port to signal port	
Fundamental	-16.7 dbm
2nd harmonic	-13.3 dbm
3rd harmonic	-25 dbm
4th harmonic	-29 dbm
Total power	-11.4 dbm

It can be seen that the LO isolation for the first mixer is 5.4 db, and that the greatest contribution to the leakage is the fundamental frequency. By comparison, the effect of harmonics greater than the third is small. However, it will be shown later that, although small, the contribution of the higher harmonics to the leakage can be extremely troublesome to tunnel diode amplifiers.

It is interesting to note that the method of obtaining the isolation of the mixer by summing the contributions of individual measurements on the first three harmonics agrees well with the measurement using a bolometer.

In the case of the second mixer, a bolometer measurement indicated an isolation of 13.7 db. The method of obtaining the isolation by summing the contributions of the first four harmonics yields a result that differs by 0.7 db. The difference has not been accounted for. The main point of interest is that the major contributor to the leakage is the second harmonic. Better balance in the mixer has increased the rejection of the fundamental frequency and the third harmonic.

3. Circulators

The most successful tunnel diode amplifier that has been realized to date utilizes a circulator to separate input and output signals. Such an amplifier is shown as part of a receiver in Fig. 2-54. It has been found that the use of a 4-port circulator is necessary to reduce input and

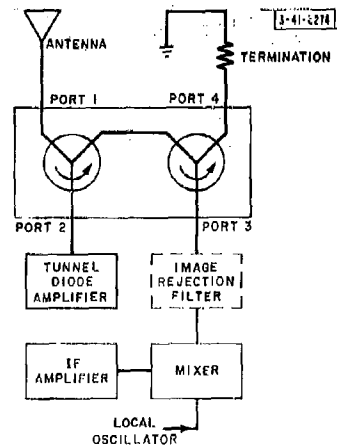


Fig. 2-54. Low-noise receiver with tunnel diode preamplifier.

output mismatch effects. It is also helpful in reducing the effects of local oscillator leakage. However, the amount of protection from LO leakage that the circulator provides is far less than was previously assumed. The problem is that the circulator maintains its characteristics over a range of frequencies that is, in general, less than an octave. The circulator cannot be relied upon to provide high isolation from the mixer to the tunnel diode at harmonics of the local oscillator. Most of the circulators operate below the frequency of ferromagnetic resonance. This means that above a harmonic of a certain order, the harmonics of the local oscillator are above the resonance frequency of the circulator. When this occurs, the paths through the circulator, which are paths of easy transmission in the signal frequency band, become paths of high isolation. Conversely, directions in the circulator that offer high isolation to frequencies within the signal frequency band become paths of low insertion loss. As a result, high-order harmonics of the local oscillator, generated within the mixer, can have a large disturbing influence on the tunnel diode. In order to demonstrate this problem, some measurements were taken on one of ten circulators recently acquired for tunnel diode amplifier construction. The characteristics of this circulator (Melabs X615-5) are as follows.

Circulator Details

Signal frequency range	850 to 950 Mcps
Insertion loss, port 2 to port 3	0.6 db
Isolation, port 3 to port 2	>40 db

Measured Characteristics

Frequency (Mcps)	Insertion Loss Port 2 to Port 3 (db)	Isolation Port 3 to Port 2 (db)	Power from Mixer 2 at Port 2 (dbm)
825	0.6	50	-66.7
2 × 825	24.4	45	-58.3
3 × 825	36.0	19.6	-44.6
4 × 825	22.5	2.7	-31.7

The fourth column shows the amount of power that leaks back to the tunnel diode amplifier at the various harmonics of the local oscillator when a mixer of type 2 is used in conjunction with this particular circulator and when the LO frequency is set at 825 Mcps. Clearly, with regard to order of importance, the fourth column should be read from the bottom upward.

A further experiment was performed to find out what effect the various harmonics had on the tunnel diode amplifier. In general, the local oscillator and its harmonics vary the bias point of the tunnel diode in a periodic manner. This causes a change in the value of the negative resistance of the diode presented to the signal frequency band and, hence, a reduction in gain. Below a leakage level of about -45 dbm, no gain compression is noticeable.

It was found that the first two harmonics had no appreciable effect on the amplifier gain. The third harmonic caused a discernible compression, and the fourth harmonic caused a compression of from about 8 to 17 db. A further serious effect observed was that the amount of compression caused by the fourth harmonic was very dependent on the setting of local-oscillator frequency.

4. Solution of the Problem

In order to obtain the full advantage of using a tunnel diode preamplifier, a filter must be placed between the tunnel diode amplifier and the mixer to reject image channel noise. Without the filter, the system sensitivity is degraded by 3 db. The filter must have minimum attenuation within the signal frequency band and a linear phase-frequency characteristic. It must also provide about 20 db of rejection within a band of frequencies (equal to the signal frequency band) centered about a frequency equal to $f_{LO} - f_{IF}$. This filter can be made a bandpass filter and, hence, can perform the additional task of providing the required amount of LO harmonic rejection. It can also probably provide 10 db of LO rejection at the fundamental frequency as an additional safety factor, thus allowing for reduced circulator isolation that occurs when the amplifier is driven from a mismatched input. In a phased array radar, the necessary isolation between the mixer and preamplifier can also be provided by an RF beam-forming matrix. High-order harmonics generated by transmitting tubes in an array where transmitting and receiving functions are combined can also prove troublesome.

E. ELECTRON-BEAM PARAMETRIC AMPLIFIER (EBPA) EVALUATION PROGRAM

An extensive testing program designed to measure the operational characteristics of the Zenith EBPA was completed recently. Particular emphasis was placed on confirming those characteristics of the EBPA that are of interest to designers of phased array radar systems.

Week-long pump-on amplitude stabilities of better than 1 db rms with concurrent pump-on phase stabilities of better than 1° rms were obtained after certain problems connected with the EBPA's sensitivity to small changes in magnetic field strength had been overcome.

The full scope and results of this evaluation program are presented in a Lincoln Laboratory report.*

SPECIAL ACKNOWLEDGMENT

The author would like to express his appreciation to Dr. J. A. Weiss for many helpful and stimulating discussions. Acknowledgment is also due F. Sterzer and A. Presser of RCA Princeton Laboratory, as well as J. Sie of Microstate Electronics Company, for many valuable discussions. The author is deeply indebted to F. X. McCabe and R. J. Sarasin who constructed the hardware described in this chapter and made the electrical measurements.

* J. H. Teele, "Operational Characteristics of 16 Electron-Beam Parametric Amplifiers in a 900 Mcps Phased Array," G-Report 41G-1 [U], Lincoln Laboratory, M.I.T. (6 August 1962), ASTIA 288223, H-444.

CHAPTER III INTERMEDIATE-FREQUENCY AMPLIFIERS FOR PHASED ARRAYS

J. DiBartolo

SUMMARY

This chapter outlines parameter limits of transformers with toroidal cores for use with amplifiers covering the frequency band 10 to 100 Mcps.

A brief description of these transformer-coupled common-base amplifiers was presented in TR-236.* However, more design details are given in this chapter for a similar amplifier with an even larger gain-bandwidth product. Plots of the theoretical bandpass and phase characteristics are included, together with experimental results on several amplifiers. Design graphs are also presented to show practical magnitudes of leakage inductances of toroidal transformers as a function of turns ratio. It was found possible to increase the self-inductance of the transformers and thereby improve the low-frequency gain of the amplifier by presetting the transformer cores with a current impulse.

Several amplifiers have been built, and their gain and bandwidth have been found to be similar. Identical layout and regular stock components were used in all cases.

The primary and secondary windings of the transformer are wound so that they have the same rotation sense, and the secondary turns are spread out to cover the entire core in order to reduce the leakage inductance.

The solution to mesh equations for the theoretical gain is arrived at by flow-graph techniques. Several graphs are introduced to show the theoretical gain, the bandwidth and the phase linearity of a typical stage.

Moreover, photographs are included to show the achieved rise time, the gain and bandwidth, the transient response and the overload condition. A typical amplifier design using these techniques has 66 db of gain and nanosecond rise, fall and recovery time.

A. INTRODUCTION

An operational phased array radar may require several thousand IF amplifiers having practically identical phase and amplitude characteristics. The amplifier characteristics should track one another over wide ranges of temperature and power-supply voltage. The ideal amplifier would meet these requirements and also be inexpensive, reliable (all-solid-state) and compact. It would require little or no tuning and use a minimum of power. The wideband amplifier described in this chapter has a linear phase vs frequency characteristic, maintains gain and phase stability for a wide range of temperature and voltage variations and can be built inexpensively using normal stock components. This is achieved by using transistors in a common-base configuration and using transformers for interstage coupling to provide adequate impedance transformation. Transformers are inherently frequency-sensitive, as evidenced by various reactive elements in their equivalent circuit. It is the object of this discussion to show how these reactive elements can be controlled and used to obtain wideband amplifiers that are relatively insensitive to variations in the transistor parameters.

* J. L. Allen, et al., "Phased Array Radar Studies, 1 July 1960 to 1 July 1961," Technical Report No. 236 (U), Lincoln Laboratory, M. I. T. (13 November 1961), ASTIA 271724, H-474.

B. BASIC TRANSFORMER REQUIREMENTS FOR GOOD FREQUENCY RESPONSE

The transistor used has a current transfer function that is fairly constant for all frequencies of interest. Therefore, one can assume that the stage gain for all frequencies in the pass band depends mainly on the parameters of the transformer. Thus, the transistor is represented as a fixed current source, but with frequency-sensitive input and output impedances.

The equivalent circuit of a typical stage of the amplifier is presented in Fig. 2-55, where C_T (3.5 pf) is the total capacitance. It is composed of: (1) the collector's depletion layer capacitance, (2) the effective capacity C_1 due to the transformer [expressed in Eq. (4) below] and (3) the stray capacitance to ground. In Fig. 2-55, R_1 is a swamping resistor used to lower the Q of the circuit; KL_p (6 μ h) and KL_s (0.45 μ h) are the effective primary and secondary self inductances while L_{Lp} and L_{Ls} are leakage inductances; M (1.5 μ h) is the mutual inductance; R_e (22 ohms) and L_e (0.036 μ h) are the series-equivalent input impedance of the transistor, and C_B is the emitter bypass capacitor. Since C_B is not a good bypass for all frequencies in the pass band, one must also include it in the equivalent circuit. It is obvious that the elements of the transformer will be the major factors that determine the frequency limits of the amplifier. Therefore, it is necessary to determine what can be done to control the transformer parameters in order to improve frequency response.

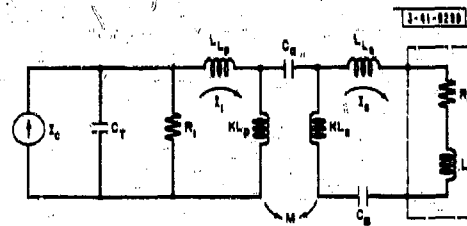


Fig. 2-55. Equivalent circuit of a typical stage.

Low mutual and stray capacitance, low leakage inductance and high values of self-inductances are basic requirements for uniform wideband response. However, it is impossible to satisfy all these conditions at the same time.

The mutual capacitance will make coupling between windings frequency-dependent; therefore it is undesirable, although it can not be eliminated entirely. Stray and transistor capacitances are significant also. The total capacitance contributed by the transformer can be calculated by means of the following equation:*

$$C_1 = \frac{1}{3} \left[\sum C_p + \frac{(N_p \mp N_s)^2}{N_p^2} \sum C_a \right] \quad (4)$$

where C_p is the primary winding capacitance, N_p and N_s are the primary and secondary turns, respectively, and C_a is the capacitance between windings. In this case, because the secondary winding has very few turns, the distributed capacitance is very small and can be neglected.

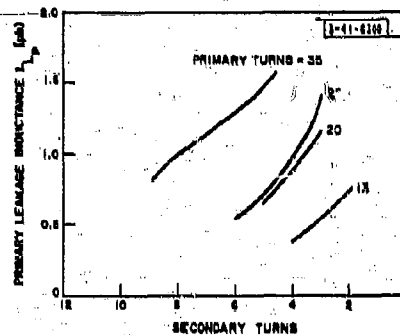
Equation (4) shows that C_1 is minimum when the sign is negative. The negative sign is obtained when both primary and secondary windings are wound with the same angular rotation.

*R. Lee, Electronic Transformers and Circuits, 2nd Ed. (Wiley, New York, 1955), pp. 219-220.

Typical values of C_1 obtained for a transformer with turns ratio 22:5 are 2.4 pf for a negative sign in Eq. (1) and 6 pf for a positive sign. The difference is indeed small, but it can be shown in practice that using the proper polarity extends the high frequency by several megacycles. The effect of this capacitance is even more significant if one proposes to build a wideband amplifier centered at a higher frequency than that considered at present.

The next most important and somewhat controllable element is the leakage inductance, which is, by definition, that portion of the primary flux that does not link the secondary winding. This inductance resonates with the total apparent capacitance C_1 and determines the high-frequency boundary of the amplifier. The value of the leakage inductance can be made small by using a toroidal core.

Fig. 2-56. Transformer leakage inductance vs primary and secondary turns.



The toroids used for these new transformers are 1/4 inch o.d. and are of the same Q-2 material used in the earlier type of amplifier.* The experimental curves of Fig. 2-56 show the relationship of leakage inductance to turns ratio for these new transformers. It follows from Fig. 2-56 that a 1:1 turns ratio would be optimum for obtaining a minimum leakage inductance. However, because we are interested in obtaining a convenient interstage impedance transformation, we must exchange turns ratio for leakage inductance. Figure 2-56 could be used as a guide for this purpose.

Finally, we consider the mutual inductance, which is defined in the following expression:

$$M = K \sqrt{L_p L_s} \quad (2)$$

where K is the coefficient of coupling and L_p and L_s are the primary and secondary self-inductance, respectively. A high value of M is necessary to obtain gain at low frequencies, but because $K \approx 1$, $M \approx \sqrt{L_p L_s}$, and a glance at Figs. 2-56 and 2-57 suggests some frequency limitations imposed by this expression. Figure 2-56 shows that leakage inductance increases as L_p and L_s increase, even when their turns ratio is constant, and Fig. 2-57 shows values of mutual inductance that can be realized as a function of turns ratio. It can be concluded, therefore, that making M very large will negate the high-frequency response. Hence, the values of M as well as those of L_p , L_s and N_p/N_s must represent the optimum compromise for best gain-bandwidth product.

* See TR-236, Part 2, Ch. V.

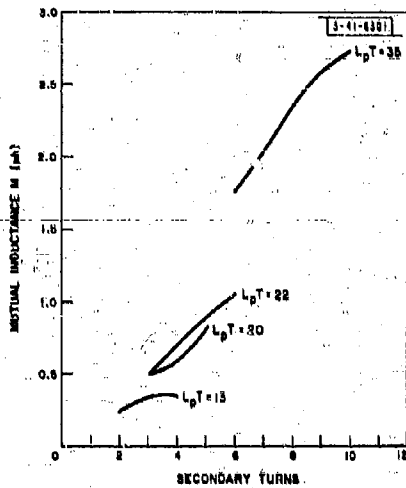
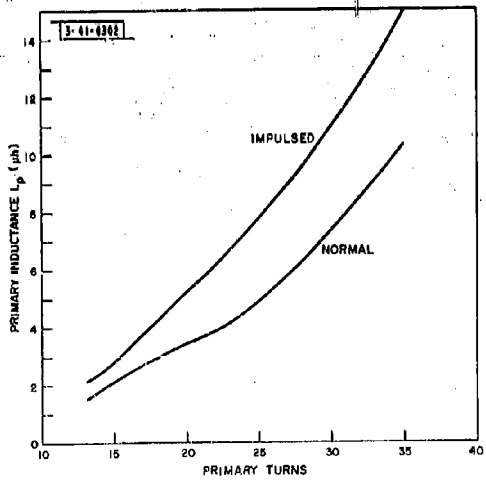


Fig. 2-57. Values of M for various turns ratios. When the core is pulsed all values of M will increase.

Fig. 2-58. Values of primary inductance before and after a current pulse is put through the core.



Thus far we have considered the high-frequency limits, and graphs have been plotted that could be used as a guide to optimization. We shall now look at the low-frequency limits. Because the primary impedance is low, a large current pulse can be put through the primary winding of the transformer. This has the effect of permanently raising the incremental permeability, hence increasing the incremental inductance. When a current pulse is sent through the winding of the transformer, it brings the magnetic state of the core to a new point on the hysteresis loop. At this point, a minor hysteresis loop is formed for the small AC signal current. Its slope is steeper than that which determined the initial permeability condition. Consequently, the incremental permeability has been increased, resulting in a greater inductance for a fixed number of turns. This helps increase the gain at low frequencies, but it has the effect of slightly increasing the loss at high frequencies. Figure 2-58 shows the values of primary inductance before and after a current impulse is put through the core. In practice, one can preset the core by brushing both ends of the primary leads against the terminals of a 22.5-volt battery without regard to polarity. The loss of the core is increased, but this is not a disadvantage because it lowers the Q of the coil. In fact, it helps reduce the peaking due to transformer resonance. Figure 2-59 shows the value of M (the coupling inductance) both before and after the application of the current impulse. It can be seen that M is larger for the latter case. The related leakage inductance has remained unchanged for almost all conditions in this figure. We have found that these cores will remain in this new state for long periods of time. Several transformers have been measured before and after saturation. The inductance of these same transformers was measured again a year later and it was found to be unchanged.

Just as the leakage inductance and the total primary capacitance determine the high-frequency limits, C_B (the emitter bypass capacitor) can be chosen to resonate with L_s (the secondary inductance of the transformer) and the input reactance of the transistor to determine the low-frequency

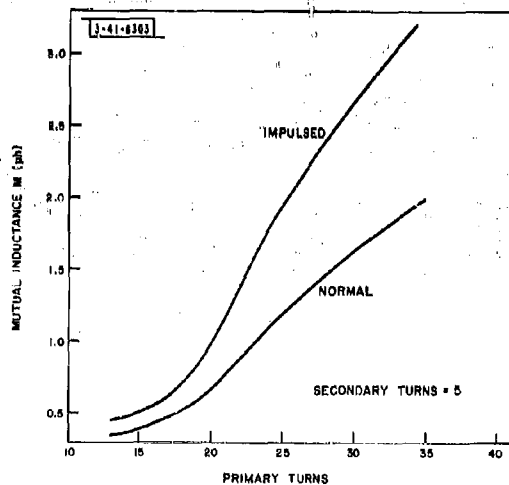


Fig. 2-59. Values of M (the coupling inductance) before and after the application of the current pulse.

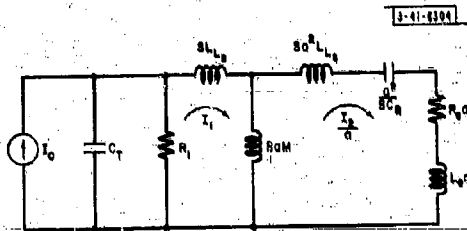


Fig. 2-60. Revised equivalent circuit of typical stage.

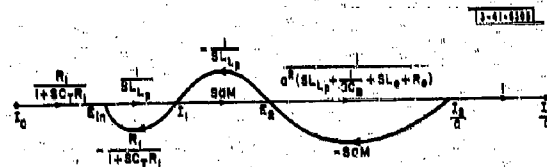


Fig. 2-61. Flow graph for obtaining transfer function of a single stage.

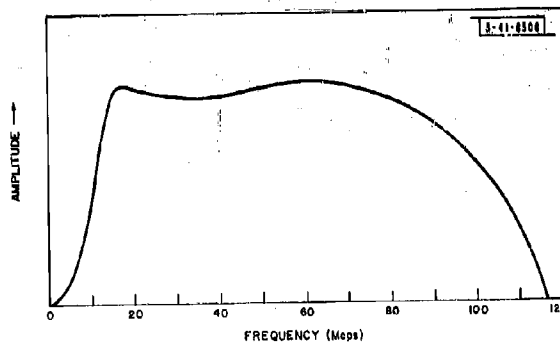


Fig. 2-62. Theoretical current gain vs frequency for a typical stage.

boundary. For the values chosen here, C_B is approximately 200 pf and it resonates with KL_p and L_{L_s} at about 17 Mcps. The Q of this circuit is very low. Therefore, there will not be a severe peaking due to its resonance.

C. ANALYSIS OF A TYPICAL STAGE

The basic equivalent circuit for one stage of this wideband, transformer-coupled amplifier is depicted in Fig. 2-55. With the aid of most of the information presented in the preceding curves, the turns of this transformer have been chosen as 22 turns for the primary and 5 turns for the secondary. Since the coupling of the primary and secondary windings is almost unity, the circuit shown in Fig. 2-55 can be represented accurately by the equivalent circuit of Fig. 2-60, for which the solution to mesh equations has been arrived at by use of a flow graph.* Figure 2-61 is the flow-graph equivalent of the preceding circuit, and the current transfer function derived from the above flow graph is

$$\frac{I_2}{I_1} = \frac{SM}{a \left[s(L_{L_p} + L_e) + R_e + \frac{1}{sC_B} \right] \left[s \left(\frac{1}{R_1} + sC_T \right) (L_{L_p} + aM) + 1 \right] + SM \left[sL_{L_p} \left(\frac{1}{R_1} + sC_T \right) + 1 \right]} \quad (3)$$

From Eq. (3) one can see how mutual inductance M , leakage inductances L_{L_p} and L_{L_s} and the total circuit capacitance C_T affect the circuit current gain at various frequencies.

Equation (3) was programmed on the IBM 7090 computer with the typical circuit values mentioned earlier. The computed plot of gain vs frequency is depicted in Fig. 2-62. This figure shows the single-stage gain to be about 12 db while the frequency bandpass extends from 10 to 110 Mcps (3-db points).

The phase vs frequency characteristic of the typical amplifier stage was also computed and is depicted in Fig. 2-63, which shows clearly that the amplifier has a linear phase vs frequency characteristic that makes it desirable for phased array applications. Figure 2-64 shows the bandpass obtained with a 6-stage amplifier. The 3-db points are 17 and 80 Mcps. The high-frequency limit for this type of amplifier could be extended to over 100 Mcps, but in that range the amplifier becomes sensitive to variations in individual transistors.

D. PRACTICAL AMPLIFIERS

Printed board circuits are used to facilitate wiring and to control stray capacitance. Amplifiers can be built to provide gain from 30 to 66 db and more. Figure 2-65 shows the circuit of a 3-stage amplifier that has a gain of 30 db. If more gain is desired, several more intermediate stages can be added following the first stage, as shown in Fig. 2-66. The input stage is arranged to provide a 50-ohm impedance over a wide band of frequencies, accomplished at the expense of noise figure. Actually, a 33-ohm resistor is placed in series with the input of the amplifier and becomes an integral part of input impedance. The output stage impedance averages 50 ohms throughout the frequency range of interest. The transistor used throughout is the 2N502, chosen for its high-frequency alpha cutoff and relatively low cost. Because of the low power dissipation rating of the 2N502, the maximum undistorted voltage that can be delivered to a 50-ohm load is 0.4 volt peak. However, a Western Electric 1195 can be used as the output stage to obtain linear gain for output voltages up to 2 volts peak to peak.

* S. J. Mason, "Feedback Theory; Some Properties of Signal Flow Graphs," Proc. IRE 41, 1144 (1953).

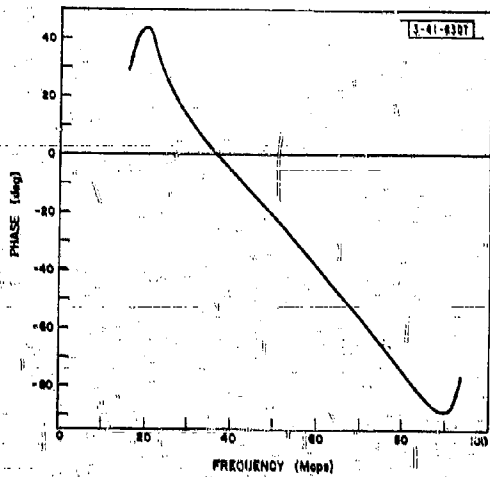


Fig. 2-63. Theoretical phase vs frequency for a typical stage.

Fig. 2-64. Typical performance of a 6-stage wideband amplifier. Gain is 66 db and the (3-db) bandwidth is 17 to 80 Mcps.

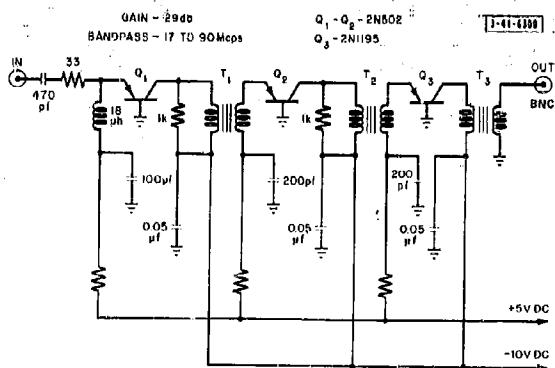


Fig. 2-65. Wideband IF amplifier (gain, 29 db; bandpass, 17 to 90 Mcps).

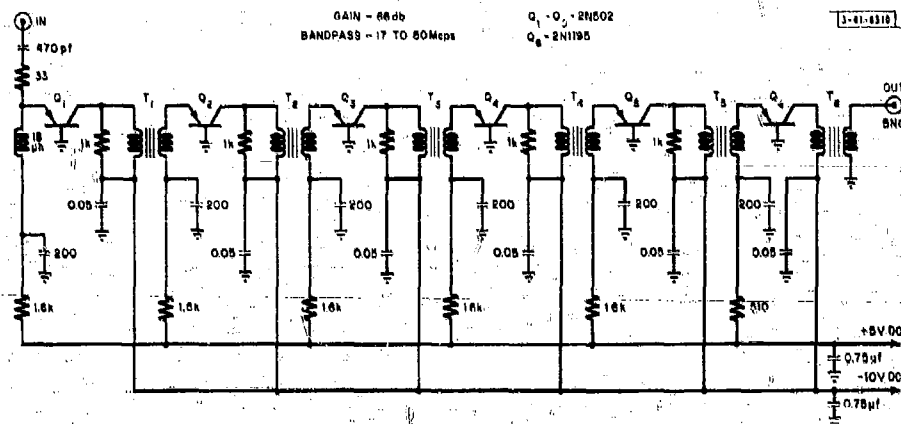


Fig. 2-66. Wideband IF amplifier (gain, 66 db; bandpass, 17 to 80 Mcps).

The biasing current is approximately 3 ma for all stages except where a Western Electric 1195 is used (≈ 9 ma). This biasing current is allowed to flow through the transformer. However, because these cores have been preset, the presence of this steady-state current will no longer affect the cores. This is an important advantage, because it prevents changes of self-inductance and, consequently, it helps stabilize the gain of the amplifier, which can be affected by changes in the bias current. However, for a constant supply voltage, the bias current is almost entirely a function of the external emitter resistor (1.6 kilohms). Therefore, we can conclude that the amplifier gain is not sensitive to the transistor's emitter-base parameter variations due to aging except for changes in alpha.

The collector supply voltage is 10 volts and can be varied ± 15 percent without altering the gain or the bandwidth of the amplifier. If it should rise to a value greater than 10 volts, the only effect would be to increase the dissipation of the collector. If the supply voltage should, on the other hand, become smaller than 8 volts, the depletion layer capacitance of the collector will increase as a function of the decreasing collector voltage, and the high-frequency gain will decrease.

In general, this type of amplifier performs very well and it is very stable even under the influence of large temperature variations. A 6-stage amplifier, for example, was enclosed in an oven where the temperature was changed from ambient to 60°C . A gain change of approximately 0.5 db was detected for this temperature change of over 30°C .

Because this amplifier uses ferramic cores, its characteristics were scrutinized when it was working in the magnetic leakage fields of an unshielded circulator but were found to be unaffected.

Some of the other properties of this amplifier can be briefly summarized with the presentation of a series of photographs. Figure 2-67, for example, shows the test pulse (0.150 μsec long) used to evaluate the amplifier. Figure 2-68 is the same pulse shown in Fig. 2-67 except that it was taken from the output of the amplifier after a 66-db pad was placed at its input. There is no evidence of distortion in this output pulse. Figure 2-69 shows the overload condition of the



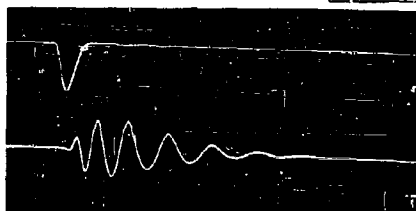
Fig. 2-67. Test pulse used to evaluate the amplifier. The calibration is 0.4 v/cm and 0.05 μ sec/cm; $f_0 = 50$ Mcps.

Fig. 2-68. The pulse taken from the output of the amplifier after the pulse shown in Fig. 2-67 and 66 db of padding have been connected at the input.



Fig. 2-69. The pulse taken from the output of the amplifier after the conditions described for Fig. 2-68 have been changed by the removal of a 20-db pad. The time base has been extended to include the effects of initial and steady-state conditions. The calibration is 1 v/cm and 0.1 μ sec/cm.

Fig. 2-70. Approximation of an impulse response.



amplifier for a pulse 0.3 μsec long. Two points are worth noticing: the short duration of the initial transient and the fact that the amplifier completely recovered from a 20-db overload within 30 nsec. The transient response is emphasized even more in Fig. 2-70, which represents the response to an impulse. The carrier frequency used in all the preceding photographs is 50 Mcps.

The necessity of using a small emitter bypass capacitor to improve the low-frequency gain was pointed out earlier. It should be apparent that by using such a small-value capacitor we have improved the recovery time under overload conditions. Figure 2-71 depicts the response to a 3.5- μsec pulse, and Fig. 2-72 is the overload condition for the same 3.5- μsec pulse. The latter pictures show clearly the duration of the initial transient and the recovery time of the amplifier. This type of amplifier finds diversified uses in the laboratory. Figure 2-73 shows this amplifier, which also has been used, successfully, as a wideband switch by gating the bias voltage (see Part 2, Ch. VI).



Fig. 2-71. Reproduction of a 3.5- μsec pulse. The calibration is 0.4 v/cm and 0.5 $\mu\text{sec}/\text{cm}$.



Fig. 2-72. The pulse shown in Fig. 2-71 after the amplifier has been subjected to overload conditions. The calibration is 1 v/cm and 0.5 $\mu\text{sec}/\text{cm}$.

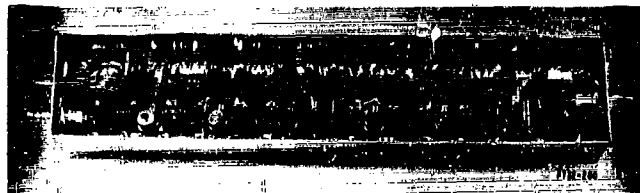


Fig. 2-73. Six-stage wideband IF amplifier (open view).

BIBLIOGRAPHY

P. R. Gillette, K. Oshima and R. M. Rows, "Measurement of Parameters Controlling Pulse-Front Response of Transformers," *Trans. IRE, PGCP CP-3*, 20 (1956).

M. M. Maddox and M. D. Storer, "A Design Method for Wide Band Balanced and Screened Transformers in the Range 0.1 - 200 Mc/s," *Electronic Engineering* **29**, 524 (1957).

T. R. O'Meara, "A Comparison of Thin Tape and Wire Windings for Lumped-Parameter, Wide-Band, High-Frequency Transformers," *Trans. IRE, PGCP CP-6*, 49 (1959).

H. H. Skilling, *Electrical Engineering Circuits* (Wiley, New York, 1957).

CHAPTER IV A PHASED ARRAY RECEIVING SYSTEM

SUMMARY

L. Cartledge

This chapter describes all the components of the receiving system being installed in the 16-element test array. The receiving system consists of a passive multiple beam-forming matrix, a multiposition switch, two solid state receivers and interbeam interpolation circuitry. Each of these components, as well as the available test results, is described in detail.

A. INTRODUCTION

W. P. Delaney

A 16-element phased array receiving system that uses an RF beam-forming matrix, a diode beam-selection matrix and a monopulse interpolation unit is being implemented in the linear array test facility. The purpose of this system is to demonstrate time-sharing of multiple receiver beams and to study techniques for enhancing the angular accuracy of fixed-position multiple-beam systems.

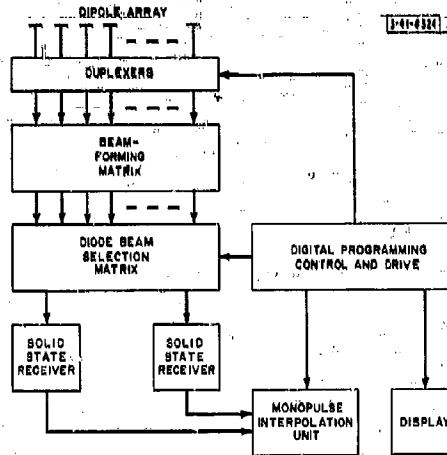


Fig. 2-74. Block diagram of receiver.

Figure 2-74 shows a block diagram of the system. A signal received by the 16-element dipole array passes through a solid state duplexer (see Part 2, Ch. I) into the RF beam-forming matrix.* The matrix simultaneously forms 16 antenna beams that are fixed in angular position. The diode beam-selection matrix selects two adjacent beams at the command of the digital control unit and delivers these beams through two solid state receiver chains to the monopulse interpolation unit. The diode matrix is described in Sec. B of this chapter; the receiver chains are described in Sec. C; the monopulse unit is described in Sec. D. The digital control unit was described in an earlier report.†

* J. L. Allen, et al., "Phased Array Radar Studies, 1 July 1960 to 1 July 1961," Technical Report No. 236 (U), Lincoln Laboratory, M. I. T. (13 November 1961), pp. 19-53, ASTIA 271724, H-474.

† J. L. Allen, et al., "Phased Array Radar Studies, 1 July 1959 to 1 July 1960," Technical Report No. 228 (U), Lincoln Laboratory, M. I. T. (12 August 1960), pp. 121-134, ASTIA 249470, H-335.

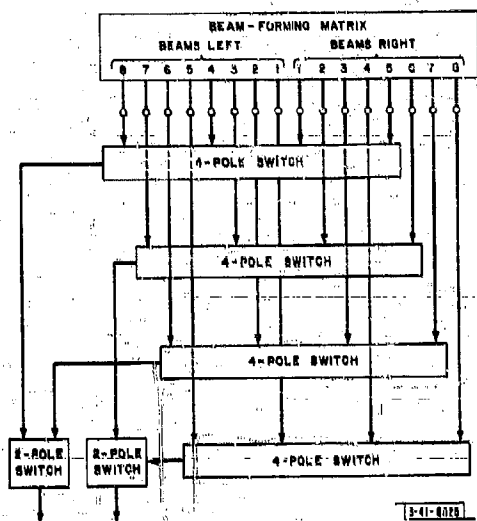


Fig. 2-75. Beam-selection matrix layout.

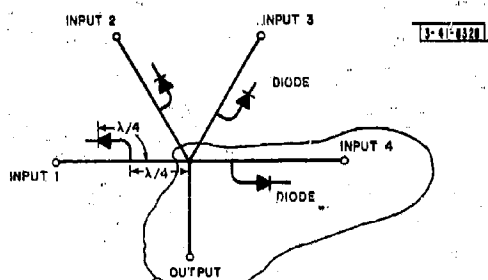
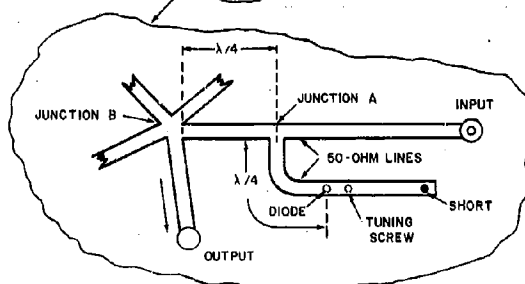


Fig. 2-76. Four-pole diode switch.



The receiving system will operate at a center frequency of 900 Mcps with a bandwidth of 2 Mcps. The basic antenna beams are 6° wide in the horizontal plane as a result of the linear array and 6° wide in the vertical plane as a result of the parabolic reflector surface. The monopulse sum beam is formed by adding two adjacent beams. This results in a 9° × 6° beamwidth and theoretical first sidelobes of -23 db. The 15 receiver beams cover a ±45° angular sector around broadside.

At present, most of the piece parts of the receiver system are either finished or undergoing final bench testing. It is expected that the over-all system noise temperature will be about 800° K. This relatively high noise temperature is due to 3.3 db of RF loss preceding the receiver channels which have a 5-db noise figure. The beam-forming matrix has a 1.1-db insertion loss, and the diode switch matrix has a 0.6-db insertion loss. The remaining 1.6-db loss is due to interconnecting cables. Long runs of flexible cable are used so that the receiver hardware can be placed in an easily accessible location in the test facility.

The monopulse interpolation circuitry should provide an angular accuracy of ±0.3° for high signal-to-noise ratios.

B. RF BEAM-FORMING AND BEAM-SELECTION SYSTEM

W. P. Delaney

1. Beam-Selection Matrix

The beam-selection matrix is a 16-input, 2-output digitally controlled microwave switch. The basic building blocks of the matrix are single-pole, 4-position switches and single-pole, 2-position switches. Figure 2-75 shows how these basic switches are arranged to permit the switching of two adjacent antenna beams to the two output terminals.

Figure 2-76 shows a schematic diagram of the 4-pole switch.* The switch is fabricated in Teflon 3A† strip transmission line using a 1/4-inch ground plane spacing. The varactor diode

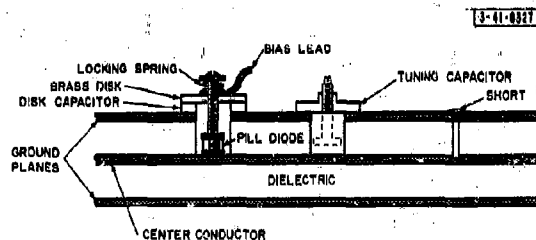


Fig. 2-77. Detail of diode mounting and tuning (side view of strip transmission line).

(MA4256) is located a quarter-wavelength back from the input line on a 50-ohm stub. The diode is shunted across the line, and the bias is brought in by a screw terminal that contacts the top of the diode pill package (see Fig. 2-77). The bias contact screw and lead are bypassed at RF frequencies by a barium-titanate disk capacitor.

When the diode is forward-biased (3-ma forward current) it appears as a low resistance of about 1 ohm. This very low resistance appears as a very high resistance at the junction of the stub line and the main line (junction A, Fig. 2-76), and energy is readily transmitted past this

*The 2-pole switch used in the beam-selection matrix is similar to the 4-pole switch.

†The characteristics of this material are discussed in TR-236, pp. 57-60.



Fig. 2-78. Four-pole switch.

TABLE 2-V AVERAGE CHARACTERISTICS OF 4-POLE SWITCHES (Average of Four Units)			
Frequency (Mcps)	Insertion Loss (db)	Isolation (db)	VSWR
880	0.60	22	1.35:1
890	0.35	29	1.2:1
900*	0.30	41	1.06:1
910	0.35	27	1.16:1
920	0.50	21	1.3:1

* Design frequency.

junction to junction B, where the three other input lines and the output line meet. If the other three input lines present open circuits at junction B, the energy will pass to the output port. Three open circuits are presented at junction B by reverse-biasing the respective diodes at -4 volts. The capacity of the diode at this bias is about 1.5 pf. The combination of the inductive short and the tuning capacitor (Fig. 2-77) is used to tune out this capacity and thus present an open circuit at the diode. This open circuit reflects as a short at junction A and as an open at junction B.

The major problem encountered with switches of this kind was achieving a reliable mechanical arrangement for biasing the diodes. The bypass capacitors are brittle and will fracture if too much pressure is applied by the brass disk. Also, the input VSWR to the switch is sensitive to the pressure applied to the diode by the bias contact screw. It was found that a Dupont H-film disk made a more reliable bypass capacitor than the barium-titanate disk. The switches are currently being refitted with the H-film disks. An internal biasing technique that eliminates many of these problems is discussed in Part 2, Ch. II.

2. Experimental Results on Individual Switches

Four 4-pole switches were fabricated for the beam-selection matrix. Figure 2-78 shows one of the switches, and Table 2-V summarizes the average characteristics of the four switches. At the design frequency of 900 Mcps, the electrical characteristics are very satisfactory. The isolation changes most rapidly with frequency because it depends on the transforming property of two quarter-wavelength lines.

A 900-Mcps measurement was also made to determine the phase errors between the four transmission channels in each switch. One channel was used as reference, and the magnitude of the phase shift between that channel and the other three channels was measured. The magnitude of the phase errors averages 1.9° for the four switches; the worst phase error was 5.5° in one channel of one switch.

The 2-pole switches had characteristics as good as or better than the 4-pole switches. Insertion loss was 0.2 to 0.3 db across the 880- to 920-Mcps frequency range. Isolation was 43 db at 900 Mcps and decreased to 20 db at 880 and 920 Mcps. VSWR's were from less than 1.17 to 1 over this frequency range, and the phase errors at 900 Mcps were less than 1° .

The switches have a turn-on time of less than 1 μ sec and a turn-off time of about 50 μ sec. The long turn-off time is due to the large capacitance (0.015 μ f) of the RF bypass capacitor, which has a discharging time constant of 15 μ sec. The use of the DuPont H-film bypass capacitor should reduce the turn-off time to less than 1 μ sec.

3. Test Results on the Combined RF Beam-Forming and Diode Beam-Selection Matrices

The beam-selection matrix was connected to the beam-forming matrix with RG-9 cables (Fig. 2-79). The interconnecting cables also served as phase-compensating* line lengths for the RF matrix. The entire unit was tested with a 16-element linear array of dipoles.

In general, the antenna patterns taken had higher sidelobes than patterns taken on the RF matrix alone. These higher sidelobes are due to the open circuits placed at the beam outputs

* For a discussion of the problem of phase-compensating RF beam-forming matrices, see W. P. Delaney, "An RF Multiple Beam Forming Technique," 41G-0012 (U), Lincoln Laboratory, M. I. T. (9 August 1961), ASTIA 262017, H-334.

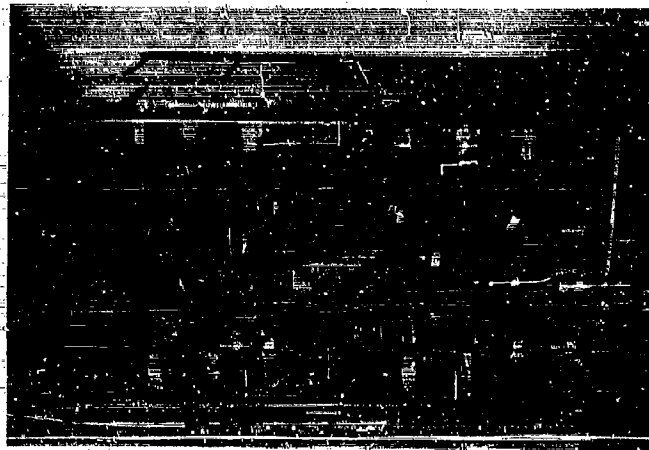


Fig. 2-79. Beam-selection matrix and beam-forming matrix.

of the beam-forming matrix by the beam-selection matrix. Two of the 16 beams of the beam-forming matrix are transmitted through the selection matrix by the forward biasing of certain switch diodes. The remaining 14 beams are open circuits because their respective switches are in the "off" condition. Thus, energy received on these "off" beams is reflected back through the beam-forming matrix and is reradiated. During the "return trip" back through the matrix, this energy has several opportunities to couple to the two "on" beams because of the finite directivity of the directional couplers in the matrix. Any energy coupled from an "off" beam to an "on" beam will tend to raise the response of the "on" beam in the vicinity of the "off" beam. As an example, if beam 4 right of the matrix is an "on" beam, it is transmitted through the diode switch. Consider that beam 5 left is an "off" beam. It was shown in an earlier report* that the isolation between beams 4 right and 5 left for this matrix has a low value (15 db). Thus, when looking at an antenna pattern of beam 4 right, we can expect a high sidelobe of about 15 db to appear in the vicinity of beam 5 right. Figure 2-80 shows such an antenna pattern on beam 4 right. The high sidelobe (-14 db) to the left of the main beam occurs at an angle of 29° from broadside, which is the position of beam 5 left. In Fig. 2-81 all the beam terminals of the matrix except 4 right were terminated in matched loads and the antenna pattern of 4 right was taken again. Note the absence of the high sidelobe due to 5 left and the over-all reduction in sidelobes due to the matched terminations on all beam ports. It should be noted that the above example used the lowest measured value of isolation between any two beams. The average isolation between beams is 28 db; thus, this effect is not as severe on other beams. The measured patterns showed increases in sidelobe levels that averaged 1 to 3 db for far-out sidelobes. The near-in sidelobes were not affected very much. This problem of coupling from the "off" beams can be reduced by increasing the directivity of the couplers in the beam-forming matrix (especially those couplers at the beam-terminal end) or by using a more complex microwave switch which absorbs energy at a 50-ohm impedance level in its "off" position.

* Ibid.

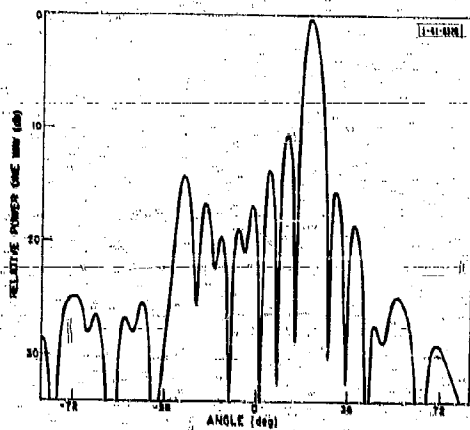


Fig. 2-80. Pattern of beam 4 right. All other beam ports are open-circuited.

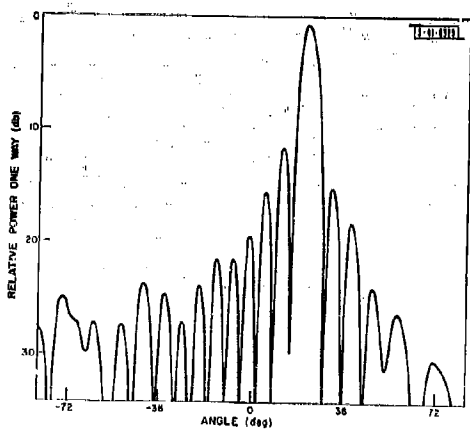


Fig. 2-81. Pattern of beam 4 right. All other beam ports are terminated in 50 ohms.

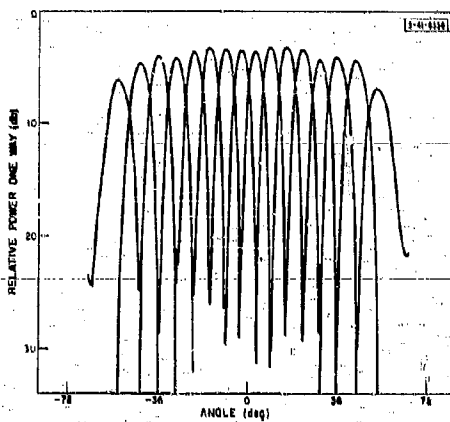


Fig. 2-82. Major lobes of all 16 beams as selected by the beam-selection switch.

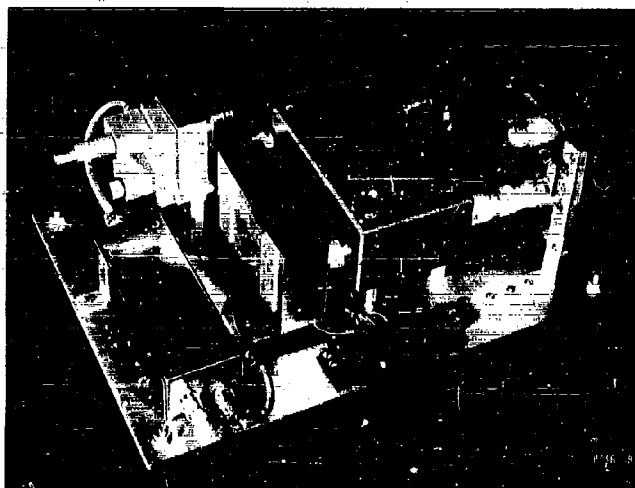


Fig. 2-83. An all-solid-state receiver.

Figure 2-82 shows the main lobes of all 16 beams formed by the beam-forming matrix and selected by the beam-selection matrix. Beam peaks occurred close to the theoretical positions, with a worst-case error of 2° in beam 7 right. The sum beams (formed by adding adjacent antenna beams) have occasional high sidelobes (16 to 18 db down) as a result of the previously mentioned effect of mismatches at the beam terminals. These spurious sidelobes are much more noticeable in the sum beam because the theoretical sidelobes for these beams are much lower than those of the component beams. The difference beams generally had shallow nulls (13 to 20 db) because of the phase errors in the matrix-compensating cables and the diode switches and because of the energy coupled from other beams.

These results are certainly not representative of the best one can expect to achieve with a beam-forming matrix followed by a diode beam-selection matrix. By careful design, it is reasonable to expect 30 db of minimum isolation between beam terminals on a beam-forming matrix; thus, the spurious-sidelobe problem can be minimized. For monopulse operation, particular care should be exercised to achieve very small phase errors in the diode switching networks.

C. SOLID STATE RECEIVERS

W. J. Inpe

An all-solid-state receiver is shown in Fig. 2-83. It consists of a limiter, tunnel diode amplifier, mixer and IF amplifier. The limiter was designed by D. Temme and is similar in construction to the diode switch described in Part 2, Ch. I, but is operated with zero bias. The limiter provides 20 db of minimum isolation and has an insertion loss of 0.2 db at small-signal levels. The corresponding VSWR is 1.1. The limiter can withstand several watts of average power and can withstand peak powers far in excess of the leakage anticipated for the tunnel diode.

The tunnel diode amplifier has already been described in detail (Part 2, Ch. II). Each amplifier is biased to provide 18 db of gain; the measured noise figure was 4.3 db. The 3-db bandwidth is 35 Mcps.

A Sage Laboratories balanced mixer performs signal frequency conversion to 30 Mcps IF. A transistorized IF amplifier provides 29 db of gain. The IF strip was supplied by J. DiBartolo, and is of the type described in Part 2, Ch. III.

Two of these receivers will be used in the phased array receiver.

D. INTERBEAM INTERPOLATION SYSTEM

H. J. Greenberger

1. Introduction

The output of a lossless beam-forming matrix like that described in Part 2, Ch. I is a number of fixed beams in space. In order to determine the angular position of a target to less than a beamwidth, a system comparing the energy in two adjacent beams is used. Because of its similarity to monopulse tracking systems, this system has been called a monopulse angular interpolator. It differs from the conventional monopulse tracker, being an open-loop system in which the magnitude of the output is proportional to the angle from a line midway between the two beams (see Fig. 2-84). The output is unambiguous (single-valued) out to the third sidelobe; therefore, it can be used for deghosting the sidelobe returns. The display is a B-scan of fourteen lines, each one corresponding to a transmitted beam position. The interpolator output perturbs the scan to an intermediate position corresponding to the azimuth of the target and brightens the trace to indicate its presence.

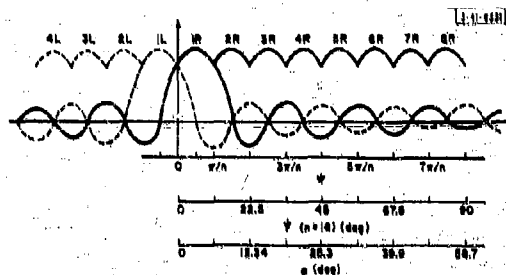


Fig. 2-84. Output of 16-element beam-forming matrix.

The interpolator has not yet been integrated into the receiving array; however, preliminary measurements indicate that an interpolator accuracy of $1/20$ of a beamwidth over a 50-db dynamic range can be achieved.

2. System Description

The output of the beam-forming matrix* consists of 16 beams of the form

$$A = \frac{\sin(n\psi)}{n \sin \psi}$$

separated by π/n radians, where n is the number of elements in array.

The angle ψ is not a real-space angle, but is related to a real-space angle by

$$\psi = \frac{\pi d}{\lambda} \sin \alpha$$

where α = angle from array broadside.

Figure 2-84 shows beams 1 right and 1 left with the abscissa calibrated both in real space and in ψ space. Portions of the main lobes of other beams are also shown.

Two adjacent beams A and B can be represented by

$$A = \frac{\sin n(\psi + \pi/2n)}{n \sin(\psi + \pi/2n)}$$

and

$$B = \frac{\sin n(\psi - \pi/2n)}{n \sin(\psi - \pi/2n)}$$

The sum and difference of these two beams are particularly useful, since there is no ambiguity between their ratio and the magnitude of the angle off antenna boresight for angles up to $\psi = \pi/2$. Taking the sum and difference and simplifying, we obtain

$$\Delta = B - A = -\frac{4}{n} \left[\frac{\cos n\psi \sin \psi \cos \pi/2n}{\cos 2\psi + \cos \pi/n} \right]$$

* See Part 2, Ch. 1; also, TR-236, Part 2, Ch. 1.

and

$$\Sigma = B + A = \frac{4}{n} \left(\frac{\cos n\psi \cos \psi \sin \pi/2n}{\cos 2\psi - \cos \pi/n} \right)$$

Negative values of A, B, Δ and Σ correspond to relative reversals of phase. If phase information is destroyed, as in a video detector, only the absolute magnitude of A, B, Δ and Σ are recovered. In this system, the ratios B/A and Δ/Σ are taken after the signal has been video-detected; therefore,

$$|B/A| = \left| \frac{\sin(\psi + \pi/2n)}{\sin(\psi - \pi/2n)} \right|$$

and

$$|\Delta/\Sigma| = \left| \frac{\tan \psi}{\tan \pi/2n} \right|$$

These two functions are sketched in Fig. 2-85. There is great advantage in using the Δ/Σ ratio for interpolation because it is symmetrical, relatively smooth, has a zero at the crossover of the two beams, and the poles are far removed from the main lobes. There is a sense ambiguity, however, since the function is even. This can be removed by comparing the phase of Δ with that of Σ.

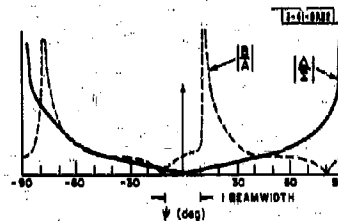


Fig. 2-85. Plots of $|B/A|$ and $|\Delta/\Sigma|$ as a function of ψ .

In this system, an equivalent method was used. An amplitude comparison circuit was used to determine whether $|A| > |B|$ or $|B| > |A|$. From Fig. 2-85 it can be seen that this method gives unambiguous sense information to $\psi = \pm 45^\circ$. All target returns in the main lobe and first three sidelobes are resolved unambiguously.

An amplitude-comparison sense system was chosen over a phase-comparison system primarily because of the availability of the logarithmic amplifiers. A phase-comparison system requires a wide-dynamic-range, phase-stable limiter and operates at a low signal-to-noise ratio for angles close to the beam crossovers. The equivalent problem in the amplitude-comparison system is to build two log amplifiers that track over the desired dynamic range. In the region near the crossover, $d|A/B|/d\psi$ is approximately 6 db/degree; therefore, in order to indicate correct sense for angles greater than 0.05 of a beamwidth (0.3°), the log amplifiers should track within ± 1.8 db. This is well within the capabilities of these amplifiers.

A functional diagram of the monopulse interpolator is shown in Fig. 2-86. The sum and difference is taken in a 30-Mcps hybrid ring. The four outputs are then amplified in similar logarithmic amplifiers. Over a wide dynamic range, the incremental output of these amplifiers

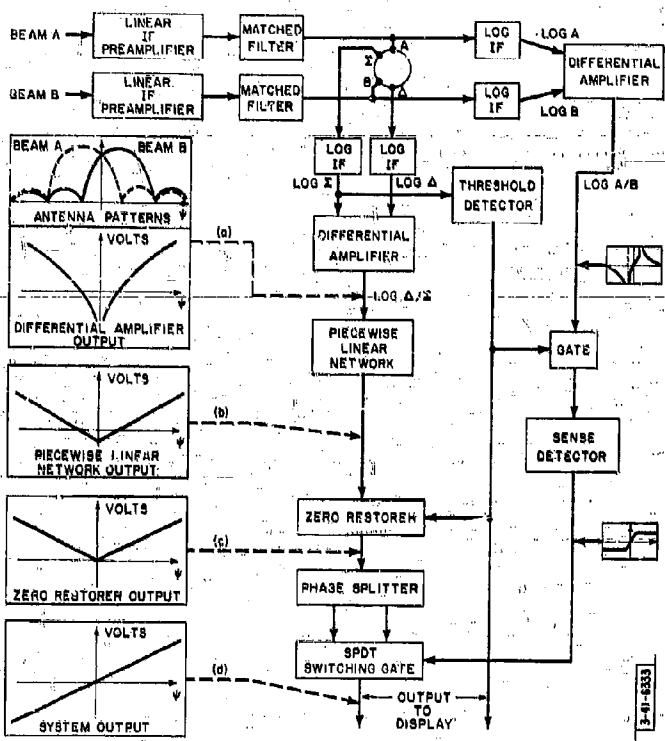


Fig. 2-86. Block diagram of monopulse interpolator.

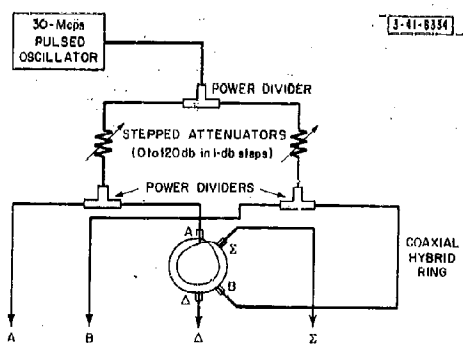


Fig. 2-87. Target simulator for monopulse interpolator.

is proportional to the logarithm of the incremental input. If the input level is sufficiently high, logarithmic action can occur on noise, and the output is proportional to the log of the input plus a constant term. Division is effected by subtracting logarithms, the constant term disappearing in the process.

The output of the differential amplifier as a function of V is shown in (a) of Fig. 2-86. By passing the signal through a nonlinear network, the output amplitude is made a linear function of angle [(b) of Fig. 2-86]. A DC component is added to make zero amplitude correspond to zero angle [(c) of Fig. 2-86]. The sense ambiguity is removed and the desired linear system output is shown in (d) of Fig. 2-86.

3. Test Results

The over-all system was tested by simulating the signal that would be present at the output of the IF preamplifiers. A pulsed 30-Mcps oscillator was used as a signal source, and the adjacent beams were synthesized by using a power divider and two variable attenuators (Fig. 2-87). A target flying through the beam was simulated by calculating the ratio of energy in adjacent beams for a particular angle and adjusting the attenuators accordingly.

The test results on two targets having a difference in cross section of 50 db are shown in Fig. 2-88. An interpolation accuracy of ± 5 percent is indicated. For this series of tests, the phase and amplitude at the input to the hybrid were balanced to give the best null at the difference port. Since, under operating conditions, the input may be as much as 2° to 3° out of phase and 1 db in amplitude, the accuracy of the system will be less than that of the interpolator alone.

The interpolator contains no memory devices or delays, and the bandwidth of the elements in the system is sufficiently large so that the response time is limited by the matched filter. The filter used (Fig. 2-89) approximates a matched filter with a high- Q , undercoupled resonant transformer placed at the input to the log amplifiers. This location was chosen because sufficient preamplification existed so that the following wideband circuitry would not degrade the noise figure. In addition, it was felt that the flattening effect of the log amplifier on the matched pulse facilitated amplitude measurements at video. The output of the matched filter and the log amplifiers to a 10- μ sec pulse is seen in Fig. 2-90.

The need for a filter with a monotonically decreasing pulse response is apparent from the figure. Any slight ringing in the trailing edge would appear as a trailing ghost at the output of the log amplifiers. This dictated the choice of the undercoupled resonant transformer as a filter element.

Figure 2-91 illustrates the waveforms at four points in the system for targets having high signal-to-noise ratios and located at the beam crossover. The upper and lower traces of 2-91(a) show the output of the log amplifiers and indicate a sum-to-difference ratio greater than 30 db (that of the hybrid ring alone). If the phase and amplitude errors of the rest of the radar are taken into account, the average difference null will probably be only slightly greater than 20 db. To indicate 0° for these nulls, the differential amplifier saturates for ratios greater than 22 db. This can be seen from Fig. 2-91(b). After the zero restoration, the signal is gated by the threshold detector and possibly inverted by the sense switch. The waveform at the output of the interpolator is shown in Fig. 2-91(b) (lower trace).

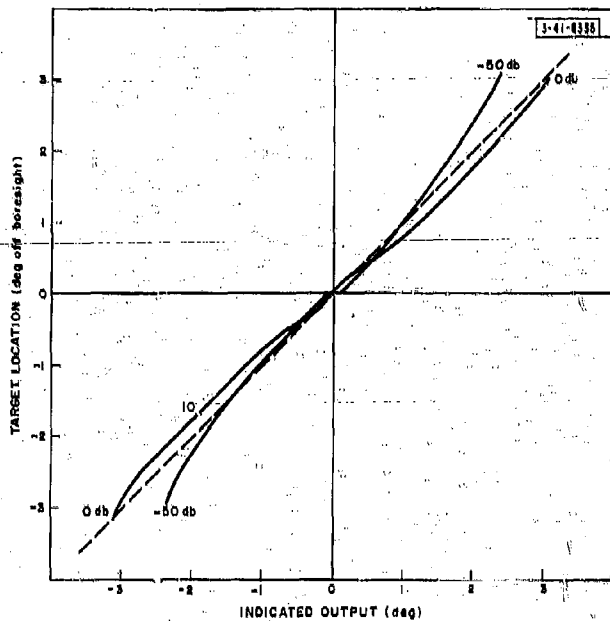


Fig. 2-88. Monopulse interpolator accuracy (simulated target).

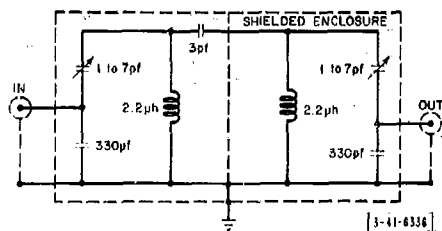
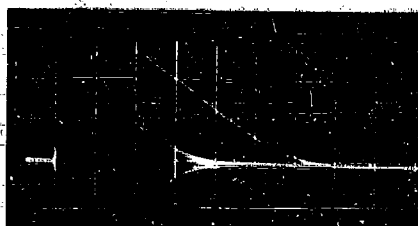


Fig. 2-89. Matched filter approximation.



Upper trace: output of log amplifier
 Lower trace: output of matched filter
 Scale: 10 μ sec/cm

Fig. 2-90. System response to a 10- μ sec pulse.

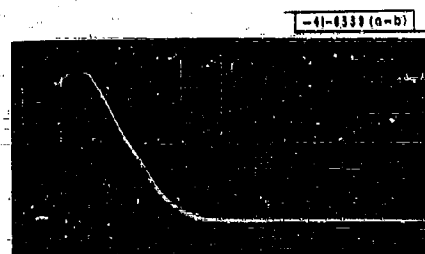


(a) Upper trace: output of sum log amplifier
 Lower trace: output of difference log amplifier



(b) Upper trace: output of piecewise linear network
 Lower trace: output of interpolator

Fig. 2-91. Simulated target at beam crossover, high S/N (scale: 10 μ sec/cm).

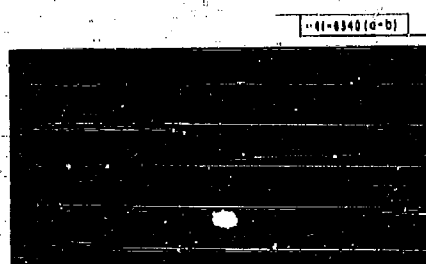


(a) Upper trace: output of sum log amplifier
Lower trace: output of difference log amplifier

(b) Upper trace: output of piecewise linear network
Lower trace: output of interpolator



Fig. 2-92. Simulated target at beam peak, high S/N (scale: 10 μ sec/am).



(a) Target at beam crossover.

(b) Target at beam peak.



Fig. 2-93. Interpolator output for various signal levels (difference in input level between traces = 10 db).

Figure 2-92 is similar to 2-91 except that the target is at a beam peak. Two things worth noting are the close tracking of the log amplifiers over a wide dynamic range and the deviation of the trailing edge from a straight line (log of an exponential decay), which is an indication of the absolute accuracy of the amplifiers.

The output of the interpolation over a fairly large dynamic range is shown in Fig. 2-93(b). These waveforms are for a simulated target at the beam crossover and at the beam peak similar to Fig. 2-91(b) and 2-92(b). Those of higher input levels are wider because of the sensitivity of the threshold detector. The output level in Fig. 2-93 is not absolutely flat because the log amplifiers do not track perfectly. The dip at the right of all the pulses is due to the region of maximum tracking error which can be seen as a slight separation of traces in Fig. 2-92(a).

The monopulse system is ready to be installed in the array and no difficulty is foreseen in coupling to the present display. Further tests and studies, concerned mainly with stability and methods of improving system accuracy, will be made with the intent of determining the feasibility of a similar system for a short-pulse radar ($<1 \mu\text{sec}$).

CHAPTER V TRANSMITTER DEVELOPMENT

SUMMARY

The bulk of this chapter is devoted to a detailed description of the 900-Mcps transmitting system that is being implemented in our linear test array. This system is composed of 16 transmitting modules and their supporting gear. Transmitting amplifiers and modulators are discussed, as are the monitoring system, digital phase shifter drivers and the RF and power distribution systems.

The development of the low-power solid state modulators for very-short-pulse systems is discussed, and brief mention is made of some techniques that might reduce the cost of wideband transmitting arrays. Finally, the present status of developmental tubes for phased array transmitters is outlined.

A. INTRODUCTION

D. M. Bernella

The 900-Mcps transmitter work carried on during the past year has been concerned primarily with the integration of components into the transmitting module design and with the fabrication of 16 modules and 9 spare units for a linear test array. This work has been completed with the exception of the fabrication of the spare units and some of the phase shifter and monitor-duplexer printed boards. In addition, the array power supplies have been built, and the mounting rack for installation of the 16 modules has been installed and cabled for power and control distribution. During the coming year, this first-generation transmitting test array will be used as a general learning tool to evaluate array component and system philosophy, reliability, stability, etc. It is felt that the experience gained in the construction and operation of this low-power modular array will be helpful in designing optimum modules for future higher-powered systems.

B. 900-Mcps TRANSMITTER SYSTEM

D. M. Bernella

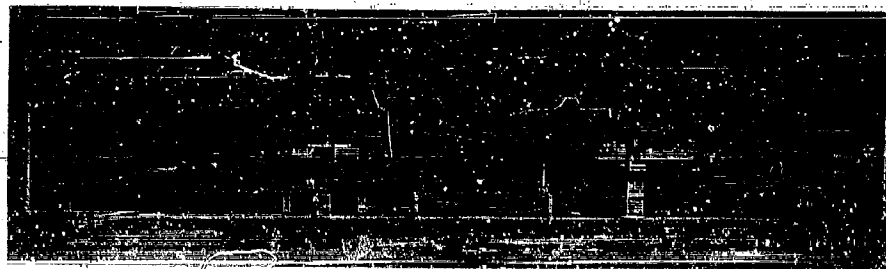
1. Modules

The basic electrical design and component layout of the 900-Mcps transmitting module was shown in breadboard form in TR-236* (Fig. 2-85, p. 112). The following parameters were set as goals for this design:

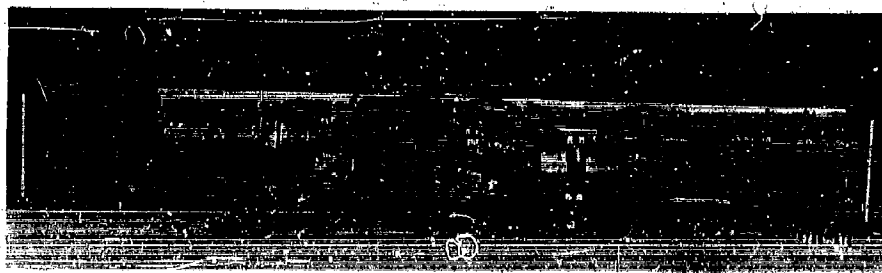
RF power output	5 kw peak at 50 watts average
High-voltage DC input	4 kv
Center frequency	900 Mcps
Signal bandwidth	≥ 10 Mcps
Pulsewidth	0.1 to 10 μ sec

A breadboard was constructed and tested to the above specifications. This model consisted of only the basic amplifiers and modulator, with no phase or amplitude control and no integrated monitoring system. The specifications were met except that the minimum pulsewidth was 0.2 μ sec.

* J. L. Allen, et al., "Phased Array Radar Studies, 1 July 1960 to 1 July 1961," Technical Report No. 236 [U], Lincoln Laboratory, M. I. T. (13 November 1961), ASTIA 271724, H-474.



(a) Side view.



(b) Top view.

Fig. 2-94. 900-Mcps transmitter module.

This was not considered a serious compromise and the first prototype module was fabricated. This prototype contained neither the digital diode phase shifter nor the monitor-duplexer boards, but did have a trombone line stretcher and amplitude control. Phase monitoring was done with the use of directional couplers and 900-Mcps printed circuit hybrids. A simple control circuit was employed for the protection of the high-voltage supply and also for the modulator and RF tubes in the event of the loss of cooling water.

During subsequent tests of this model, it was found that the parasitic suppressor resistors on the modulator plates failed after several hours of operation and often failed after the first test. This problem was traced to the modulator pulse transformer, which had been designed for a maximum 10- μ sec pulse. In order to achieve a 10- μ sec RF pulse with good rise and fall time, it was necessary to have the video modulation overlap the RF pulse. The resulting modulation pulse was 12 μ sec long. This excessive pulse length caused the transformer core to saturate under maximum load as the temperature increased; all the voltage then appeared across the resistors, causing them to explode. Therefore, two transformers were mounted in series to reduce the voltage time product each had to handle. This not only stopped the resistor failure, but also revealed the fact that the modulator DC input voltage could be increased to 5000 volts DC and the RF power output increased to a peak of 10 kw. The transformers eventually failed under this voltage, but because no harm to the RF tubes was apparent, a new pulse transformer capable of operating at 5000 volts DC with a 15- μ sec pulse was ordered. Since this transformer had to be developed to match the power and size limitations, the prototype was not received until late spring of 1962. Since the installation of the first prototype transformer the RF tubes have operated for approximately 200 hours with no apparent degradation. This transformer has now been installed in all units. The increase in power output caused a reduction in gain of the over-all amplifier chain to 27 db from the original 30 db available in the module having peak power of 5 kw.

The final design layout is basically the same as the original breadboard except for minor changes that facilitate the fabrication and maintenance of the module [see Figs. 2-94(a) and (b)]. Most of the connectors, cabling, relays, etc., are stock items or modifications of stock items; therefore the over-all design is far from optimum with regard to compactness. It has become quite apparent that in future designs it will be imperative to design these components specifically for the phased array application.

2. System Description

An over-all block diagram of the transmitting system is shown in Fig. 2-95. The RF energy from the exciter is transmitted to a 16-port printed-circuit hybrid feed system constructed by Sanders Associates. Each output port of the corporate feed is connected to a transmitting module through approximately 12 feet of RG-9B/U coaxial cable. The module itself is adjusted to a set electrical length by means of the input line stretcher feeding into the 4-bit digital diode phase shifter. The output of the phase shifter at approximately 30 watts peak power is used to drive the RF amplifier into saturation. This effectively eliminates the amplitude variations caused by the varying insertion loss of the phase shifter as the bits are switched.

The final amplifier raises the output power to a peak of 10 kw and is coupled through a dielectric-filled circulator into the monitor-duplexer printed circuit board. Because of the narrow bandwidth of the RF amplifiers, it was necessary to use a circulator to isolate the antenna VSWR variation caused by the scanning of the transmitted beam. Energy from the circulator

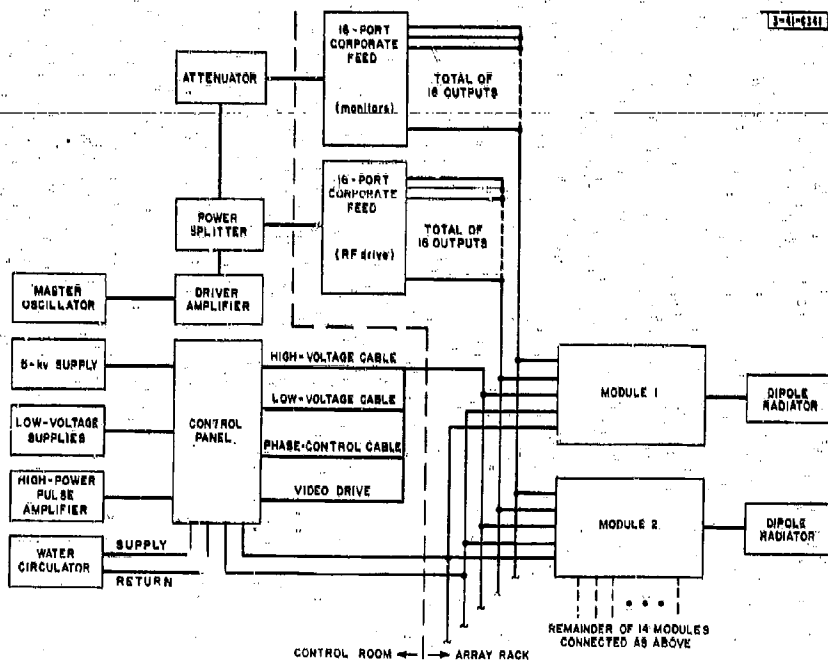


Fig. 2-95. Block diagram of transmitter and rack distribution.

passes through the duplexer-monitor board to the antenna, a portion being coupled off and compared in amplitude and phase with a fixed monitor input pulse. The difference pulse is sent to the alarm circuit, which energizes a warning light whenever the difference exceeds a preset level.

Gating control, low-level phase shifter controls and DC power are applied to the module through the three plugs mounted on the front panel. An internal control circuit is used to protect the module if the cooling water should be lost and in the event of improper sequence during module installation or a short in the high-voltage line. The low-level phase shifter drive is applied to the phase shifter driver amplifier. This eliminates the need for distributing high-level video pulses in separate cables. The video drives for the modulators are all paralleled from the same line and fed to the modules via short coaxial lines.

Each module will be set to a reference phase and amplitude in a test setup and then installed in the array.

C. CIRCUIT AND COMPONENT DESCRIPTION OF 900-Mcps SYSTEM

D. M. Bernella

1. Corporate Feeds and RF Cables

The 900-Mcps phase bridge (described in Part 2, Ch. 1) was used to measure the relative phase and amplitude difference between the output ports of the two corporate feeds. Figures 2-96 and 2-97 are plots of the phase and amplitude variations referenced to their respective means.

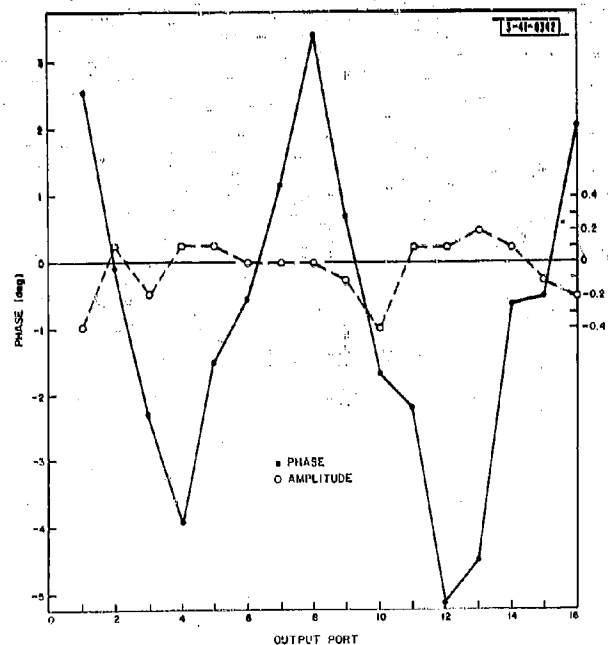


Fig. 2-96. Phase and amplitude errors at various ports of corporate feed 2 (900 Mcps).

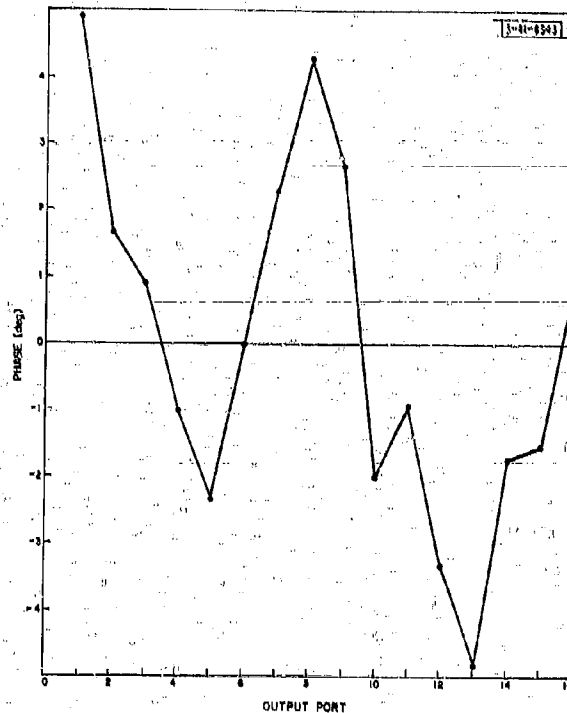


Fig. 2-97. Phase error at each port of corporate feed 3.

A systematic error is apparent from the plots, since the maximum deviation occurs at the ports near the edge of the structure. In view of the narrow bandwidth of this system, it seemed reasonable to compensate for the errors in the corporate feeds by cutting the RF cables to the proper lengths. This was done for phase compensation only; the resulting phase differences at the cable terminations are plotted in Figs. 2-98 and 2-99 for the amplifier and monitor distributions. The solid lines represent the center frequency of 900 Mcps, while the dotted and dashed lines represent $900 \text{ Mcps} \pm 5$. It is apparent from these results that in a system with wider bandwidth, all cabling will have to be identical, and corporate feeds will have to be constructed much more accurately. One of the Sanders Associates corporate feeds is shown in Fig. 2-100.

2. Control Circuitry

The internal module control circuitry consists of F-1, WRY-1, RY-1, RY-2, TD-1, and R-15 (see Fig. 2-101). Operation is such that, when the main power cable is plugged into the module face, +6 and -6 volts are connected across the terminals of WRY-1. This relay consists of a water-flow switch connected in series with the coil of a small (10-ma) relay coil (shown in Fig. 2-102). The flow-switch orifice is such that its contacts are made with 7 cc/sec of water flow and broken below 5 cc/sec. The normal water flow through the module system is 10 cc/sec.

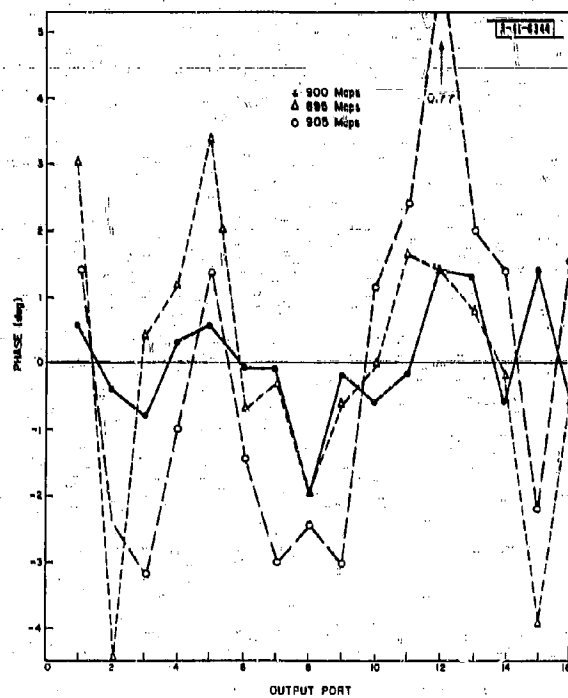


Fig. 2-98. Phase errors at each port of corporate feed 2 compensated with cables.

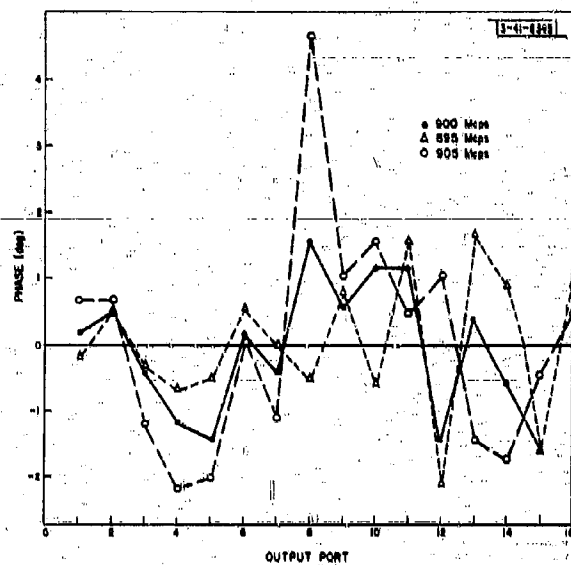


Fig. 2-99. Phase errors at each port of corporate feed 3 compensated with cables.

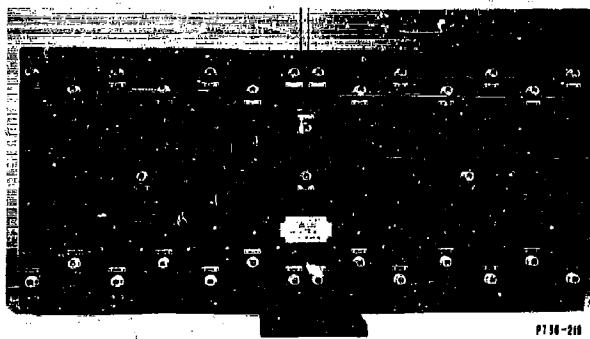


Fig. 2-100. Corporate feed.

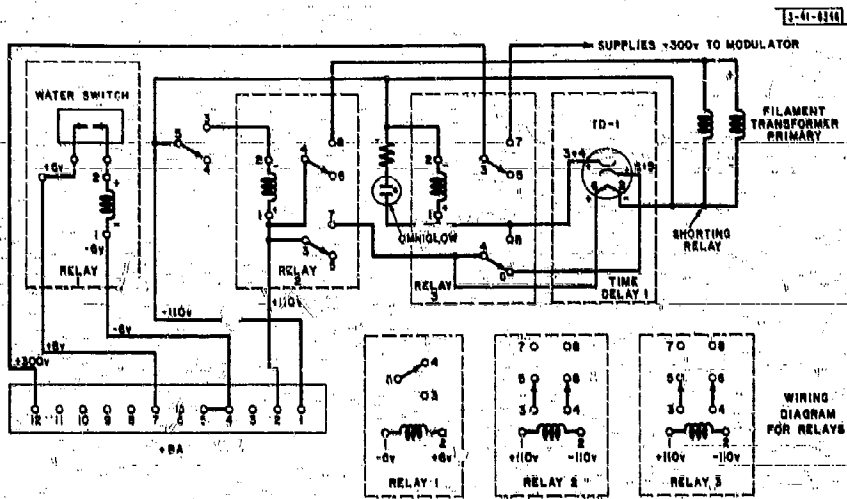


Fig. 2-101. Control circuit.

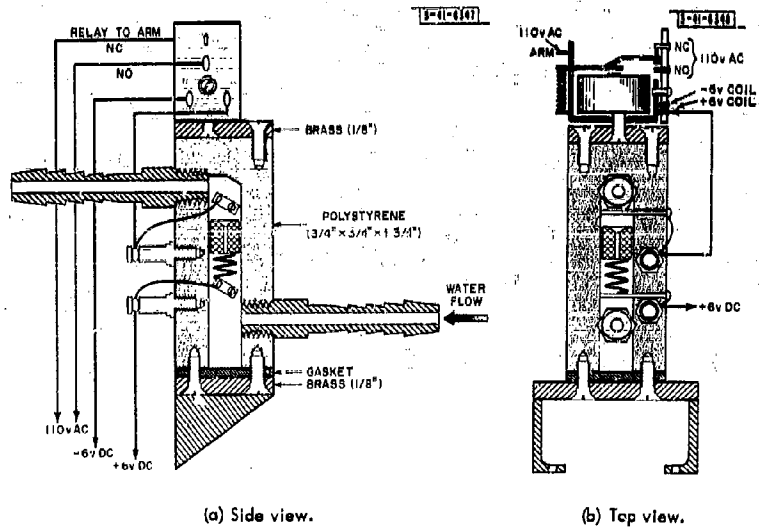


Fig. 2-102. Cross section of water switch.

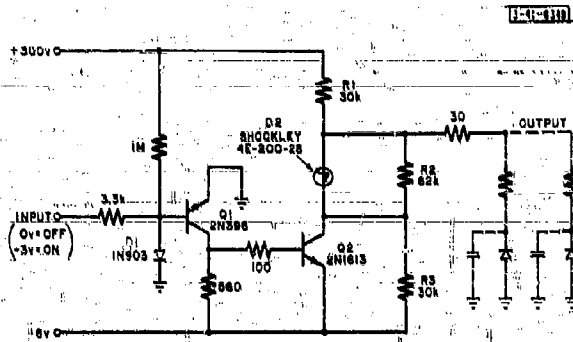


Fig. 2-103. Phase shift driver (one bit shown).

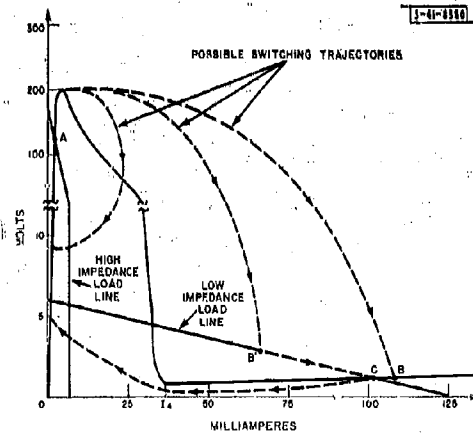


Fig. 2-104. V-I characteristic of Shockley 4E200-28 PNPN diode.

The primary AC current is broken by the relay contacts; therefore, the module is "dead" until the coolant is flowing properly. When WRY-1 is energized, 115 volts AC is applied to RY-1 and RY-3. RY-3 is used to short out the high-voltage charging resistor used to protect the high-voltage fuse F-1 during initial charging of the energy storage capacitor. Therefore, the high-voltage cable must be attached to the module before the main power is applied. RY-1 energizes the filament transformer for the modulator and RF tubes and the filament of TD-1, a 45-sec time delay that allows the tubes to warm up before screen voltage is applied to the modulator through the contacts of RY-2. RY-2 is a self-holding relay that removes the filament voltage from TD-1.

3. Phase Trimmer

Phase adjustment inside the module is accomplished with a trombone-type line stretcher and the tuning adjustments of the RF amplifiers. The limited physical space in the module prevented the incorporation of a full-wavelength line stretcher, but it was found that the over-all phase angle could be adjusted through at least 180°, without significantly affecting the output power, by changes in the amplifier tuning and coupling probes. Thus, with the two methods, it is possible to set the phase to any reference.

4. Diode Phase Shifter Driver Amplifier

H. J. Greenberger

The 4-bit diode phase shifter is described in detail in Part 2, Ch. 1. The function of the phase shift drivers is to accept a digital control signal from the radar programmer and to supply the correct bias for the phase shifter diodes. The programmer generates a 4-bit word for each module corresponding to the desired phase shift. This word is sent to the phase shift driver as one of two DC levels on four parallel lines. The driver, which consists of four independent circuits, transforms this control signal into the bias for the phase shifter diodes (225-volt reverse bias, 50 ma per diode forward bias). A schematic is shown in Fig. 2-103.

The switching element is a Shockley 4E200-28 PNP diode whose voltage-current characteristic is shown in Fig. 2-104. There are two stable points of operation, A and C, which lie on different load lines.

Simplified schematics corresponding to circuit conditions for these states are shown in Figs. 2-105(a) and (b).

The PNP diode is switched from high impedance to low impedance by switching G_2 on. The breakdown voltage of the diode is exceeded and the output capacitance supplies sufficient charge so that the instantaneous voltage and current follows a trajectory to B or B'. The phase shifter diodes become forward-biased and the switching trajectory then continues to the stable operating point C.

When G_2 is switched off, the current in the PNP diode is reduced to a value below the holding current I_h , and the circuit follows the switching trajectory back to point A.

The switching times depend upon the characteristics of the diode and the time required to charge and discharge the capacitance across the output. (This amounts to approximately 150 pf evenly divided between the self-capacitance of the PNP diode and that of the phase shifter diode mount.) Approximately 0.4 μ sec is required to switch the PNP diode to its low-impedance state, with negligible time required to discharge the capacitance. In switching back to the high-impedance state, 5 μ sec is required for the PNP diode and 20 μ sec for charging the capacitance

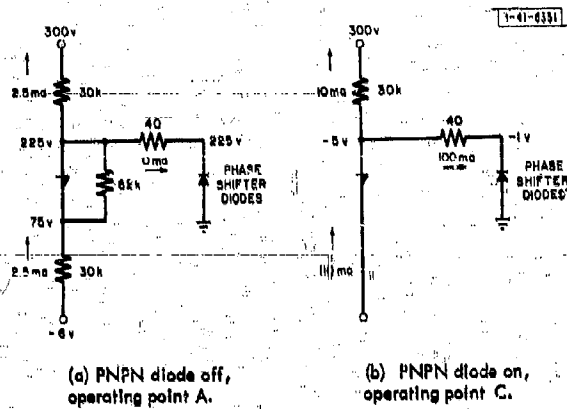


Fig. 2-105. Simplified schematic for determining high and low impedance load lines.

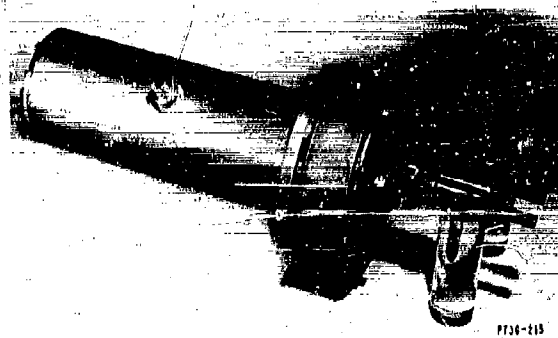


Fig. 2-106. 900-Mcps cavity amplifier with tube and output coupler exposed.

to 95 percent of its steady-state value. The charging time constant cannot be reduced much further because of stability and heat dissipation problems. If the capacitance is reduced too much, the switching trajectory will follow a path similar to the one shown at the far left in Fig. 2-104, thus producing a saw-tooth oscillation. The lower limit on R_1 is determined by the need to reduce the current in the PNP diode below I_n in order to switch to the low resistance state. If Q_2 avalanches at 100 volts and the minimum value of I_n is 10 ma, then R_1 must be greater than 20 kilohms. A value of 30 kilohms has been chosen to provide an additional safety factor.

The only problem encountered to date has been the difficulty in eliminating the heat from R_1 . Under worst conditions, with all four bits on, 12 watts are dissipated. The air inside the driver is heated to over 150° F, causing erratic operation of some transistors and diodes. This problem has been reduced by potting these resistors in a sand-loaded epoxy of high thermal conductivity, which offers a heat conductive path to the module keel. Preliminary experiments show a reduction of air temperature to 120° F. Experiments to determine the most efficient potting material are continuing.

5. RF Amplifiers

The RF amplifier design is the same as that described in TR-236 with the exception of a change in the method of attaching the output cavity end plate. The increased plate voltage (5000 volts DC) necessitated the use of metal screws for the plate. The nylon screws did not hold the assembly tightly enough and corona formed at the mica-filled gap. Nylon bushings replaced the Teflon bushings used to insulate the ground potential screws from the high-voltage end cap, since the Teflon exhibited enough cold flow to allow the end cap to loosen and again form corona.

The output loop was tuned by adding a 3- μ f capacitor in series with the loop. This formed an excellent match into a 50-ohm load, and the network has shown no sign of deterioration under testing (see Fig. 2-106).

6. Modulators

M. Siegel

As noted earlier, it was discovered that considerably more than 5 kw could be extracted from the 7649 amplifiers, without causing breakdown, by increasing the pulse voltage on the plate and screen of the amplifier. Hence, it was decided to increase the capability of the modulator. The modulator described in TR-236 was redesigned around a larger pulse transformer.

The resultant modulator is a hard-tube circuit that produces three output pulses (5 kv at 4.8 amp for the final amplifier plate, 3.2 kv at 1.6 amp for the driver plate and 670 volts at 0.5 amp for the two screens) for a total of 30 kw of peak video output at an average power level of 300 watts. The output video pulsewidth can be varied from 0 to 15 μ sec, thus providing sufficient overlap so that the RF pulse can be sandwiched inside the video pulse. Hence, the width and rise time of the module's RF output pulse are determined by the width and rise time of the RF drive pulse and the RF amplifier bandwidth.

The video rise time is limited by the rather large shunt capacity in the RF amplifier DC blocks. The plate bypasses are about 300 pf. These capacities, when fed from the essentially constant current modulator, limit the video rise time to between 1/2 and 1 μ sec.

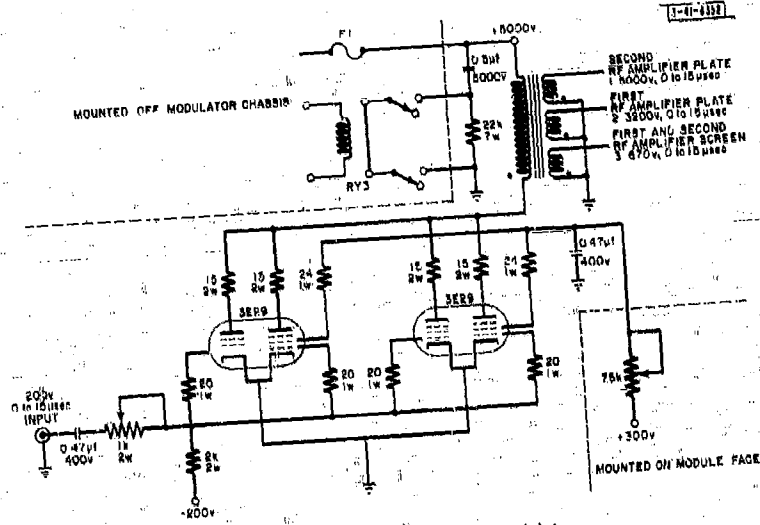


Fig. 2-107. Schematic diagram of modulator.

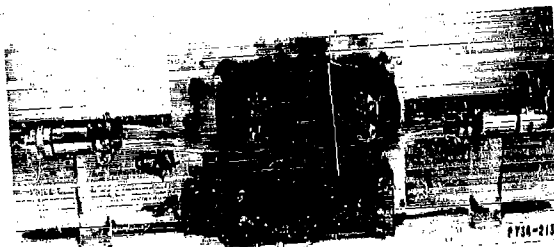


Fig. 2-108. Modulator (top view).

Two 3E29 tubes in parallel are required to produce the 6-amp current pulse, each 3E29 tube being rated at 3 amp of peak current when used at 0.01 duty ratio. The potentiometer which had been used previously in the cathode circuit of the 3E29 was intended to provide cathode degeneration useful in limiting the peak tube current and in shaping the leading edge of the video pulse, but was found to be unnecessary at the higher plate voltage.

This new high-voltage version of the pulse modulator has been found to operate conservatively into the required load and, in general, components operate cooler than in the original version. A schematic and a photograph of the final modulator are shown in Figs. 2-107 and 2-108, respectively. As can be seen, the components that develop most of the heat, the 3E29's and the pulse transformer, are mounted so as to provide maximum conduction of heat to the aluminum chassis, which is water-cooled. The plates of the 3E29's are provided with small parasitic suppressor resistors that also act as fuses and disconnect the tubes in case of arc-over.

7. Circulator

During the initial tests of the prototype module, a 25-ohm load was attached to the output of the final amplifier through a line stretcher to simulate a varying 2-to-1 impedance shift [Fig. 2-109(a)]. The resulting power output variations [Fig. 2-109(b)] indicated that the cavity Q was too high to work into this type of mismatch. Therefore, the circulator was incorporated into the design for isolation. These printed circuit circulators were developed by HYLETRONICS Corporation and have been successfully tested at 6 kw of peak power (60 watts average) with port 2 shortened and a load on port 3. No specific tests at higher power have been carried out, but the circulators in the modules have been operating at 10 kw of peak output with no apparent failures. The test results of phase and VSWR measurements are shown for several circulators in Figs. 2-110 and 2-111.

8. Duplexer-Monitor Printed Circuit Boards

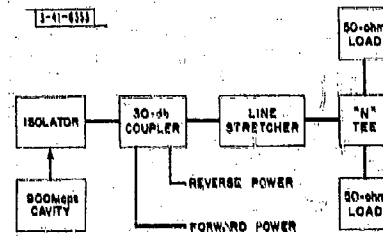
The monitor section of this board subtracts a small fraction of the transmitter signal from an external "reference" signal. The resulting difference signal is fed to the detection circuit described in Sec. C-9 of this chapter. The duplexer section protects the receiver during the transmitter "on" time as in a conventional radar. This monitor-duplexer board is described in detail in Part 2, Ch. I of this report.

9. Phase and/or Amplitude Error Detection Circuit

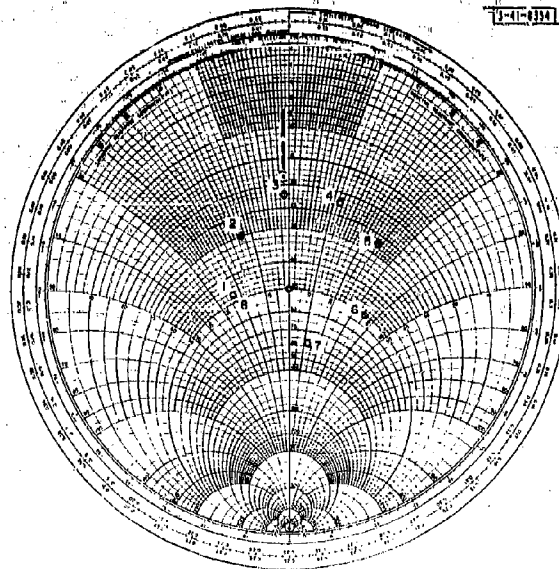
J. DiBartolo

A measuring system must be more reliable than that which is being measured. In an effort to keep the circuitry as simple as possible and thereby enhance reliability, no effort was made to differentiate between phase and amplitude errors in the monitoring equipment. Error detection is accomplished by subtracting the transmitted pulse vectorially from a fixed monitor pulse and sensing when the amplitude of the difference pulse exceeds a predetermined level. The two signals are combined at the RF level in a traveling-wave directional coupler mounted on the duplexer-monitor board. The amplifier chain is adjusted to produce a pulse 180° out of phase with and equal in amplitude to the monitor pulse. The difference waveform is sent to the alarm control box, which is adjusted to operate a warning signal whenever the nulled voltage amplitude exceeds the preset threshold level of the circuit. A schematic and photograph of this box are shown in Figs. 2-112 and 2-113, respectively.

POWER OUTPUT TABLE		
Output Power into 25-ohm Load		Power Radiated (kw)
Forward (kw)	Reverse (kw)	
4.2	300	3.90
3.8	380	3.42
3.6	460	3.14
3.4	520	2.88
3.8	550	3.25
4.4	540	3.86
4.3	400	3.90
4.4	320	4.08

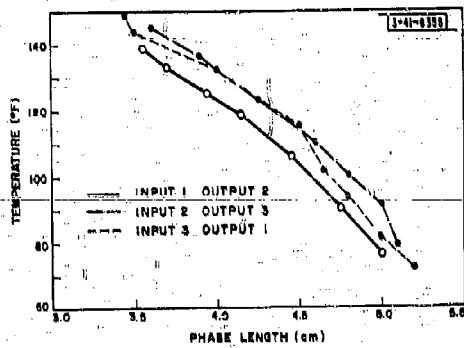


(a) Diagram of setup.

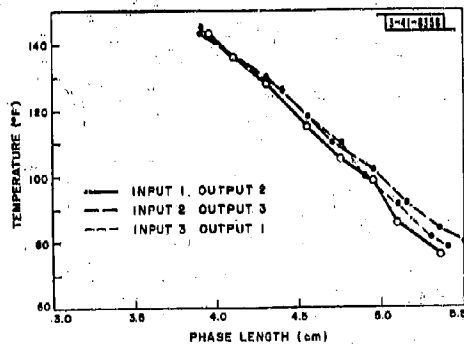


(b) Smith Chart plot of Z vs line stretcher position.

Fig. 2-109. Test setup for measuring amplifier performance into a mismatch.

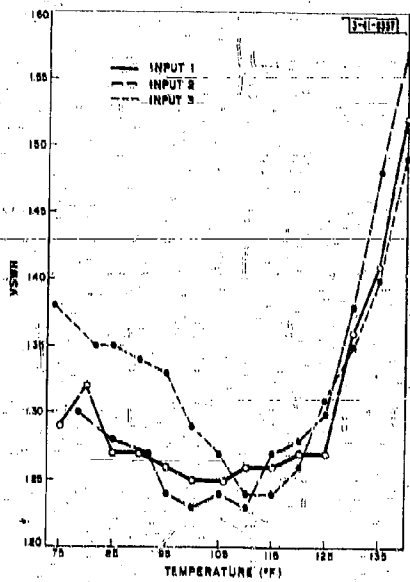


(a) Circulator 22.

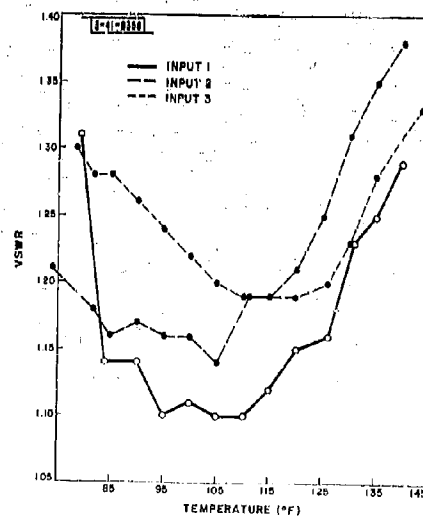


(b) Circulator 46.

Fig. 2-110. Phase length vs temperature.

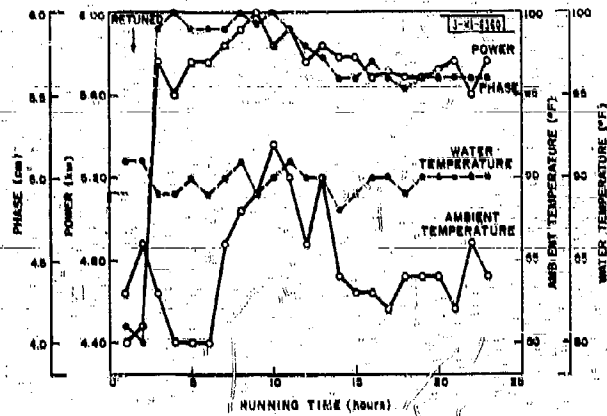


(a) Circulator 22.

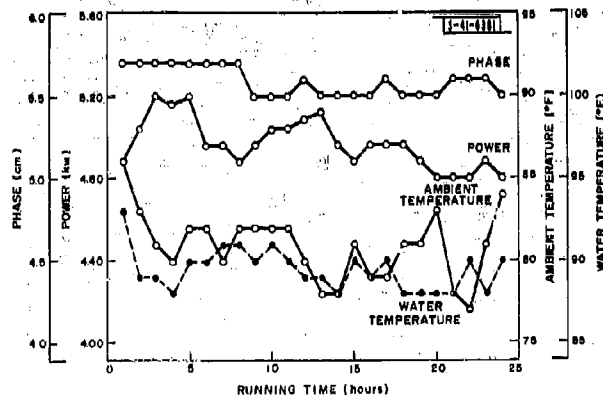


(b) Circulator 46.

Fig. 2-111. VSWR vs temperature.



(a) Typical results at 4 kv with module unboxed.



(b) Typical results at 4 kv with module enclosed.

Fig. 2-14. Stability test results (one module).

The 900-Mcps error signal is carried to the alarm circuit through a short piece of coaxial cable and detected with an M4303 Microwave Associates diode. The merits of this detector are described in Part 2, Ch. III, along with the microwave printed circuit.

The input transistor T_1 in Fig. 2-112 is used in a grounded base configuration to give temperature stability and afford sufficient voltage gain to fire the silicon-controlled switch when a few millivolts of error signal are applied. Component R_1 provides the sensitivity control which sets the alarm level at any desired value. The emitter followers T_2 and T_3 are used to provide isolation and to maintain a high gain by presenting a constant high loading impedance to the first stage.

The narrow bandwidth of the transmitter amplifiers causes the leading and trailing edges of the pulse to have phase and amplitude characteristics different from those of the pulse center section; therefore, large spikes appear at both ends of the error pulse. To overcome this difficulty, only the center portion of the pulse is examined. A 2- μ sec lumped constant delay was placed between T_2 and T_3 . The resulting delayed pulse is combined with the undelayed pulse from T_2 in a three-way "and" gate. Because the monitor phase and amplitude are fixed and will coincide with the transmitted pulses when the transmitters are in the proper phase, the monitor system is activated only when the antenna scans to the horizon position, at which time an "on" pulse is sent to the third gate input. The gate gives a positive output voltage if an error is detected.

In effect, the presence of an error voltage turns on the silicon-controlled switch (SCR). Two 3-volt lamps placed in series with it will light up when the SCR starts conducting. A push button on the control panel is provided to momentarily interrupt the current and reset the controlled switch.

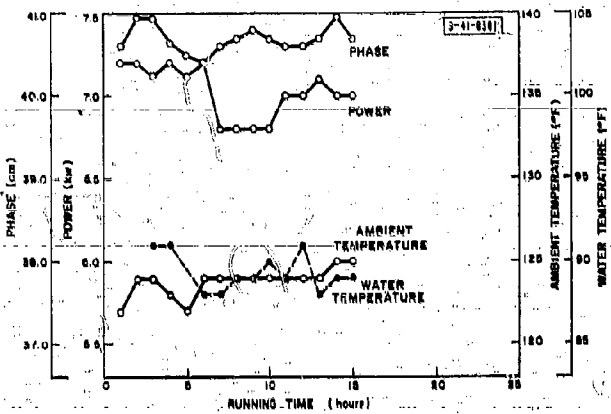
This alarm circuit has been tested on the bench and in the transmitting modules. The results indicate that the error level can be set to function reliably for the detection of $\pm 2^\circ$ of phase error at ± 0.35 -db of amplitude error. The coupled energy was approximately 35 db below the transmitter output of 10 kw peak. No degradation of performance was noted to 60°C during the oven heat test.

D. 900-Mcps AMPLIFIER PERFORMANCE

D. M. Bernella

While all the transmitter modules are presently operating at the 10-kw peak power output level, the bulk of the testing during the past year has been done at the 5-kw power level because, until recently, the higher-power pulse transformers were not available. Therefore, bench testing of some of the spare units will be continued in the future along with the experimental work being done with the 16-element linear transmitting array. In addition to the over-all testing, a large portion of the time during the past six months has been devoted to the development of a phase-amplitude bridge capable of accurate cable-length measurements and to methods of constructing RF cables to specific lengths. This work is described in detail in Part 2, Ch. III.

Figures 2-114(a) and (b) show the test results of the first production module during two 24-hour periods. Figure 2-114(a) gives the results when the module was operated without its box enclosure, and Fig. 2-114(b) shows the results when the module was enclosed. In preparation for the tests, the module was run for several hours to reach its operating temperature, then tuned and all adjustments locked. The module was then shut off and allowed to cool before the tests began. It can be seen that both power output and phase followed the ambient temperature variations quite closely when the module was open and were much more stable when the enclosure



(c) Results at 5 kv.

Fig. 2-114. Continued.

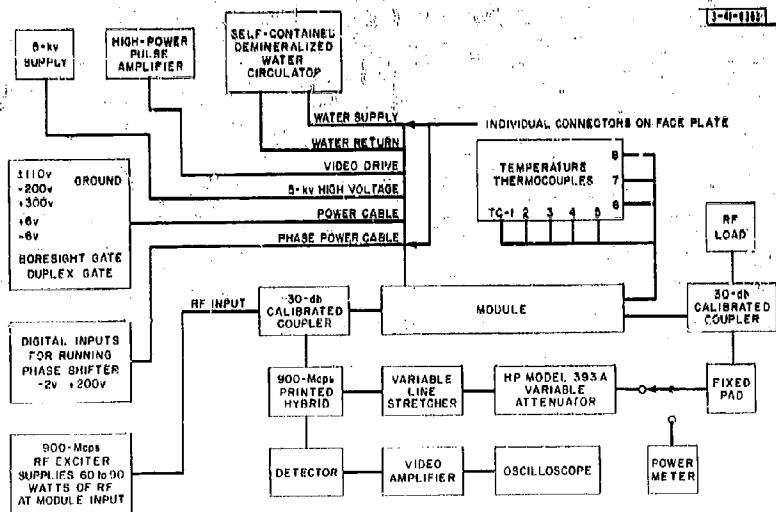


Fig. 2-115. Block diagram of stability test setup.

was in place. Plots of the temperature variations in both cases show the cooling system to be adequate to maintain stable operation within reasonable limits when it is enclosed. A similar test is shown in Fig. 2-114(c) for a transmitter module operating at the higher power level. This unit also had the digital diode phase shifter installed and was enclosed in its casing. A block diagram of the experimental setup for the tests is shown in Fig. 2-115.

Although the test data are far from complete, information obtained thus far certainly shows the tetrode amplifiers to be stable enough for phased array application. It is expected that complete results on the phase-amplitude characteristics will be available in the future.

E. TRANSMITTER POWER CONTROL CIRCUITS

W. W. Carpenter

1. Introduction

As the linear test array grew, it became evident that some form of centralized control and monitoring of the various power and other supplies was necessary. At one point it was noted that 28 switches scattered over the penthouse and in the radome were being used to control the transmitter. In an effort to improve this situation, the essential control functions were outlined, and circuitry for the various requirements was designed. It was decided to use a 24- to 28-volt DC system for the control circuitry. A brief description of the transmitter control circuitry follows.

2. Low-Voltage Controls

When the main switch on the transmitter control panel is in the "on" position, a 24-volt signal is sent to the central water-cooling system, which sends back a 24-volt signal if it is in normal operating condition. This signal initiates the "high-voltage-on" sequence. If no such signal is received, a water malfunction lamp will light. Under normal conditions a relay will turn on the regulated 117-volt primary supply to the modules. This relay will also activate a time delay relay that, when it has cycled, will allow another relay system to sample the 200-volt negative-bias power supply and connect it to the transmitter if the voltage is correct. The relay that performs this function also starts a second time delay relay that supplies 24 volts to three other relays when its cycle is completed. These relays sense and act on the status of the video driver and high-voltage supplies.

DC power for the video driver is obtained from a supply whose AC primary circuit is controlled by that one of the three relays mentioned above which is seeking a DC return for its coil. The relay coil circuit includes a microswitch that is attached to the motor-driven variac controlling the video driver output. If this variac is in any position other than "off," the control relay is de-energized. However, a "video drive lower" button on the console will be able to lower the variac control until the microswitch closes and energizes the relay. If the relay is in a de-energized position, a lamp will indicate "recycle driver." The second relay of the three-relay group samples the amount of high voltage present at the output of the module "plate" supply. The third relay energizes when the other two have signaled that the proper condition exists for turning on the driver and the modulator screen supplies.

Driver and screen voltage cannot be applied until the second relay has closed, indicating that 1 kv or more of high voltage has been applied to the module "plate" bus. This is accomplished by a comparison circuit on a printed circuit card and a voltage divider that closes a set of relay contacts when the specified voltage has been reached. These contacts, in turn, energize

the third relay. The transmitter can then be brought to full power by applying additional voltage and drive power gradually.

Note that the above procedure is completely automatic except for turning on the main "on" switch and for varying the video-driver and high-voltage levels. Note also that, once the array is operating at full power, individual modules can be removed and replaced by removing and replacing plugs without going through the entire cycle.

3. High-Voltage Controls

Plate power for the modules is taken from a 6-kv DC supply capable of 20 kw of DC output. The output is led from this supply to a regulator unit (actually two units, one for the linear array and one for the transmitter test facility). The regulator unit includes 24-volt control sequences for certain functions.

The first of these is a safety check. The application of a 24-volt signal from the driver panel will turn on the regulator filaments and energize an interlock string. Interlocks are located on the supply output cables, on the regulator cooling system and on the start end of a 5-minute time delay relay. If all conditions are satisfactory when the time delay unit has run its cycle it will operate two high-voltage relays, one immediately and the second only if the input to the regulator is correctly interlocked. The first high-voltage relay will connect the output of the regulator to the transmitters and to the voltage sampling circuits, and the second will connect the regulator input to the main high-voltage supply. The first relay is interlocked with the regulator output control so that the output cannot be switched to the transmitters unless the regulator output control is set for zero output. Hence, the voltage must be recycled to zero in order to apply high voltage to the transmitter. The regulator control unit contains two identical high-voltage sensing circuits controlling two separate relays. One closes when 1000 volts or more is present at the regulator output; the second opens a holding circuit and shuts down the high-voltage system whenever a preset upper limit has been reached. The second one is a safety feature while the first one is used to complete the driver control sequencing described in Sec. E-2 of this chapter.

F. SOLID STATE MODULATOR STUDIES FOR 100-kw PHASED ARRAY TRANSMITTER TUBE

M. Siegel

The expected application of phased arrays to long-range-discrimination radars has changed the requirements normally placed on the modulator of the transmitter. The requirement for both high sensitivity and range and Doppler resolution has dictated the use of pulse trains for the transmitted waveform. To achieve the required resolution, the pulse repetition frequency (prf) within a given pulse train must be very high, and the individual pulses in the pulse train should approximate impulses in so far as the state of the art will permit.

A first approximation to a potentially useful pulse train might consist of a pulse train made up of perhaps 30 pulses of 100-nsec pulsewidth, separated in time by as little as 10 nsec. Future improvements on this pulse train might consist of narrowing the pulsewidth of the individual pulses from 100 nsec to 40 nsec.

Because the amount of average power to be handled by these arrays will be very large (perhaps many megawatts), the modulation efficiency should be as high as possible. For this reason and since very fast rise and fall times will be required, "plate" modulation has been ruled out, and low-level, or grid, modulation with the highest μ reasonably obtainable is being considered (see Part 3, Ch. III).

Since Lincoln Laboratory is subcontracting the development of a traveling-wave tube (TWT) for phased array evaluation purposes, the modulator requirements for a typical high-powered TWT have been examined, it being understood that some of the requirements for a TWT modulator would be somewhat similar to modulator requirements for other types of power amplifiers.

The 100-kw traveling-wave tubes being developed require anode-to-cathode voltages of approximately 23 kv with the cathode grounded and the collector at a positive potential. The grid modulator, therefore, rests at cathode potential and does not have to float at high voltage. This eliminates isolation transformers and reduces stray capacitance. The modulator output pulse is required to move from a 150-volt negative bias to approximately 250 volts positive, for a total swing of 400 volts. The grid capacity is expected to be approximately 50 μ f, and the grid current during the pulse is 4 to 8 amp.

Since it may be desirable to provide, for each transmitter module, a separate modulator having good reliability and life characteristics, it was decided to attempt to make each modulator a solid state unit. The concept of having an individual modulator for each module will be useful if it is necessary in building a large array to have the timing of the video modulation correspond to the pointing delay.

The devices investigated for use as the switch in the modulator circuit included silicon-controlled rectifiers (SCR's), avalanche transistors and 4-layer diodes.

At the present time, 4-layer diodes similar to the Shockley 4E-200 series and transistors similar to the Western Electric 2N1765 are being tested in this modulator. The basic problems that beset these solid state devices when used as fast high-power switches involve the following:

- (1) Breakover voltage
- (2) Peak current limitation
- (3) Turn-on time (rise time and pulse delay)
- (4) Turn-off time (fall time and recovery time)
- (5) Rate effect
- (6) Reliability and reproducibility vs age and temperature

Since it is not a requirement to have variable pulsewidth capability in the desired pulse train, the use of a delay line modulator is quite feasible. Also, since standard resonant charging of this delay line is not compatible with state-of-the-art switches, and resistive charging is not able to meet the fast recharge requirement demanded by the high pri, the type of recharging that was decided on as being the only feasible one was recharging the delay line through a series switch.

It should be mentioned that the main reason for discarding the standard resonant recharging network was that the value of the inductance required to resonate with the effective capacitance of the delay line to recharge the delay line was entirely incompatible with the value of inductance needed to reduce the current through the shunt switch to a value less than its holding current (the holding current is that value of current below which the switch will open up, that is, become a high impedance).

A further improvement on the series switch recharging circuit would be the addition of resonant recharging. This addition is made primarily to improve the efficiency of the recharging network, since if the series switch is used without the resonant circuit, the modulator recharging circuit would be limited to the standard 50 percent efficiency of any RC charging network. In this manner the efficiency can be increased to that of an LC resonant network. The type of circuit that was examined first is shown in Fig. 2-116.

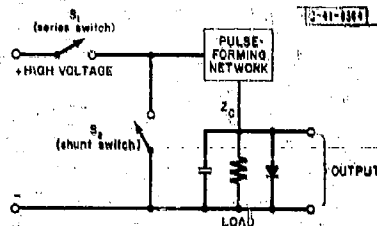


Fig. 2-116. Simplified resonant charging circuit.

Triggering Procedure:— A few microseconds before an output pulse was required, S_1 would be triggered to close, charging the pulse-forming network (PFN) through S_1 and the parallel combination of the load and the load diode. As soon as the PFN was recharged, S_1 would open because of the reverse voltage placed across it from the delay line reflection produced by properly mismatching the Z_C of the delay line to the load impedance Z_L . At this time S_2 would be triggered to close, thus discharging the PFN through S_2 and Z_L and producing an output pulse. Again because of the mismatch between the Z_C of the PFN and Z_L , a reverse voltage would be placed across S_2 , thus helping it to shut off. The entire modulator would then await the arrival of another trigger to S_1 , just before a new pulse is required from the output, and the process would repeat. It should be noted that one trigger is all that is necessary to generate an output pulse even though S_1 and S_2 are sequentially triggered, since the delay between triggering S_1 and S_2 is fixed and can be internally generated. The problems associated with this modulator stem from switch limitations described below.

Switch Limitations:— Initially, it is desired to achieve output pulse rise times of 100 nsec; 10-nsec rise times are the ultimate goal. The best rise times that were achieved experimentally with the 4-layer diodes tested were 100 nsec into primarily resistive loads. When capacitive loads are used, the rise time will probably be even poorer. The 3-junction transistors (Western Electric units) that were tested had rise and fall times of 50 nsec, again into essentially resistive loads.

Both the 4-layer diodes and the 3-junction transistors can be placed in series, provided compensating RC networks are used across them. Hence, both are able to withstand the full voltage without breaking down. The 4-layer diode has a 200-volt breakdown voltage, while the 3-junction transistor has up to a 400-volt breakdown voltage. Parallel operation of these units is, in general, not recommended because of the difficulty in balancing currents through the individual units. The 4-layer diode units were rated at 20 to 30 amp peak, while the 3-junction transistors were rated to 50 amp peak.

The only solid state devices that appear to be faster at present (but which have less peak current capability) are some avalanche transistors that can switch from 0 to 2 amp in a few nanoseconds. The peak voltage of these devices, however, is considerably below the required voltage. Series arrangements of these will be tested in the future.

Thus far, one of the most troublesome problems with these switches has been recovery time. The best of these devices take 2 or 3 μ sec to recover and the worst take more than 10 μ sec. It has been difficult, therefore, to get these switches to run at 100-keps rates, where only 5 μ sec is allotted for each switch (S_1 and S_2) to fire and completely recover (S_1 fires and recovers in 5 μ sec; then S_2 fires and recovers in the remaining 5 μ sec to make a total of 10 μ sec, or 1 pulse repetition period at 100 keps).

Rate Effect:— Another difficult problem arises due to a phenomenon known as "rate effect." Since SCR's and 4-layer diodes are charge-operated devices, i.e., their relative impedance is determined in part by the quantity of charge in the vicinity of the junction area, they can be triggered from a high impedance to a low impedance not only by increasing the voltage across them to a voltage higher than their breakover voltage, but also by the displacement current resulting from a rapid rate of change of voltage across their terminals (hence the name "rate effect"). Typically, spurious switching will occur in the device at a voltage as low as one-half or less of its breakover voltage if the voltage is applied to it too rapidly. A typical device might switch at 40 percent below its normal breakover voltage if dV/dt is of the order of 20 volts/ μ sec. It happens, therefore, that when S_2 is required to close in nanoseconds and S_1 is expected to be open (high impedance), the closing of S_2 also closes S_1 because of the rate effect. The power supply then shorts to ground through both SCR's and, since there can be little resistance in the charging circuit or discharging circuits (because of efforts to minimize charge and discharge time constants), a current greater than the holding current flows through both S_1 and S_2 to ground; and it is impossible to turn either of these devices off. It is apparent that some sort of filtering action is needed to isolate the dV/dt across S_1 from S_2 , and vice versa.

A modified version of the series-switch charging circuit described above makes use of resonant charging to improve the efficiency of the recharge network and also provides filtering action between the switches, minimizing rate effect both on discharge and recharge (see Fig. 2-117). Note that when S_1 is fired, the maximum voltage gradient placed across S_2 is determined by the resonant circuit composed of L , C , and C_{TUN} ; conversely, when S_2 is fired, the maximum voltage gradient placed across S_1 is also determined by the resonant circuit. This is indicated in Fig. 2-117.

These, then, are some of the basic problems associated with switching and modulation when very fast pulses are required at high repetition frequencies and moderate voltage levels and currents.

The present level of achievement with the series-switch, shunt-switch delay line modulator has been the attainment of 1.5-amp, Gaussian-shaped, 100-nsec pulses (50-nsec rise and fall time) into 50 ohms at 100 kcps or, alternatively, 4-amp, Gaussian-shaped, 100-nsec pulses into 50 ohms at 40 kcps. Typical waveforms are shown in Fig. 2-118; and Fig. 2-119 is a photograph of a printed-circuit type of experimental modulator.

G. HYBRID ARRAYS FOR GREATER BANDWIDTH

L. Cartledge

System studies indicate that signal bandwidths as great as 10 percent at L-band might be required of high-power array radars. This bandwidth is too large for a simple phased array, one where all steering delays are modulo 2π radians, if the beamwidth is to be much smaller than about 5° .* The classical solution to this problem is to replace the phase shifters with true time delay shifters. Time delay shifters have at least two significant disadvantages. First, the precision required corresponds to the number of beam positions to be used and, second, the introduction and removal of many wavelengths of delay cause undesirably large changes in the loss through the shifter.

The hybrid array (which is not presented here as a new idea) suggests itself as a reasonable compromise solution. It can be developed by dividing a large phased array into subarrays small

* See TR-236, Part 3, Ch. II.

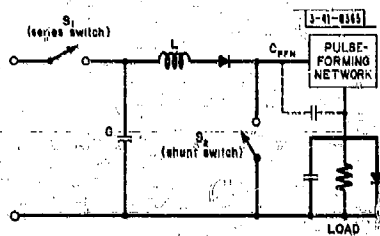
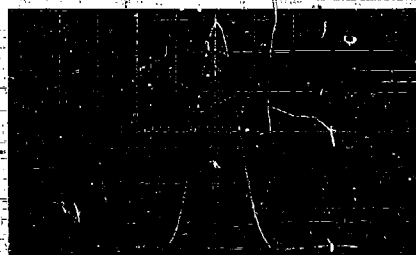


Fig. 2-117. Modified resonant charging circuit with rate-compensating filter.



(a)

Pulse Voltage: 60 v
 Pulse Current: 1.2 amp
 Pulse repetition frequency: 100 kcps



(b)

Pulse Voltage: 250 v
 Pulse Current: 5.0 amp
 Pulse repetition frequency: 1 kcps

Fig. 2-118. Typical waveforms.

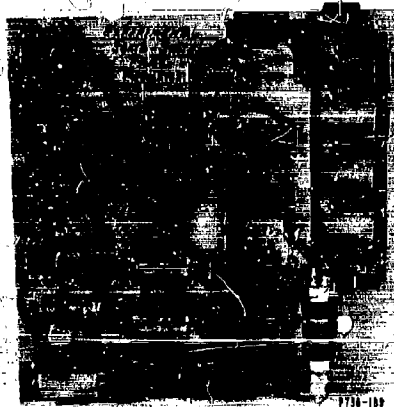


Fig. 2-119. Experimental solid state modulator.

enough so that buildup time is not a problem. The individual subarrays could then be driven by true time delay shifters. This arrangement (depicted for a linear array in Fig. 120) would reduce the number of costly and complicated time delay shifters required and, hence, would reduce the penalty in efficiency and complexity paid for added bandwidth. The actual reduction in the number of delay shifters that can be realized in this way would vary with frequency, bandwidth and the amount of density tapering that is done, if any. As density tapering becomes more extreme, the number of active elements per subarray decreases. Thus, a saving amounting to a factor of 80 could probably be realized in a moderately tapered array (20-db sidelobes).

If the transmitted signal is a simple amplitude-modulated signal like a train of short pulses and if the final amplifiers can be modulated fast enough, wide signal bandwidths can be realized by phase shifting the RF carrier and introducing the appropriate steering delay into the video paths to the various amplifiers. It should be noted that, regardless of the steering system used, the modulation must be delayed, if the transmitted pulses are short compared to the buildup time of the array, in order to preserve the over-all efficiency of the transmitting system.

H. POWER AMPLIFIER TUBES FOR PHASED ARRAYS

L. Cartledge

Requirements for a phased array amplifier tube were listed in a previous report.^{*} These requirements can be summarized as follows: 100-kw peak-power output at 1 percent duty at L-band, with 10 percent bandwidth and phase and amplitude stability suitable for use in phased arrays.† In addition, low-level modulation is required for pulsewidths from 0.1 μ sec to 100 μ sec, and the tube must be small so that it could fit into a square hole 1/2 wavelength on a side.

The development of a high-pervance traveling-wave tube to meet these requirements was initiated. The problem was complicated somewhat by the decision to develop an "inverted" tube, i.e., this TWT is to operate with its cathode at ground potential and with the high voltage applied to the slow wave structure and the collector. Several experimental tubes have been built under this program, and problems involving the gun design, slow-wave structure, DC insulation and arc-over, output window design and mechanical structure have been solved. It has not been possible as yet to focus the beam adequately with permanent magnets in the small space allowed (4 1/2-inch diameter). This development, being carried on by the Watkins Johnson Company of Palo Alto, California, is continuing.‡

Other tubes with comparable power and bandwidth either are being developed or have been proposed. One forward-wave§ and one backward-wave¶ crossed-field "amplifier" are presently under development, and triode configurations similar to those of some existing super-power UHF tubes have been proposed.‡

*TR-236, p. 105.

†TR-236, Part 2, Ch. III.

‡J. W. Sedin and K. W. Slacum, "A Grounded-Cathode L-Band Pulsed TWT Amplifier," Conference Paper presented at the Electron Devices Meeting of the IRE, PGED, Washington, D. C. (25-27 October 1962).

§H. McDowell and A. Wilczek, "An L-Band Crossed Field Amplifier Chain," Conference Paper presented at the Electron Devices Meeting of the IRE, PGED, Washington, D. C. (25-27 October 1962).

¶Raytheon's QKS-1012. See L. Clampitt, M. Huse and W. Smith, "Measurement of Phase Characteristics of High-Power Microwave Tubes," Conference Paper presented at the IEEE National Convention, New York (March 1963).

‡RCA's proposed A-15197, for example.

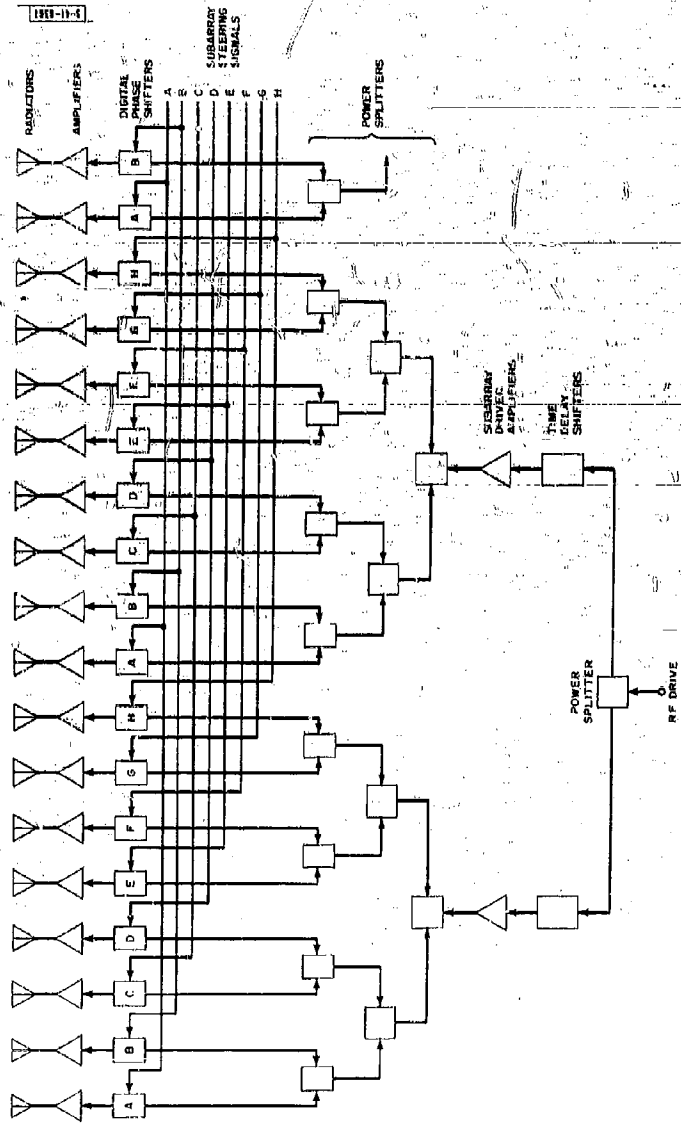


Fig. 2-120. Section of linear hybrid transmitting array.

SPECIAL ACKNOWLEDGMENT

The technicians who worked on the transmitter section of the phased array radar during the period covered by this report were A. G. Baker, M. DeSapio, L. J. Garrlar and L. W. Robertson. Their contributions are gratefully acknowledged.

CHAPTER VI SPECIAL-PURPOSE TEST EQUIPMENT

S. Spocerl

SUMMARY

This chapter is devoted to a description of the special-purpose test equipment developed for use with the experimental phased array test facility. The equipment described reflects a gradual shift in emphasis from proving the feasibility of arrays (the automatic monitoring equipment) to designing arrays with high all-around capability (the short-pulse test equipment).

A. INTRODUCTION

The special-purpose test equipment, which was developed to simplify the performance monitoring and component testing of experimental phased arrays, has been described in previous reports.*† The first part of this chapter covers the improvements made since those reports were written.

The basic test system consists of four units: a coherent frequency synthesizer, an automatic data printer, an IF sampler and an automatic phase meter.† Of these, the first two have had the widest use and have been changed most since last described. Consequently, they alone are reviewed here.

The automatic data printer is described first. It is much more versatile than earlier versions and should be adequate for all anticipated future needs. The discussion then shifts to recent changes in the coherent frequency synthesizer, which provides more independent outputs at each frequency as well as short-pulse capability. The remainder of the chapter covers the results of a very recent foray into the realm of short pulses and large-signal bandwidths. The interest in short pulses is indicative of lessening concern with the mechanics of arrays (achieving sufficient stability) and an increasing concern with performance (e.g., providing enough bandwidth for sophisticated signal design).

B. AUTOMATIC DATA PRINTER

1. Introduction

The automatic data printer is a digital data recording system consisting of a digital voltmeter, an input scanner, a servotyper and a control unit. The control unit provides sufficient operational flexibility to allow variable print-out format, control of external switches such as an IF sampler,† and programming of test variables during a data run. The automatic data printer is also capable of controlling an IBM summary punch to provide punched card records of channel amplitude and phase in an experimental array. These cards may be processed in a computer to determine the array rms phase and amplitude errors vs time.‡

* J. L. Allen, et al., "Phased Array Radar Studies, 1 July 1959 to 1 July 1960," Technical Report No. 228 [U], Lincoln Laboratory, M. I. T. (12 August 1960), ASTIA 249470, H-335.

† J. L. Allen, et al., "Phased Array Radar Studies, 1 July 1960 to 1 July 1961," Technical Report No. 236 [U], Lincoln Laboratory, M. I. T. (13 November 1961), ASTIA 271724, H-474.

‡ A program was written by N. A. Doucett of Group 41 and has been used to process the results of several tests. See Part I, Ch. II, Sec. G-1 of this report and also J. H. Teale, "Operational Characteristics of 16 Electron-Beam Parametric Amplifiers in a 900 Mcps Phased Array," 41G-1 [U], Lincoln Laboratory, M. I. T. (6 August 1962), ASTIA 288223, H-444.

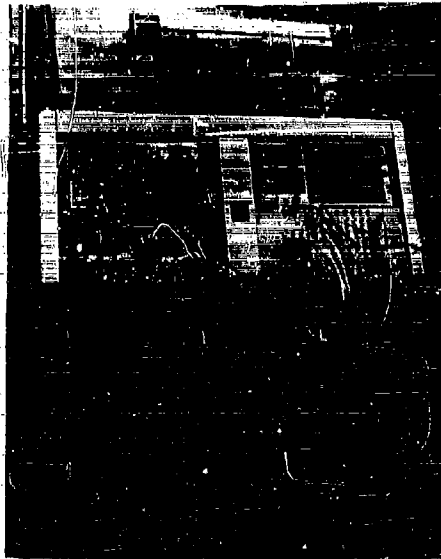


Fig. 2-121. Automatic data printer.

06/27/62-1240-11 -0.211 I2 -0.307 I3 -0.380 I4 -0.538 I5 +4.138
A1 +0.162 A2 +0.167 A3 +0.161 A4 +0.166 A5 +0.179 A6 +0.177 A7 +0.166 A8 +0.165
P1 -0.048 P2 -0.048 P3 -0.077 P4 -0.039 P5 -0.010 P6 +0.030 P7 -0.118 P8 -0.088

Fig. 2-122. Sample output record.

2. Over-All Description

The most recent version of the automatic data printer is shown in Fig. 2-121. The solenoid-operated typewriter is at the top. On the left, from top to bottom, are the digital date clock and the digital time clock. To the right are the control unit, the input scanner and an AC-to-DC converter.

3. Output Format

A sample of the output record from an actual data run is shown in Fig. 2-122. The complete set of readings taken at one clock time is referred to as a data set. The data set is further divided into data groups and individual readings. As shown in Fig. 2-122, the date and time of day are printed once per data set. They are followed by the first data group, in this case 5 readings with L-prefixes which signify local oscillator and test signal levels. The second data group consists of eight readings, the signal amplitudes of eight receivers undergoing test in a test rack. The third data group displays the phase of the eight receiver outputs with respect to a reference channel. The readings shown must be multiplied by appropriate scale factors (which are determined at the beginning of a run) in order to arrive at the actual amplitude and phase values.

4. Control Unit

The control unit contains two stepping-switch subassemblies driven by a self-contained power supply and pulsor. The operating program is determined by front panel controls and also by two patch panels, one accessible from the front and one located inside. A close-up view of the front panel is shown in Fig. 2-123(a). The left side of the panel contains a power switch, a start button, a switch that controls the number of data groups (from 1 to 9) and four switches that control the size of the first four data groups (1 to 24 readings each). The right side houses a patch panel used to program additional data groups and the (up to) three-character code that identifies each reading. Figure 2-123(b) shows a view of the inside of the control unit. The power supply/pulsor unit is to the left, and one of the stepping-switch subassemblies is immediately behind the front panel. The other subassembly is at the rear of the control unit.

5. Input Scanner

The input scanner contains miniature relays that are energized by the control unit. The relays provide switching of two poles to 24 positions in step with the reading number (in each data group) and switching of another two poles to nine positions in conformance with the group number. A close-up of the input scanner front panel is shown in Fig. 2-124.

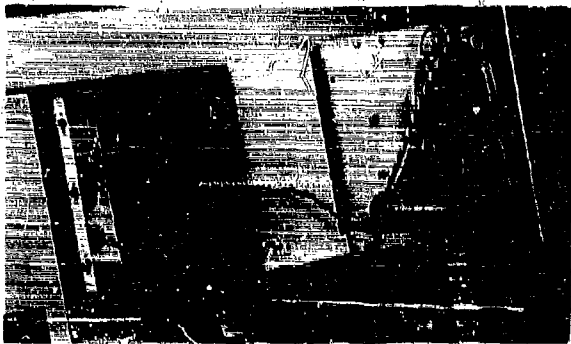
6. Digital Date Clock and Timer

A front panel view of the digital date clock and timer is shown in Fig. 2-125. The digital date clock is a stepping-switch unit that is advanced daily by the digital time clock to provide a digital readout of the day and the month. It also provides contact closures so that the day, month and year can be printed out.

The timer section sends a "start-reading" pulse to the control unit at chosen intervals of from one minute to one hour. This pulse is synchronized with the digital time clock so that the latter's time change does not occur while the time is being printed. If a channel is noisy, the digital voltmeter does not settle within a preset interval; therefore, another timer is provided to advance the control unit to another channel.



(c) Front panel.



(b) Side view.

Fig. 2-123. Control unit.

Fig. 2-124. Input scanner front panel.

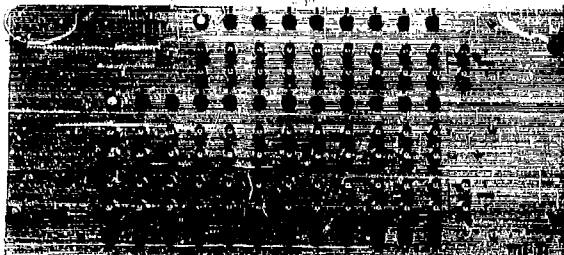


Fig. 2-125. Digital date clock and timer front panel.



7744-102

7. Power Supply/Pulsar Unit and Machine Timing

The power supply/pulsar subassembly is located inside the control unit [Fig. 2-123(b)]. It supplies 24 volts DC for indicator lights and relays as well as two separate, but related, pulsed 24-volt outputs. Figure 2-126 shows the timing of these pulses relative to stepping-switch motion in the control unit. The P24 stands for pulsed 24 volts and is used to advance all stepping switches. Since the stepping switches move only after the energizing (or cocking) pulse is gone, the same P24 pulses can be used to actuate the solenoids of the servotyper for print-out of information.

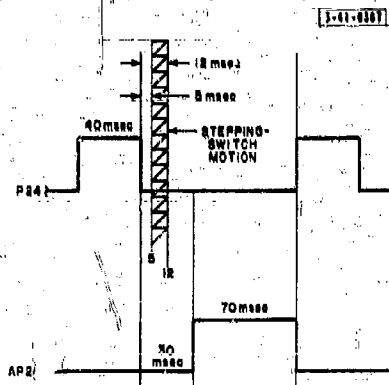


Fig. 2-126. Machine timing diagram.

The servotyper thus prints under the control of a particular stepping-switch position before the stepping switch moves to the next position. No inductive circuits are broken while (full) current is flowing, so arcing is minimized. The AP24 (antipulse 24) is another set of pulses interlaced with the P24 pulses in such a way that they also occur during periods of no stepping-switch motion (see Fig. 2-125). These pulses are used solely to actuate the servotyper red-ribbon/black-ribbon and upper-case/lower-case solenoids. By using AP24 it is possible to change, to upper case (for example) very shortly after moving to a new stepping-switch position, then print a character while cocking the stepping switch to advance it to the next position.

8. Summary of Special Features

The special features of the automatic data printer are summarized below:

- Print-out of both date and time makes possible positive identification of each reading set.
- Three characters can be programmed for each reading to serve as an identity code.
- Nine data groups of one to 24 readings each can be printed. The length of each group is independently controllable.
- The input scanner is relay-operated and can be remotely located.
- Key test variables can be programmed during the test by the control unit.

- (f) The control unit can provide one-way control of auxiliary switches (such as an IF set pointer) through its three output pulses: advance pulse (after each read), reset (after each data group) and final reset (after the last data group).
- (g) The stepping-switch mechanism is nonarcing and is unaffected by power interruptions.
- (h) Provision is made for handling auxiliary inputs.
- (i) A lock-up circuit is provided that stops the digital voltmeter from cycling if it does not settle within a preset interval. Such an occurrence is identified by the printing of a small e (for error) if the polarity was negative, and a capital E if the polarity was positive. If the voltmeter was on "ratio" an asterisk is printed instead of an R. Since the digital voltmeter cycles the most significant digits first, a locked reading still may be approximately correct.
- (j) A digital time delay is provided by an Automatic Electric OCS stepping switch that interrupts the cycle of the control unit whenever a servotyper carriage return is initiated. This prevents loss of data through attempted typing during a carriage return.
- (k) In addition to programmed carriage returns, an automatic carriage return is provided when the servotyper reaches the right margin stop.
- (l) The machine timing provides control of red ribbon/black ribbon and upper case/lower case on the same stepping-switch position that prints a character.

9. Stepping-Switch Pulser

The stepping-switch pulser is an auxiliary unit that contains the same circuits as the power supply/pulser of the control unit. Its outputs are 24 volts DC, P24 and AP24. These may be used to check stepping-switch circuits or for any other application requiring 2-amp 24-volt pulses of 10 msec to 4 sec duration. A photograph of the unit is shown in Fig. 2-127.



Fig. 2-127. Stepping-switch pulser.

C. COHERENT FREQUENCY SYNTHESIZER

1. Introduction

The coherent frequency synthesizer is essentially the same as the one reported in TR-236. A few changes are in process that will extend the usefulness of the synthesizer; these are described in the following sections.

2. Substation Concept

The present synthesizer has six isolated outputs at each frequency except 870 and 900 Mcps. This number was found to be too small to provide for the local oscillator needs of the experimental test array and receiver test rack and, in addition, supply a number of outputs for special requirements. Accordingly, it is planned to use the basic synthesizer modules to build a master frequency synthesizer that will feed a number of substations located at the various test sites. The substations will amplify and power-split each frequency to provide a number of independent outputs sufficient to meet local test needs.

3. Extension to 60 Mcps

A doubler module has been built that accepts 30 Mcps and doubles it to 60 Mcps. This 60 Mcps is then amplified in a 60-Mcps power amplifier module to provide 2 watts of output. The 60 Mcps is required for testing wideband receiver components with a 60-Mcps center frequency. These are described in more detail at the end of this chapter.

4. Up-Mixing to Provide a 900-Mcps Test Signal

The old synthesizer obtained an 870-Mcps LO frequency and a 900-Mcps test signal by multiplication from a 30-Mcps base. When 900 Mcps is not required for use as a test signal, it is best that it be turned off to eliminate leakage. Also, it is desirable on occasion to vary the 900 Mcps around its nominal frequency value. This can be more readily accomplished in a system that mixes 30 Mcps with 870 Mcps to obtain the 900 Mcps.

Some experiments were conducted using balanced mixers intended for receiver use. The mixers contain one forward and one reverse diode and provide a 30-Mcps IF output when supplied with 900- and 870-Mcps inputs. If the reverse diode is replaced with a forward diode, and the mixer is driven with 30 and 870 Mcps, the following typical performance is obtained:

<u>Inputs</u>	<u>Outputs</u>
38 mw at 870 Mcps	2.4 mw at 900 Mcps (desired)
25 mw at 30 Mcps	3.6 mw at 870 Mcps (undesired)

The mixer exhibits a 10-db conversion loss for the smaller input signal and a 10-db suppression of the undesired (870 Mcps) input. The conversion loss can be reduced by increasing the ratio of the input signal levels, but the total diode dissipation per unit output increases. Although better performance could be obtained with a mixer specifically designed for this application, particularly with respect to rejection of 870 Mcps in the output, the mixers on hand work well enough to be useful.

A module has been built that contains a buffer amplifier for the 870-Mcps input, a balanced up-mixer and an amplifier/filler following the up-mixer output. The output of the module is 50 mw at 900 Mcps.

A similar module has been built to provide 930 Mcps (obtained by mixing 60 and 870 Mcps).

5. Generation of 0.1- μ sec RF and IF Pulses

A requirement arose for phase-coherent, 0.1- μ sec, 60-Mcps IF pulses to be used in testing wideband IF strips and phase detectors. This requirement motivated some experiments on a

PIN diode switch to determine its suitability as a pulse modulator (see Part 2, Ch. I). Initial measurements were made with 10 Mcps from the coherent frequency synthesizer to trigger a Hewlett-Packard sampling oscilloscope. The 10 Mcps was also used to control the transmission of the diode switch for a 930-Mcps signal (also derived from the coherent frequency synthesizer). Figure 2-128 shows a 30-nsec RF pulse obtained in this fashion, as well as the same pulse coherently mixed down to 60-Mcps. The envelope rise and fall times are quite good, but the phase during the pulse* varies considerably as a result of the capacitance variation of the diode in its reverse-bias state, a consequence of the sine-wave switching waveform. (The diode is off when the switch is transmitting.)

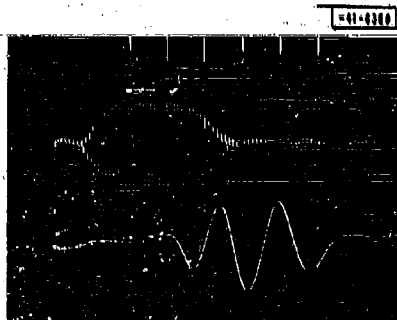


Fig. 2-128. RF and IF pulses produced by a diode switch driven with a 10-Mcps sine-wave switching signal.

An improved test setup is shown in Fig. 2-129. Ten Mcps is used to trigger the sampling oscilloscope, which in turn triggers a 0.1- μ sec pulse generator (the avalanche pulser described in Sec. D-2 of this chapter). The pulse generator is triggered by the oscilloscope sync output so that the pulse will occur shortly after sweep start. The pulse generator, in turn, puts out a negative 0.1- μ sec pulse that turns off the diode in the diode switch, allowing the switch to pass the 930-Mcps signal from the balanced up-mixer/930-Mcps amplifier. A portion of the resulting 0.1- μ sec 930-Mcps pulse is fed to channel A of the sampling oscilloscope, and the remainder is coherently mixed down to 60 Mcps and displayed on channel B. The resulting oscilloscope presentation is shown in Figs. 2-130(a) and (b).

Figure 2-130(a) was obtained by using a single-section diode switch with approximately 25 db of rejection in the off state. Figure 2-130(b) shows the result of using a 2-section diode switch controlled by the same video pulse source (the avalanche pulser). The rejection is much better (about 50 db), but at the expense of slightly higher switching transients.

These results were obtained with prototype components and, therefore, are not the best that can be achieved. They are sufficiently encouraging, however, so that a permanent facility for generating coherent IF and RF 0.1- μ sec pulses is planned. A multisection diode switch will be used to reduce the switch-off leakage to less than 60 db.

* This can not be determined from Fig. 2-128 but was measured using a phase detector (Sec. D-4 of this chapter).

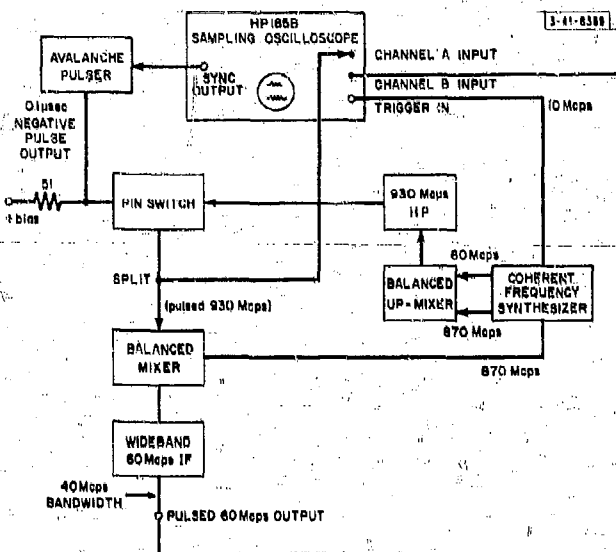
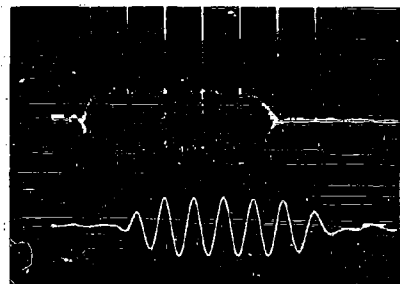
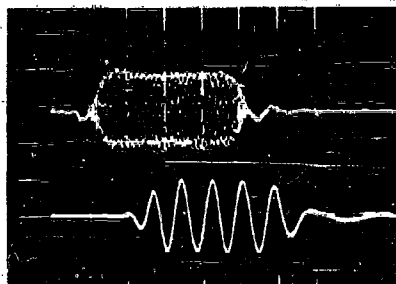


Fig. 2-129. Test setup for generating 0.1-μsec RF and IF pulses.



(a) One-section diode switch.



(b) Two-section diode switch.

Fig. 2-130. Diode switch characteristics.

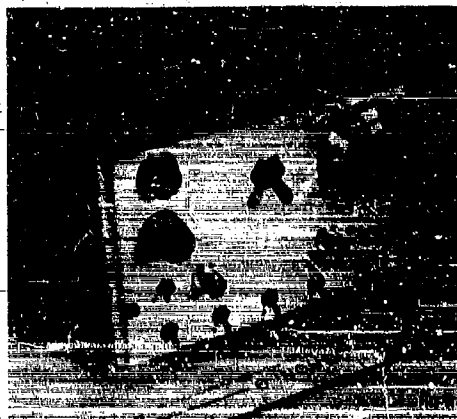


Fig. 2-131. Avalanche pulser.

Fig. 2-132. Multiple exposure showing all pulse output widths.

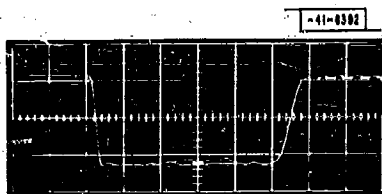
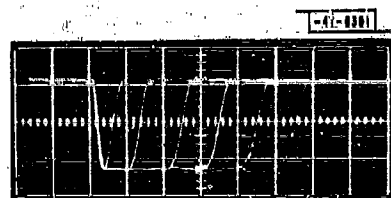
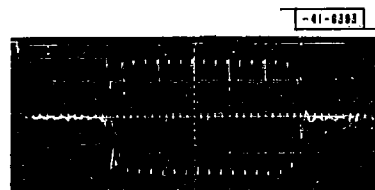


Fig. 2-133. 0.25- μ sec pulse output.

Fig. 2-134. 0.25- μ sec 60-Mcps pulse.



D. SHORT-PULSE TEST EQUIPMENT

1. Introduction

The recurrent requirement for defense radars with ever improved resolution and discrimination capabilities has intensified interest in sophisticated signal designs with large time-bandwidth products (pulse bursts appear to be quite suitable). Unfortunately, it is difficult to build matched filters for the signals, especially if some flexibility of transmitted waveform is desired. Another serious problem is posed by the high data rates produced by high-resolution signals.

A logical approach would be to reduce the data rate by selective matching to the particular range and Doppler-resolution cells that convey the maximum target information in a given situation. The system should be flexible so that as the target situation changes, the resolution cells observed can be changed also.

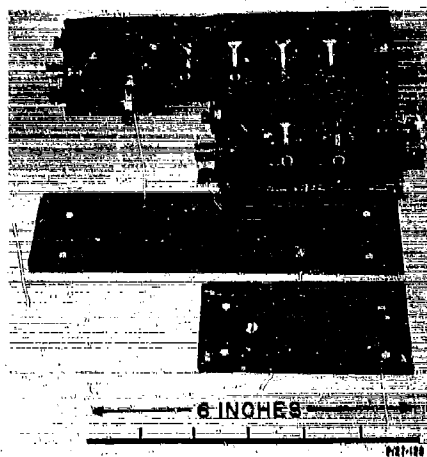
The test equipment described in this section is the result of initial efforts directed toward the development of a line of receiver components that might be used in a selectively matched receiver/data processor. The test units are actually more aptly described as accessories useful in testing wideband receiver components. These accessories were designed with emphasis on compactness, convenience and adequacy for certain specific uses, rather than extreme performance specifications. The equipment built thus far starts by generating relatively short video pulses. These can be converted to IF, power-split, amplified, multiplexed or phase-detected, according to the requirements of the component test being performed.

2. Avalanche Pulser

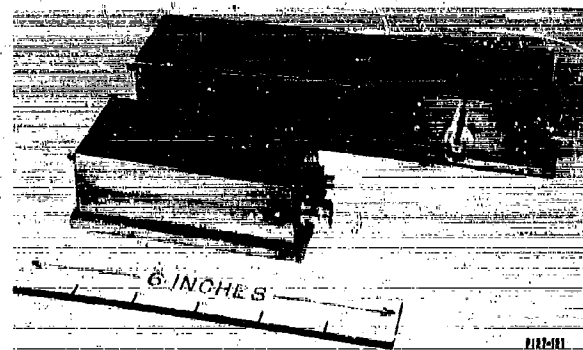
The avalanche pulser (Fig. 2-131) was built to serve as a source of moderately fast-rise short pulses. It derives its name from the use of a 2N709 transistor in the avalanche breakdown region. A row of switches along the bottom of the panel permits selection of sections of a lumped constant charge line to control the output pulsewidth. The width is controllable in steps from 20 to 250 nsec, as shown in the multiple exposure in Fig. 2-132. The 250-nsec pulse is shown by itself in Fig. 2-133. Output is a negative 4.5 volts into a 50-ohm load. The pulser may be operated in three modes: triggered, synchronized, or self-controlled (free running), depending upon the setting of the repetition rate control (the hellpot in the upper-right-hand portion of Fig. 2-131). Repetition rate in the self-controlled mode varies with pulsewidth, and ranges from 200 kcps to 1 Mcps for the 20-nsec pulse and from 14 to 70 kcps for the 250-nsec pulse.

3. Signal Gate

The signal gate is a diode bridge that is switched into conduction by the output from the avalanche pulser (applied through a transformer). Various diodes and bridge configurations were tried in an attempt to obtain the best-shaped output pulse and a minimum of CW leakage at frequencies up to 60 Mcps. Of the stock diodes available, 1N903's performed best. In a one-section switch, the best leakage level obtained (at 60 Mcps) was -30 db. This performance can be improved by cascading gates, but at the cost of increased complexity in the driving circuitry. A photograph of a 250-nsec, 60-Mcps pulse is shown in Fig. 2-134. The -30 db leakage level is sufficient for many tests, including IF pulse response and rise-time measurements. When lower leakage is required, the gated IF amplifier described in the next section can be used.



(c) Open.



(b) Closed.

Fig. 2-135. Gated IF amplifier and 20-db buffer IF amplifier.



Fig. 2-136. Frequency response.



Fig. 2-137. Gating characteristics.

4. Gated IF Amplifier

A photograph of a gated IF amplifier is shown in Fig. 2-135. This unit has 40 Mcps of bandwidth centered at 60 Mcps (Fig. 2-136). It can be switched from transmission to 80 db of rejection in 0.5 μ sec (Fig. 2-137). The IF amplifier functions normally when no gating signal is applied or when the gating level is more positive than -1 volt. The IF amplifier is turned off by a level more negative than -2 volts. This makes it compatible with most logic including Digital Equipment Corporation (DEC) logic levels. The gated IF amplifier can be used for IF switching, multiplexing or generating IF pulses with low CW leakage (-80 db). The rise and fall time is adequate for many tests. The gated IF amplifier can also be used as an overlap gate for the signal gate described in Sec. D-3 of this chapter. This combination provides a fast-rise IF pulse with extremely low CW leakage, except in a small region around the pulse where the leakage level is -30 db. A schematic of the gated IF amplifier is shown in Fig. 2-138. The unit is an adaptation of a wideband amplifier design described in Part 2, Ch. III.

5. 60-Mcps Hybrid Ring

A 60-Mcps hybrid ring (Fig. 2-139) was constructed from 75-ohm coaxial cable in order to provide port impedances suitable for use in a 50-ohm system. The 20-db isolation bandwidth is approximately 20 Mcps and the device is quite useful as a low-loss power splitter. The sum and difference output responses to a 250-nsec, 60-Mcps IF pulse are shown in Fig. 2-140. The vertical scale of the sum output is reduced by 20 db to facilitate comparison with the difference output.

6. Low-Pass Filter

A need arose for a low-overshoot, low-pass filter that would block 60 Mcps, yet have a rise time of the order of 25 nsec for use with 100-nsec pulses. Various designs were investigated, including maximally linear phase designs. The design selected was a 7-pole Butterworth, equal resistive terminations (chosen to be 50-ohm) filter. By shunting the center inductor with a 100-ohm resistor, the filter characteristics are modified so that there is practically no overshoot (0.5 percent). Other values of overshoot may be obtained with increased resistor values. The filter was built in a coaxial structure to provide a solid ground path; the resulting unit is shown in Fig. 2-141. The filter is used to eliminate carrier components from the outputs of phase detectors and amplitude detectors that must respond to 100-nsec pulses. It can also be used to shape the video pulse output of the avalanche pulser to produce a pulse with controlled rise and fall times. Since the design can be scaled (in the sense of having practical realizations) from cut-off frequencies of lower than 200 kcps to at least 30 Mcps, a wide variety of controlled pulse shapes can be obtained.

Figure 2-142 shows the response of a 20-Mcps cutoff filter (25 Mcps without modifying resistor) to a 100-nsec pulse. The input is shown displaced vertically downward with respect to the output.

The impulse response of the filter was measured by applying a 250-nsec "impulse" to a 1/100 frequency scaled model. The resulting response is shown in Fig. 2-143, with the input pulse superimposed. The vertical scale for the input pulse is 2 volts/cm, whereas that for the output pulse is 0.2 volt/cm. The time scale in the photograph is 0.5 μ sec/cm, which should be interpreted as 5 nsec/cm to obtain the actual impulse response of the filter. Knowledge of the impulse

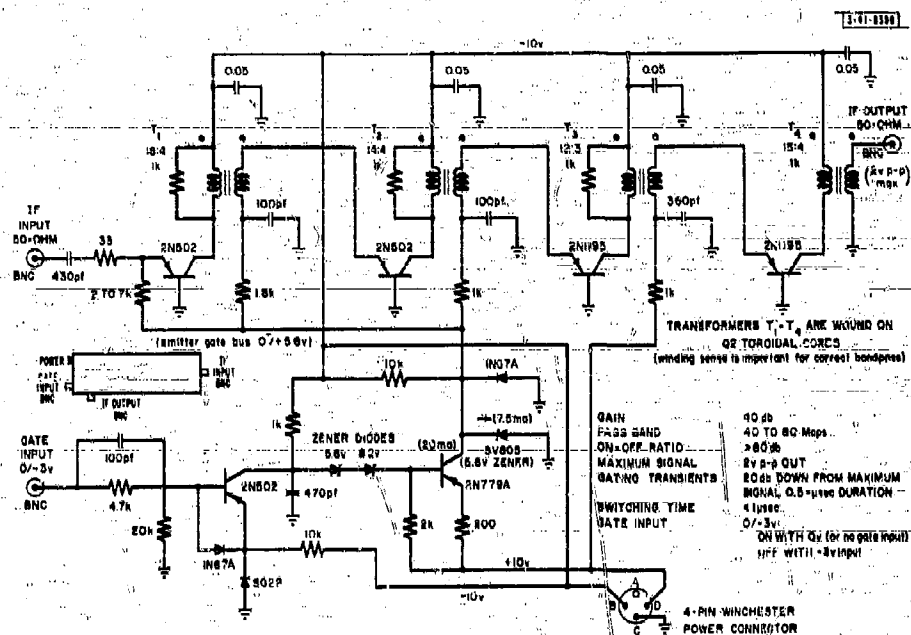


Fig. 2-138. Schematic diagram of a 60-Mcps gated IF amplifier.

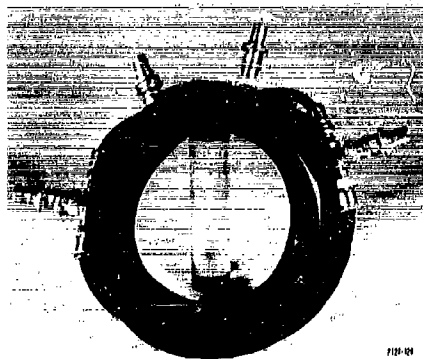


Fig. 2-139. 60-Mcps hybrid ring.

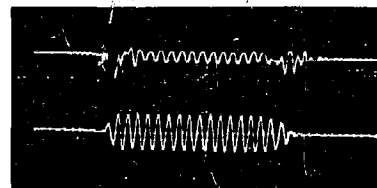


Fig. 2-140. Hybrid ring short-pulse response.



(a) Assembled.

(b) Disassembled.

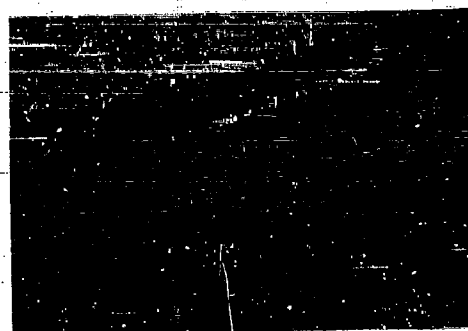


Fig. 2-141. Low-pass filter.



Fig. 2-142. Pulse response.

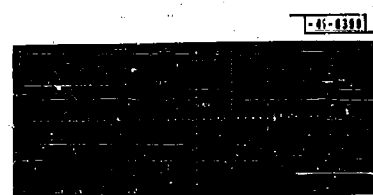
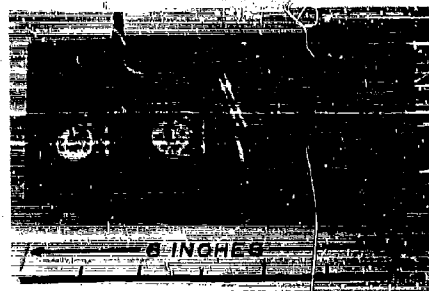


Fig. 2-143. Impulse response.

response is useful in calculating the magnitude of the phase transient that should appear in an ideal phase detector output in response to short IF input pulses.

7. 60-Mcps Phase Detector

A 60-Mcps phase detector was built for use with 100-nsec pulsed IF signals. The design consists of a wideband transformer/diode combination (the actual phase detector) plus a wideband video amplifier that can supply a 2-volt peak-to-peak signal to a 50-ohm load. A photograph of the phase detector assembly is shown in Fig. 2-144. A 60-Mcps trap is included that eliminated the bulk of the 60-Mcps reference signal in the output. Phase and gain trimmers are also provided. The phase detector schematic is shown in Fig. 2-145. The video amplifier has a low-frequency cutoff of 10 cps, but is DC-coupled out to avoid the necessity for an extremely large output capacitor (which would be required to maintain a 10-cps cutoff with a 50-ohm load). For this reason, a DC level adjustment is also provided so that the output can be set to zero in the absence of input signal. The phase detector output is intended to be fed through one of the filters (described in Sec. 6 of this chapter), which serves to further suppress the 60-Mcps reference signal, as well as input signal sidebands. When this is done, the output for a 100-nsec IF input



(a) Top view.

(b) Oblique view.

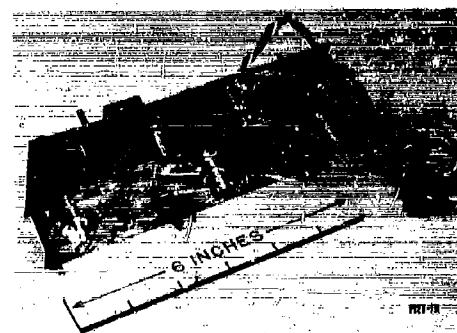


Fig. 2-144. 60-Mcps phase detector.

-41-8402



Fig. 2-147. Amplitude detector output.

pulse is as shown in Fig. 2-146. Four conditions of signal input vs reference signal phase are shown. The phase transients are most evident for phase angles near 0° and 180° , are of roughly 40-nsec duration and correspond to approximately 6° peak phase error. These transients are affected by the bandwidth of the input signal and the video filter. A calculation based on the measured impulse response of the video filter (which assumed a perfect section of sine wave as an input pulse) would appear to indicate an irreducible minimum transient of the same duration but of one-half to one-third the amplitude actually observed.

The phase detector may be converted to an amplitude detector which has limited dynamic range, but which is nevertheless useful when only low-level inputs are available. This conversion is accomplished by orienting both diodes in the phase detector in the same direction (Fig. 2-147) and by supplying a bias current of 7.5 ma DC to the reference input connector. The output pulse obtained in this fashion is shown in Fig. 2-147.

PART 3
SUPPORTING STUDIES

CHAPTER I
MUTUAL COUPLING IN LARGE ARRAYS

SUMMARY

J. L. Allen

This chapter recounts the activities engaged in during the reporting period that were directed toward a better understanding of the effects of mutual coupling in large arrays.

The first section deals with theoretical inquiries into the question of minimizing the effects of coupling in large arrays of regularly spaced, identical radiators, or, more specifically, of minimizing the change in element impedance with array beam-pointing angle. It is proven that a constant-impedance, single-mode antenna element is fundamentally impossible. Furthermore, if one is interested only in the aggregate effects of coupling, such as the array gain and the impedance variation of interior elements of an array with beam-pointing angle (as opposed to concern about the exact nature of coupling between two antennas as a function of spacing), it is established that any optimum element has only slightly less mismatch with scan than the performance attainable by using (in an optimum manner) thin dipoles situated above a ground plane.

The second section deals with the experimental and analytical analysis of the effects of coupling on an array of unequally spaced dipoles. It is shown that (a) the patterns which result in practice differ markedly from those predicted if mutual coupling is ignored, but agree reasonably well with those predicted when coupling is included; (b) when the beam is scanned, the actual sidelobe structure changes in a more complex manner than would be the case with an equally spaced array, and this change is not predicted if mutual coupling is ignored and (c) the gain of this particular array as a function of scan angle is only about 1/4 db less than that of an equal-length, amplitude tapered array. Roughly speaking, the effect of the coupling in unequally spaced arrays is to partially counteract the unequal spacing effect on the pattern for pointing angles near broadside (i.e., to "flatten" the illumination) and to increase the taper for wide scanning angles.

A. INTRODUCTION

The aim of the mutual coupling studies conducted as a part of this project is to provide a better understanding of what might be called the "aggregate effects" of coupling in arrays and the degree to which they differ for different types of radiators. Specifically, we are interested in the questions of the variation in the gain of a large array with scan angle and the variation in the impedance of a typical element with scan angle. The details of the coupling between individual elements are viewed as only a means to an end, albeit an important and interesting one. The questions that we would ultimately like to be able to answer are: (1) the degree to which the aggregate effects of coupling are dependent upon the type of radiator used and (2) the quantitative magnitude of the aggregate effects to be expected.

To provide some quantitative insight into the aggregate effect of coupling for a particular type of radiator as a function of a few variable parameters, we have previously analyzed linearly

polarized arrays of dipoles above a ground screen.*† We now wish to acquire the same degree of understanding with respect to other possible array radiators. Unfortunately, direct mathematical analysis of the coupling between more structurally complex radiators does not appear practical, but two alternative approaches suggest themselves.

The first approach is to resort to an experimental program and measure the effects of interest in small arrays of a hopefully representative selection of radiators. While we intend to conduct such an investigation (see Sec. B-6), a purely experimental approach is loaded with the pitfalls of "incorrectly interpreting incomplete data taken improperly." To help preclude such difficulties, some analytic investigation is certainly desirable. Since a direct attempt to describe mathematically the coupling between specific elements (in the manner of Carter's equations‡ for thin dipoles) is probably futile, it appears that the most probable avenue to improved theoretical understanding of coupling effects lies in the direction of our specific interest: examination of the aggregate effects of coupling without reference to detailed mechanisms. To this end, we have been investigating analytically the questions of array gain and array directivity as a function of array beam-pointing angle. Some interesting results have been obtained (see Secs. B-4 and B-5) that appear to shed some light on the degree to which different radiators may differ in impedance characteristics, and on the minimum impedance variation with scan angle that may be realizable.

Finally, we have extended some previous work§ on the effects of coupling on arrays of unequally spaced dipoles. Computed patterns as a function of beam-pointing angle on a 10-dipole array are presented. It is shown that they cast some doubt on the utility of unequal spacing (as opposed to "density tapering"¶ in which the elements are equally spaced but the drives omitted from some) as a means of shaping the beams from scanned arrays of closely spaced elements.

B. BASIC INVESTIGATIONS

J. L. Allen

1. The Gain-Directivity Discrepancy for a Constant Impedance Element

It has been established previously♦ that the gain measured at the peak of the main beam of a large, regularly spaced array of identical radiators, "fed" in such a manner that the elements do not mutually couple through the feed structure, can be expressed as

$$G(\varphi_{00}, \theta_{00}) = g(\varphi_{00}, \theta_{00}) \eta N \quad (1)$$

where $\varphi_{00}, \theta_{00}$ are spherical coordinates that define the pointing direction of the main beam (see Fig. 3-4), N is the number of elements in the array and η is the array taper efficiency ($\eta \leq 1$). The function $g(\varphi_{00}, \theta_{00})$ is the "element gain function";♦ the gain as a function of angle

* J. L. Allen, et al., "Phased Array Radar Studies, 1 July 1960 to 1 July 1961," Technical Report No. 236 (U), Lincoln Laboratory, M. I. T. (13 November 1961), ASTIA 271724, H-474.

† J. L. Allen, "Gain and Impedance Variations in Scanned Dipole Arrays," Trans. IRE, PGAP AP-10, 566 (1962).

‡ J. D. Kraus, *Antennas* (McGraw-Hill, New York, 1950), Ch. 10.

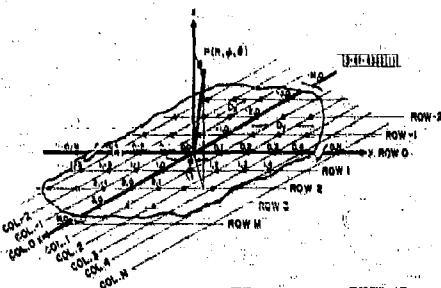
§ J. L. Allen and W. P. Delaney, "On the Effect of Mutual Coupling on Unequally Spaced Dipole Arrays," Trans. IRE, PGAP AP-10, 784 (1962). [Note: Figs. 2 and 3 of this paper are interchanged.]

¶ R. E. Willey, "Space Tapering of Linear and Planar Arrays," Trans. IRE, PGAP AP-10, 369 (1962).

♦ TR-236, pp. 299-306.

♦ See, for example, TR-236, pp. 206-209.

Fig. 3-1. Generalized planar array geometry.



of a "typical" element measured in the array environment with all other elements terminated in their normal generator impedance.

It is important to note that the above result is based upon defining gain to involve the ratio of the power density at the peak of the main beam to the total power available from the transmitter. Thus, any mismatches in the array result in a lowered gain, and the array gain definitely depends upon both the array pattern and the array impedance properties.

It is necessary to draw a careful distinction here between the array gain $G(\varphi_{00}, \theta_{00})$ and the array directivity $U(\varphi_{00}, \theta_{00})$.^{*} The latter involves the ratio of the power density at the peak of the main beam at $\varphi_{00}, \theta_{00}$ to the total power radiated; consequently, it is completely specified by the array far-field pattern magnitude.

It is shown in Appendix A [Eq. (A-10)] that the directivity of an array, with the main beam pointed in the $\varphi_{00}, \theta_{00}$ direction and with grating lobes at angles $\varphi_{lk}, \theta_{lk}$, satisfying Eq. (A-3) of the appendix, is[†]

$$U(\varphi_{00}, \theta_{00}) = \frac{4\pi D_x D_y}{\lambda^2} \eta N \frac{1}{\sum_k \frac{g(\varphi_{lk}, \theta_{lk})}{g(\varphi_{00}, \theta_{00})} \frac{1}{\cos \theta_{lk}}} \quad (2)$$

where, using Eq. (A-7) we have replaced the element pattern ratio of Eq. (A-3) by the gain function ratio for later utility. The elements are assumed to be placed on a rectangular grid D_x by D_y in this notation, but this restriction is not fundamental.

If we reflect upon the significance of the difference in definitions of gain and directivity, it is noted that if the array is assumed lossless (an assumption that will be used tacitly hereafter), the array directivity and gain can differ only as a result of losses due to impedance mismatches with the directivity representing an upper bound on gain. Comparing Eqs. (1) and (2), we see that this implies a fundamental constraint on the shape of the gain function:

^{*} Throughout this section, we will reserve upper case G and U for array gain and directivity, respectively, and lower case g and u for element gain and directivity, respectively (as determined in a passively terminated array).

[†] For angles for which no grating lobes exist, Eq. (2) reduces to the familiar

$$U(\varphi_{00}, \theta_{00}) = 4\pi \frac{D_x D_y}{\lambda^2} \eta N \cos \theta_{00}$$

$$g(\varphi_{00}, \theta_{00}) \leq 4\pi \frac{D_x D_y}{\lambda^2} \frac{1}{\sum_k \frac{g(\varphi_{0k}, \theta_{0k})}{g(\varphi_{00}, \theta_{00})} \frac{1}{\cos \theta_{0k}}} \quad (3)$$

If one could realize an element that maintained a constant impedance over some prescribed beam-pointing angles, the array gain and directivity would be equal for all scan angles and, for this element, Eq. (3) would be an equality. At first glance, one might conclude that such an element need satisfy Eq. (3) as an equality only over the range of angle that one intends to scan. However, if we remember that the mechanism that causes the apparent element impedance variation associated with mutual coupling is the coupling into an antenna of the resultant field from surrounding radiators, then it is nonsensical to suggest the existence of an element that either does or does not couple to this field, depending upon the phase difference between neighboring antennas (i.e., the beam-pointing angle). Consequently, we must seek an element that undergoes no change in impedance for any beam-pointing angle, including angles which produce grating lobes for the element spacing used. It follows from Eq. (3) that the gain function of this "ideal" element must be

$$g(\varphi_{00}, \theta_{00}) = \frac{4\pi D_x D_y}{\lambda^2} \frac{\cos \theta_{00}}{n(\varphi_{00}, \theta_{00}, D_x, D_y)} \quad (4)$$

where $n(\varphi_{00}, \theta_{00}, D_x, D_y)$ is the number of grating lobes in real space that an array with a D_x by D_y element grid allows when the main beam of the array is pointed in the $\varphi_{00}, \theta_{00}$ direction.

However, since Eq. (4) specifies the value of the element pattern over all space, the equation can be used to determine the element pattern directivity as well as the gain.

For example, if we concentrate our attention temporarily on an array with $D_x = D_y = \lambda/2$ (for ease of mathematical manipulation), there is only one major lobe for any scan angle, and Eq. (4) indicates that the value of the gain function in the broadside direction must be, numerically,

$$g(0, 0) = \pi \quad (5)$$

for an element matched for maximum array gain when the beam is pointed at broadside. Furthermore, Eq. (4) implies that the variation with angle of the element pattern of any constant impedance element must be*

$$|f(\varphi, \theta)| = \sqrt{\cos \theta} \quad (6)$$

By the definition of directivity, the broadside directivity of an element above an infinite ground plane is

$$u(0, 0) = \frac{g(0, 0)}{\frac{1}{4\pi} \int_0^{2\pi} \int_0^{\pi/2} g(\varphi, \theta) \sin \theta d\theta d\varphi} \quad (7)$$

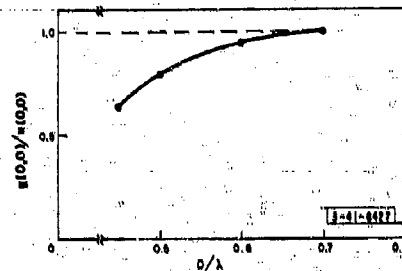
and one finds that an element with a power pattern given by $\cos \theta$ must have an element directivity at broadside of

$$u(0, 0) = 4 \quad (8)$$

* It would seem that any such element must have circular symmetry since the pattern has no ϕ dependence.

Thus, it is seen that the element gain must be less than the element directivity for half-wavelength spacing. Furthermore, it is obvious that the discrepancy will increase for spacings of less than a half-wavelength, since Eq. (4) indicates that the gain will decrease as the product $D_x D_y$, whereas the directivity will remain that of a $\cos \Theta$ power pattern, as given by Eq. (8). Finally, the directivity implied by (4) has been calculated for spacings greater than a half-wavelength by numerical integration for a square element grid in the range where at most one grating lobe can exist: $1/2 \leq D_x = D_y \leq 1/\sqrt{2}$. Figure 3-2 shows a plot of the calculated directivity at broadside $\Theta_{00} = 0$ compared with the gain function value at that angle. It is apparent that the discrepancy continues to exist for spacings of interest for wide-angle scanning (the significance of the apparent vanishing of the discrepancy at $1/\sqrt{2}$ spacing has not been pursued).

Fig. 3-2. Plot of the ratio of the broadside element gain function to the broadside element pattern directivity for fictional "constant impedance element" for $D_x = D_y = D$.



The existence of this discrepancy certainly seems to cast doubt upon the validity of the assumption of the existence of a "constant impedance element." However, before rejecting the idea completely, we must examine more closely the implications of the discrepancy.

2. An Examination of the Implications of the Discrepancy

The implication of the discrepancy between the gain and directivity of an element that we postulated to have no mismatch with variation of array phasing (beam-pointing angle) can be made apparent by re-examining our assumptions and our definitions of terms. In order to equate Eqs. (1) and (2), in addition to assuming lossless antennas and feeds, it was necessary to assume that all the power from the array transmitters was radiated and no mismatches existed under the condition that the entire array was radiating.* On the other hand, the element gain function is determined by passively terminating all the elements except the one in question, and exciting that one. Thus, the implication of the discrepancy begs an explanation based upon the difference between the two conditions: (1) all the elements radiating and (2) one element radiating, all others passively terminated.

One possibility, as cited above, is that the apparent impedance of the antenna must differ under the two conditions of interest and that our assumption of a constant impedance element violates fundamental laws. That is, when all the elements are radiating, a wave is coupled into any particular element and travels backward toward the generator. To cancel this wave and eliminate the loss in radiated power it represents, it is necessary to set up a reflection from the

* The assumption of an infinite array, implicit in this argument, implies that there is no discernible illumination taper, other than the linear pointing phase, across any finite section of the array. Thus, illumination tapering effects would be eliminated.

element with respect to its own generator (leading to the commonly used concept that the element impedance changes with the excitation of the surrounding elements). While this reflection "fixes" the element in the presence of the others (for one particular value of coupled field) so that the element appears matched under these conditions, it is obvious that turning off the other element generators, as one would do to measure the element gain function, will again make the element appear mismatched, and this would cause some loss of available power due to reflection in the excited element. In addition, still more available power is lost in the termination of these inactive elements because of the parasitic excitation of other elements. The results of these two types of losses (which are both really due to the same mechanism and, therefore, must always co-exist) is that only a fraction of the available power is radiated into space when a single element is excited. This can account for a gain-directivity discrepancy.

For any element for which this mechanism does account for the discrepancy, it is obvious that the apparent element driving impedance in the array must vary with scan angle. This follows from the fact that there must be power from the other radiators coupled into the element to establish the discrepancy, and the total field in the vicinity of one radiator due to the others certainly varies with the array phasing (pointing angle).

A question of fundamental importance is: "Are there other phenomena that can lead to a gain-directivity discrepancy without requiring an element impedance that varies with scan angle?"

It has been suggested, for example, that the use of traveling-wave antennas, with the possibility of a directional coupling^{*†} phenomena, could lead to less element impedance variation with scan angle than is incurred with such resonant antennas as dipoles. An equivalent circuit for two such radiators might be as indicated in Fig. 3-3. However, it does not appear that any directional coupling mechanism can account for a gain-directivity discrepancy under the usual assumption that the result of directional coupling is the rescattering (not the absorption) of power coupled from adjacent elements. Rescattering alone certainly cannot alter the element gain vs directivity characteristic, since it is not a loss mechanism. Therefore, it would appear that two

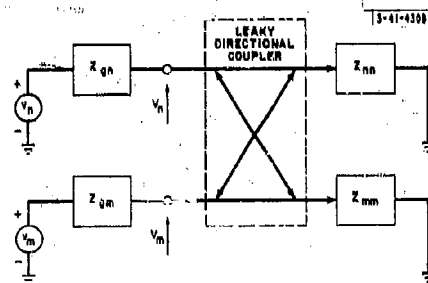


Fig. 3-3. Equivalent circuit for independently driven traveling-wave antennas.

* G. E. Mueller and W. A. Tyrell, "Polyrod Antennas," *BSTJ* **26**, 387 (1947).

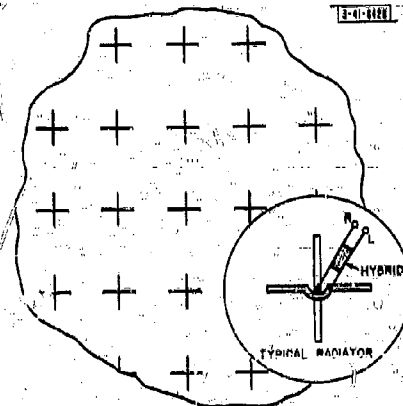
† J. L. Allen, et al., "Phased Array Radar Studies, 1 July 1959 to 1 July 1960," Technical Report No. 228 (U), Lincoln Laboratory, M. I. T. (12 August 1960), ASTIA 249470, H-335.

‡ W. E. Rupp, "Coupled Energy as a Controlling Factor in the Radiation Patterns of Broadside Arrays," *Abstracts of the Eleventh Annual Symposium, USAF Antenna Research and Development Program, University of Illinois, Monticello, Illinois, 16-20 October 1961.*

elements having essentially the same gain-function shape must have approximately the same variation in mismatch (more precisely, reflection coefficient magnitude) with scan angle in a planar array, even if one is a traveling-wave antenna and the other a dipole, for example. (Note that we are making a statement regarding only the aggregate effect of the coupling of many elements, and not the details of the coupling between, for example, two isolated elements.)

A phenomenon has been pointed out recently* that does appear capable of causing a gain-directivity discrepancy peculiar to circularly or elliptically polarized elements and that may allow an element to have essentially the same impedance in free space and in an array of active elements (at least when the array is phased for broadside radiation). However, this constancy of impedance is paid for in terms of significant element depolarization.

Fig. 3-4. Segment of planar array of crossed dipoles arranged to radiate nominally circularly polarized radiation. L indicates terminal that radiates left-hand circular polarization; R indicates terminal that radiates right-hand circular polarization.



This effect can be illustrated by analyzing the behavior of an array of circularly polarized radiators, as, for example, the array of hybrid-coupled dipoles, indicated schematically in Fig. 3-4. If each linear component of the circular polarization is considered separately, inspection will show that when all the elements are excited in phase, vertical dipoles couple only to vertical dipoles and horizontal dipoles couple only to horizontal dipoles. If we now consider all elements except the center element radiating left-hand circular polarization, the power mutually coupled into the center element will appear at the radiator port appropriate to radiate right-hand circular polarization, as illustrated by Fig. 3-5. By virtue of this difference in the terminal associated with the radiated and the mutually coupled power, it would appear possible to place a circularly polarized radiator in an array of similar radiators with little change in element driving impedance, at least when the array is phased for broadside.

However, mutual coupling is still working to diminish the gain of an element. If the right-hand circular port is terminated, power is lost in that termination, lowering the value of the element gain function at broadside. If the terminal is left unmatched, an orthogonal component of radiation is generated that will vary in amplitude with array-pointing angle, producing a

*L. J. Parodi and R. W. Kraut, "Mutual Effects Between Circularly Polarized Elements," Antenna Arrays Section of the Abstracts of the Twelfth Annual Symposium, USAF Antenna Research and Development Program, University of Illinois, Monticello, Illinois, 16-19 October 1962.

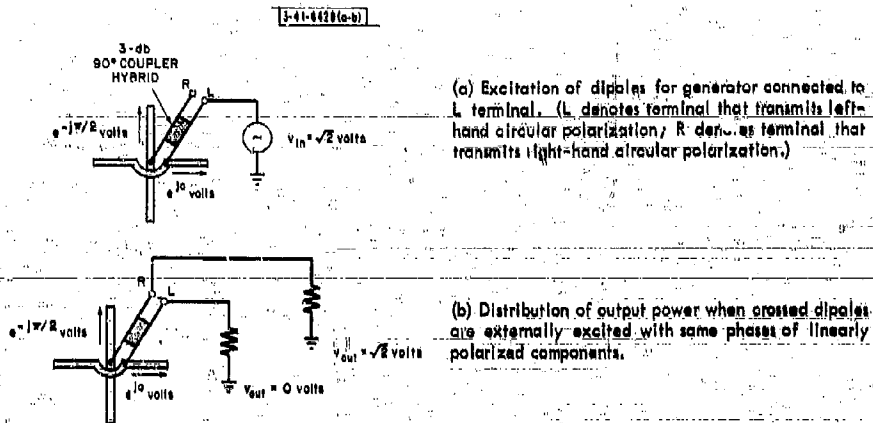


Fig. 3-5. Illustration of difference in excited terminals depending upon origin of excitation.

polarization loss varying with scan angle, and consequent gain reduction. To prevent this loss, one must mismatch the individual radiators in such a manner that the power coupled into the right-hand circular terminal is exactly canceled by a reflection from the dipoles in a manner similar to the matching technique normally used with linearly polarized antennas. This method of canceling the cross-polarized radiation (which obviously works correctly at only one particular angle) leads again to element impedance that is different when all the elements are excited compared with the case where all elements but one are passively terminated, and we are "back where we started" with a gain-directivity difference due (at least partly) to element-impedance variation.

This polarization effect, rather than a directional coupling mechanism, might explain the low coupling that has been observed between pairs of elements such as log-periodics* and helices,† i.e., experiments have indicated that there is little effect on the impedance of one element when another excited element is brought nearby. Rather than being the consequence of the fact that these are traveling-wave antennas and may function as if coupled by a leaky directional coupler, the low element-to-element coupling may be due to the polarization properties of such elements. A helix is a circularly polarized element, and the forms of log-periodics investigated seem to be at least elliptically polarized. Therefore, these radiators may behave as elliptically polarized radiators with reactive terminations (actually, no termination) on one sense of circular polarization. By the foregoing reasoning, mutual coupling effects would tend to be manifested as a depolarization rather than as an impedance change, at least for a broadside array. Unfortunately, the previous studies did not attempt to coordinate element polarization and element impedance properties.

* TR-236; also W. E. Rupp, *op. cit.*

† A. R. Stratoti and E. J. Wilkinson, "An Investigation of the Complex Mutual Impedance between Short Helical Array Elements," *Trans. IRE, PGAP AP-7*, 279 (1959).

In summary, it seems reasonable to suspect from the gain-directivity discrepancy that a constant-impedance element can be had (if at all) only by introducing some mechanism which converts all mutual coupled power into a mode orthogonal to that which couples to the element generator, such as the "opposite-sense-circular" coupling described above. Furthermore, at least in this case, achieving maximum array gain does not permit the waste of this orthogonal power; while reradiating it causes undesirable effects in itself. Attempting to correct these effects leads again to an element which exhibits variable impedance with scan angle.

It is logical, then, to seek some indication of the extent to which the impedance variation can be controlled (an "optimum" element in the sense of minimum mismatch over some range of scan angle). In the following investigation, we will not explicitly include the possibility of depolarization losses, but rather confine our attention to radiators for which the only loss phenomenon allowed is element mismatch.

3. The Gain-Directivity Discrepancy for Nonconstant Impedance Elements

In order to frame some general conclusion about the difference in aggregate mutual coupling effects in elements whose impedance varies with scan angle, let us examine the effect on the gain-directivity discrepancy if we permit the element impedances to vary with scan angle.

As a reference point, it will be assumed that we adjust the impedance of the generators driving the array elements so that the array is exactly matched when the beam is pointed at broadside. We will also assume $D_x/\lambda < 1$, $D_y/\lambda < 1$, so that only one major lobe exists for broadside radiation. Equality then applies in Eq. (3) for this angle, and

$$g(0, 0) = 4\pi \frac{D_x D_y}{\lambda^2}$$

That is, by suitable impedance matching, the magnitude of the gain function at broadside for an element with varying impedance can be made equal to that of the "constant impedance" element of the previous section.

However, since the element impedance varies with scan angle, the array gain must be less than the gain of an array with constant impedance elements for outer angles; thus, the gain function for a variable impedance element cannot be numerically greater at any angle than that of a constant impedance element, and will be less for all angles except those for which the array is matched (which we designate as the angle $0, 0$). Thus, the gain function of the variable impedance element which has been matched at broadside will not be as broad as a "constant impedance" gain function; consequently, the directivity of a variable impedance element in an array must be greater than that of a constant impedance element.

For example, consider a large array where $D_x = D_y = \lambda/2$. No grating lobes exist for any scan, and Eq. (3) can be written as an equality since the inequality is a result of mismatch loss, $1 - |\Gamma|^2$. Therefore, we can write

$$g(\theta_{00}, \theta_{00}) = 4 \cos \theta_{00} [1 - |\Gamma_a(\theta_{00}, \theta_{00})|^2] \quad (9)$$

where $\Gamma_a(\theta_{00}, \theta_{00})$ is the reflection coefficient associated with a typical element of an array as a function of the array beam-pointing angle when the entire array is excited. The assumption that the element is matched at broadside imposes the constraint

$$\Gamma_a(0, 0) = 0$$

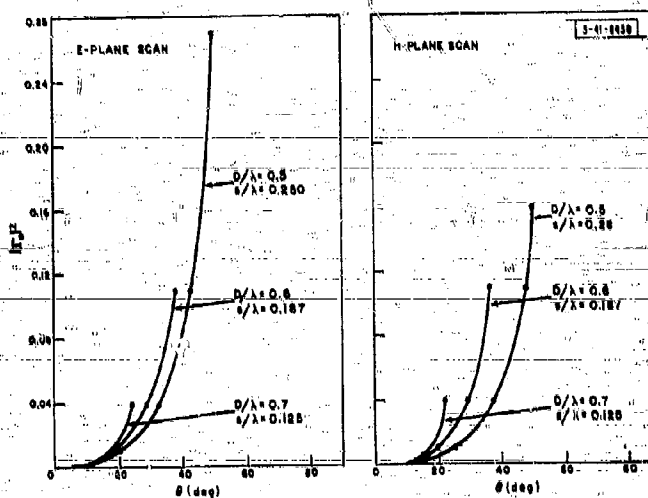


Fig. 3-6. Ratio of power reflected to power available ($|\Gamma_{\theta}|^2$) vs scan angle.

Substitution of Eqs. (9) and (7) leads directly to the conclusion that the gain-directivity discrepancy not only exists for variable impedance elements, but will increase with the degree of integrated impedance variation with scan. Therefore, we see that for any element, the inequality

$$\frac{g(0,0)}{u(0,0)} < \frac{\pi}{4} \approx 0.786 \quad (11)$$

follows from Eqs. (5) and (8), with the magnitude of the discrepancy proportional to the integrated (over all space) value of $|\Gamma(\varphi_{00}, \theta_{00})|^2 \cos \theta_{00}$, as indicated by Eqs. (8) and (10).

While this fact does not seem to lead directly to a measure of the impedance performance of an optimum element, let alone its configuration, it does provide a standard against which known elements can be compared. In fact, by comparing a known element, it is possible to infer certain bounds on the performance of an optimum element.

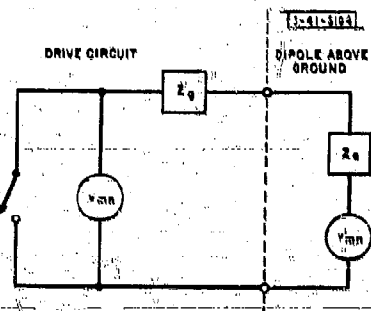
4. The Magnitude of the Gain-Directivity Discrepancy for Dipole Radiators Above a Ground Plane

An element available for comparison is a thin, half-wavelength dipole, mounted above a ground plane. From previous studies⁸ the curves (Fig. 3-6) can be generated for the reflection coefficient incurred by scanning in the two principal planes of dipole arrays with various square-element grids, when the dipoles are mounted at approximately the optimum[†] height above the ground plane for each spacing. It is apparent that for minimum VSWR (but not necessarily minimum numbers of elements), a spacing of $\lambda/2$ should be used. Let us examine how the gain-directivity ratio of a dipole in an array with half-wavelength spacing at its optimum height ($s = \lambda/4$) compares with the limiting value of Eq. (11).

*TR-236, Fig. 3-31, p. 233; Figs. 3-35 and 3-36, p. 235.

†TR-236, Fig. 3-21, p. 224.

Fig. 3-7. Equivalent circuit of dipole and drive circuit.



We will assume each element to be independently driven by a voltage generator of internal impedance Z_g (Fig. 3-7). The generator on the right accounts for any mutually coupled voltage going into the dipole. The notation Z_a represents the impedance of a single isolated dipole $\lambda/4$ above ground. It will be assumed that only one element is driven - specifically, the center element ($m = n = 0$) of a large array having the geometry shown in Fig. 3-1. All other elements are passively terminated by closing the shorting switch. Only "first order" coupling will be considered, i.e., it will be assumed that the only coupling of significance to the m th element is that between it and the driven element. (The error introduced by neglecting higher-order coupling should be negligible, as will become apparent from the numbers involved.)

Under the assumption of lossless elements, the gain-directivity ratio of an element is numerically equal to the ratio of the power radiated into distant space by the element (when all others are passively terminated) to the power available from the generator of the active elements. Two mechanisms reduce the ratio to less than unity: (1) the reflected power absorbed in the generator resistance of the driven element arising from the mismatch that appears when the other elements are turned off and (2) the power coupled into the parasitically excited element feeds and absorbed in their termination.

The two losses are easily computed by circuit theory. Expressed in the form of ratios to the power available from the driven element generator, the ratio of power absorbed in the driven element is

$$\frac{P_d}{P_a} = 1 - \frac{\left[1 + \operatorname{Re} \frac{Z_M(0,0)}{R_a} \right]}{\left| 1 + \frac{Z_M^*(0,0)}{2R_a} \right|^2} \quad (12)$$

where R_a is the real part of the self-impedance Z_a , and $Z_M(\varphi_{00}, \theta_{00})$ is that part of the impedance of an active element (array phased to point the beam in that $\varphi_{00}, \theta_{00}$ direction) that is due to mutual coupling. Re denotes the real part of the quantity. Explicitly,

$$Z_M(\varphi_{00}, \theta_{00}) = \sum_{m,n \neq 0} Z_{mn,00} \exp[jk(mD_x \sin \theta_{00} \cos \varphi_{00} + nD_y \sin \theta_{00} \sin \varphi_{00})] \quad (13)$$

where $Z_{mn,00}$ denotes the mutual impedance between the m th element and the center element. The notation $m, n \neq 0$ implies the term $m = n = 0$ is excluded from the summation (a derivation

of Eq. (13) is given in TR-236, pp. 209-240). The fractional power dissipated in the parasitically excited elements is found to be

$$\frac{P_p}{P_a} = \frac{\left[1 + \operatorname{Re} \frac{Z_M(0,0)}{R_a}\right]^2 \sum_{m,n \neq 0} \left|\frac{Z_{mn,00}}{2R_a}\right|^2}{\left|1 + \frac{Z_M^*(0,0)}{2R_a}\right|^2 \left|1 + \frac{Z_M^*(0,0)}{2R_a}\right|^2} \quad (14)$$

In TR-236,[†] it is established that for thin, half-wavelength dipoles spaced on $\lambda/2$ centers $\lambda/4$ above ground, the following approximate numerical values apply:

$$Z_M(0,0) = 64.6 - j30.2$$

$$R_a = 85.7$$

The values (in ohms) of $Z_{mn,00}$ were scaled from computed[‡] data (Fig. 3-8) for the first two "rings" of elements surrounding the driven element. The values of $|Z_{mn,00}/2R_a|$ for each parasitic element are indicated in Fig. 3-9,[§] and the factor of Eq. (14) is found to be

$$\sum_{m,n \neq 0} \left|\frac{Z_{mn,00}}{2R_a}\right|^2 = 0.2749 \quad (15)$$

It is then found that

$$\frac{P_p}{P_a} = 0.227 \quad (16)$$

and

$$\frac{P_d}{P_a} = 0.090 \quad (17)$$

Thus, for these elements,

$$\frac{g(0,0)}{u(0,0)} = 1 - [0.227 + 0.090] = 0.683 \quad (18)$$

A comparison of this value with the bound calculated in Eq. (11) indicates that the $\lambda/2$ dipoles ($D_x = D_y = 0.5\lambda$) mounted $\lambda/4$ above ground have a gain-directivity ratio of 0.87 of the ideal value of $\pi/4$.

5. An Estimate of the Minimum Impedance Variation Realizable with Any Radiator

Having "pegged" the gain-directivity ratio of the dipole $\lambda/4$ above ground to be only a fraction (0.87) of the upper bound value of $\pi/4$, there remains the important question of the implication of

[†] TR-236, Fig. 3-31, p. 233.

[‡] Using Carter's equations, as given in J.D. Kraus, *op. cit.*

[§] The small numerical values of this quantity represent our justification for concerning ourselves with only "first order" coupling.

this result for the choice of elements to be used in an array. Specifically, if the dipole is not the optimum element (from a mismatch standpoint, at least) we ask: (a) What element is? (b) How good is the "best" element?

We can provide an approximate answer to the second question, which in turn leads to some inferences about the answer to the first.

Returning to the dipole, the ratio of total power lost to the available power when a single element was radiating was found to be

$$\frac{P_{\text{tot}}}{P_a} = \frac{P_r/P_a}{P_a} = 0.317 \quad (19)$$

whereas if we could approach a constant impedance element arbitrarily closely, we could have

$$\left. \frac{P_{\text{tot}}}{P_a} \right|_{\text{min}} = 1 - \pi/4 = 0.213 \quad (20)$$

It appears, therefore, that one could assess the best element-mismatch-behavior achievable by investigating the reduction in mutual impedances consistent with bringing Eq. (19) into better numerical agreement with Eq. (20) by use of the relationships between the mutual impedances and the losses, as specified by Eqs. (12) and (14). In particular, we will suppose that by some mystical process it is possible to scale all $Z_{mn,00}^\dagger$ by some complex constant β (this form of reduction is not, of course, unique or necessarily even possible; however, the magnitude of the effect obtained is such that a more carefully considered model seems of questionable value).

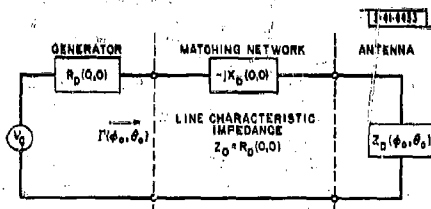


Fig. 3-10. Circuit for matching a radiator at broadside.

First, in order to limit the choice of β 's somewhat, we will assume that what we specifically desire to minimize is the reflection coefficient incurred in each element when the entire array is scanned to an equal angle in the two orthogonal principal planes. For an antenna with a matching circuit equivalent to that in Fig. 3-10, the reflection coefficient of a typical element as seen by its generator, for a beam-pointing angle φ_0, θ_0 is, by definition,

$$\Gamma(\varphi_0, \theta_0) = \frac{Z_D(\varphi_0, \theta_0) - Z_D(0, 0)}{Z_D(\varphi_0, \theta_0) + Z_D^*(0, 0)} \quad (21)$$

[†]The reader is reminded that $Z_{mn,00}$ is defined in terms of the coupling between antenna feeds. It is immaterial in this analysis whether the rescattered power from the parasitic elements is simply related to $Z_{mn,00}$ or not (it might not be if the elements couple directionally, for example); therefore the following argument appears valid for at least all linearly polarized radiators.

or, in terms of

$$Z_D(\varphi, \Theta) = Z_0 + \beta Z_M(\varphi, \Theta)$$

where $Z_M(\varphi, \Theta)$ is defined by Eq. (13),

$$\Gamma(\varphi_0, \Theta_0) = \frac{\beta Z_M(\varphi_0, \Theta_0) - \beta Z_M(0, 0)}{2R_a + \beta Z_M(\varphi_0, \Theta_0) - \beta^* Z_M^*(0, 0)} \quad (22)$$

Let us postulate that we wish to scan to 50° in both principal planes, and restrict allowable values of β to those which yield

$$|\Gamma(0, 50^\circ)| = |\Gamma(90^\circ, 50^\circ)|$$

From TR-236 (Fig. 3-31, p. 233) we see that, if we take $\varphi = 0$ as the E-plane of the array,

$$Z_M(0, 50^\circ) = (-36 - j57) \text{ ohms}$$

$$Z_M(90^\circ, 50^\circ) = (71 + j105) \text{ ohms}$$

$$Z_M(0, 0) = (61 - j30) \text{ ohms}$$

$$R_a = 86 \text{ ohms}$$

to slide-rule accuracy. Figure 3-11 shows computed plots of the principal plane reflection coefficients for $|\beta| = 3.0$ and 0.8 as a function of this phase of β .

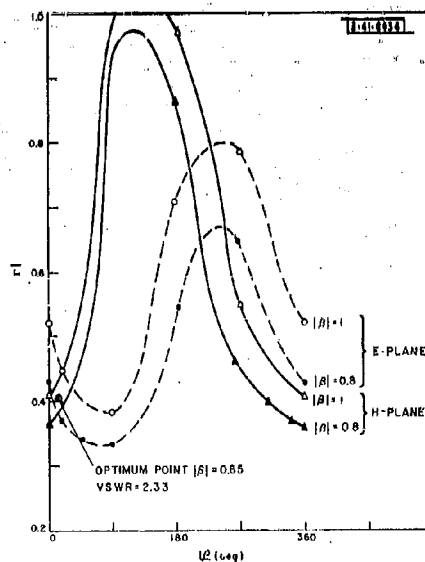


Fig. 3-11. Principal plane reflection coefficient magnitude vs mutual impedance modification factor β .

It can be seen that the E- and H-plane reflection coefficients are equal for two values of phases, with the value of the phase nearest zero clearly giving the minimum $|\Gamma|$ (the fact that $|\Gamma| > 1$ for some phases of β is perhaps an indication of the "constraints" that nature may place on realizable mutual impedances). A value of $\beta = 0.80$ [15°] was chosen for further examination as a value of β that might equalize the $|\Gamma|$'s. This value was inserted in Eqs. (12) and (14) and it was found that

$$\frac{P_d}{P_a} = 0.070$$

$$\frac{P_p}{P_a} = 0.15$$

Thus, for this fictitious reduced mutual coupling element,

$$\frac{P_{tot}}{P_a} = \frac{P_d + P_p}{P_a} = 0.22 \quad (23)$$

Comparison with Eq. (20) would appear to indicate that we should be able to reduce the mutual impedance and, hence, the losses still a bit further. It should be recalled, however, that we cannot actually expect to reach the value given by Eq. (20), because the actual element directivity is slightly increased by the mismatch with scan angle.

Thus, it appears certain that the mismatch associated with a complex mutual impedance reduction of 0.8 at an angle of about 15° (about 1.0 db reduction) represents a lower bound on achievable mismatch with scan angle of 50°. Figure 3-11 indicates that the appropriate value of $|\Gamma|$ is about 0.38, corresponding to an achievable VSWR at 50° of not less than 2.23.

6. Theoretical Conclusions and the Need for Experimental Support

From the data in Fig. 3-6 and the results of the preceding section, we can tentatively conclude that the VSWR behavior of the optimum element with scan would be approximately as indicated by the curve in Fig. 3-12. This curve approximately defines the minimum VSWR to be expected in scanning to equal angles θ from broadside in both principal planes for an optimum element.

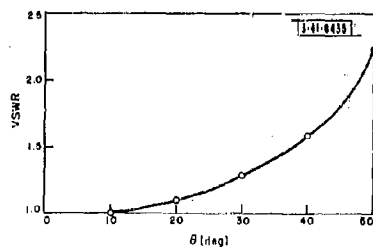


Fig. 3-12. Approximate minimum achievable VSWR for scanning to equal angles θ in both principal planes of a planar array.

Returning to the question of the performance of dipoles, it should be noted that the value $s = 0.25\lambda$ used in the calculations does not appear to be quite the optimum height above ground, but was the closest height to the optimum for which extensive data exist. Results of the previous

study indicate that the optimum for 50° scan is slightly greater than this value and results in a VSWR of about 2.4 in both planes - a value significantly near our lower bound.

One might even be tempted to speculate that there may be qualitatively little difference in the magnitude of the aggregate coupling effects realizable with most types of radiators commonly considered for wide-angle-scanning arrays (i.e., elements which have broad free-space element patterns or, alternatively, low free-space gain) if they are adjusted to provide maximum array broadside gain. However, this is a tentative conclusion that requires a carefully executed experimental program for confirmation. Particular attention must be paid to the qualification "realizable," since it is apparent from the foregoing studies* that one can easily and unwittingly fail to use any particular type of element in an optimum way (e.g., with dipoles, fail to choose the optimum dipole-to-ground plane spacing for the grid spacing used).

7. Future Plans for Investigation of Mutual Coupling Effects

Only with a better understanding of the coupling details associated with the various classes of elements can we be sure we are evaluating that class of element fairly in an experimental program. To achieve better understanding of coupling effects in circularly polarized radiators, an attempt should be made to analyze quantitatively an array consisting of infinitely thin, half-wavelength, crossed dipoles, fed in quadrature above a ground plane (Fig. 3-3). This study could be similar in scope to the one previously reported for linear dipoles in TR-236, except, of course, for the additional concern about depolarization. Such a study might shed light on the extent to which this effect may explain previous observations and lead to enhanced over-all understanding of mutual effects.

The only apparent stumbling block to such a study is the lack of tabulated mutual impedance data for "skewed" dipoles that are required to describe the coupling between orthogonal linear dipoles. This appears to pose no major difficulty, however, since the appropriate formulas are well known† and appear to be amenable to numerical integration.

In order to carry out a careful, meaningful, experimental investigation of coupling between complex elements without incurring the difficulties inherent in attempting to make accurate phase and amplitude measurements of loose coupling between parts of radiators, we plan to construct a small planar array to measure these aggregate effects directly. On the basis of our previous studies, a 7×7 array would appear to be large enough for reasonably accurate impedance determination on the center element. However, in order to avoid a complex structure, with variable phase shifters, it seems advantageous to utilize multiple beam-forming matrices. Consequently, we are in the process of procuring ten 8-input, 8-output, parallel-fed, simultaneous beam-forming matrices.‡§ The resulting 8×8 array will allow the determination of the element driving impedance at a sufficient number of scan angles to obtain smooth curves of the effects to be measured (a possible 64 points).

*TR-236, pp. 225; also in J. L. Allen, "Gain and Impedance Variations in Scanned Dipole Arrays," Trans. IRE, PGAP AP-10, 566 (1962).

†P. S. Carter, "Circuit Relations in Radiating Systems and Applications to Antenna Problems," Proc. IRE 20, 1004 (1932).

F. H. Murray, "Mutual Impedance of Two Skew Antenna Wires," Proc. IRE 21, 154 (1933).

‡J. Butler and R. Lowe, "Beam Forming Matrix Simplifies Design of Electronically Scanned Antennas," Electronic Design (12 April 1961), p. 170.

§J. P. Shelton and K. S. Kelleher, "Multiple Beams from Linear Arrays," Trans. IRE, PGAP AP-9, 154 (1961).

At the L-band frequency to be used, the matrix and its associated cables will be μ m small enough and light enough for portability. To obtain data on a wide range of element types, we hope to capitalize on this portability by offering our services to interested groups in the industry for "on-the-spot" element impedance vs scan determination on their arrays. These measurements could be made in exchange for permission granting us free use of the data collected in any unclassified context.

C. EFFECTS OF MUTUAL COUPLING ON AN UNEQUALLY SPACED DIPOLE ARRAY

J. L. Allen and
W. P. Delaney

We have recently reported* the effect of mutual coupling on the broadside pattern of an unequally spaced dipole array. In this section, we will report results for the off-broadside patterns of the same array.

The use of unequal spacing of equally excited antennas as a means of beam shaping has been the subject of several investigations.† The technique can be shown‡ to be capable of producing a close-in sidelobe pattern that is very nearly the Fourier transform of the density of the elements, under the common assumption that mutual coupling can be neglected. However, even under this assumption, one tends to lose control of the pattern farther out in the sidelobe region, the sidelobe level being primarily governed by the number of elements actually used. The loss in pattern control seems to become quite pronounced at an angle about halfway to the grating lobe position one would obtain from an array with equal element spacings corresponding to the closest element spacing of the unequally spaced array. Thus, for control of the bulk of the antenna pattern appearing in real space, it is apparent that some of the elements should be fairly closely spaced (e.g., on the order of half a wavelength). However, at such close spacing, mutual coupling is certainly quite strong.§

While mutual coupling is very strong in equally spaced arrays with close spacings, the effects of this coupling on the shape of the antenna pattern is not severe. This is due to the fact that in the regular environment afforded almost all elements by the equal spacing, the effects of mutual impedance are primarily to scale the pattern (vary the gain) in a nearly constant manner over the entire pattern. Put another way, virtually all the element patterns are identical and pattern multiplication is a satisfactory approximation.

However, this regular environment is not present in unequally spaced arrays, and it is apparent that the effects of coupling on an unequally spaced array can not be so easily treated.

To explore the severity of coupling effects on such arrays, we constructed a 16-element linear array of parallel dipoles, using a variable element spacing (Table 3-1). This spacing was calculated to produce a first sidelobe level of -23 db in the absence of coupling, with the beam pointed at broadside. The fact that the spacings are not quite symmetric about the array center results from a quirk in the computer program used to generate the spacings. Since the error is

* J. L. Allen and W. P. Delaney, *op. cit.*

† Recent papers which also include bibliographic references to other work include:

A. L. Maffett, "Array Factors with Non-Uniform Spacing Parameter," Trans. IRE, PGAP AP-10, 131 (1962).

M. G. Andreaen, "Linear Arrays with Variable Interelement Spacings," Trans. IRE, PGAP AP-10, 137 (1962).

‡ TR-236, pp. 291-298.

§ J. L. Allen, "Gain and Impedance Variation in Scanned Dipole Arrays," Trans. IRE, PGAP AP-10, 566 (1962).

Element Spacing*	Spacing (wavelength)
1-2	1.051
2-3	0.837
3-4	0.704
4-5	0.612
5-6	0.561
6-7	0.531
7-8	0.500
8-9	0.500
9-10	0.510
10-11	0.520
11-12	0.561
12-13	0.622
13-14	0.704
14-15	0.837
15-16	1.041

*Antenna elements are numbered from 1 to 16.

on the order of 1 to 2 percent, the asymmetry effects were not expected to be noticeable, which indeed proved to be the case. The resulting array is shown in Fig. 3-13; a close-up of one of the dipoles is shown in Fig. 3-14. Broadside patterns were taken on the array using a well-matched corporate feed with an impedance level chosen to match the impedance of an isolated dipole. This choice of impedance seemed likely to represent the best average match for all spacings (this assumption was not verified, however). Broadside patterns were taken and compared with the patterns computed, with mutual coupling neglected. The resulting discrepancy is shown in Fig. 3-15. Most notably, the first sidelobe levels were 8 to 10 db above those predicted, with a general tendency of the far-out sidelobes to range about 2 db above the level predicted. The pattern was then recomputed, taking mutual impedance into account by assuming that Carter's* thin-dipole coupling formulas would give a satisfactory approximation, and by using image theory. It was assumed that each antenna was independently driven by a voltage generator, with internal impedance equal to the conjugate impedance of a single, isolated dipole, one-quarter above a ground plane; i.e., the generator impedance was $85.7 - j72.5$ ohms. The resulting comparison is shown in Fig. 3-16, and it can be seen that the agreement is much better.

*J.D. Kraus, *op. cit.*



Fig. 3-13. Unequally spaced array.

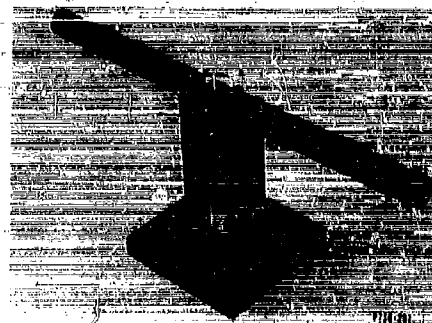


Fig. 3-14. Close-up of a typical dipole.

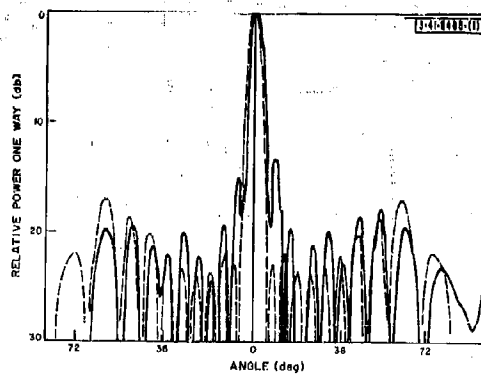


Fig. 3-15. Comparison of the measured pattern (solid line) and the pattern computed ignoring mutual coupling (dashed line).

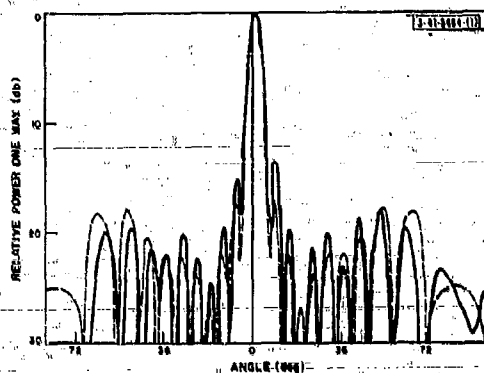


Fig. 3-16. Comparison of measured pattern (solid line) and pattern computed using Carter's equations for mutual coupling (dashed line).

One might at first surmise that the array spacings could be designed in a straightforward manner by taking mutual impedance into account. Certainly such an approach would be possible, but if the array is to be electronically scanned, still further problems arise. As one would expect, the patterns of the individual elements of the array, taken with all the other elements passively terminated (these patterns being the factor that weight the contribution of each element to the array pattern), vary markedly across the array. Figure 3-17 shows the element patterns of some of the first eight elements. Note that the gain of the outer elements in the region around broadside runs about 2.5 db above that of the center elements, increasing the contribution of the outer elements to the pattern and thereby tending to "flatten" the illumination of the array, thus explaining the increased close-in sidelobe level. However, the center element patterns are broader than the outer patterns, indicating that as the beam is scanned, angles will be reached where the center elements contribute more heavily on a per-element basis, and one would anticipate that the pattern would change markedly from that obtained near broadside, yielding lower sidelobes, lower gain and broader beamwidth.

To check this presumption quantitatively in an expeditious fashion, we investigated patterns by computation, including mutual effects, by using Carter's equation. No experimental verification was attained because of the phasing difficulties involved. However, on the basis of agreement in the broadside case, we feel that the computed patterns are reasonably accurate. The patterns for scan angles of up to 39° are shown in Figs. 3-18 through 3-25. We computed patterns under the independent generator assumption using the value of steering phase shift in the generator voltage appropriate in the absence of coupling. For reference, Fig. 3-26 shows the extreme pointing angle calculated when mutual coupling was ignored.

The computed data can be summarized as follows:

- (1) The first sidelobes generally decrease with increasing scan angle from -17 db for a broadside beam to a level of about -25 at the extreme scan angle of 39° . In addition, as one would anticipate even in the absence of mutual coupling, wide scan angles accentuate the high sidelobe level that exists far out in the pattern.

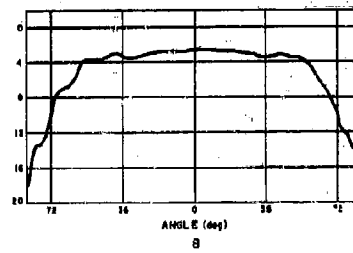
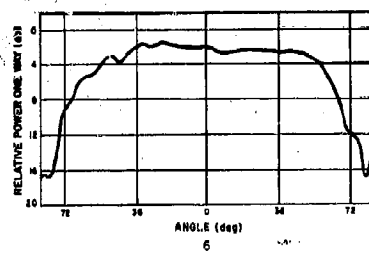
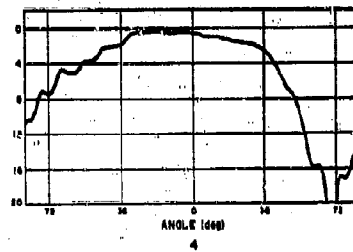
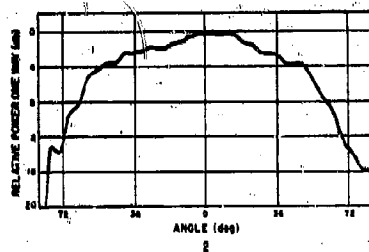
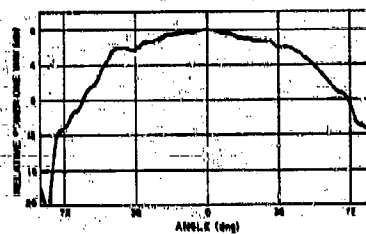
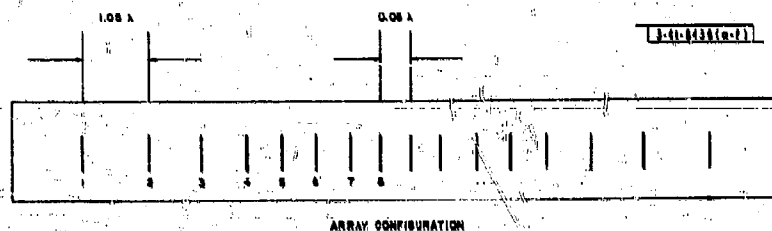


Fig. 3-17. Element patterns of some elements of the unequally spaced array.

Fig. 3-18. Beam 1 left.

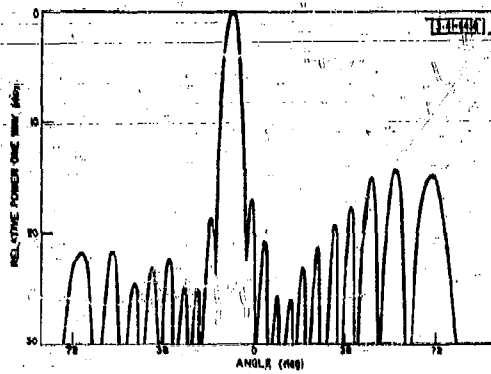
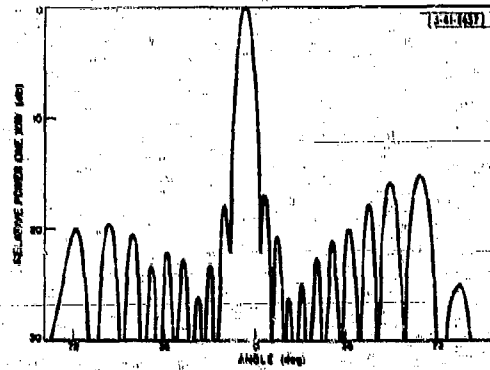
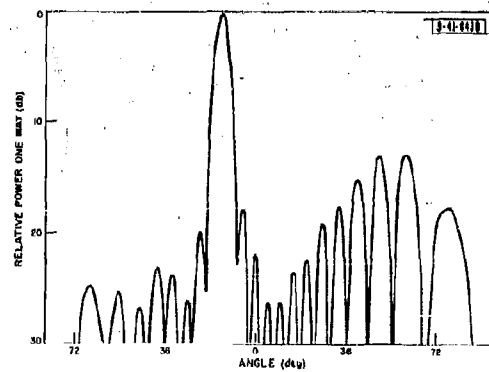


Fig. 3-19. Beam 2 left.

Fig. 3-20. Beam 3 left.



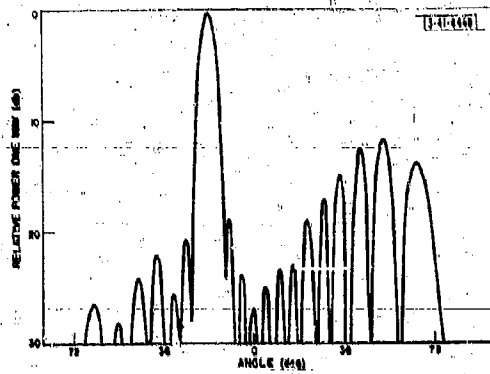


Fig. 3-21. Beam 4 left.

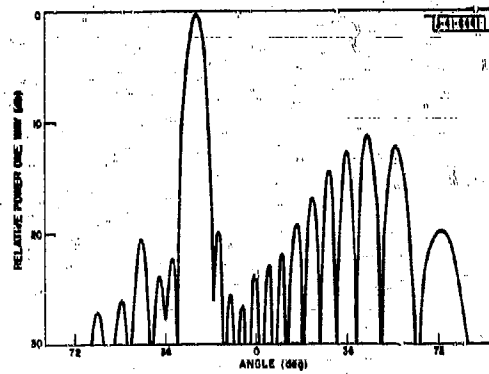


Fig. 3-22. Beam 5 left.

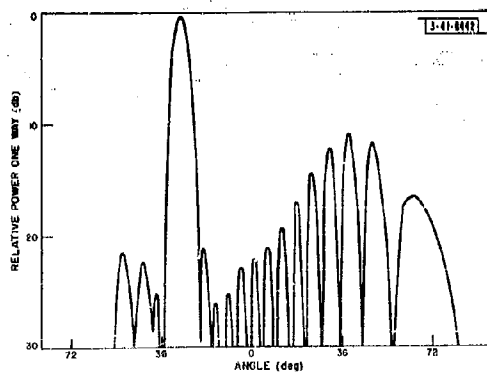


Fig. 3-23 Beam 6 left.

Fig. 3-24. Beam 7 left.

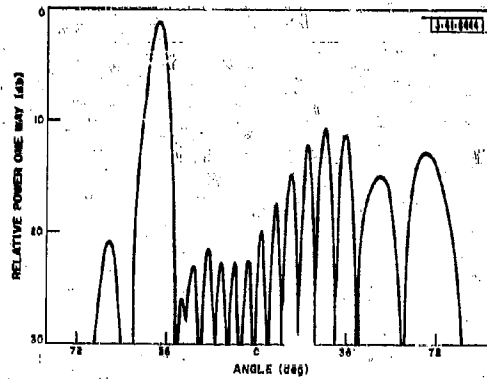
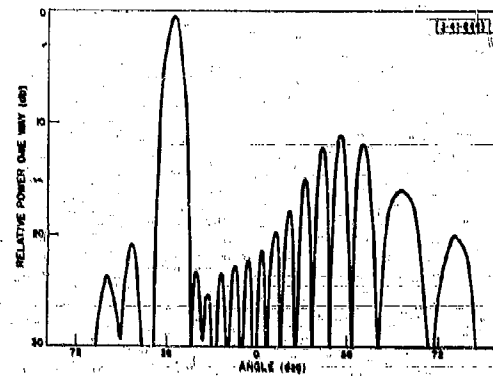
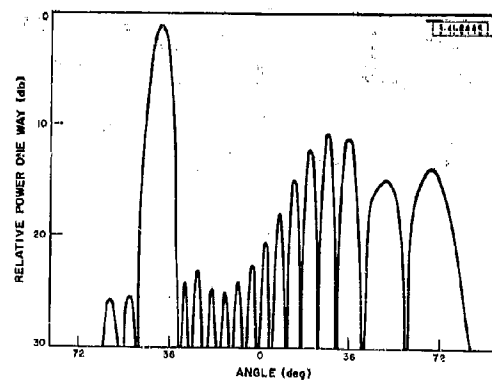


Fig. 3-25. Beam 8 left.

Fig. 3-26. Beam 8 left,
without mutual coupling.



- (2) The computed data showed a beamwidth that varied from the one predicted when coupling was ignored. The coupling narrowed the beamwidth by about 10 percent for pointing angles near broadside and increased it by about 10 percent over that predicted without coupling for a pointing angle of 39° .
- (3) The program was set up to actually compute the gain (taking impedance mismatch effects into account) as a function of scan angle. When the results are compared with the gain of an equivalent-length, half-wavelength-spaced array having the same dipole elements (which would require 22 elements), it is found that the unequally spaced array has an aperture efficiency of about 83 percent for all scan angles investigated; i.e., the efficiency at an angle θ from broadside was given by $83 \cos^2 \theta$. The gain of the equally spaced array was computed from previously calculated element gain functions for parallel dipole linear arrays.† For comparison, the maximum illumination efficiency attainable from a cosine-squared-on-a-pedestal pattern for a 17-db sidelobe level is 87 percent. Thus, the unequally spaced array is seen to be somewhat inefficient, but not seriously so.

In summary, mutual coupling appears to affect the performance of unequally spaced arrays markedly when the elements are in the half-to-one-wavelength spacing region (and presumably to a lesser extent for greater spacing). Perhaps the most annoying effect is that the pattern changes markedly with scan angle. It is apparent from this exercise that mutual effects must be considered in the design of such arrays using dipoles as radiators. Furthermore, on the basis of the results given in Sec. B, it seems likely that no other type of radiator will render the problem negligible.

* That is, the sum of the interelement spacing plus an additional length approximately equal to one outer element spacing (actually, the additional length should be equal to the spacing that would be used if another pair of elements were added; see TR-228, pp. 162-170).

† Unpublished calculations similar to those reported in TR-236 for planar arrays.

APPENDIX A

In this appendix we will derive an expression for the directivity of a large array of equally spaced, identical radiators. Although the geometry used (Fig. 1) is that of an array with elements placed on a rectangular grid, the results are applicable to any regular grid.

A convenient approximation to the pattern of an array is to consider the far-field $\bar{F}(\varphi, \theta)$ to be the product of a typical element pattern $\bar{f}(\varphi, \theta)$ measured on a single driven element in a passively terminated array, and the far-field pattern $A_c(\varphi, \theta)$ of a continuous aperture with a scalar illumination "equivalent" to the array illumination. In the geometry of Fig. 1, if the current in the m th element due to the generator attached to that element is I_{mn} , the "equivalent" continuous aperture illumination is $I(x, y)$, such that

$$I(x, y) = I_{mn} \quad (A-1)$$

to which $A_c(\varphi, \theta)$ is related by

$$A_c(\varphi, \theta) = \iint_{\text{aperture}} I(x, y) \exp\left\{j \frac{2\pi}{\lambda} (x \sin \theta \cos \varphi + y \sin \theta \sin \varphi)\right\} dx dy \quad (A-2)$$

In other words, we invoke the usual representation of the array far-field as the product of an "element factor" and an "array factor," except that we choose to approximate the latter with the pattern of a continuous aperture.

This approximation should be increasingly good as the array size increases if (1) the array amplitude taper is such that the bulk of the power in the pattern resides in the main lobe and near-in sidelobes (implying that the exact structure of the far-out sidelobes is of little consequence in any arguments concerning power density integrals) and (2) no grating lobes exist. The latter restriction is severe, but easily removable if the first is fulfilled. To cope with grating lobes, we merely consider the array factor to be the superposition of as many continuous aperture patterns as there are grating lobes. If $\theta_{lk}, \varphi_{lk}$ define the location of a major lobe of the array factor, given implicitly by the solutions of

$$\sin \theta_{lk} \cos \varphi_{lk} = \sin \theta_{00} \cos \varphi_{00} = \frac{l}{2\pi} \quad , \quad l = 0, \pm 1, \text{ etc.} \quad (A-3a)$$

$$\sin \theta_{lk} \sin \varphi_{lk} = \sin \theta_{00} \sin \varphi_{00} = \frac{k}{2\pi} \quad , \quad k = 0, \pm 1, \text{ etc.} \quad (A-3b)$$

($\theta_{00}, \varphi_{00}$ is the main-lobe pointing direction), then we can write*

$$\bar{F}(\varphi, \theta) \approx \bar{f}(\varphi, \theta) \sum_l \sum_k A_c(\varphi, \varphi_{lk}; \theta, \theta_{lk}) \quad (A-4)$$

where $A_c(\varphi, \varphi_{lk}; \theta, \theta_{lk})$ defines the scalar pattern at the general angle φ, θ , resulting from a continuous aperture with the appropriate amplitude taper and the proper linear phase to position

*The justification for a representation of this type is discussed in TR-228, pp. 162-166 for linear arrays, from which the planar case follows.

the pattern maximum at the angles $\varphi_{lk}, \theta_{lk}$; i.e., if $I(x, y)$ is the illumination producing a beam of the desired shape at the angle $\theta = 0$, the pattern $A_c(\varphi, \varphi_{lk}; \theta, \theta_{lk})$ is produced by an illumination

$$I_{lk}(x, y) = I(x, y) \exp[-j \frac{2\pi}{\lambda} (x \sin \theta_{lk} \cos \varphi_{lk} + y \sin \theta_{lk} \sin \varphi_{lk})] \quad (A-5)$$

The directivity of the pattern specified by Eq. (A-4) is then, by definition,

$$U(\varphi_{00}, \theta_{00}) = \frac{4\pi |f(\varphi_{00}, \theta_{00})|^2 \sum_{l,k} |A_c(\varphi_{00}, \varphi_{lk}; \theta_{00}, \theta_{lk})|^2}{\int_0^{2\pi} \int_0^{\pi/2} |f(\varphi, \theta)|^2 \sum_{l,k} |A_c(\varphi, \varphi_{lk}; \theta, \theta_{lk})|^2 \sin \theta \, d\theta \, d\varphi} \quad (A-6)$$

where the integration limits assume the elements to radiate only into half-space ($z > 0$). Note that the typical element pattern and the element gain function are related by

$$g(\varphi_{00}, \theta_{00}) = C |f(\varphi_{00}, \theta_{00})|^2 \quad (A-7)$$

where C is a constant of no consequence for our uses.

Equation (A-7) can be greatly simplified if we recall the assumption that the array illumination concentrates almost all the power density in $A_c(\varphi, \varphi_{lk}; \theta, \theta_{lk})$ in the region around $\varphi_{lk}, \theta_{lk}$. Consequently, in the numerator, only the $l=k=0$ term will be of significant amplitude. In the denominator, after squaring the double sum, we will have a quadruple sum of the form

$$\sum_k \sum_l \sum_m \sum_n A_c(\varphi, \varphi_{lk}; \theta, \theta_{lk}) A_c^*(\varphi, \varphi_{mn}; \theta, \theta_{mn})$$

Under our assumptions, "cross product" terms ($k \neq m, l \neq n$) will give a negligible contribution to the sum. Finally, if we assume that $|f(\varphi, \theta)|^2$ varies slowly with respect to $A_c(\varphi, \varphi_{lk}; \theta, \theta_{lk})$, we can write the resulting simplified directivity expression as

$$U(\varphi_{00}, \theta_{00}) = \frac{4\pi |A_c(\varphi_{00}, \varphi_{00}; \theta_{00}, \theta_{00})|^2}{\sum_l \sum_k \frac{|f(\varphi_{lk}, \theta_{lk})|^2}{|f(\varphi_{00}, \theta_{00})|^2} \int_0^{2\pi} \int_0^{\pi/2} |A_c(\varphi, \varphi_{lk}; \theta, \theta_{lk})|^2 \sin \theta \, d\theta \, d\varphi} \quad (A-8)$$

Note from Eqs. (3) and (5) that

$$A_c(\varphi_{00}, \varphi_{00}; \theta_{00}, \theta_{00}) = A_c(\varphi_{lk}, \varphi_{lk}; \theta_{lk}, \theta_{lk})$$

for all l and k . Thus, we can write

$$U(\varphi_{00}, \theta_{00}) = \frac{1}{\sum_l \sum_k \frac{|f(\varphi_{lk}, \theta_{lk})|^2}{|f(\varphi_{00}, \theta_{00})|^2} \left| \frac{\int_0^{2\pi} \int_0^{\pi/2} |A_c(\varphi, \varphi_{lk}; \theta, \theta_{lk})|^2 \sin \theta \, d\theta \, d\varphi}{4\pi |A_c(\varphi_{lk}, \varphi_{lk}; \theta_{lk}, \theta_{lk})|^2} \right|} \quad (A-9)$$

however, the term in braces is just the reciprocal of the directivity of scalar aperture producing a single beam in the $\varphi_{lk}, \theta_{lk}$ direction, which is well known* to be given by

$$U_s(\varphi_{lk}, \theta_{lk}) = \frac{4\pi A \eta}{\lambda^2} \cos \theta_{lk}$$

for an aperture of area A . Making use of this fact in Eq. (A-9) and converting to a discrete array by replacing A by $ND_x D_y$, we can reduce Eq. (A-8) to

$$U(\varphi_{00}, \theta_{00}) = 4\pi \frac{D_x D_y}{\lambda^2} \eta N \frac{1}{\sum_l \sum_k \left| \frac{U(\varphi_{lk}, \theta_{lk})}{U(\varphi_{00}, \theta_{00})} \right|^2 \frac{1}{\cos \theta_{lk}}} \quad (A-10)$$

For a single principal lobe, the element pattern cancels in the expression and we have the familiar result

$$U_0(\varphi_{00}, \theta_{00}) = 4\pi \frac{D_x D_y}{\lambda^2} \eta N \cos \theta_{00} \quad (A-11)$$

*S. Silver, Microwave Antenna Theory and Design, M. I. T. Radiation Laboratory Series, Vol. 12 (McGraw Hill, New York, 1949).

CHAPTER II A QUANTITATIVE EXAMINATION OF THE RADAR RESOLUTION PROBLEM

J. L. Allen

In order to design any type of radar most effectively, a fundamental quantitative understanding of the ability of radar to perform the principal functions of detection, resolution and measurement is a prerequisite. The first and last functions have been the subject of many excellent writings. The second, however, has been treated in only a few papers and the results reported therein seem either to stop short of usable quantitative results, or to predict resolution capability beyond what one would intuitively expect.

Consequently, some time was spent delving into the resolution problem, and a separate report* on the subject has been prepared. In this report, the ability of a radar to resolve overlapping signals is examined. It is shown that the primary limitation on resolution is the unpredictable difference between the actual received signal and the waveform for which the target receiver is matched (i.e., the distortion in the received signal).

The effects of signal distortion on the shape of the "ambiguity function" are examined in terms of a wideband random process model for the distortion. The statistics of the ambiguity function sidelobe region in the presence of the distortion are related in a simple manner to the statistics of the distortion process.

The optimum two-target resolver for the distorted signal is then derived and its performance is examined for two different conditions of a priori knowledge concerning the signal: (1) all parameters of both target returns known exactly, with only the presence or absence of the second target uncertain, and (2) the phase and amplitude of either or both returns unknown, but all other parameters exactly known. These two cases make evident the comparative seriousness of wideband distortion and lack of a priori knowledge. Probability of detection vs probability of false-alarm curves are derived for both cases.

The performance of two nonoptimum two-target resolvers that are simpler from a circuitry viewpoint than the optimum resolver is examined. Included in the nonoptimum resolver is the usual "matched" (to a single, isolated return) filter.

It is quantitatively demonstrated that for nearly complete overlap in time of the received waveforms from the two targets (even though for "compressed" signals the targets may be separated by more than the width of the main lobe of the ambiguity function), the resolvability of a small target in the presence of a large target tends to become independent of the radar sensitivity. Thus, for sufficiently large cross-section difference, resolution can be achieved only by lowering the ambiguity function sidelobe uncertainties, as one would intuitively expect. The optimum vs nonoptimum resolver performances differ primarily in the rate at which targets become resolvable with decreasing overlap.

*J. L. Allen, "A Quantitative Examination of the Radar Resolution Problem," Technical Report No. 281 (U), Lincoln Laboratory, M. I. T. (17 September 1962), ASTIA 295573.

CHAPTER III SHORT PULSE EFFECTS ON TRANSMITTER EFFICIENCY

M. Siegel

SUMMARY

This chapter presents a theoretical description of the losses that occur in modulated amplifiers during the video pulse rise and fall times. These losses can become a major fraction of the total losses if the transmitted pulsewidths are of the same order of magnitude as the rise time. An expression for the losses in the electron beam of the amplifier tube is derived and combined with an expression for the losses in parasitic capacity at the modulated element.

Results are presented for three classes of amplifier stages: plate modulated stages, low- μ grid modulated stages and high- μ grid modulated stages.

A. INTRODUCTION

Because of the increased attention currently being given to the multibeam resolution problem, the use of narrower and narrower pulses in pulse codes and pulse trains is becoming common. Phased array radars are being called upon to deal with these pulse trains, and the phased array transmitter efficiency is influenced by their nature. Three basic types of modulation have been proposed for various phased array transmitters:

- (1) Plate modulation.
- (2) Grid modulation (low- μ grid, modulating anode).
- (3) Grid modulation (high- μ grid).

When these three modulation techniques are applied to the generation of narrow pulses (small pulsewidths), it is no longer possible to disregard the energy wasted during the rise and fall time of the pulse, or the energy required to charge the stray capacitance associated with the modulator output and the power amplifier input. This "wasted" energy can be a considerable fraction of the total energy in the pulse.

In an attempt to evaluate the reduction of efficiency resulting from this "wasted" energy, the following analysis of the three modulation techniques was made. The results are presented in the form of a family of curves showing efficiency vs pulsewidth for various rise time to pulsewidth ratios, and a family of curves has been drawn for each of the three types of modulation. Efficiency is analyzed first in terms of the energy "wasted" in the video overlap and, second, in terms of the energy lost in charging the stray capacitance. It becomes apparent that as the pulsewidth becomes shorter, the stray capacitance becomes the most important factor.

B. BEAM PULSE EFFICIENCY

The following assumptions are made:

- (1) Rise and fall time are of equal duration and are approximately linear functions of time. (This is not too unreasonable because most often the rise and fall times are linear over the major portion of their duration since, in general, they result from a constant current source, usually a pentode or tetrode charging or discharging the capacitance associated with the circuit.)
- (2) Useful energy is available only during the flat region of the video pulse; i.e., the energy available during the rise and fall time is wasted.

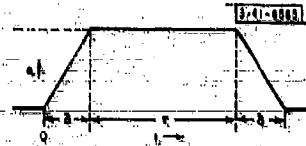
This assumption can be justified because of the nature of the discrimination problem. The resolution requirements are such that the only limitations on the leading and trailing edge should be the bandwidth of the transmitter tube (typically 50 or 100 Mcps) and the speed with which the RF drive pulses can be gated on and off (typically a few nanoseconds). Therefore, the slower rising video waveform will not deteriorate the output RF pulse if the RF drive comes on only during the flat-top region of the video pulse.

- (3) The pulse is of the following form:

δ = rise time

r = useful pulsewidth

$\frac{\delta}{r}$ = $\frac{\text{rise time}}{\text{pulsewidth}}$



- (4) All computations will be carried out on an energy-per-pulse basis.
- (5) Because of the assumed symmetry of the pulse, the energy "wasted" in the fall time will be assumed equal to that of the rise time. Therefore, from this point on, only the energy wasted in the rise time will be computed and then doubled when making efficiency calculations.
- (6) When plate efficiency is discussed in this report, it will be understood to include only the effect of energy wasted in the rise and fall time and in the modulator, and not the DC-to-RF conversion efficiency (usually approximately 33 percent). This latter efficiency will be discussed at the end of this chapter.

Case I: Plate Modulation of the Power Amplifier

In an electron-beam device that is plate-modulated, the following expression for the beam current is valid:

$$i_b = Ke_b^{3/2} \quad (1)$$

where

i_b = beam current

e_b = beam voltage

K = perveance = constant

The instantaneous plate power p - real part ($e_b i_b$) $\approx e_b i_b$

$$p = e_b (Ke_b^{3/2}) = Ke_b^{5/2} \quad (2)$$

The energy E developed within any interval is expressed as

$$E = \int p dt \quad (\text{integrated over the interval}) \quad (3)$$

The following tabulation shows the instantaneous power generated during the intervals that are of interest.

Interval	Instantaneous Voltage	Instantaneous Power
$t \leq 0$	$e_b = 0$	$p = 0$
$0 \leq t \leq \delta$	$e_b = \frac{E_{bb}}{\delta} t$	$p = K \left(\frac{E_{bb}}{\delta} \right)^{5/2} t^{5/2}$
$\delta \leq t \leq \delta + \tau$	$e_b = E_{bb}$	$p = K(E_{bb})^{5/2}$

The energy developed during the interval $t \leq 0$ is

$$E = 0 \quad (4)$$

The energy "wasted" during the interval $0 \leq t \leq \delta$ (the rise time) can be expressed as

$$\begin{aligned} E' &= \int_0^{\delta} p dt = \int_0^{\delta} K \left(\frac{E_{bb}}{\delta} \right)^{5/2} t^{5/2} dt = \left[K \left(\frac{E_{bb}}{\delta} \right)^{5/2} t^{7/2} \times \frac{2}{7} \right]_0^{\delta} \\ &= \frac{2K}{7} \left(\frac{E_{bb}}{\delta} \right)^{5/2} \delta^{7/2} = \delta \left[\frac{2K(E_{bb})^{5/2}}{7} \right] \end{aligned} \quad (5)$$

The energy developed during the interval $\delta \leq t \leq \delta + \tau$ (the useful region) can be expressed as

$$\begin{aligned} E &= \int_{\delta}^{\delta+\tau} p dt = \int_{\delta}^{\delta+\tau} K(E_{bb})^{5/2} dt \\ &= [K(E_{bb})^{5/2} t]_{\delta}^{\delta+\tau} = K(E_{bb})^{5/2} \times \tau \end{aligned} \quad (6)$$

Therefore,

$$\begin{aligned} \text{partial pulse efficiency}^* &= \frac{\text{useful pulse energy}}{\text{useful pulse energy} + \text{"wasted" energy (in rise and fall time)}} \\ &= \frac{1}{1 + \frac{\text{wasted energy}}{\text{useful energy}}} \\ &= \frac{1}{1 + \frac{2 \times \delta \left[\frac{2K(E_{bb})^{5/2}}{7} \right]}{K(E_{bb})^{5/2} \times \tau}} \end{aligned}$$

The following equation expresses in a useful form the value of partial pulse efficiency when plate modulation is employed:

$$\text{partial pulse efficiency}^* \text{ (for plate modulation)} = \frac{1}{1 + \frac{4}{7} \left(\frac{\delta}{\tau} \right)} \quad (7)$$

* These efficiency expressions do not include the effect of stray capacitance, nor of circuit losses in the modulator and grid; therefore, they are termed "partial efficiencies."

Case II: Grid Modulation of the Power Amplifier

The total current I_T in a gridless (triode) tube can be expressed as*

$$I_T = I_a + I_g = G(\mu V_g + V_a)^{3/2} \quad (8)$$

where

$$I_a = \text{anode current} \quad V_a = \text{anode voltage} \quad \mu = \frac{V_a}{V_g} \left| \frac{I_T}{I_a} \right| = \text{constant}$$

$$I_g = \text{grid current} \quad V_g = \text{grid voltage} \quad G = \text{constant}$$

The value of μ determined above is reasonably accurate, since μ varies little as I_a varies. Also, it will be assumed that the grid current is small with respect to the plate current; therefore,

$$I_a = K_1 G (\mu V_g + V_a)^{3/2} \quad (9)$$

where K_1 = proportionality constant between the plate current and the total space current. (This is probably not a constant, but the variation is small because $I_g \ll I_a$.) Assume $K_1 \approx 1$.

It is assumed that the plate voltage $V_a = E_{bb}$ = constant, and also that the grid drive pulse is of the form:



$$\begin{aligned} \text{instantaneous anode power} \quad \text{real part } [e_a i_a] &\approx e_a i_a \\ &= E_{bb} [K_1 G (\mu V_g + E_{bb})^{3/2}] \quad (10) \end{aligned}$$

The following tabulation shows the instantaneous power generated during the intervals that are of interest:

Interval	Instantaneous voltage v_g	Instantaneous Power P
$t \leq 0$	0	0
$0 < t < \delta$	$\frac{E_{G1}}{\delta} t$	$E_{bb} K_1 G \left[\mu \left(\frac{E_{G1}}{\delta} t + E_{bb} \right) \right]^{3/2}$
$\delta \leq t \leq \delta + \tau$	E_{G1}	$E_{bb} K_1 G (\mu E_{G1} + E_{bb})^{3/2}$

*A. H. W. Beck, Thermionic Valves, Their Theory and Design [Cambridge (England) University Press, 1953].

The energy developed during the interval $t \leq 0$ is

$$E = 0 \quad (14)$$

The energy "wasted" during the interval $0 \leq t \leq \delta$ (the rise time) can be expressed as

$$E = \int_0^\delta p dt = \int_0^\delta E_{bb} K_1 G \left[\mu \left(\frac{E_{G1}}{\delta} \right) t + E_{bb} \right]^{3/2} dt$$

To evaluate, let

$$y = \mu \left(\frac{E_{G1}}{\delta} \right) t + E_{bb}$$

$$dy = \mu \left(\frac{E_{G1}}{\delta} \right) dt$$

therefore,

$$dt = \frac{\delta dy}{\mu E_{G1}}$$

for the following limits:

$$\text{at } t = 0 \quad y = E_{bb}$$

$$\text{at } t = \delta \quad y = \mu E_{G1} + E_{bb}$$

Then,

$$\begin{aligned} E &= \int_{E_{bb}}^{(\mu E_{G1} + E_{bb})} E_{bb} K_1 G (y)^{3/2} \frac{\delta}{\mu E_{G1}} dy \\ &= \frac{E_{bb} K_1 G \delta}{\mu E_{G1}} y^{5/2} \times \frac{2}{5} \Big|_{E_{bb}}^{(\mu E_{G1} + E_{bb})} \\ E &= \frac{2 E_{bb} K_1 G \delta}{5 \mu E_{G1}} [(\mu E_{G1} + E_{bb})^{5/2} - E_{bb}^{5/2}] \quad (12) \end{aligned}$$

The energy developed during the interval $\delta \leq t \leq \delta + \tau$ (the useful region) is

$$\begin{aligned} E &= \int_\delta^{\delta+\tau} E_{bb} K_1 G (\mu E_{G1} + E_{bb})^{3/2} dt \\ &= E_{bb} K_1 G (\mu E_{G1} + E_{bb})^{3/2} t \Big|_\delta^{\delta+\tau} \\ E &= E_{bb} K_1 G (\mu E_{G1} + E_{bb})^{3/2} \times \tau \quad (13) \end{aligned}$$

Therefore,

$$\text{partial pulse efficiency} = \frac{1}{1 + \frac{\text{"wasted" energy}}{\text{useful energy}}}$$

$$= \frac{1}{2 \times \frac{2E_{bb} K_1 G_1 \delta}{5\mu E_{G1}} + \left[(\mu E_{G1} + E_{bb})^{5/2} - E_{bb}^{5/2} \right] \frac{1}{E_{bb} K_1 G_1 (\mu E_{G1} + E_{bb})^{3/2} \times \tau}}$$

The following equation expresses in a useful form the value of partial pulse efficiency when grid modulation is employed.

$$\text{partial pulse efficiency}^3 \text{ (for grid modulation)} = \frac{1}{1 + \left(\frac{\delta}{\tau}\right) \left[\frac{4}{5\mu E_{G1}} \right] \left\{ (\mu E_{G1} + E_{bb})^{5/2} - E_{bb}^{5/2} (\mu E_{G1} + E_{bb})^{-3/2} \right\}} \quad (14)$$

The previous calculations have shown only the reduction of efficiency resulting from energy wasted in the power tube during the rise and fall time of the output pulse. To gain an appreciation of the effect that the modulator and the stray capacitance have on the over-all efficiency, an attempt will be made to evaluate a new efficiency which includes the energy wasted in the modulator and the stray capacitance for each of the preceding three modulator techniques.

C. TOTAL PULSE EFFICIENCY

1. Plate Modulation

If plate modulation is used, the modulator is required to supply the entire beam modulation power. If we assume here a soft-tube modulator or an efficient hard-tube modulator, the efficiency varies between 60 and 80 percent. We will assume 75 percent over-all efficiency. Then,

$$\text{plate and modulator efficiency} \quad (0.75) = \frac{\text{energy out (useful)}}{\text{energy out (useful) + energy wasted (rise and fall time) + energy wasted (charging and discharging stray capacitance)}}$$

From the values previously obtained for the energy developed during the three intervals that are of interest [Eqs. (4), (5) and (6)], it follows that

$$\text{plate and modulator efficiency} \quad (0.75) = \frac{K(E_{bb})^{5/2} \times \tau}{K(E_{bb})^{5/2} \times \tau + 2 \times \delta \left[\frac{2K(E_{bb})^{5/2}}{\gamma} \right] + C(E_{bb})^2} \quad (15)$$

It should be noted that the energy wasted in charging and discharging the stray capacitance is equal to twice the energy stored in the stray capacitance. This results from the fact that an amount of energy equal to that stored is lost in the RC charging of the stray capacitance during the rise time; moreover, at the termination of the pulse, the energy that was stored is discharged

*This efficiency expression does not include the effect of stray capacitance, nor of modulator and grid circuit losses, and is therefore termed "partial efficiency."

through the tube and is wasted in the fall time. Hence, twice the stored energy is wasted, so that, in the case of plate modulation,

$$\boxed{\text{plate and modulator efficiency (for plate modulation)} = \frac{0.75}{1 + \left(\frac{\delta}{\tau}\right) \frac{1}{7} + \left(\frac{1}{\tau}\right) \frac{C}{K(E_{bb})^{1/2}}} \quad (16)}$$

2. Grid Modulation

It is assumed that the grid modulator is a hard-tube modulator and that its efficiency is 75 percent. Therefore,

$$\text{energy wasted (in modulator, grid circuit, and stray capacitance)} = 1.33 \text{ energy into (grid circuit and stray capacitance)}$$

If we assume that the grid acts somewhat like a diode, we can determine the energy into the grid circuit by using the results determined from our plate-modulation example with the plate voltage of our results replaced by the grid voltage; that is, during the rise time

$$\text{energy} = \frac{2}{7} K(E_{bb})^{5/2} \delta \quad [\text{Eq. (5)}]$$

and during the useful pulse region

$$\text{energy} = K(E_{bb})^{5/2} \times \tau \quad [\text{Eq. (6)}]$$

Let

$$K_2 = \text{grid permeance} = \frac{i_{\text{grid}}}{(V_{\text{grid}})^{3/2}}$$

Then

$$\begin{aligned} \text{energy wasted} &= 1.33 \left[\frac{2}{7} K_2 (E_{G1})^{5/2} \delta + K_2 (E_{G1})^{5/2} \times \tau \right] \\ &= 1.33 K_2 (E_{G1})^{5/2} \left(\tau + \frac{4}{7} \delta \right) \end{aligned}$$

All this energy is wasted in the grid circuit; in addition, the energy wasted in charging and discharging the stray grid capacitance is

$$E_{\text{capacitance}} = 1.33 (C E_{G1}^2)$$

Therefore,

$$\text{plate and modulator efficiency} = \frac{\text{useful energy}}{\text{useful energy} + \text{energy wasted (rise and fall time)} + \text{energy wasted (modulator, the grid circuit, and stray capacitance)}}$$

From Eqs. (12) and (13) and those above,

These characteristics are similar to those of the Watkins Johnson TWT being developed for Lincoln Laboratory.

Substituting these values into the three partial-pulse efficiency expressions, we obtain the following partial pulse efficiency* expressions:

For Plate Modulation

$$\text{partial pulse efficiency} = \frac{1}{1 + \frac{4}{7} \left(\frac{\delta}{\tau} \right)}$$

For Grid Modulation (low- μ grid)

$$\text{partial pulse efficiency} = \frac{1}{1 + \frac{4}{7} \left(\frac{\delta}{\tau} \right) + \frac{1}{10} \left(\frac{\delta}{\tau} \right)^2 + \frac{1}{10} \left(\frac{\delta}{\tau} \right)^3 + \frac{1}{10} \left(\frac{\delta}{\tau} \right)^4 + \frac{1}{10} \left(\frac{\delta}{\tau} \right)^5 + \frac{1}{10} \left(\frac{\delta}{\tau} \right)^6 + \frac{1}{10} \left(\frac{\delta}{\tau} \right)^7 + \frac{1}{10} \left(\frac{\delta}{\tau} \right)^8 + \frac{1}{10} \left(\frac{\delta}{\tau} \right)^9 + \frac{1}{10} \left(\frac{\delta}{\tau} \right)^{10}}$$

For Grid Modulation (high- μ grid)

$$\text{partial pulse efficiency} = \frac{1}{1 + \frac{4}{7} \left(\frac{\delta}{\tau} \right) + \frac{1}{10} \left(\frac{\delta}{\tau} \right)^2 + \frac{1}{10} \left(\frac{\delta}{\tau} \right)^3 + \frac{1}{10} \left(\frac{\delta}{\tau} \right)^4 + \frac{1}{10} \left(\frac{\delta}{\tau} \right)^5 + \frac{1}{10} \left(\frac{\delta}{\tau} \right)^6 + \frac{1}{10} \left(\frac{\delta}{\tau} \right)^7 + \frac{1}{10} \left(\frac{\delta}{\tau} \right)^8 + \frac{1}{10} \left(\frac{\delta}{\tau} \right)^9 + \frac{1}{10} \left(\frac{\delta}{\tau} \right)^{10}}$$

These three efficiency expressions have been plotted vs (δ/τ) . The resulting graphs indicate the effect on the efficiency as pulse shape is changed, i.e., when the pulse shape varies between a perfectly rectangular pulse (at $\delta/\tau = 0$) and a very slowly rising trapezoidal pulse $\delta/\tau \gg 1$. It can be seen that when just the energy lost in the rise and fall time in the tube is considered, plate modulation is most efficient, high- μ grid modulation is next most efficient, and low- μ grid modulation is least efficient. This results from the fact that in the grid modulation cases the beam voltage is at full E_{bb} during the entire rise and fall time. Hence, the energy wasted is greater than in the plate modulation case where the beam voltage rises with the beam current (see Fig. 3-27). Substituting this time into the total pulse efficiency expressions, we obtain the following:

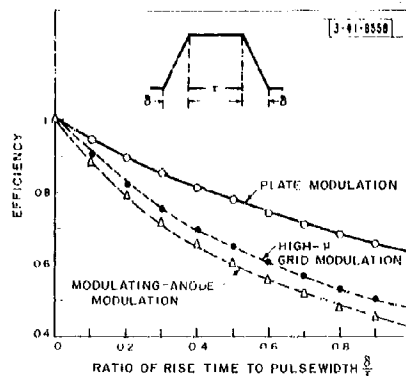
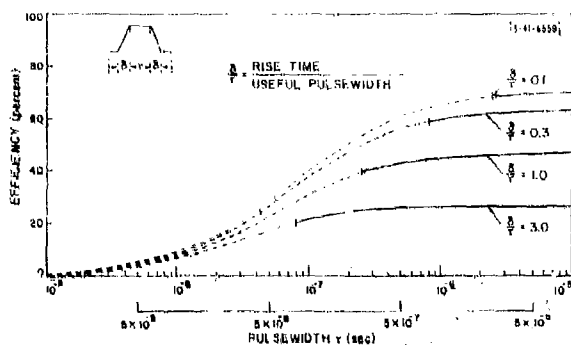


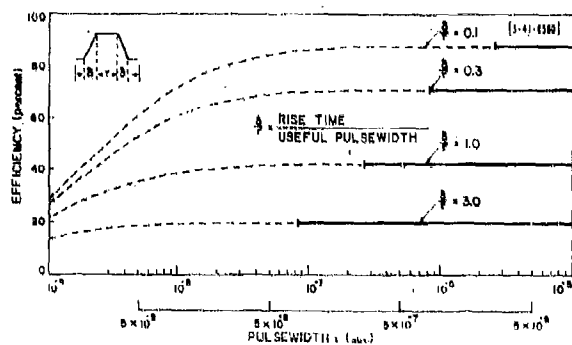
Fig. 3-27. Partial pulse efficiency vs (δ/τ) (ratio of rise time to useful pulsewidth).

* These efficiency expressions do not include the effect of stray capacitance, nor of modulator and grid circuit losses, and therefore are termed "partial efficiencies":

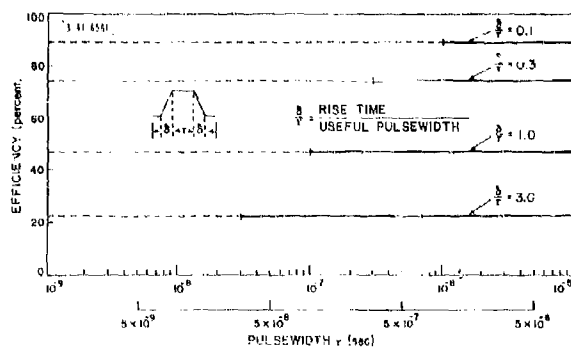
$$\text{partial pulse efficiency} = \frac{\text{useful pulse energy}}{\text{useful pulse energy} + \text{energy wasted in rise and fall time}}$$



(a) Plate modulation. Here, grid-circuit wasted energy is not a factor (see below).



(b) Grid modulation (low- μ grid modulating anode).



(c) Grid modulation (high- μ grid).

Fig. 3-28. Pulse efficiency vs pulsewidth. Pulse efficiency does not include the DC to RF conversion efficiency (usually 33 percent) present in most microwave tubes.

$$\text{Pulse efficiency} = \frac{\text{useful pulse energy}}{\text{useful pulse energy} + \text{"wasted" energy (in plate-circuit rise and fall time)} + \text{"wasted" energy (in modulator, the grid circuit and stray capacitance)}}$$

Dashed segments of the curves denote regions currently beyond the state of the art.

For Plate Modulation

From Eq. (16)

$$\text{plate and modulator efficiency} = \frac{0.75}{1 + \left(\frac{\delta}{\tau}\right) \frac{4}{7} + \left(\frac{1}{\tau}\right) \frac{5 \times 10^{-11}}{2 \times 10^{-6} (10^5)^{1/2}}}$$

$\text{plate and modulator efficiency (for plate modulation)} = \frac{0.75}{1 + \left(\frac{\delta}{\tau}\right) 0.572 + \left(\frac{1}{\tau}\right) 7.92 \times 10^{-8}}$	[see Fig. 3-28(a)]
--	--------------------

For Grid Modulation (low- μ grid)

As before,

$$E_{bb} = 100 \text{ kv}$$

$$\mu = 4$$

$$G = 2 \times 10^{-6} \frac{\text{amp}}{\text{volt}^{3/2}}$$

$K = 1$ (valid if grid current \ll plate current; in a modulating-anode tube this is true)

$$E_{G1} = 25 \text{ kv}$$

$$K_2 = 0 \left(\text{since } K_2 = \frac{i_{\text{grid}}}{(V_{\text{grid}})^{3/2}} \approx \frac{0}{(V_{\text{grid}})^{3/2}} \approx 0 \right)$$

$$C_{\text{stray}} = 50 \mu\text{f}$$

From Eq. (18)

$$\text{plate and modulator efficiency} = \frac{1}{1 + \left(\frac{\delta}{\tau}\right) \frac{1}{1.32} + \left(\frac{1}{\tau}\right) \frac{2.32 \times 10^{-9}}{10^5 \times 25 \times 10^{-6} (2.5 \times 10^4)^{1/2}}}$$

$\text{plate and modulator efficiency (for low-}\mu \text{ grid)} = \frac{1}{1 + \left(\frac{\delta}{\tau}\right) 1.32 + \left(\frac{1}{\tau}\right) 2.32 \times 10^{-9}}$	[see Fig. 3-28(b)]
--	--------------------

For Grid Modulation (high- μ grid)

$$E_{bb} = 21 \text{ kv}$$

$$E_{G1} = 360 \text{ v}$$

$$\mu = 140$$

$$G = 5 \times 10^{-6} \frac{\text{amp}}{\text{volt}^{3/2}} \text{ (microperveance } 5 \text{ gm)}$$

$K_1 = 1$ (i.e., as a first approximation assume the anode current approximately equals the total space current, since $i_{\text{grid}} \leq 1/10 i_{\text{plate}}$)

$$E_R \text{ (cutoff)} = 150 \text{ v}$$

$$C = 50 \mu\text{f}$$

$$K_2 = \frac{I_{grid}}{(V_{grid})^{3/2}} = \frac{1.8 \text{ amp}}{(210 \text{ V})^{3/2}} = 5.94 \times 10^{-4} \frac{\text{amp}}{\text{volt}^{3/2}}$$

From Eq. (16),

$$\text{plate and modulator efficiency} = \frac{1}{1 + \left(\frac{\delta}{\tau}\right) (1.075) + \left(\frac{\delta}{\tau}\right)^2 4.32 \times 10^{-12}}$$

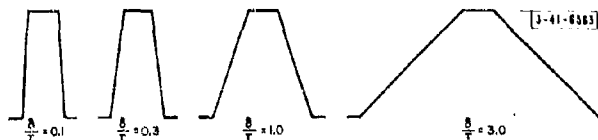
For $\tau \sim 10^{-9}$ the last term in the denominator is negligible. This implies that the energy wasted in the modulator and grid circuits and stray capacitance has negligible effect on the over-all efficiency in the high- μ grid case over the pulsewidths of interest. Therefore:

$$\text{plate and modulator efficiency (for high-}\mu \text{ grid)} = \frac{1}{1 + \left(\frac{\delta}{\tau}\right) 1.075} \quad [\text{see Fig. 3-28(c)}]$$

Note that for this high- μ grid case, efficiency vs τ curves for constant (δ/τ) will be horizontal lines, which appears reasonable. Since, if energy in the modulator, grid, and capacitance can be neglected, the ratio of the energy in the rise and fall time to the energy in the useful region of the pulse is constant for constant (δ/τ) ; the efficiency, therefore, remains constant as τ varies.

Typical values for the constants in each case are now substituted into these efficiency expressions and curves plotted (efficiency vs pulsewidth for each of the three types of modulation).

The interesting region for τ (the pulsewidth) varies between one nsec and ten msec (10^{-9} to 10^{-5} sec); therefore, plots of efficiency vs τ are drawn for four δ/τ ratios: $\delta/\tau = 0.1$, $\delta/\tau = 0.3$, $\delta/\tau = 1.0$, $\delta/\tau = 3.0$. In these curves δ/τ is used as the parameter. This presentation allows the shape of the pulse on the graphs to stay constant as pulsewidth is varied. The appearance of the pulses for the assumed δ/τ ratios is as follows:



E. CONCLUSIONS

Examination of the plotted curves of efficiency reveals that for narrow pulsewidths (10^{-9} to 10^{-7} sec) one of the terms that reduces the efficiency considerably is the wasted energy in the stray capacitance. This is a constant independent of pulsewidth, and when this wasted energy in the capacitance becomes large with respect to the energy in the pulse, the efficiency decreases rapidly. The effect of this energy is largest in the plate modulation case since the stray capacitance has to be charged to the full plate voltage; since energy is proportional to the voltage

squared, the efficiency curve for the plate modulation case exhibits in a most pronounced manner the effect of this wasted energy.

In the grid modulation low- μ grid (modulating probe) case, the voltage to which the stray capacitance has to be charged is reduced at best to $E_{bb}/4$. Therefore, the effect of the wasted energy in the stray capacitance is seen at the narrower pulsewidths but to a much less degree than in the plate modulation case; i.e.,

$$\left[\frac{E_{bb}/4}{E_{bb}} \right]^2 = \frac{1}{16}$$

In the grid modulation high- μ grid case, the voltage to which this stray capacitance has to be raised is considerably reduced, i.e., to E_{bb}/μ . Therefore, the effect of this wasted energy is reduced by approximately $1/\mu^2$ (which is very small if μ is large). It can be seen from the curves that over the pulsewidths of interest this wasted energy has negligible effect. All the curves asymptotically approach horizontal lines as τ is increased, since at this time the only wasted energy of importance is the energy wasted in the plate circuit during the rise and fall time of the pulse. Since the curves are plotted for constant (δ/τ) ratios, the efficiency approaches a constant as τ is increased.

An attempt to show the state of the art in the generation of narrow pulses is also indicated on these curves. It is assumed that rise times of the order of magnitude of 0.1 μsec are achievable with high- μ grid modulation, and 0.25 μsec with plate modulation and low- μ grid modulation. The portion of the curves requiring performance better than this have been dotted. (Also see Fig. 3-29.)

Break points or regions are observed in the various curves where the particular modulation technique becomes very inefficient. For example: In the plate modulation case, from 10^{-7} to 10^{-6} sec is a break region where the efficiency is almost halved. In the low- μ grid modulation

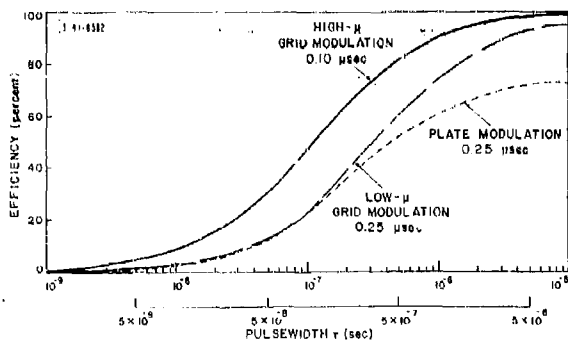


Fig. 3-29. Pulse efficiency vs pulsewidth as indicative of state of the art. Pulse efficiency does not include the DC to RF conversion efficiency (usually 30 percent) present in most microwave tubes.

$$\text{Pulse efficiency} = \frac{\text{useful pulse energy}}{\text{useful pulse energy} + \text{"wasted" energy (in plate-circuit rise and fall time)} + \text{"wasted" energy (in modulated, or the grid circuit and stray capacitance)}}$$

case, a break region occurs between 10^{-9} to 5×10^{-8} sec; it is noted that in the high- μ grid modulation case no break region occurs at all.

With regard to cost and space requirements, the plate modulation technique is obviously the most costly, both in space and in money. The low- μ grid modulation scheme, since it must be capable of high-voltage isolation and high-voltage grid pulses E_{bb}/μ , is the second most costly, both in space and in money. It would appear that, since the high- μ grid modulation scheme involves a very low voltage grid pulse, and with some possible configurations no high-voltage isolation is required, the modulator can be comparatively inexpensive with regard to both space and money. It is recognized that for the high- μ grid modulation specified, 20 tubes of smaller peak power (100 kw) would have to be modulated to duplicate the low- μ grid modulation of one 2-megawatt tube. It is still believed, however, that a modulator to modulate 20 low-voltage pulse tubes could be built at considerably less cost in space and money than a modulating-anode modulator or a plate modulator.

It should be stated that the efficiencies as given by the curves apply only to the video or pulse efficiency and do not include the loss which occurs in converting from DC to RF in the power amplifier. This DC to RF conversion is usually of the order of magnitude of 30 to 33 percent; therefore, the over-all plate efficiency is determined by multiplying the efficiencies given on the curves by 0.33.

In conclusion, grid modulation utilizing a grid with as high a μ as possible appears, from the point of view not only of efficiency but also of cost and space, to be the optimum way to modulate power amplifiers for narrow-pulse operation.

Curves useful in predicting the video efficiency have been presented as a function of pulse-width for three modulation techniques.

CHAPTER IV MINIMUM-COST ARRAY CONFIGURATIONS

I. Cartledge

SUMMARY

This chapter presents a purely formal method for minimizing the cost of a phased array system when the cost of the elements is known. Algebraic design equations are derived for minimum-cost tracking and surveillance array configurations.

A. INTRODUCTION

The radar capability desired from a phased array radar can be expressed in the form

$$\bar{p} n_t^\alpha n_r^\beta - \Gamma = 0 \quad (1)$$

where \bar{p} is the average power radiated per element in watts, n_t is the number of transmitting elements, n_r is the number of receiving elements and Γ , α and β are constants which can be derived from coverage and other radar requirements.

The cost of building and operating a phased array can be expressed as

$$C = C_t n_t + C_p \bar{p} n_t + C_r n_r \quad (2)$$

where C_t is the cost of providing, installing and operating a transmitter module (plus a suitable portion of the structure and overhead costs) in dollars per element, C_p is the cost of producing average power in dollars per watt and C_r is the over-all cost of providing, installing and operating a receiving element (in dollars per element).

The cost C of Eq. (2) can be minimized subject to the constraint of Eq. (1) by partial differentiation with a LaGrangian multiplier. This process (which is carried out in detail in Appendix A, Sec. I) yields the following design equations. For $\alpha \neq 1$,

$$\bar{p} = \frac{C_t}{(\alpha - 1) C_p} \quad (3)$$

$$n_t = \left[\frac{\Gamma (\alpha - 1)^{(\beta + 1)} C_p C_r^\beta}{\beta^\beta C_t^{\beta + 1}} \right]^{1/(\alpha + \beta)} \quad (4)$$

$$n_r = \frac{\beta}{\alpha - 1} \frac{C_t}{C_r} n_t \quad (5)$$

The constants α , β and Γ will be evaluated for three cases: volume searching, multitarget tracking with a rectangular receiving aperture and multitarget tracking with a "Mill's cross" receiving aperture.

B. SURVEILLANCE CASE

In the volume search case, Γ is found by manipulating the radar range equation to get adequate signal-to-noise ratio for the desired probabilities of detection and false alarm over the

desired volume. In the simple case where the volume to be searched is a sector of a sphere with the radar at the center,

$$\bar{p}n_t n_r = \Gamma_s = \frac{5\pi r^4 K T_e L \Theta R}{2D_x D_y \lambda^2 \eta^2 T_f \sigma} \quad (6)$$

where

r is the maximum range in meters,

K is Boltzmann's constant 1.34×10^{-23} ,

T_e is the receiver effective temperature in $^{\circ}K$,

L is the system loss,

Θ is the solid angle to be searched in steradians,

R is the ratio $2E/N_0$ needed for the desired \bar{p}_d and \bar{p}_n ,

D_x and D_y are the horizontal and vertical element spacings in wavelengths (in two orthogonal directions). Note that the maximum allowable D is a function of the maximum scan angle to be used*

λ is the wavelength in meters,

η is the aperture efficiency,

T_f is the "frame time" to completely cover the volume of interest,

σ is the target cross section in square meters (specified by the "customer").

Since $\alpha = 1$ in this case, Eqs. (3), (4) and (5) do not apply. Extrema do not occur for finite nonzero \bar{p}_d and \bar{p}_n . Since the values of \bar{p} that can be achieved in practice have an upper limit, we re-examine the cost with \bar{p} fixed and the constraint

$$\bar{p}n_t n_r = \Gamma_s - 0 \quad (7)$$

This examination is carried out in detail in Appendix A, Sec. II [Eqs. (A-7) through (A-14)] and results in

$$n_r = \frac{(C_t + C_p \bar{p})}{C_r} \quad (8)$$

$$n_t = \sqrt{\frac{\Gamma_s C_r}{\bar{p}(C_t + C_p \bar{p})}} \quad (9)$$

C. TRACKING CASE

In the tracking case, the required signal-to-noise ratio is a function of the angular accuracy desired and the aperture geometry. The constraint equation can be obtained by equating the R given by the radar range equation with that required for angular accuracy. For example, consider a filled rectangular aperture. The required standard deviation in angle $\delta\theta$ is specified by

* J. L. Allen, et al., "Phased Array Radar Studies, 1 July 1960 to 1 July 1961," Technical Report No. 236 [U], Lincoln Laboratory, M. I. T. (13 November 1961), p. 291, ASTIA 271724, H-474.

the "customer." Maximum element spacings D_x and D_y are set by the desired maximum coverage angles (which are specified by the "customer"). In the case of a rectangular aperture,*

$$\delta\theta_x = \frac{3}{\pi \sqrt{R}} \left(\frac{\lambda}{L} \right) = \frac{\sqrt{3}}{\pi \sqrt{R} n_x D_x} \quad (10)$$

Similarly,

$$\delta\theta_y = \frac{\sqrt{3}}{\pi \sqrt{R} n_y D_y} \quad (11)$$

Multiplying Eq. (10) by Eq. (11) and rearranging, we get

$$R = \frac{3}{\pi^2 D_x D_y n_x n_y \delta\theta_x \delta\theta_y} \quad (12)$$

(n_x and n_y are the number of receiving elements in a row and a column, respectively; hence, $n_r = n_x n_y$).

The radar range equation can be rearranged for array radars:

$$R = \frac{E_e n_t^2 n_y D_x^2 D_y^2 \lambda^2 \eta^2 \sigma}{2\pi r^4 L K T_c} \quad (13)$$

where E_e is the transmitted energy per look per element.

Now equate the right-hand members of Eqs. (12) and (13) and multiply both sides of the result by N/T_c , where N is the number of targets to be tracked and T_c is the "frame time." Note that

$$\frac{E_e N}{T_c} = \bar{P} \quad (14)$$

$$\bar{P} n_t^2 n_r^2 = \frac{6r^4 L K T_c}{D_x^3 D_y^3 \pi \lambda^2 \eta^2 T_c \sigma \delta\theta_x \delta\theta_y} = \Gamma_t \quad (15)$$

Equations (3), (4) and (5) apply.

In the case of a symmetrical Mill's-cross receiving aperture using identical crossed lines one element wide, for equal angular accuracy in both planes, Eqs. (10) and (11) become

$$\delta\theta = \frac{2\sqrt{3}}{\pi \sqrt{R} n_r D} \quad (16)$$

*R. Manasse, "Summary of Maximum Theoretical Accuracy of Radar Measurements," Technical Series Report No. 2 [U], MITRE Corporation, Bedford, Massachusetts.

Squaring and rearranging Eq. (16) gives

$$R = \frac{12}{\pi^2 n_r^2 D^2 \delta \theta^2} \quad (17)$$

Combining Eq. (17) with Eq. (13), with n_r in Eq. (13) replaced by $n_r/2$, gives

$$\bar{p} n_t^2 n_r^3 = \frac{48 N^4 L K T_e}{\pi D^6 \lambda^2 \eta^2 \sigma \delta \theta^2 \Gamma_a} = \Gamma_e \quad (18)$$

Again, Eqs. (3), (4) and (5) apply.

If the angular accuracy of the Mill's cross is not symmetrical, two constraint equations with corresponding LaGrange multipliers are required. This process is completed in Appendix A, Sec. III, and gives rise to the following design equations:

$$n_t = \sqrt{\frac{C_p C_r^3}{27 C_t^4} \Gamma_a \left[(D_x \delta \theta_x)^{-2/3} + (D_y \delta \theta_y)^{-2/3} \right]^3} \quad (19)$$

$$n_x / n_y = \frac{C_t n_t}{C_t} \quad (20)$$

$$\frac{n_x}{n_y} = \left(\frac{\delta \theta_y}{\delta \theta_x} \right)^{2/3} \quad (21)$$

$$\bar{p} = \frac{C_t}{C_p} \quad (22)$$

where

$$\Gamma_a = \frac{6 r^4 L K T_e N}{\pi D_x^2 D_y^2 \lambda^2 \eta^2 \sigma \Gamma_e} \quad (23)$$

APPENDIX A
PARTIAL DIFFERENTIATION WITH A LAGRANGIAN MULTIPLIER

I. GENERAL CASE

The cost can be expressed as

$$C = C_t n_t + C_p \bar{p} n_t + C_r n_r + \xi (n_t^\alpha \bar{p} n_r^\beta - \Gamma) \quad (\text{A-1})$$

By partial differentiation we obtain:

$$\frac{\partial C}{\partial n_t} = C_t + C_p \bar{p} + \alpha \xi n_t^{\alpha-1} \bar{p} n_r^\beta = 0 \quad (\text{A-2})$$

$$\frac{\partial C}{\partial \bar{p}} = C_p n_t + \xi n_t^\alpha n_r^\beta = 0 \quad (\text{A-3})$$

$$\frac{\partial C}{\partial n_r} = C_r + \beta \xi n_t^\alpha \bar{p} n_r^{\beta-1} = 0 \quad (\text{A-4})$$

$$\frac{\partial C}{\partial \xi} = n_t^\alpha \bar{p} n_r^\beta - \Gamma = 0 \quad (\text{A-5})$$

Eliminating ξ from Eqs. (A-2) and (A-3) yields

$$C_t n_t = (\alpha - 1) C_p \bar{p} n_t$$

whence

$$\bar{p} = \frac{C_t}{(\alpha - 1) C_p} \quad (\text{A-6})$$

Eliminating ξ from Eqs. (A-3) and (A-4) yields

$$n_r = \frac{\beta C_p n_t \bar{p}}{C_r} = \frac{\beta C_t}{(\alpha - 1) C_r} n_t \quad (\text{A-7})$$

Substituting Eqs. (A-6) and (A-7) into Eq. (A-5) yields

$$n_t = \left[\frac{\Gamma (\alpha - 1)^{(\beta+1)} C_p C_r^\beta}{\beta^\beta C_t^{\beta+1}} \right]^{1/(\alpha+\beta)} \quad (\text{A-8})$$

II. SURVEILLANCE CASE WHERE \bar{p} IS SET BY PRACTICAL CONSIDERATIONS

Where \bar{p} is set by practical considerations, Eq. (A-1) becomes

$$C = (C_t + C_p \bar{p}) n_t + C_r n_r + \xi (\bar{p} n_t n_r - \Gamma) \quad (\text{A-9})$$

By partial differentiation we obtain:

$$\frac{\partial C}{\partial n_t} = (C_t + C_p \beta) + \xi \beta n_t = 0 \quad (\text{A-10})$$

$$\frac{\partial C}{\partial n_t} = C_t + \xi \beta n_t = 0 \quad (\text{A-11})$$

$$\frac{\partial C}{\partial \xi} = \beta n_t n_r - F_g = 0 \quad (\text{A-12})$$

Combining Eq. (A-8) with Eq. (A-9) yields

$$n_t = \frac{(C_t + C_p \beta)}{C_t} n_t \quad (\text{A-13})$$

Combining Eqs. (A-12) and (A-13) yields

$$n_t = \frac{F_g C_t}{\beta(C_t + C_p \beta)} \quad (\text{A-14})$$

III. ASYMMETRIC MILL'S CROSS

In the case of an asymmetric Mill's cross aperture,

$$R_x = \frac{3}{\pi^2 n_x^2 D_x^2 \theta_x^2} = \frac{E_0 n_t^2 n_x D_x^2 D_y^2 \lambda^2 \eta^2 \sigma}{2\pi r^4 LKT_e} \quad (\text{A-15})$$

$$R_y = \frac{3}{\pi^2 n_y^2 D_y^2 \theta_y^2} = \frac{E_0 n_t^2 n_y D_x^2 D_y^2 \lambda^2 \eta^2 \sigma}{2\pi r^4 LKT_e} \quad (\text{A-16})$$

Multiply Eqs. (A-15) and (A-16) by N/T_f and rearrange to obtain

$$\beta n_t^2 n_x^3 = \frac{I_c}{D_x^2 \theta_x^2} \quad (\text{A-17})$$

and

$$\beta n_t^2 n_y^3 = \frac{I_c}{D_y^2 \theta_y^2} \quad (\text{A-18})$$

where

$$I_c = \frac{6r^4 LKT_e N}{\pi D_x^2 D_y^2 \lambda^2 \eta^2 \sigma T_f}$$

and

$$C = C_p n_t + C_p \bar{n}_t + C_p n_x + C_p n_y + \xi \left[n_t^2 n_x^3 \bar{n} - \frac{\Gamma_x}{D_x^2 \delta \theta_x^2} \right] + \psi \left[n_t^2 n_y^2 \bar{n} - \frac{\Gamma_y}{D_y^2 \delta \theta_y^2} \right] \quad (\text{A-19})$$

Set

$$\frac{\Gamma_x}{D_x^2 \delta \theta_x^2} = \Gamma_x \quad \text{and} \quad \frac{\Gamma_y}{D_y^2 \delta \theta_y^2} = \Gamma_y \quad (\text{A-20})$$

Then

$$\frac{\partial C}{\partial n_t} = C_p + C_p \bar{n} + 2\xi n_t n_x^3 \bar{n} + 2\psi n_t n_y^2 \bar{n} = 0 \quad (\text{A-21})$$

$$\frac{\partial C}{\partial n_x} = C_p + 3\xi n_t^2 n_x^2 \bar{n} \quad (\text{A-22})$$

$$\frac{\partial C}{\partial n_y} = C_p + 3\psi n_t^2 n_y^2 \bar{n} = 0 \quad (\text{A-23})$$

$$\frac{\partial C}{\partial \bar{n}} = C_p n_t + \xi n_t^2 n_x^3 + \psi n_t^2 n_y^2 = 0 \quad (\text{A-24})$$

$$\frac{\partial C}{\partial \xi} = n_t^2 n_x^3 \bar{n} - \Gamma_x = 0 \quad (\text{A-25})$$

$$\frac{\partial C}{\partial \psi} = n_t^2 n_y^2 \bar{n} - \Gamma_y = 0 \quad (\text{A-26})$$

Equations (A-21) and (A-24) are combined to obtain

$$\bar{n} = \frac{C_p}{C_p} \quad (\text{A-27})$$

Equations (A-22), (A-23) and (A-24) can be combined to obtain

$$n_x + n_y = \frac{3C_p}{C_p} n_t \quad (\text{A-28})$$

Finally, the above results, combined with Eqs. (A-25) and (A-26), yield

$$n_t = \sqrt{\frac{C_p^3 C_p}{27 C_p^4} \left[\Gamma_x (D_x^2 \delta \theta_x^2)^{-2/3} + \Gamma_y (D_y^2 \delta \theta_y^2)^{-2/3} \right]^{3/2}} \quad (\text{A-29})$$

and

$$\frac{n_x}{n_y} = \left(\frac{D_y^2 \delta \theta_y^2}{D_x^2 \delta \theta_x^2} \right)^{1/3} \quad (\text{A-30})$$